Near-infrared induced release for localized on-demand drug delivery

Near-Infrared Induced Release for Localized On-Demand Drug Delivery

PROEFSCHRIFT

ter verkrijging van de graad van doctor aan de
Technische Universiteit Eindhoven, op gezag van de
rector magnificus, prof.dr.ir. C.J. van Duijn, voor een
commissie aangewezen door het College voor
Promoties in het openbaar te verdedigen
op maandag 16 november 2009 om 16.00 uur

door

Mikaël Allan Myriam Eugène Vertommen

geboren te Ottignies, België

Dit proefschrift is goedgekeurd door de promotor:

prof.dr.ir. J.T.F. Keurentjes

Copromotoren:
dr.ir. R. Hoogenboom
en
dr.ir. M.F. Kemmere

Summary

By non-invasive external triggering of drug release from an implant, pulsewise administration can be realized according to the patient's needs and at specific locations in the human body. In comparison to more traditional delivery forms (e.g. oral or by injection), externally triggered drug release potentially offers the advantage of increased patient compliance due to easy and painless dosing, higher bioavailability, and lower doses of potent drugs, thereby reducing the toxic side effects commonly associated with systemic administration.

The main focus in this thesis is on externally triggered on-demand release of relatively small drug molecules using the large change in diffusivity occurring near the glass transition temperature (T_g) of a polymer matrix. When the polymer is in the glassy state ($T < T_g$), the entrapped drug is virtually immobile, while in the rubbery state ($T > T_g$) the high amount of free volume and flexibility of the polymer chains allows diffusion of the drug out of the implant. The rate of diffusion greatly depends on the size, shape and flexibility of the drug, as well as its relation to the flexibility of the polymer chain. To a certain extent, these phenomena can be described by the free volume theory (FVT). However, the FVT has mainly been applied to describe diffusion of relatively small solutes in rubbery polymer-solute systems, whereas only a limited amount of research has dealt with its application to large solutes, such as drug molecules. Chapter 5 demonstrates that to use the FVT for diffusion of larger molecules approaching the size of polymer jumping units, a better understanding of polymer/drug dynamics is required.

Non-invasive thermal triggering of drug release is achieved using near-infrared radiation (NIR), bordering on visible red light in the electromagnetic spectrum. The low absorption of water and tissue chromophores in this region allows for a relatively high penetration of NIR into the human body of up to several centimeters, making it attractive for biomedical applications. Since most polymers do not intrinsically absorb NIR, an NIR-absorbing compound is required. Here, a quaterrylenebis(dicarboximide) derivative, exhibiting a

maximum in absorption around 780 nm, is incorporated into polymer matrices by conventional polymer processing techniques without affecting the T_g. UV-Visible spectroscopy reveals the formation of face-to-face stacked molecular aggregates on incorporation of this dye by solvent casting, which can be suppressed by incorporation or post-processing at elevated temperature. Although dye aggregation affects the absorption spectrum, the absorption at the wavelength of the NIR-source can effectively be controlled by increasing the dye concentration. Using a 785 nm NIR-laser, initial heating rates of over 3ºC s^{-1} and steady state temperature increases as high as 80ºC are reached.

To investigate the effect of NIR-dye distribution on heat generation inside the polymer matrix in aqueous environment, a finite element (FE) model for NIR-induced heating is developed. Since the main resistance to mass transfer is located at the polymer/water interface, heat generation should mainly be located at the surface of the implant. Coating the implant with a dye containing layer therefore yields the best combination of high surface temperatures without exposing the inside of the implant to excessive temperatures. The FE-model is subsequently used to estimate the temperatures that can be achieved *in vivo* using NIR, taking into account scattering and absorption by skin and subcutaneous tissue. Compared to aqueous environment (*in vitro*), higher temperatures are induced *in vivo* due to a lower amount of heat dissipation. By using an insulating layer, the tissue can be protected from high temperatures, thus preventing tissue damage from occurring and enabling NIR-induced drug release.

Experimentally, both *in vitro* and *in vivo*, repeated and reproducible on-off release of ibuprofen is demonstrated by non-invasive selective heating of a polylactide implant using near-infrared radiation, attaining on-off ratios in excess of 1,000. Oversaturation of the implant ensures replenishment of released ibuprofen by partial dissolution of the drug crystals providing a constant concentration of ibuprofen dissolved in the polymer and, consequently, a constant driving force for release. Although the large plasticizing effect of ibuprofen lowers the T_g of the polymer to about 0ºC (i.e. the bulk polymer is in a rubbery state), release of ibuprofen at body temperature is extremely low, attributed to the spontaneous formation of a glassy surface layer. Drug release can thus be controlled by changing the temperature of this switching layer around T_g. In addition, this self-sealing mechanism provides an intrinsic safety precaution, as rupture of the implant will not

result in dose dumping. The simple design of an implant based on the glass transition switch thus offers an appealing drug delivery system. It should be realized, however, that strict requirements are imposed on the polymer, and that new solubility and diffusivity data need to be generated for each new drug/polymer combination.

Although the T_g can be effectively used to switch on and off the release of 'simple' drug molecules, controlling release of large molecules, such as peptide drugs, is impossible. For this reason, an alternative mechanism is explored based on the reversible swelling capability of a hydrogel around the so-called lower critical solution temperature (LCST). A drug reservoir is covered by a thermoresponsive composite membrane, consisting of a microporous polymeric support and a hydrogel graft layer. Above the LCST of the hydrogel (on-state), the shrunken state of the graft layer appears to only partially cover the membrane, allowing protein permeation through the uncovered pores. Provided the grafting degree is high enough, the swollen hydrogel covers the membrane completely below the LCST (off-state), thus preventing protein permeation. In this way, reversible on/off-switching of protein permeation through a thermoresponsive composite membrane with negligible permeation in the off-state is demonstrated. The on-demand release mechanism proposed in this thesis is based on switching the membrane surface coverage rather than previously reported switches based on effective pore size or hydrogel mesh size, thus allowing for higher fluxes in the on-state, since permeation is not limited by pore-narrowing.

Both the T_g- and the LCST-concept permit long-term and patient-friendly administration of a wide variety of medicines, ranging from systemic dosing of drugs with low oral bioavailability to drugs required locally. This thesis presents a proof of principle for on-demand drug delivery using a laser as NIR-source. From a commercial point of view, it is expected that the use of cheaper light emitting diodes (LEDs) in the NIR range can lead to the design of hand-held devices suitable for near-infrared induced drug delivery in both a clinical and home environment.

Samenvatting

Door medicijnafgifte vanuit een implantaat van buitenaf aan- en uit te schakelen, kan op niet-invasieve wijze gepulseerde dosering worden bereikt naar de behoeften van de patiënt. Deze lokale extern gereguleerde toediening biedt in vergelijking met traditionele toedieningsvormen (bv. oraal of via injectie) mogelijk het voordeel van toenemende medicatietrouw van patiënten als gevolg van makkelijke en pijnloze dosering, hogere biologische beschikbaarheid, en lagere benodigde doses van krachtige medicijnen. Dit laatste leidt ertoe dat toxische bijwerkingen, die vaak met systemische toediening gepaard gaan, worden verminderd. Potentiële toepassingen omvatten patiënten die last hebben van chronische pijn of terugkerende ontstekingen (zoals reumatoïde artritis), en lokale toediening van krachtige cytostatica tijdens chemotherapie.

Dit proefschrift richt zich voornamelijk op extern geschakelde afgifte van relatief kleine moleculen, waarbij gebruik wordt gemaakt van de grote verandering in diffusiesnelheid rondom de glasovergangstemperatuur (T_g) van een polymeermatrix. Als het polymeer in de glasachtige toestand is ($T < T_g$), kan het opgesloten medicijn vrijwel niet bewegen, terwijl de medicijnmoleculen in de rubberachtige toestand ($T > T_g$) uit het implantaat kunnen diffunderen door het toegenomen vrije volume en de flexibiliteit van de polymeerketens. De diffusiesnelheid hangt in grote mate af van de grootte, vorm en flexibiliteit van het medicijnmolecuul, ook in relatie tot de flexibiliteit van de polymeerketens. Tot op zekere hoogte kan dit worden beschreven door de vrije volume theorie (FVT). De FVT is echter voornamelijk toegepast op de diffusie van relatief kleine moleculen in rubberachtige polymeren, terwijl slechts weinig onderzoek zich richt op de toepassing voor grotere moleculen, zoals medicijnen. Hoofdstuk 5 toont aan dat een beter begrip van polymeer/medicijn interactie noodzakelijk is om de FVT te kunnen gebruiken voor diffusie van grote moleculen.

Medicijnafgifte wordt thermisch geïnduceerd met behulp van nabij-infrarode straling (NIR), grenzend aan het zichtbare rode licht in het elektromagnetische spectrum. Door de relatief lage absorptie van chromoforen in water en weefsel in dit golflengtebereik kan

NIR tot enkele centimeters indringen in het menselijk lichaam, waardoor het aantrekkelijk wordt voor biomedische toepassingen. Aangezien de meeste polymeren nauwelijks NIR absorberen, moet gebruik worden gemaakt van een NIR-absorberende toevoeging. In dit onderzoek wordt een quaterryleenbis(dicarboximide)-derivaat gebruikt, met een absorptiepiek rond 780 nm, die met behulp van conventionele polymeerverwerkingstechnieken kan worden ingemengd in polymeren matrices zonder de T_g te beïnvloeden. UV-Vis spectroscopie toont de vorming van moleculaire aggregaten aan indien deze kleurstof wordt ingemengd door middel van een solvent-casting techniek. De hoeveelheid aggregaten kan worden verminderd door nabewerking van de ontstane matrix bij verhoogde temperatuur. Hoewel de aggregatie het absorptiespectrum beïnvloedt, kan de mate van absorptie bij de golflengte van de NIR-bron wel effectief worden gestuurd met de concentratie van de kleurstof. Met behulp van een 785 nm NIR-laser worden zo initiële opwarmsnelheden van meer dan 3ºC s^{-1} en toenames in de eindtemperatuur van meer dan 80ºC bereikt.

Om het effect van de verdeling van de kleurstof op de warmteontwikkeling binnenin de polymeermatrix in een waterige omgeving te onderzoeken, is een eindig elementen model voor NIR-geïnduceerde opwarming ontwikkeld. Aangezien de voornaamste weerstand voor massatransport zich aan het polymeer/water oppervlak bevindt, zou warmteontwikkeling ook voornamelijk aan het oppervlak van het implantaat moeten plaatsvinden. Het coaten van het implantaat met een kleurstof bevattende laag leidt daarom tot de beste combinatie van een hoge oppervlaktetemperatuur zonder dat de binnenkant van het implantaat wordt blootgesteld aan te hoge temperaturen. Het eindig elementen model is vervolgens toegepast om de temperatuur af te schatten die *in vivo* kan worden bereikt, waarbij rekening wordt gehouden met verstrooiing en absorptie van licht door de huid en onderhuids weefsel. Er worden in vergelijking met een waterige omgeving (*in vitro*) hogere temperaturen bereikt als gevolg van verminderde warmte-afgifte aan de omgeving. Het omliggende weefsel kan worden beschermd tegen hoge temperaturen door gebruik te maken van een isolerende laag rondom het implantaat, waardoor schade aan het weefsel wordt voorkomen en NIR-geïnduceerde medicijnafgifte mogelijk wordt.

Experimenteel is, zowel *in vitro* als *in vivo*, herhaald en reproduceerbaar aan- en uitschakelen van de afgifte van ibuprofen als modelstof aangetoond door niet-invasieve selectieve opwarming van een polylactide implantaat met behulp van NIR, waarbij aan/uit-verhoudingen van medicijnafgifte van meer dan een factor 1000 worden bereikt. Oververzadiging van het implantaat zorgt voor aanvulling van het afgegeven ibuprofen door het gedeeltelijk oplossen van medicijnkristallen, waardoor een constante hoeveelheid ibuprofen opgelost blijft in het polymeer, zodoende leidend tot een constante drijvende kracht voor afgifte. Ook al zorgt het grote plasticerende effect van ibuprofen voor een verlaging van de T_g van het polymeer tot ongeveer 0ºC (de bulk van het polymeer verkeert daarmee in een rubberachtige toestand), de afgifte van ibuprofen bij lichaamstemperatuur blijft toch heel laag, wat wordt toegeschreven aan de spontane vorming van een glasachtige oppervlaktelaag. Medicijnafgifte kan zodoende gestuurd worden door de temperatuur van deze schakellaag te veranderen rond T_g. Daarnaast zorgt dit zelfafsluitende mechanisme voor een intrinsiek veiligheidsaspect, aangezien een breuk van het implantaat niet direct zal leiden tot volledige afgifte van de gehele medicijnvoorraad, waarmee een overdosis wordt voorkomen. Dit eenvoudige ontwerp van een implantaat gebaseerd op de T_g-switch biedt zodoende een aantrekkelijk afgiftesysteem. Men moet zich wel realiseren dat er strikte eisen worden gesteld aan het polymeer, en dat nieuwe oplosbaarheid- en diffusiedata moeten worden bepaald voor elke nieuwe medicijn/polymeer combinatie.

Hoewel de T_g effectief kan worden toegepast om de afgifte van 'eenvoudige' medicijnmoleculen aan- en uit te schakelen, is het reguleren van de afgifte van grote moleculen, zoals peptiden, onmogelijk. Om deze reden is ook een alternatief mechanisme onderzocht, dat is gebaseerd op het reversibel zwellen van een hydrogel rond de laagste kritische oplosbaarheidstemperatuur (LCST). Een medicijnreservoir wordt daarbij bedekt met een temperatuurgevoelig membraan, bestaande uit een microporeuze polymeren drager bedekt met een hydrogel laag. Boven de LCST van de hydrogel, zorgt de ongezwollen toestand ervoor dat het microporeuze membraan slechts gedeeltelijk bedekt is, waardoor eiwitpermeatie door de onbedekte poriën mogelijk wordt. Indien voldoende hydrogel is aangebracht, bedekt de gezwollen hydrogel het membraan volledig beneden de LCST, waardoor permeatie van het eiwit wordt verhinderd. Op deze manier kan

reversibel aan/uit-schakeling van eiwitten door temperatuurgevoelige membranen worden bewerkstelligd, waarbij verwaarloosbare permeatie in de uit-toestand wordt aangetoond. Het afgiftemechanisme dat in dit proefschrift wordt voorgesteld is gebaseerd op het veranderen van de bedekkingsgraad van het membraanoppervlak, in tegenstelling tot eerder gerapporteerde mechanismen gebaseerd op de effectieve poriegrootte of vrije volume binnen de hydrogel, waardoor hogere afgiftesnelheden in de aan-toestand kunnen worden bereikt aangezien permeatie niet wordt beperkt door porievernauwing.

Zowel de T_g- als het LCST-concept kunnen leiden tot patiëntvriendelijke toediening van een groot aantal medicijnen, variërend van systemische toediening van medicijnen met een lage orale biologische beschikbaarheid tot medicijnen die slechts lokaal toegepast dienen te worden. Dit proefschrift dient als een 'proof of principle' voor medicijnafgifte met behulp van een laser als nabij-infrarode bron. Vanuit een commercieel standpunt kan verwacht worden dat met behulp van de goedkopere LED-technologie handzame apparaten kunnen worden ontwikkeld die geschikt zijn voor nabij-infrarood geïnduceerde medicijnafgifte, zowel geschikt voor thuisgebruik als in een klinische omgeving.

Table of Contents

CHAPTER 1

Near-Infrared Radiation in Controlled Drug Delivery

Abstract

Based on an overview of drug delivery methods, the need for a pulsatile drug release system that can be repeatedly switched on and off in a non-invasive manner is discussed, specifically focusing on near-infrared radiation (NIR) as an external thermal trigger. Some current biomedical applications of NIR are addressed, which are mainly based on the relatively high transparency of tissue to NIR. The main focus in this thesis is on the controlled release of relatively small drug molecules, induced by NIR, using the large change in diffusivity inside a polymer matrix as the glass transition temperature (T_g) of the polymer is traversed. In the rubbery state, the high amount of free volume and flexibility of the polymer chains allows release of the drug, whereas the drug molecules are virtually immobile in the glassy state below T_g. In addition, an alternative switching mechanism is presented based on reversible swelling and shrinking of a hydrogel layer grafted onto a porous support, which is suitable for on-demand release of large peptide drugs.

1.1 Methods of drug delivery

The U.S. Food and Drug Administration (FDA) recognizes a total of 108 routes of administration [1], which roughly pertain to either the location of administration, or the method of administration. The most common methods of administration involve direct delivery into the gastrointestinal (GI) tract (i.e. oral or enteral administration), parenteral administration by injection or infusion, inhalation, topical application of for instance skin cream or eye drops, and transdermal delivery by for example nicotine or opioid patches. Each of these drug delivery methods has advantages and disadvantages. Obviously, for drugs required topically at exposed surface areas (e.g. dermal, opthalmic), or easily accessible orifices (e.g. auricular, nasal, vaginal, and inhalational), the drugs should be directly administered to the desired location. From the view point of patient-comfort and ease of administration, oral administration is the most preferable method when the drug is required inside the human body, especially when systemic administration is required. However, this route of administration requires a passage through the GI-tract, thus exposing drugs to the acidic environment of stomach fluids, which reduces the bioavailability of the drug compared to intravenous administration (which by definition is 100%). A lot of research has focused on protecting the active pharmaceutical ingredient (API) by for example encapsulation of the API by an enteric coating [2- 5], thus ensuring that release and subsequent resorption of the drug occur inside the intestines. Other methods offering efficient systemic administration include inhalational, and transmucosal routes, e.g. oral (buccal and sublingual), nasal and rectal administration, although the resulting bioavailability differs depending on the drug characteristics and formulation. Transdermal delivery is attractive from a patient's point of view, but the impenetrability of the stratum corneum, which indeed serves as the body's protective barrier, complicates this route. Even though intravenous administration ensures optimal bioavailability, it is the most risky route since the body's natural defenses are circumvented, thus posing a possible risk for infections and contaminations resulting from improper use. In addition, patient discomfort is an important reason to avoid this route when possible.

Often drugs are only required locally, so that systemic administration unnecessarily exposes the body to the drug, potentially causing harmful side effects [6]. In addition, a

higher dosage of the drug is required compared to local administration since dilution of the drug occurs inside the blood stream. This has prompted a vast amount of research on drug targeting, in which the drug circulating in the blood stream, often encapsulated inside liposomes or polymer micro- and nanospheres, is preferentially absorbed at the required location [2,5,7,8]. In a different approach, drugs can be released locally from an implant, thus ensuring a maximum concentration of the drug near the implant [9- 13].
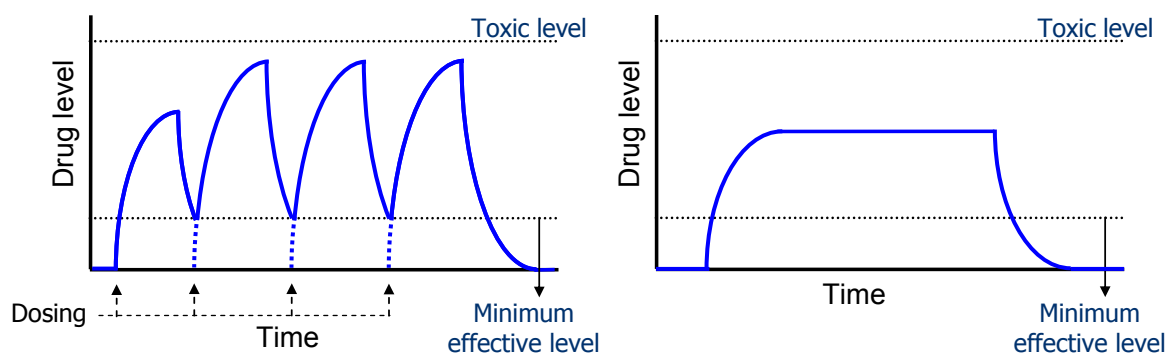
Figure 1.1: Classification of drug delivery classification. **A** Traditional drug delivery **B** Sustained zero-order release.

Besides achieving local release, the drug release profile is a large area of research. In the case of traditional systemic drug delivery, repeated dosing is required to maintain the drug concentration above the minimum effective level. In addition, care should be taken that the concentration does not exceed the toxic level at any time, which is particularly difficult for drugs exhibiting a narrow therapeutic index (i.e. minimum effective and toxic level are close) (Figure 1.1A). A lot of research has therefore focused on sustained zero-order release [7,8,14,15], i.e. a release profile in which a constant drug release rate is achieved in time (Figure 1.1B), most often by slow degradation of a coating [16] or the polymer matrix itself [17,18], swelling controlled release [19], or osmotic pumps [20]. These systems can either be implantable [16-20], or based on polymeric micro- and nanospheres circulating in the blood stream [7,8]. However, many therapeutic applications do not require a constant drug release or, in the case of habituation or resistance to medication, even benefit from pulsatile administration, such as post-surgical pain control and the treatment of infections. In comparison to more traditional delivery

forms, local pulsatile release potentially offers the advantage of increased patient compliance due to easy and painless dosing, higher bioavailability, and lower amount of drugs required due to local delivery, thus allowing for the use of potent drugs.

Pulsatile release can be achieved in three different ways, i.e. preprogrammed administration from an implant designed to release drugs at a certain time interval, internally regulated by the human body as a response to a change in the environment of the drug delivery device (e.g. glucose, antibodies, urea, and pH), and externally triggered on-demand from outside the human body [21-24]. Although both preprogrammed and internally regulated drug delivery systems are advantageous from the point of view that self-regulation ensures 100% patient compliance as the patient does not have to remember to take his medication, these methods prohibit any external intervention which is desirable or necessary for certain applications, such as pain control. Moreover, internally regulated systems most often concern hydrogel systems, which are quite efficient for protein delivery, but perform less well for smaller drug molecules.

External regulation of on-demand drug release has been reported using a number of different stimuli [23,24]. Ultrasound has been used to induce polymer degradation, thus triggering drug release [25,26]. Polymer dissolution by electrical triggering has also been demonstrated, in which disintegration of a solid polymer complex into two water-soluble polymers allows drugs to be released [27]. However, these destructive mechanisms complicate long-term application. In other electrical triggering approaches, drug release has been triggered by switching the oxidation state of an electroactive component inside multilayer nanocomposite films [28] or by electrochemical [29] and electrothermal [30] activation mechansims from multireservoir microhips. Unfortunately, these methods suffer from complex multistep fabrication techniques.

Alternatively, thermal triggers have been used for non-destructive on-off switching of drug release based on the lower critical solution temperature (LCST) [31,32]. Around this temperature, a reversible volume phase transition takes place driven by entropic considerations. Swelling and shrinking of a hydrogel exhibiting an LCST around body temperature can thus be used to control drug release. For non-invasive thermal triggering, oscillating magnetic fields [33], near-infrared radiation [34], and a radiofrequency field

[35] have been used. However, the attained on-off ratios using the LCST transition have been limited to values in the order of 70 [34,36-38], and the relatively high leakage in the off-state reduces the effective lifetime of the implant. In the current work, alternative strategies to achieve on-demand drug release are explored, focusing on near-infrared radiation as external trigger.

1.2 Near-infrared radiation in biomedical applications

Electromagnetic radiation is described by the quantum theory, first introduced by Albert Einstein [39], as bundles of wave energy called photons. Electromagnetic radiation thus has both wave and particle character, and can be described as having a wavelength or frequency, and a corresponding energy (Eqn. 1-1). For heat generation inside tissue, it is the particle character which can be used to describe absorption of the photons, whereas scattering of radiation is understood using the wave character of radiation.

$$E = h \cdot f = \frac{c}{\lambda} \qquad \text{[Eqn. 1-1]}$$

where E : energy [J]

    h : Planck's constant ($=6.63 \cdot 10^{-34}$ J s^{-1}) [J s]

    f : frequency [s^{-1}]

    c : speed of light ($=3.00 \cdot 10^{8}$ m s^{-1}) [m s^{-1}]

    λ : wavelength [m]

Electromagnetic radiation ranges from radio waves at the low frequency (high wavelength) end to gamma radiation at the high frequency end. Infrared radiation borders on the low energy end of visible light (*infra* = below) in the electromagnetic spectrum. Near-infrared radiation (NIR) is the part of infrared radiation closest to visible red light and is characterized by a relatively low absorption by water and tissue chromophores, termed the therapeutic window (Figure 1.2). In particular, the low absorption of water in this region allows for a relatively high penetration of NIR into the human body of up to several centimeters, making it attractive for biomedical applications [40,41].

Many tomographic diagnostic techniques make use of the dominant scattering properties over absorption of NIR in tissue. Due to multiple scattering of incident photons information is obtained from back-scattered radiation, which, often in combination with

fluorescence techniques, reveals information on the composition and heterogeneity of tissue [42].
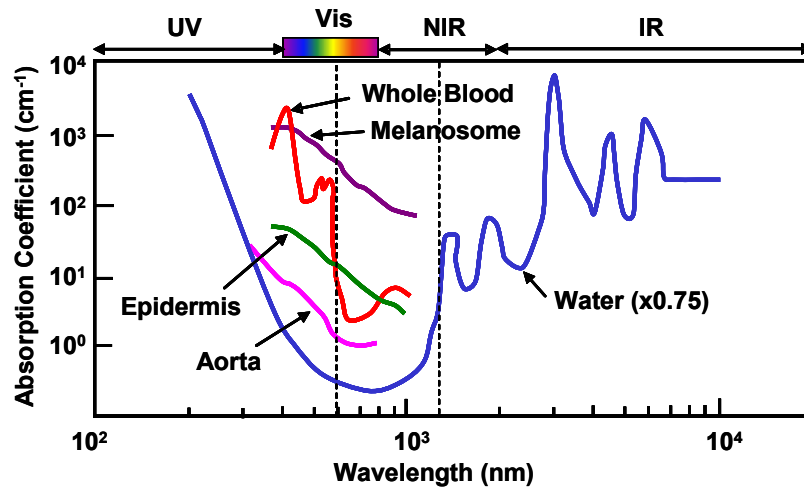
Figure 1.2: Therapeutic window, indicated by the dashed lines, in which absorption by water and tissue chromophores is relatively low (adapted from [41]).

Therapies which use absorption of visible and NIR radiation as opposed to the scattering properties, include low power laser therapy and photodynamic therapy. For the former, absorption of radiation results in an increase of oxidative metabolism in mitochondria, which subsequently stimulates various beneficial photobiochemical processes. This is used in various clinical applications, ranging from pain treatment to the treatment of inflammations. In contrast, photodynamic therapy is used to destroy or modify tissue, e.g. tumors, and relies on the absorption of radiation by an injected photosensitizer, which in the presence of enodogeneous oxygen produces toxic singlet oxygen [42].

Laser tissue welding is becoming increasingly popular in clinical practice. Here, high power lasers are used to achieve high temperature increases where tissue is to be joined, resulting in coagulation of tissue. Although this is often performed using far infrared laser (e.g. CO_2-lasers) because of the high absorption of water in this wavelength region, a relatively new approach involves the use of NIR diode lasers around a wavelength of 800 nm, in which an NIR dye is applied to the tissue of interest. In this case, a much more specific heating of the tissue can be achieved, thus minimizing damage to surrounding tissue [42]. In fact, a similar approach is used in the current work, in which an NIR dye is incorporated into a polymeric implant in order to induce selective heating of the polymer

implant, without affecting surrounding tissue. The NIR dye used in this research, as well as its absorption spectrum, is illustrated in Figure 1.3.
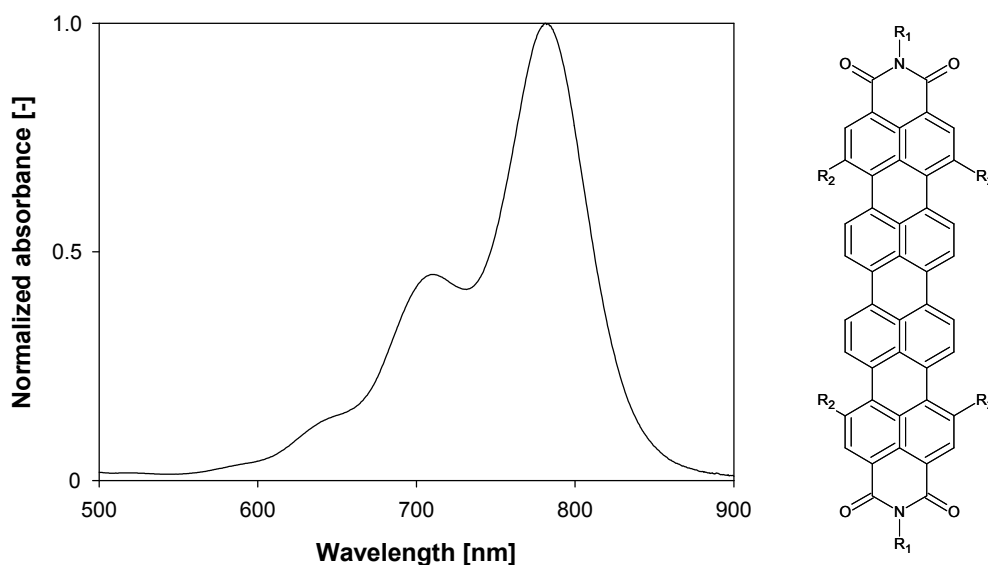
Figure 1.3: Absorption spectrum of a commercially available quaterrylenebisdicarboximide dye in dichloromethane solution.

Previously, metal nanoshells that strongly absorb NIR radiation have been synthesized, and incorporated into a thermosensitive hydrogel [34,43,44]. The drug delivery system itself suffers from the limitations of an LCST-based drug delivery system mentioned in the previous section. However, an attractive feature of the nanoparticles is that the maximum wavelength can be tuned depending on the thickness of the gold shell relative to the dielectric core (e.g. Au_2S [34,43] or SiO_2 [44]). Although this is indeed an attractive feature of these particles, it also encompasses a rather laborious synthesis procedure with a relatively low yield. In addition, incorporation of these nanoparticles into a polymer matrix, such as is necessary for the drug delivery system described in this thesis, is less straightforward due to compatibility issues with organic solvent used in a solvent casting process, requiring additional surface functionalization [45]. Moreover, aggregation of these particles may occur during processing, thus affecting their absorption [46,47].

Another application related to NIR-induced drug release reported in literature [48,49] involves burst release of drugs encapsulated in liposomes containing hollow gold

7

nanoparticles, which similarly exhibit tunable absorption in the NIR region. On irradiation by NIR, the liposomes release their drug contents, attributed to either a temperature increase [48] or transient cavitation effects [49]. Similarly, carbon nanotubes have been used as NIR absorbing agents that simultaneously act as (protein) drug carriers [50]. These nanotubes are targetted to deliver drugs directly into the cells, followed by NIR triggering to release the drug inside the cell. Although these mechanisms can indeed also be termed on-demand drug delivery, these applications are limited to single burst release, whereas the current work focuses on achieving long-term repeated on-demand drug delivery. Carbon nanotubes could in fact be used instead of the dye depicted in Figure 1.3, but dispersibility of carbon nanotubes in a polymer matrix is not straightforward [51]. Moreover, doubts concerning the toxicity of carbon nanotubes have recently been raised [52].

1.3 Scope of thesis

1.3.1 Glass transition switch
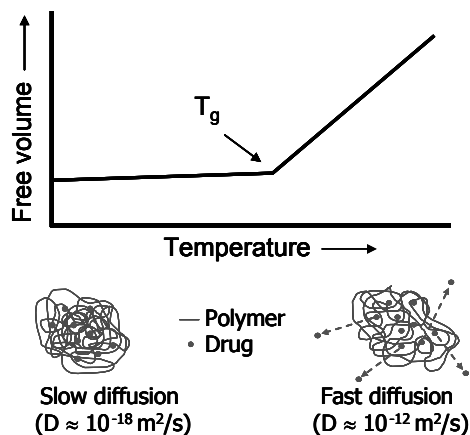
Figure 1.4: Dramatic increase in free volume near the glass transition temperature (T_g) leading to an increase in diffusion coefficient by several orders of magnitude.

In this thesis, the glass transition temperature (T_g) is used as a thermoresponsive switch. Around T_g, a large increase in free volume occurs, resulting in a dramatic increase in diffusion of dissolved drug molecules (Figure 1.4). Below T_g, the polymer is in a glassy state, and the rigid polymer chains prevent drug from diffusing out of the implant. In the

rubbery state, the polymer chains become highly flexible thus inducing drug release from the implant. A polymer is chosen, such that the T_g of the polymer is higher than the fever temperature (~43ºC), so that at physiological conditions, the polymer is in a glassy state. NIR is used as external trigger to induce a temperature increase of the polymer implant. Since polymers do not intrinisically absorb NIR, a commercial NIR dye is incoporated into the polymer matrix, which exhibits a maximum in absorption around 780 nm (Figure 1.3), i.e. where a minimum in water absorption occurs (Figure 1.2). The dye is non-toxic, thus making it suitable for medical devices [53]. A schematic overview of the drug delivery concept is given in Figure 1.5.

Skin   Skin   Skin

Tissue   NIR ON   Tissue   NIR OFF   Tissue

| Glassy polymer matrix homogeneously incorporated with drugs | Polymer matrix becomes rubbery due to heat production, inducing drug release | Remaining drug frozen in glassy matrix |

Procedure can be repeated as long as a sufficient amount of drug remains in matrix
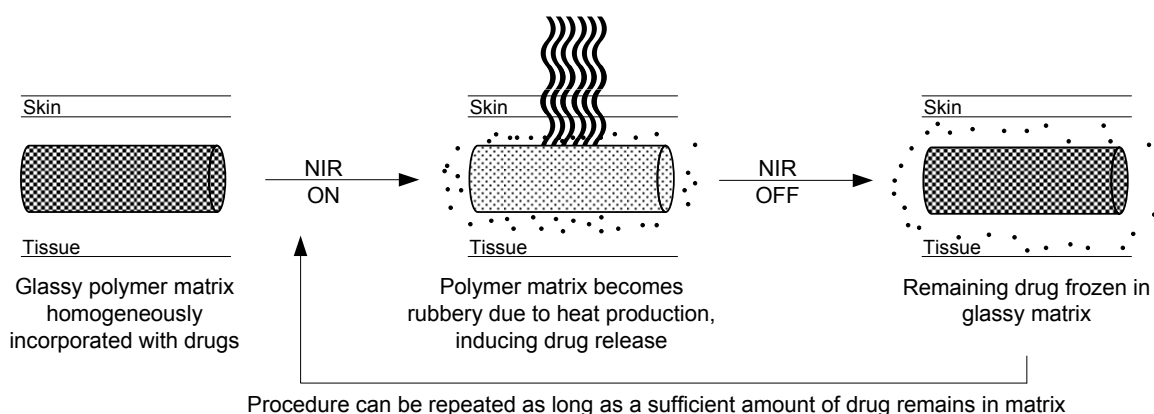
Figure 1.5: On-demand drug delivery, remotely triggered using NIR radiation from a dye-doped drug-containing polymeric implant, exhibiting a T_g of approximately 10-15ºC above fever temperature.

The glass-rubber transition has been used previously in controlled drug delivery, albeit in a completely different approach [54]. Here, drug is incorporated into a glassy *hydrophilic* polymer matrix. On contact with water, water diffuses into the polymer thus swelling the polymer. At the diffusing water front, the matrix becomes rubbery, resulting in drug release. Although this is indeed a type of glass-rubber transition, it is entirely different from the mechanism proposed in this thesis, in which a temperature increase in a *hydrophobic* polymer induces drug release. Moreover, the swelling mechanism does not enable pulsatile release, but is an irreversible process limited to release kinetics governed by the sorption process.

Besides research performed in our group [55,56], the T_g has been mentioned previously as a thermoresponsive switch for drug release, measured experimentally by membrane

permeation measurements [57,58]. However, no proposal for a thermal triggering mechanism has been given, and no demonstration of the reversibility of the process has been demonstrated. In fact, all experiments have only been peformed at fixed temperatures. Moreover, Fujimori *et al.* [58] conclude that T_g in combination with swelling of the polymer leads to the observed high permeation, thus raising doubts as to the reversibility of the process.

1.3.2 *Thermoresponsive membranes*

The T_g can be effectively used to switch on and off the release of 'simple' drug molecules from a polymeric implant. However, an increasing amount of therapies involves the delivery of large molecules [59]. Examples include the relatively new technique of gene therapy and the delivery of various peptide hormones [60]. These molecules are much larger than the available free volume normally present inside glassy polymers, and it can thus not be expected that an effective switch around T_g can be accomplished. In addition, proteins are very susceptible to thermal degradation and denaturation at relatively moderate temperatures. Therefore, the induced temperature cannot involve too high temperatures, and a different switching mechanism is evaluated involving the previously discussed lower critical solution temperature. The drug is encapsulated by a microporous membrane covered with a hydrogel layer capable of reversible shrinking and swelling around the LCST. In the shrunken state (i.e. above LCST), pores in the membrane are uncovered, allowing free permeation of the drug molecules through the pores, whereas in the swollen state, the pores are covered, preventing release of the protein (Figure 1.6)

Skin	Skin	Skin
Tissue	Tissue	Tissue
Peptide drugs encapsulated by porous membrane grafted with swollen hydrogel	Hydrogel shrinks due to temperature increase, allowing release of drug through uncovered pores	Temperature returns below LCST, so that swollen gel covers pores again

NIR ON → NIR OFF →

Procedure can be repeated as long as a sufficient amount of drug remains in implant

Figure 1.6: On-demand drug delivery, remotely triggered using NIR radiation from a dye-doped membrane, exhibiting an LCST of 1-5ºC higher than the fever temperature.

1.4 Thesis outline

This thesis is mainly dedicated to understanding different aspects involved in externally triggered drug delivery using the glass transition concept. Incorporation of an NIR dye in a polymer matrix and the effect of the incorporation method on the optical and thermal properties are discussed in **Chapter 2**. The implications of these findings for implant design are addressed in **Chapter 3**, in which a finite element model is correlated to experimental heating results. Also, an estimate of temperatures obtained *in vivo* is given, taking into account absorption and scattering effects in tissue. In addition, mass transfer considerations are touched upon, which is further elaborated in **Chapter 5**, dealing with a fundamental consideration of drug diffusion in terms of available free volume. In **Chapter 4**, the feasibility of the drug delivery concept is demonstrated both *in vitro* and *in vivo,* in which on/off ratios as high as a factor 1,000 are obtained. The concept of an alternative thermoresponsive switch for large therapeutic agents is illustrated in **Chapter 6**, where permeation of the model protein bovine serum albumin through a poly(ethylene terephthalate) track etched membrane is regulated by a swellable hydrogel graft layer covering the pores. Finally, the potential and challenges of the presented T_g-switch in clinical or patient-controlled applications are discussed in **Chapter 7**.

References

[1]   FDA Center for Drug Evaluation and Research Data Standards Manual: *C-DRG-00301,* last revision: January 11 2006.

[2]   Carino, G. P., Jacob, J. S., Mathiowitz, E. Nanosphere based oral insulin delivery. *J. Contr. Rel.* **65**, 261-269 (2000).

[3]   Mathiowitz, E. *et al.* Biologically erodable microspheres as potential oral drug delivery systems. *Nature* **386**, 410-414 (1997).

[4]   Shen, Z. & Mitragotri, S. Intestinal patches for oral drug delivery. *Pharm. Res.* **19**, 391-395 (2002).

[5]   Chen, H., Torchilin, V., Langer, R. Polymerized liposomes as potential oral vaccine carriers: stability and bioavailability. *J. Contr. Rel.* **42**, 263-272 (1996).

[6]   Langer, R. Drug delivery and targeting. *Nature* **392** (Suppl.), 5-10 (1998).

[7]   Allen, T. M., Cullis, P. R. Drug delivery systems: entering the mainstream. *Science* **303**, 1818-1822 (2004).

[8]   Freiburg, S. & Zhu, X. X. Polymer microspheres for controlled drug release. *Int. J. Pharm.* **282**, 1-18 (2004).

[9]   Lambert, T. L. *et al.* Localized arterial wall drug delivery from a polymer-coated removable metallic stent: kinetics, distribution, and bioactivity of forskolin. *Circulation* **90**, 1003-1011 (1994).

[10]   Lincoff, A. M., Furst, J. G., Ellis, S. G., Tuch, R. J., Topol, E. J. Sustained local delivery of dexamethasone by a novel intravascular eluting stent to prevent restenosis in the porcine coronary injury model. *J. Am. Coll. Cardiol.* **29**, 808-816 (1997).

[11]   Sonoda, S. *et al.* Taxol-based eluting stents from theory to human validation: clinical and intravascular ultrasound observations. *J. Invasive Cardiol.* **15**, 109-114 (2003).

[12]   J. Urquhart, *Ophthalmic Drug Delivery Systems*, Academy of Pharmaceutical Science, Washington, D.C., 1980, 105-118.

[13]   Goodson, J. M., Haffajee, A, Socransky, S. S. Periodontal therapy by local delivery of tetracycline. *J. Clin. Periodontol.* **6**, 83-92 (1979).

[14]   Langer, R. Invited review polymeric delivery systems for controlled drug release. *Chem. Eng. Commun.* **6**, 1-48 (1980).

[15]   Ghosh, S. Recent research and development in synthetic polymer-based drug delivery systems. *J. Chem. Res.* **4**, 241-246 (2004).

[16]   Lee, E. S., Kim, S. W., Kim, S. H., Cardinal, J. R., Jacobs, H. Drug release from hydrogel devices with rate-controlling barriers. *J. Membr. Sci.* **7**, 293-303 (1980).

[17]   Chandrasekaran, S. K. & Paul, D. R. Dissolution-controlled transport from dispersed matrixes. *J. Pharm. Sci.* **71**, 1399-1402 (1982).

[18]   Gurny, R. Doelker, E., Peppas, N. A. Modelling of sustained release of water-soluble drugs from porous, hydrophobic polymers. *Biomaterials* **3**, 27-32 (1982).

[19]   Conte, U. & Maggi, L. A flexible technology for the linear, pulsatile, and delayed release of drugs, allowing for easy accommodation of difficult in vitro targets. *J. Contr. Rel.* **64**, 263-268 (2000).

[20]   Wright, J. C. *et al.* A one-year implantable, osmotic delivery system (Duros leuprolide implant) for the treatment of advanced prostate cancer. In *Proceedings of the 24th International Symposium on Controlled Release of Bioactive materials*, 59-60 (Controlled Release Society, Minneapolis, Minnesota, USA, 1997).

[21]   Richards Grayson, A. C. *et al.* Multi-pulse drug delivery from a resorbable polymeric microchip device. *Nat. Mater.* **2**, 767-772 (2003).

[22]   Stubbe, B. G., De Smedt, S. C., Demeester, J. "Programmed polymeric devices" for pulsed drug delivery. *Pharm. Res.* **21**, 1732-1740 (2004).

[23]   Kost, J. & Langer, R. Responsive polymeric delivery systems. *Adv. Drug Deliver. Rev.* **46**, 125-148 (2001).

[24]   Sershen, S. R. & West, J. L. Implantable, polymeric systems for modulated drug delivery. *Adv. Drug. Deliv. Rev.* **54**, 1225-1235 (2002).

[25]   Kost, J., Leong, K., Langer, R. Ultrasound-enhanced polymer degradation and release of incorporated substances. *P. Natl. Acad. Sci. USA* **86**, 7663-7666 (1989).

[26]   Aschkenasy, C. & Kost, J. On-demand release by ultrasound from osmotically swollen hydrophobic matrices. *J. Control. Release* **110**, 58-66 (2005).

[27]   Kwon, I. C., Bae, Y. H., Kim, S. W. Electrically erodible polymer gel for controlled release of drugs. *Nature* **354**, 291-293 (1991).

[28] Wood, K. C. *et al.* Electroactive controlled release thin films. *P. Natl. Acad. Sci. USA* **105**, 2280-2285 (2008).

[29] Santini, J. T., Cima, M. J., Langer, R. A controlled-release microchip *Nature* **397**, 335-338 (1999).

[30] Prescott, J. H. *et al.* Chronic, programmed polypeptide delivery from an implanted, multireservoir microchip device, *Nat. Biotechnol.* **24**, 437-438 (2006).

[31] Hoffman, A. S., Afrassiabi, A., Dong, L. C. Thermally reversible hydrogels: II. Delivery and selective removal of substances from aqueous solutions. *J. Control. Release* **4**, 213-222 (1986).

[32] Bae, Y. H., Okano, T., Hsu, R., Kim, S. W. Thermo-sensitive polymers as on-off switches for drug release. *Makromol. Chem.-Rapid* **8**, 481-485 (1987).

[33] Hergt, R. *et al.* Maghemite nanoparticles with very high AC-losses for applications in RF-magnetic hyperthermia. *J. Magn. Magn. Mater.* **270**, 345-357 (2004).

[34] Sershen, S. R., Westcott, S. L., Halas, N. J., West, J. L. Temperature-sensitive polymer-nanoshell composites for photothermally modulated drug delivery. J. Biomed. Mater. Res. 51, 293-298 (2000).

[35] Gannon, C. J. *et al.* Carbon nanotube-enhanced thermal destruction of cancer cells in a noninvasive radiofrequency field. *Cancer* **110**, 2654-2665 (2007).

[36] Satarkar, N. S., Hilt, J. Z. Magnetic hydrogel nanocomposites for remote controlled pulsatile drug release. *J. Control. Release* **130**, 246-251 (2008).

[37] Peng, T. & Cheng, Y.-L. Temperature-responsive permeability of porous PNIPAAm-*g*-PE membranes, *J. Appl. Polym. Sci.* **70**, 2133-2142 (1998).

[38] Li, S. K., D'Emanuele, A. On-off transport though a thermoresponsive hydrogel comoposite membrane. *J. Control. Release* **75**, 55-67 (2001).

[39] Einstein, A. Über einen die Erzeugung und Verwandlung des Lichtes betreffenden heuristischen Gesichtspunkt. *Ann. Physik* **17**, 132-148 (1905).

[40] Weissleder, R. A clearer vision for *in vivo* imaging. *Nat. Biotechnol.* **19**, 316-317 (2001).

[41] Mobley, J. & Vo-Dinh, T. in *Biomedical Photonics* (ed. Vo-Dinh, T.) 2-1 – 2-75 (CRC, Boca Raton, 2003).

[42] *Biomedical Photonics* (ed. Vo-Dinh, T.), CRC, Boca Raton, 2003.

[43] Sershen, S. R., Westcott, S. L., West, J. L., Halas, N. J. An opto-mechanical nanoshell-polymer composite. *Appl. Phys. B.* **73**, 379-381 (2001).

[44] Bikram, M., Gobin, A. M., Whitmire, R. E., West, J. L. Temperature-sensitive hydrogels with SiO_2-Au nanoshells for controlled drug delivery. *J. Contr. Rel.* **123**, 219-227 (2007).

[45] Pham, T., Jackson, J. B., Halas, N. J., Lee, T. R. Preparation and characterization of gold nanoshells coated with self-assembled monolayers. *Langmuir* **18**, 4915-4920 (2002).

[46] Quinten, M. The color of finely dispersed nanoparticles. *Appl. Phys. B* **73**, 317-326 (2001).

[47] Hirsch, L. R. *et al.* Metal nanoshells. *Ann.Biomed. Eng.* **34**, 15-22 (2006).

[48] Skirtach, A. G. *et al.*The role of metal nanoparticles in remote release of encapsulated materials. *Nano Letters* **5**, 1371-1377 (2005).

[49] Wu, G. *et al.* Remotely triggered liposome release by near-infrared light absorption via hollow gold nanoshells. *JACS* **130**, 8175-8177 (2008).

[50] Kam, N. W. S., O'Connell, M., Wisdom, J. A., Dai, H. Carbon nanotubes as multifunctional biological transporters and near-infrared agents for selective cancer cell destruction. *P. Natl. Acad. Sci. USA* **102**, 11600-11605 (2005).

[51] Grossiord, N., Loos, J., Koning, C. E. Strategies for dispersing carbon nanotubes in highly viscous polymers. *J. Mater. Chem.* **15**, 2349-2352 (2005).

[52] Poland, C. A. *et al*. Carbon nanotubes introduced into the abdominal cavity of mice show asbestos-like pathogenicity in a pilot study. *Nat. Nanotechnol.* **3**, 423-428 (2008).

[53] Additives aid laser welding. *Plastics, additives and compounding* **7**, 34-35 (2005).

[54] Colombo, P., Bettini, R., Santi, P., De Ascentiis, A., Peppas, N. A. Analysis of the swelling and release mechanisms from drug delivery systems with emphasis on drug solubility and water transport. *J. Contr. Rel.* **39**, 231-237 (1996).

[55] Bruinewoud, H. *Ultrasound-induced drug release from polymer matrices: the glass transition temperature as a thermo-responsive switch*. PhD dissertation, Eindhoven: TU Eindhoven (2005).

[56] Rovers, S.A., Dietz, C.H.J.T., Hoogenboom, R., Kemmere, M.F., Keurentjes, J.T.F. Reversible on-demand drug release from iron oxide incorporated polymeric matrices using an alternating magnetic field as external trigger, *in preparation*.

[57] Kydonieus, A. F. Decker, S. C., Shah, K. R. Temperature activated controlled release. *Proc. Int. Symp. Contr. Rel. Bioact. Mater.* **18**, 417-418 (1991).

[58] Fujimori. J., Yoshihashi, Y., Yonemochi, E., Terada, K. Application of Eudragit RS to thermo-sensitive drug delivery systems. II. Effect of temperature on drug permeability through membrane consisting of Eudragit RS/PEG 400 blend polymers. *J. Contr. Rel.* **102**, 49-57 (2005).

[59] Lee, K. Y. & Yuk, S. H. Polymeric protein delivery systems. *Prog. Polym. Sci.* **32**, 669-697 (2007).

[60] Breimer, D. D., Future challenges for drug delivery. *J. Contr. Rel.* **62**, 3-6 (1999).

CHAPTER 2

Near-Infrared Induced Heating of a Dye-Doped Polymer Matrix

Abstract

Heating of dye-doped polymer matrices induced by near-infrared radiation (NIR) is demonstrated, where incident radiation is efficiently transformed into heat by a quaterrylenebis(dicarboximide) dye. UV-Visible spectroscopy reveals the formation of face-to-face stacked molecular aggregates (H-aggregates) on incorporation of this dye by solvent casting. Post-processing or direct incorporation at elevated temperatures suppresses aggregate formation. Although H-aggregates diminish absorption at the wavelength of the NIR source, and thus the amount of heat generated, the efficiency of heat generation is not necessarily affected due to the absence of photoluminescent processes. Moreover, the exponential relationship of absorption with concentration renders the influence of aggregation on the final surface temperature at the investigated dye concentrations negligible. In contrast, the heating rate depends linearly on concentration, and thus aggregation can reduce the initial heating rate to some extent. The significant temperature increase attained in aqueous environment offers promising perspectives for use in remotely triggered on-demand drug release.

2.1 Introduction

The present work focuses on heating a polymer implant using near-infrared radiation (NIR) as external energy source with potential use in thermoresponsive drug release. Infrared radiation is limited by visible light on the high energy side and microwaves on the low energy side in the electromagnetic spectrum. The NIR region borders on the visible region, ranging from a wavelength of approximately 750 to 2500 nm. In the range of 700-1100 nm, the so-called therapeutic window, water exhibits a minimum in absorption, and in addition, the main blood and tissue chromophores display a relatively low absorption in this region, thus enabling penetration up to several centimeters into the human body [1,2]. An implant capable of absorbing NIR enables selective heating of the implant, without heating the surrounding tissue, resulting in remotely triggered drug release.

As polymers do not intrinsically absorb NIR, an NIR absorbing additive needs to be incorporated into the polymer matrix. Previously, NIR absorbing metal nanoshells have been synthesized [3-5], and incorporated into a thermosensitive hydrogel [3,4]. However, preparation of these nanoparticles is laborious providing relatively low yields and incorporation into polymer matrices is not straightforward. Here, we use a commercially available quaterrylenebis(dicarboximide) dye (QBDC) exhibiting a maximum absorption around 780 nm, which can easily be incorporated into many common polymer matrices. QBDCs display a far lower luminescence quantum yield than their perylene analogues [6], which implies that a relatively large amount of absorbed radiation is transformed to heat. However, the quantum yields of heat formation and photoluminescence of aromatic compounds are often affected by their tendency to form molecular aggregates [7-9]. Moreover, dye aggregation can affect the absorption coefficient at a certain wavelength as well as the absorption maximum [7-12], which also influences heat production and distribution in the polymer matrix. It is therefore essential to investigate the aggregation behavior of the dye molecules in the polymer matrix.

In this study, a commercially available QBDC is incorporated into a poly(methyl methacrylate) matrix and is characterized by absorption spectroscopy. The influence of dye concentration, processing method and sample geometry on dye aggregation, heating

rate and resulting temperature profile induced by laser irradiation at a wavelength of 785 nm are discussed by measuring the surface temperatures of the matrices by non-contact infrared radiation thermometry.

2.2 Absorption and dye aggregation

When (near-infrared) radiation encounters a medium by which it is absorbed, the intensity of the radiation decreases exponentially with distance. This decrease depends on the concentration of the absorbing compound (i.e. the QBDC dye) and the absorption coefficient of this compound at the wavelength of the incident radiation. At sufficiently low concentrations, the absorption coefficient remains constant and the intensity profile through the medium is given by Eqn. 2-1. This equation can also be defined in terms of absorbance, resulting in the well known Beer-Lambert law, stating that absorbance is proportional to concentration and path length (Eqn. 2-2).

$$I_x = I_0 \, 10^{-\varepsilon_\lambda \, C \, x} \qquad\qquad\qquad\qquad [2\text{-}1]$$

$$Abs = -\log\left(\frac{I_L}{I_0}\right) = \varepsilon_\lambda \cdot C \cdot L \qquad\qquad\qquad [2\text{-}2]$$

where Abs : absorbance   [a.u.]
  I_x, I_L : intensity after traveling
  a distance x or L   [W m^{-2}]
  I_0 : intensity of incident radiation   [W m^{-2}]
  ε_λ : molar absorption coefficient at wavelength λ [L mol^{-1} m^{-1}]
  C : concentration of absorbing compound   [mol L^{-1}]
  x : penetration depth   [m]
  L : path length   [m]

As long as the absorption coefficient is independent of dye concentration, the intensity profile can effectively be controlled by varying this concentration (Figure 2.1). Assuming all absorbed radiation is transformed into heat, the intensity gradient in Figure 2.1 is a direct measure for local heat generation (Q_x), and consequently strongly influences the temperature profile inside a near-infrared absorbing matrix. However, the formation of molecular dye aggregates can affect the absorption coefficient, and the amount of radiation transformed into heat. Among other things, photoluminescent processes can

diminish the quantum yield of the desired non-radiative thermal relaxation from the excited to the ground state. Often encountered aggregation forms include co-facial stacked molecules (H-aggregates), or head-to-tail arranged molecules (J-aggregates) (Figure 2.2).
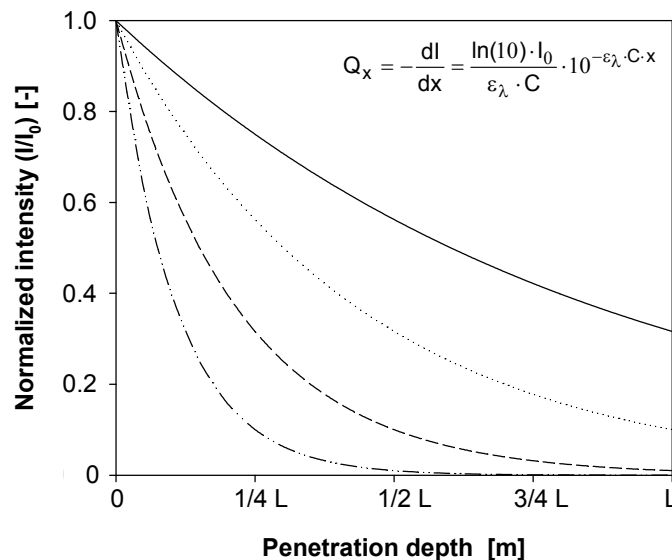
Figure 2.1: Effect of concentration on intensity profile in an absorbing medium. $\varepsilon_\lambda \cdot C = 1/2 \cdot L$ (——), $\varepsilon_\lambda \cdot C = L$ (⋯⋯), $\varepsilon_\lambda \cdot C = 2 \cdot L$ (- - - -), $\varepsilon_\lambda \cdot C = 4 \cdot L$ (– ·· –).

The formation of aggregates leads to splitting of the excited state due to interaction of the dipole moments of the individual molecules, and thus results in the formation of new energy transitions []. In the case of parallel transition dipoles, the lower energy transition is forbidden based on quantum mechanical considerations. Keeping in mind that energy is inversely related to wavelength, this is observed as a weak bathochromic shift (red-shift) of the onset of absorption in the absorption spectrum. The transition to the upper state is strongly allowed, causing the hypsochromic shift (blue-shift) of the absorption maximum. The exact transitions visible in the absorption spectrum depend on the detailed molecular structure of the aggregate. In contrast to these stacked aggregates, the lower energy transition in head-to-tail arranged aggregates is strongly allowed and the upper energy transition is forbidden. If the angle (α) of the monomers with the longitudinal axis is higher than 54.7°, the aggregates are termed H-aggregates, whereas at angles lower than this critical angle, the aggregates are termed J-aggregates. In general, the latter are

18

strongly fluorescent, whereas hardly any photoluminescence occurs in H-aggregates. Thus, if aggregation occurs, H-aggregates are favored over J-aggregates for efficient heat generation.
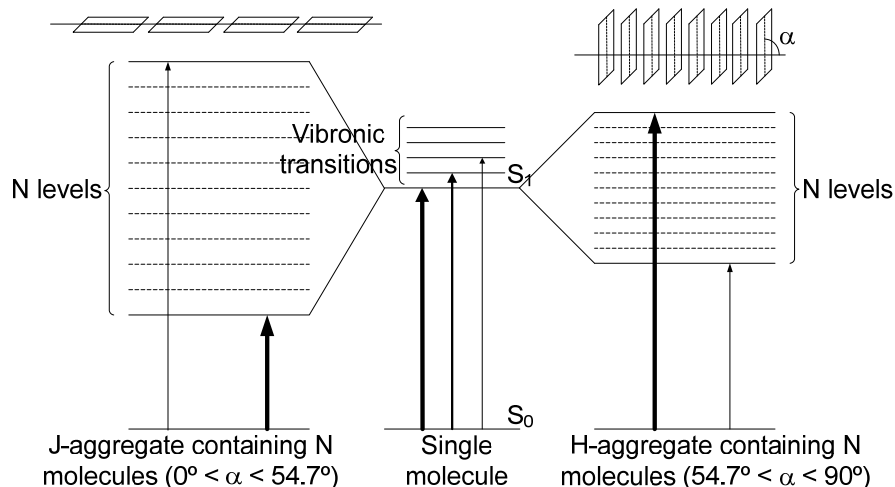
Figure 2.2: Schematic representation of splitting of the first excited state (S_1) in an aggregate containing N monomers. Electrostatic interactions between molecules with permanent dipole moments, which could affect the position of the absorption band as a whole, are neglected.

2.3   Experimental

2.3.1   Materials

Poly(methyl methacrylate) ($M_w \sim 120{,}000$ g/mol, $T_g \sim 99$ºC) (PMMA) was purchased from Aldrich and used as received. Lumogen® IR788 (L-IR788), a commercial quaterrylenebis(dicarboximide)-based compound was obtained from BASF AG and used as received. Dichloromethane ($\geq 99.8\%$) (DCM) and ethyl acetate (EtOAc) ($\geq 99.5\%$) were obtained from Merck KGaA.

2.3.2   Additive incorporation

L-IR788 was incorporated into the polymer matrix either by solvent casting or by compounding. Subsequently, polymer discs were prepared by compression at elevated temperature.

2.3.2.1 Solvent casting

Solvent casting was performed using an approximately 16% (w/w) polymer solution. Typically, the solution contained approximately 1000 mg of polymer and 4 mL DCM. After stirring with a magnetic stirrer for two hours to ensure complete dissolution, the solution was cast in a glass Petri dish (∅: 76 mm) and covered with perforated Parafilm® to allow slow evaporation of the solvent in the fume hood. After several days, the resulting polymer film (typically around 200 μm in thickness) was removed from the Petri dish. Finally, it was placed in a vacuum oven overnight.

2.3.2.2 Compounding

Compounding was performed in a custom built twin screw mini compounder (5 g capacity). The polymer (~ 4.0 g) and L-IR788 (~ 2.0 mg) were premixed with a spatula for 2 minutes. The mixing time inside the compounder was approximately 5 minutes at a temperature of 220ºC.

2.3.2.3 Compression molding

Several circles with a diameter of 24 mm, amounting to a total weight of approximately 500 mg, were punched from the solvent cast film and placed in a custom built manual press. After two hours in the oven at 160ºC, polymer discs with a diameter of 25.4 mm and a typical thickness of approximately 1 mm were obtained by compression in the press, followed by cooling with water to room temperature.

For compression of compounded discs, the same procedure was followed, with the exception that no circles could be punched since the extrusion process yielded a strand of polymer. Therefore, small pieces of the extruded strand were cut into pieces and placed in the press.

2.3.3 Absorption spectroscopy

Absorption spectra of solutions of L-IR788 in DCM and EtOAc were measured on a UV-2501 PC (Shimadzu, 400 nm/min scan speed, 0.5 nm resolution) in a quartz cuvette (1 mm or 10 mm path length), the reference cuvette containing only the organic solvent. Absorption spectra of the polymer films and discs were measured on a Uvikon XL

UV-VIS spectrophotometer (Bio-Tek, 800 nm/min scan speed, 1 nm resolution). Films and discs were placed in a sample holder and measured directly without a reference sample, as small variations in thickness render a reference sample useless.

2.3.4 NIR laser heating

2.3.4.1 Laser characteristics

The laser diode used in this study was a 785 nm laser diode with a maximum power of 1000 mW, built into an HPM750(785-1000)J laser diode module (Power Technology, Inc.). The laser was coupled into a multimode fiber (numerical aperture (N.A.): 0.22; $\varnothing$: 200 μm) with an efficiency of about 75%. The output power could be continuously adjusted between 0 and 750 mW, and was operated in continuous wave mode. The beam divergence was given by 2·N.A.·distance, e.g. at a distance of 30 mm between sample and fiber exit, the diameter of the laser spot equaled 13.2 mm. The intensity profile of the laser beam as it exited the fiber is given in Figure 2.3. This relative profile remained the same at all distances and approached a Gaussian distribution.
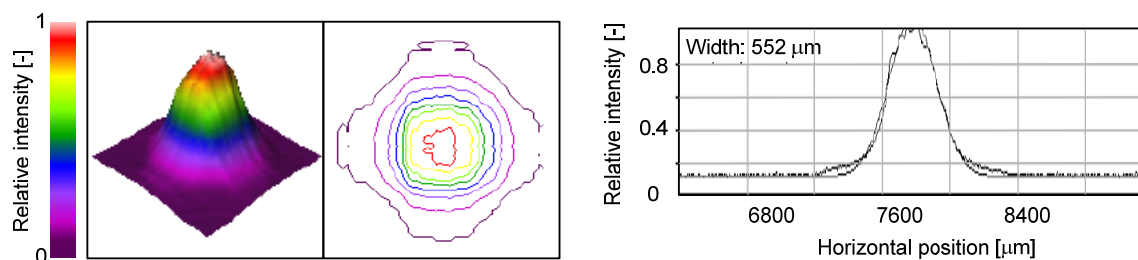
Figure 2.3: 3-D laser intensity profile and cross section of intensity profile.

2.3.4.2 NIR-induced heating in air

The experimental set-up is depicted in Figure 2.4A. A circular target was placed in a self-centering sample holder (SCL04, Thorlabs GmbH), and placed at a certain distance from the laser beam. Two infrared temperature sensors (SP I-TEC 2060, Sensor partners B.V.), which measured the surface temperature at the front and back of the sample, were fixed to an x,z-positioning system (PT3/M, Thorlabs GmbH) and positioned in such a way that they were centered on the target. The positioning system allowed a horizontal and vertical translation of 25 mm, with an accuracy of 0.01 mm. The measuring spot size of the

sensors was approximately 1 mm. By placing the sensors at an angle of 45° with the sample, a horizontal translation of 1 mm with the positioning system coincided with a translation of 1 mm on the sample surface. After the laser was switched on, the beam was blocked by a power meter (Model 407A, Spectra-Physics) to allow the beam to stabilize for approximately 60 s. As soon as the power remained constant, the power meter was removed and the measurement started.
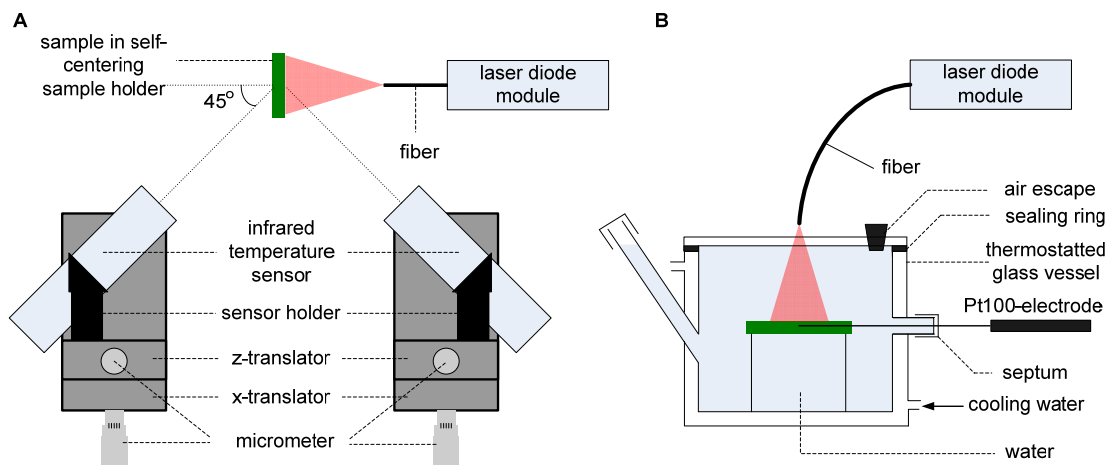
Figure 2.4: Schematic representation of experimental set-ups in air (A) and aqueous environment (B).

2.3.4.3 NIR-induced heating in aqueous environment

The experimental set-up is illustrated in Figure 2.4B. A hole with a diameter of approximately 1 mm, just large enough to fit in a Pt100 temperature sensor (UNR-351-0.5 Class A, Netsushin Ltd. Japan), was drilled into the polymer sample. The disc was placed in a thermostatted glass vessel, and filled with water, after which the Pt100 sensor was positioned in the hole through a septum on the right. The vessel was sealed with a sealing ring and a glass lid, which was clamped to the vessel. To avoid scattering by air bubbles, the remaining air was removed using an air escape hole in the lid and adding water in the inlet on the left of Figure 2.4B.

2.4 Results and discussion

2.4.1 Dye aggregation in PMMA films cast from organic solvents

In dichloromethane (DCM) solution, L-IR788 is molecularly dissolved at low concentrations, thus displaying a typical vibronic progression, indicative for the non-aggregated dye, with its main 0-0 transition at 782 nm (solid lines in Figure 2.5A). As the concentration increases (dashed lines in Figure 2.5A), a slight deviation from the Beer-Lambert law occurs, most notably for the 0-0 transition (filled symbols in inset of Figure 2.5A), but the shape of the spectrum is largely maintained.
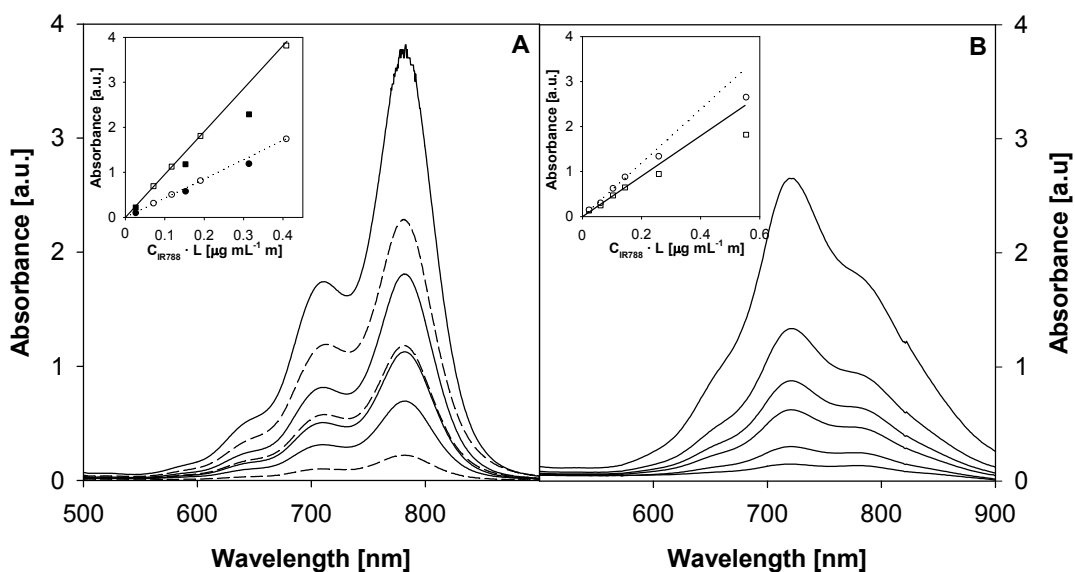
Figure 2.5: Absorption spectra of L-IR788 in DCM solution and cast in polymer matrices. **A** L-IR788 in DCM measured in a cuvette with a path length (L) of 10 mm (——: 7.2, 11.7, 19.1 and 40.8 μg/mL) and 1 mm (- - - -: 26.2, 153 and 314 μg/mL). Inset: Beer-Lambert law for the two strongest transitions at 782 (□, L: 10 mm; ■, L: 1 mm) and 711 nm (○, L: 10 mm; ●, L: 1 mm). **B** L-IR788 solvent cast in PMMA, in which concentrations are given in μg per unit volume of *polymer* (118, 304, 530, 735, 1192 and 2442 μg/mL). Thicknesses are around 200 μm. Inset: Beer-Lambert law for the two strongest transitions (□: 778 nm ○: 721 nm), which have shifted compared to molecularly dissolved L-IR788. Inserted lines serve as a guide to the eye.

A completely different absorption spectrum is observed when L-IR788 is incorporated into polymer matrices by solvent casting. The relative intensities of the two main peaks of the resulting optically homogeneous and transparent films are reversed compared to

molecularly dissolved L-IR788 (Figure 2.5B), even though the spectrum of a DCM solution containing both polymer and dye does resemble those in Figure 2.5A (data not shown). This phenomenon can be attributed to aggregation of the dye in the polymer films. Both the blue-shifted absorption maximum and the red-shifted onset of absorption indicate the formation of H-aggregates in the films. Also, the large decrease in absorption coefficient (slopes in the insets of Figure 2.5) and the broadening of the absorption bands indicate face-to-face stacking of dye molecules [13]. Apparently, the polymer is a worse solvent compared to DCM, thus favoring segregation of the dye and polymer, resulting in aggregation of dye molecules. The inset in Figure 2.5B illustrates a deviation from the Beer-Lambert law with increasing concentration, possibly indicating that the extent of aggregation increases as the concentration increases.

To obtain a better comparison to the polymer environment, the absorption of L-IR788 has been investigated in ethyl acetate (EtOAc) (Figure 2.6), since this solvent also contains an ester bond. The positions of the main peaks have shifted significantly compared to the spectrum in DCM, the low energy peak (termed peak I) now exhibiting a maximum at 765 nm, and the high energy peak (peak II) at 697 nm for very low concentration. The shift of the spectrum as a whole is not an indication of aggregation, but can be attributed to polarity of the environment (i.e. solvatochromic shift) [14]. Indeed, EtOAc is more apolar than DCM, with Hildebrand solubility parameters of 18.2 and 20.2 $(MPa)^{1/2}$ at 25°C, respectively [15]. However, both the large decrease in relative intensities of peak I and II, ultimately leading to a similar inversion of the relative intensities, and the significant shift of peak II from approximately 697 to 708 nm, illustrate the formation of aggregates. The Beer-Lambert law is clearly not applicable in EtOAc (inset in Figure 2.6A). It is obvious that in the limit of zero concentration of L-IR788, the intensities of peak I over peak II in both DCM and EtOAc are identical (Figure 2.6B), i.e. only molecularly dissolved L-IR788 is present. As concentration increases, aggregate formation in EtOAc occurs immediately, whereas the formation of aggregates in DCM only occurs at higher concentrations. The peak intensity ratios for the solvent cast PMMA films in Figure 2.6B suggest that the extent of aggregation in the polymer films is slightly higher than in ethyl acetate. The lower mobility of the polymer chains might prevent these chains from dissolving the dye effectively, leading to increased aggregation.

Possibly, the peak intensity ratio of the dye in the polymer films increases rapidly as the concentration approaches zero (similar to L-IR788 in EtOAc). However, at these low concentrations and film thicknesses, absorbance is not measurable and can therefore not be verified.
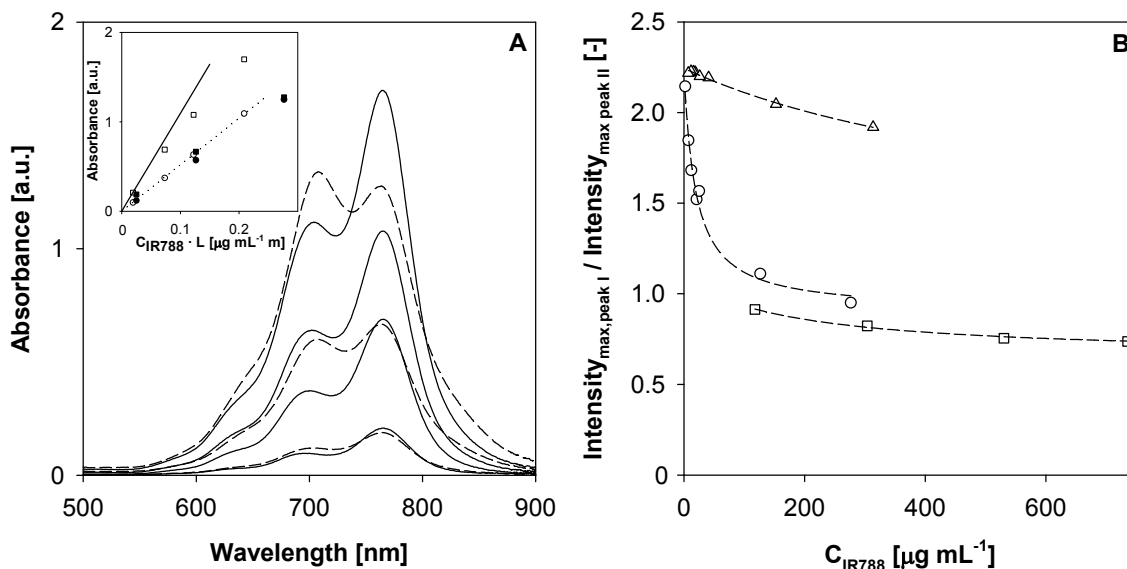
Figure 2.6: Absorption spectra of L-IR788 in EtOAc compared to absorption in DCM and PMMA. **A** L-IR788 in EtOAc (——: 1.9, 7.3, 12.3 and 20.9 µg/mL for L: 10 mm) and 1 mm (- - - -: 25.0, 126 and 277 µg/mL, for L: 1 mm). Inset: Beer-Lambert law for the two strongest transitions at 765 (□, L: 10 mm; ■, L: 1 mm) and 697 nm (○, L: 10 mm; ●, L: 1 mm). **B** Ratio of intensities of peak I over peak II (defined as the ratio of the intensities at their respective maximum absorption wavelengths) for L-IR788 in EtOAc (○), DCM (△), and cast in PMMA (□) with increasing concentration. Data points of the two cast films with the highest concentrations (1192 and 2442 µg/mL) are omitted for clarity. Their values are 0.71 and 0.69, respectively, compared to 0.74 for the highest concentration given in the graph.

Finally, the position of the peak maxima in EtOAc relative to the spectrum in solvent cast films should be addressed. Again, it is a blue-shift of the spectrum as a whole (~13 nm), suggesting that it is the environment of the dye aggregates determining the absolute position. Since the solubility parameter for PMMA is similar to that in EtOAc (around 18 $(MPa)^{1/2}$ [16]) no strong shift in the spectrum is expected based on the solubility parameter. However, a study comparing absorption spectra of dyes in polymers with those in their monomeric equivalents, among which PMMA and ethyl acetate, showed clear shifts in absorption maxima [17], which can be attributed to for example end

groups, impurities, or moisture content [17,18]. Moreover, the lower structural mobility of polymer chains might also influence the exact position of the spectrum.

2.4.2 Dye aggregation in compression molded PMMA discs

After compression molding of the polymer films well above their glass transition temperature, the spectra are restored to some extent (Figure 2.7). Based on thermodynamic considerations, aggregate formation of perylenebisimides in solution is known to decrease with increasing temperature [13]. At the elevated temperatures used here during compression molding, a similar process occurs. Rapid cooling after compression of the polymer films effectively freezes the dye into a thermodynamically unfavored state. The large size of the dye molecules prevents diffusion on an observable timescale after cooling below the glass transition of the polymer. Nevertheless, the intensity ratio of peaks I and II, the main indicator for aggregation, is still lower compared to molecularly dissolved L-IR788 and Beer-Lambert's law is no longer satisfied at higher concentrations. In addition, the position of peak II is still somewhere between that of molecularly dissolved L-IR788 and the aggregates in the cast films (Table 2.1). The resulting spectrum is thus in fact a superimposition of the absorption spectra of both aggregated and molecularly dissolved species. This is clearly illustrated by the polymer disc containing the highest concentration of L-IR788 in Figure 2.7A, in which a clear shoulder is observed presumably belonging to the non-aggregated state.

Table 2.1: Absorption coefficients (initial slopes in Figure 2.5, 2.6A and 2.7C) of the dye per unit volume of the medium in which it is present for peak I and II.

	Position peak I [nm]	ε_{peakI} [mL μg^{-1} m^{-1}]	Position peak II [nm]	ε_{peakII} [mL μg^{-1} m^{-1}]
Dichloromethane	782[†]	12.7	711[†]	5.7
Ethyl acetate	765[†]	10.8	697[†]	5.0
Solvent cast in PMMA	778[‡]	4.5	721[‡]	6.0
Compression molded in PMMA	781[‡]	10.1	714[‡]	6.4

[†] Peak position at infinite dilution

[‡] Peak position of aggregated form at relatively low concentrations
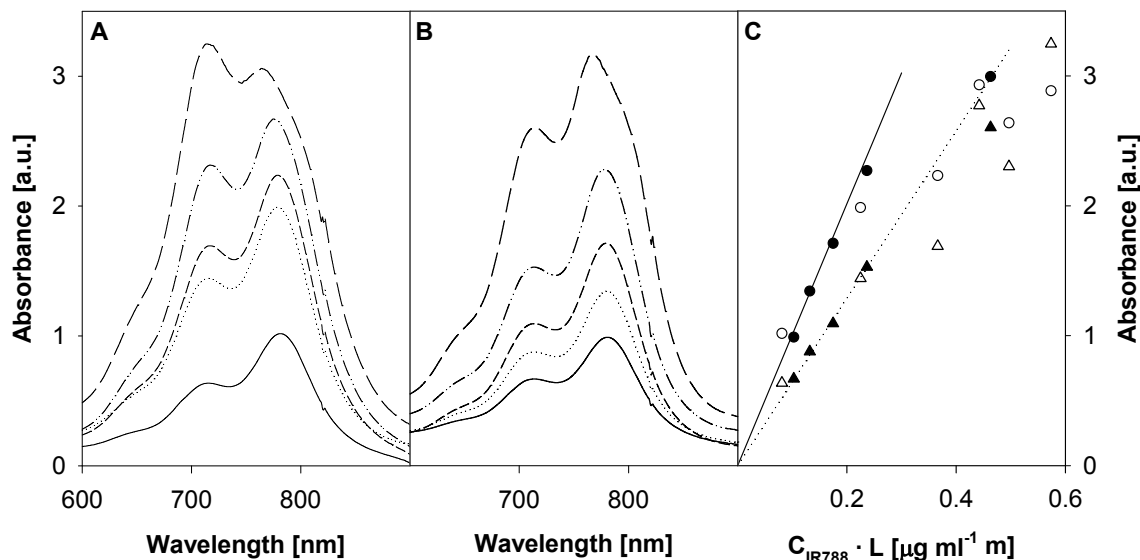
Figure 2.7: Absorption spectra of L-IR788 in compression molded polymer discs. **A** Increasing L-IR788 concentration (——: 93 μg/mL, ⋯⋯⋯: 274 μg/mL, - - - -: 427 μg/mL, − −: 531 μg/mL, − ⋅ −: 612 μg/mL, − −: 735 μg/mL) at constant sample thickness (780-874 μm). **B** Increasing sample thickness (——: 871 ± 214 μm; ⋯⋯⋯: 1120 ± 47 μm; - - - -: 1483 ± 25 μm; − ⋅ −: 2007 ± 31 μm; − −: 3930 μm) at constant L-IR788 concentration (118 μg/mL). **C** Absorbance for peak I at 781 nm in panel A (○) and B (●) and peak II at 714 nm in panel A (△) and B (▲). The lines show the validity of the Beer-Lambert law for the first data points for peak I (——) and peak II (⋯⋯⋯).

Although increased dye aggregation with increasing concentration is readily understood, it would be expected that the thickness of a polymer disc does not affect aggregation. However, when increasing the thickness at constant L-IR788 concentration, a clear blue-shift is observed for the peak with a thickness of 4 mm (Figure 2.7B). This cannot be ascribed to experimental error, but is a general trend, as can be seen in Figure 2.8A. Two series of discs with increasing thickness at constant concentration exhibit 'normal' spectra at low absorbance, whereas an absorbance higher than 2 to 2.5 results in blue-shifted peaks. Although the disc with the highest absorbance is too high to measure the complete spectrum, it does clearly illustrate the shoulder on the high wavelength side of the blue-shifted peak, suggesting that molecularly dissolved L-IR788 is still present. When comparing the ratio of the intensities of peak I and II for several series of these discs at fixed concentration (triangles in Figure 2.8B), a definite influence of thickness on aggregation is observed. Possibly, surface effects during the compounding process

influence aggregation behavior (an increasing number of solvent cast films are compounded into one disc in order to obtain a discs with increasing thickness), but no definite conclusions can be drawn. Figure 2.8B also displays a series of discs with approximately the same thickness and increasing concentration (red diamonds). There is some scatter in this ratio that, based on the results for the influence of thickness, can mainly be attributed to variations in thickness. As expected, the ratio of the peak intensities falls in the range between that of molecularly dissolved and strongly aggregated dye molecules.
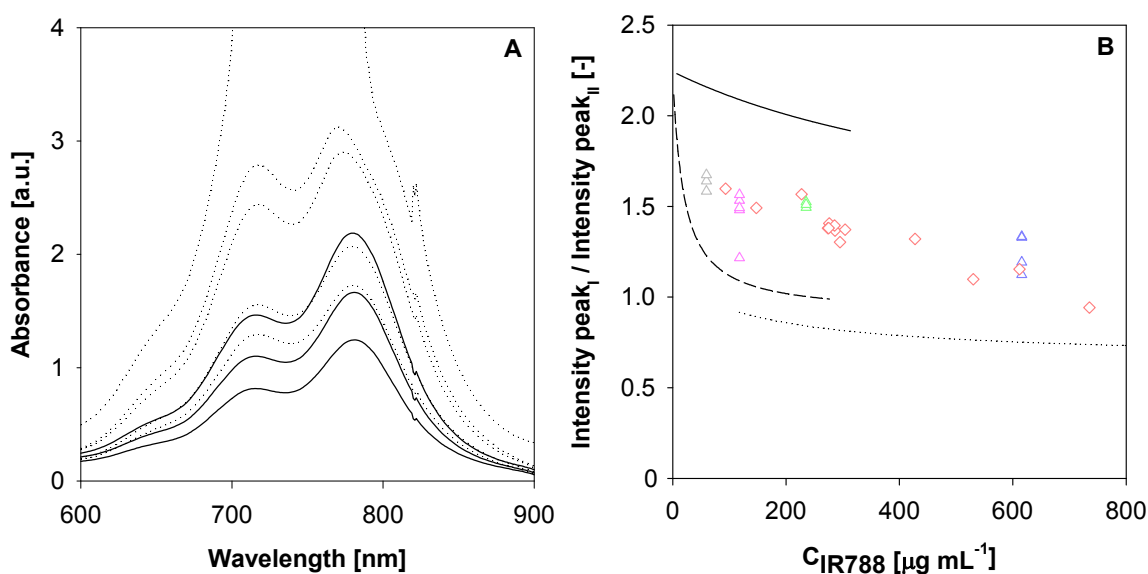
Figure 2.8: Influence of disc thickness on absorption spectrum. **A** Two series of increasing disc thickness at fixed L-IR788 concentrations: ——: 236 μg/mL, 737 ± 28 μm, 1044 ± 48 μm, and 1895 ± 28 μm, ·········: 615 μg/mL, 610 ± 24 μm, 730 ± 47 μm, 1135 ± 42 μm, 1319 ± 36 μm, and 1749 ± 18 μm. **B** Ratio of the intensities at the peak maxima of peak I over peak II. The different colored triangles denote series of increasing thickness at fixed concentrations. Diamonds denote increasing concentration with thickness between about 700 and 950 μm. The inserted lines correspond to those in Figure 2.6B for DCM (——), EtOAc (- - - -) and solvent cast films (·········).

To confirm that temperature is indeed an important factor to suppress dye aggregation and that compression molding is not influenced by aggregation during the solvent casting process, experiments were performed in which the dye is directly mixed with the polymer inside a compounder at high temperatures. The resulting material reveals that a spectrum

28

resembling that of compression molded discs is obtained after compounding (data not shown). However, small scale compounding leads to a substantial loss of material and has therefore not been further used in this work. Nevertheless, for production of dye doped polymer matrices on industrial scale, compounding would be advantageous. Finally, it should be mentioned that NIR dye compatibility is not limited to PMMA. The dye has been incorporated in various other polymers, e.g. other polymethacrylates, poly(ethylene-*co*-vinyl acetate), polylactide, and polycarbonate, thus demonstrating its broad applicability.

2.4.3 Heating of polymer matrices

Based on a simple consideration of the heat capacity of a polymer sample, an estimate can be made for the amount of energy required to induce an average increase in temperature of the sample (Eqn. 2-3). For example, to induce a 20ºC temperature increase throughout a PMMA disc (density: 1.19 g cm^{-3}; specific heat capacity: 1.38 J g^{-1} K^{-1}) with a diameter of 25 mm and a thickness of 1 mm, the amount of energy required is 16.6 J. Assuming the temperature rise should be realized within one minute and that all near-infrared radiation is converted into heat, an NIR source of almost 280 mW is required.

$$Q = m \cdot C_p \cdot \Delta T_{av} \qquad\qquad\qquad [2\text{-}3]$$

where Q : energy   [J]
          m : mass of polymer sample   [kg]
          C_p : specific heat capacity   [J kg^{-1} K^{-1}]
          ΔT_{av} : average increase in temperature   [L mol^{-1} m^{-1}]

However, this rough calculation neglects the efficiency of energy uptake by the matrix (i.e. the amount of absorbed radiation transformed into heat) as well as heat dissipation, i.e. radiative, conductive and convective losses to the environment. Moreover, as radiation originates from one side of the sample, the temperature at the irradiated side is higher than at the opposite side. A further complication arises from the fact that the NIR source used in this study exhibits an intensity distribution (Figure 2.3). The effect of NIR intensity and intensity distribution will be discussed in section 2.4.3.1. The focus in the remainder of the chapter is on the maximum surface temperature increase, i.e. the

temperature increase measured in the center of the target, which is referred to as the hot spot. The influence of dye concentration and sample thickness of compounded polymer discs is demonstrated in section 2.4.3.2. Finally, NIR-induced heating of polymer samples in aqueous environment is discussed in section 2.4.3.3.

2.4.3.1 Influence of laser intensity and intensity distribution on temperature

Figure 2.9A depicts a typical temperature increase in the hot spot in time for irradiation at different laser powers. These heating experiments are performed with the same sample and are completely reversible, indicating that neither the dye nor the polymer is degraded by NIR radiation. The surface temperature is measured at both the front (irradiated side) and back of the 1.5 mm thick sample. At higher intensities, the temperature difference between both sides of the sample increases, as the power increases. This is in accordance with Fourier's law, which states that an increase in heat flow leads to an increase in temperature difference over a certain distance. The initial heating rate, determined as the slope at $t = 0$, displays a linear dependence on laser intensity. In contrast, the steady state temperature increase, defined as the temperature increase after 10 min, shows a slight downward curve with increasing power (Figure 2.9B). This can be explained by the influence of heat transfer during irradiation. In the steady state, the heat production equals heat dissipation (Eqn. 2-4):

$$Q_{production} = Q_{dissipation} = \alpha \cdot A \cdot (T_{surface} - T_{surroundings}) \qquad\qquad [2\text{-}4]$$

where Q   : heat production and dissipation   [W]
        α : overall heat transfer coefficient   [W m^{-2} K^{-1}]
        T   : temperature   [K]

The overall heat transfer coefficient in this equation comprises the heat transfer coefficients of conduction, convection and radiation. If the overall heat transfer coefficient is independent of temperature, a linear increase of temperature with power would indeed be expected. However, both the free convection and the radiative term increase with temperature (further discussed in Chapter 3), resulting in the observed deviation from linearity. For the initial heating rate, heat transfer effects are still negligible as evidenced by the linear correlation found in Figure 2.9B.
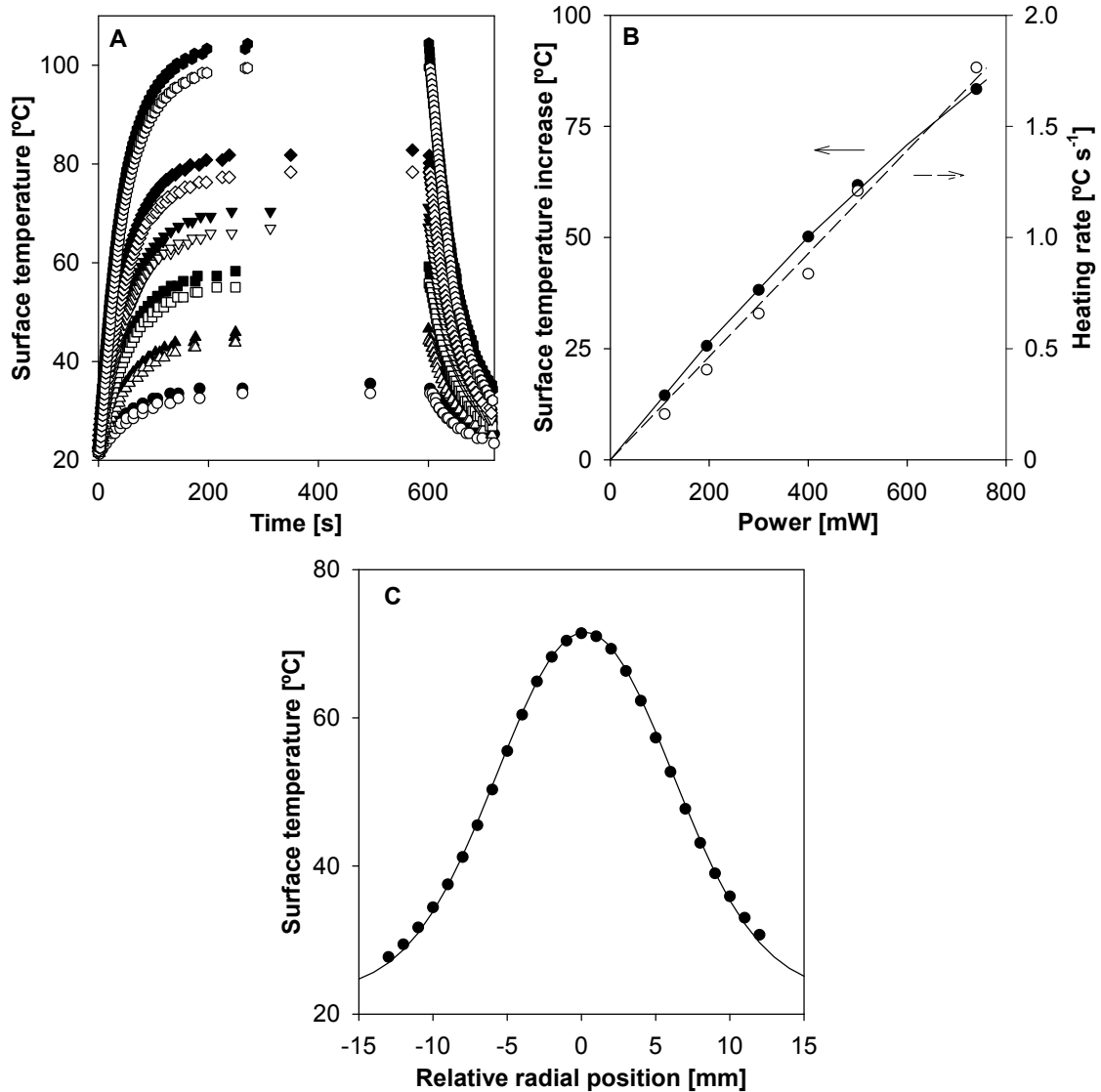
Figure 2.9: NIR heating of a dye doped polymer matrix (119 μg/mL, d: 25 mm, L: 1.5 mm, spot size: 19.8 mm) **A** Local measured surface temperatures at irradiated side (closed symbols) and back (open symbols) of sample for laser powers of 110 mW (●), 220 mW (▲), 300 mW (■), 400 mW (▼), 500 mW (◆) and 740 mW (⬤) in the hot spot. **B** Dependence of initial heating rate and steady state temperature at the irradiated side on the laser power (○ and ●, respectively). **C** Lateral steady state surface temperature distribution for a laser power of 400 mW. Solid line represents a Gaussian fit.

The influence of laser intensity distribution on the lateral steady state temperature profile is depicted in Figure 2.9C. Similarly to the laser intensity profile in Figure 2.3, the temperature profile is Gaussian. The fitted value of the full width at half maximum (FWHM) for the temperature profile is a factor 1.7 higher than that of the intensity

31

profile, which implies the occurrence of lateral conductivity, thus broadening the temperature profile. However, this temperature profile clearly indicates the importance of the NIR source for the resulting temperature profile.

2.4.3.2 Influence of dye concentration and sample thickness on temperature

Although it has been shown that absorbance increases linearly with either concentration or thickness (in the absence of dye aggregation), it is the exponential character of absorption of radiation (Eqn. 2-1) that determines the equilibrium increase in surface temperature. This is illustrated in Figure 2.10A, in which the increase in temperature in the steady state for a constant disc thickness of approximately 800 μm follows a similar trend to the absorption expressed in terms of the percentage of radiation absorbed over the thickness of the disc (△), as opposed to the logarithmic absorbance units (○). In contrast, the values found for the initial heating rates display a different correlation with concentration, which displays more similarity with the correlation in terms of absorbance units (Figure 2.10B).

Figure 2.10: Influence of dye concentration on NIR-induced heating. **A** Steady state temperature increase (■) for compression molded discs ranging from 730 to 870 μm at a laser power of 400 mW and a spot size of 24 mm. Open symbols represent absorbance in terms of percentage absorbance (△) or absorbance units (○). The scales have been chosen so that the data points for the disc with the highest concentration coincide. **B** Initial heating rates of same discs under the same circumstances.

These trends can be explained by considering the mechanism of heating. Absorption of photons is a molecular process, the extent of which is only determined by the number of chromophores encountered by incident radiation. Subsequent heat generation originates from those same molecules. This means that doubling the number of dye molecules at the surface results in twice as much local heat generation. In theory, this implies that the surface temperature of an infinitesimal slice should initially increase linearly with dye concentration. However, in reality the measured temperature originates from a finite slice of polymer, albeit a very thin slice. The decrease in intensity over this thin slice does actually exhibit a logarithmic relationship with concentration (Figure 2.1), and consequently the measured temperature also contains an exponential part. The resulting graph in Figure 2.10B is therefore somewhere between linear and exponential. The steady state surface temperature is not just determined by the amount of NIR absorbed at the surface, but depends on the amount of energy absorbed throughout the sample (Eqn. 2-4) and therefore does follow an exponential relationship. Since the absorbance is already over 80% for all these discs, even at these relatively low concentrations, any influence of aggregation with increasing dye concentration on the temperature increase is obscured. It is likely that the deflection from linearity of the initial heating rate may partly be attributed to aggregation, but this cannot be quantified due to the exponential component of the heating rate.

For the same reasons discussed previously for concentration, no effect of thickness on initial heating rate is expected for constant concentration. Figure 2.11B demonstrates the influence of thickness on the initial heating rate for three different concentrations. Although significant deviations are observed for the highest concentration, it indeed appears that the initial heat production at the surface for a fixed dye concentration remains unchanged, irrespective of sample thickness. The steady state situation is slightly more complicated. The irradiated surface temperature does not only depend on the amount of energy generated at the surface, but also on the energy produced in the rest of the polymer disc. This is primarily determined by the laser intensity profile, after which axial heat conductivity levels out the temperature differences to some extent. As the surface area of the samples remains unchanged (the sample thickness is much smaller than the diameter), heat dissipation to the environment is identical for all samples. For

low dye concentrations, where a considerable part of the radiation is still absorbed at the non-irradiated surface, increasing the thickness is accompanied by a significant amount of extra absorption of radiation. This is the case for the triangles in Figure 2.11A, which still transmit 27, 15 and 11%, resulting in an increasing surface temperature. As the dye concentration increases, the thickness at which most of the radiation is absorbed becomes increasingly smaller. For example, the transmittance for the circles and the squares ranges from only 2.5 to 0.0001%. In these cases, the extra amount of energy absorbed with increasing thickness is negligible, and, in principle, the only effect of increasing thickness is lengthening the time to reach the steady state situation. However, aggregative effects discussed in section 2.4.2 can also play a role. The deviating temperature increase of the data point with the highest concentration and thickness, corresponding to the highest absorbance spectrum in Figure 2.8A, may be attributed to aggregation. Unfortunately, this cannot be verified as the peak intensity ratio cannot be determined from the spectrum.
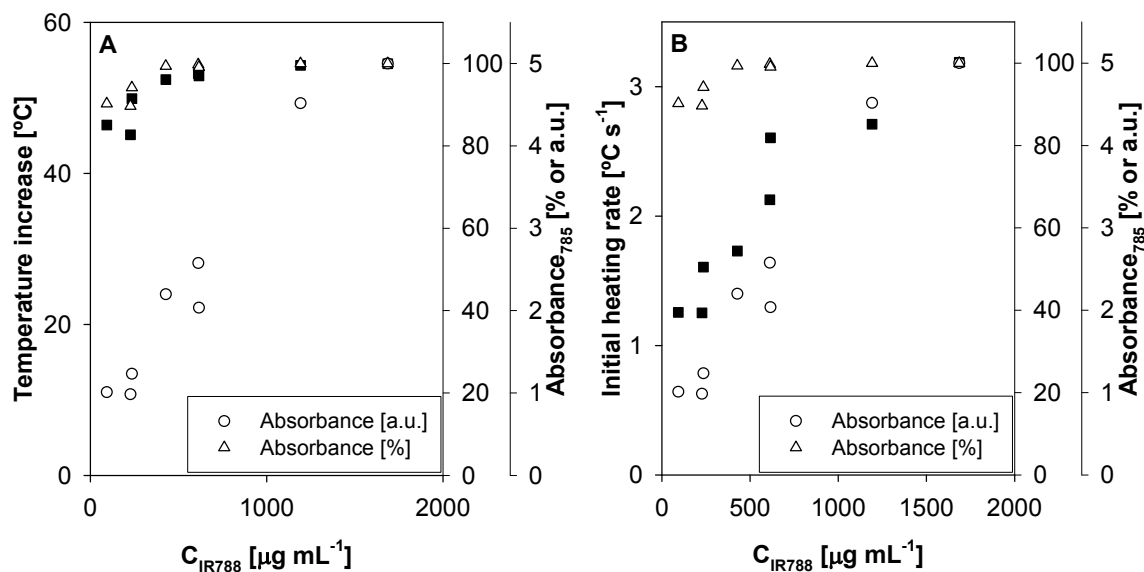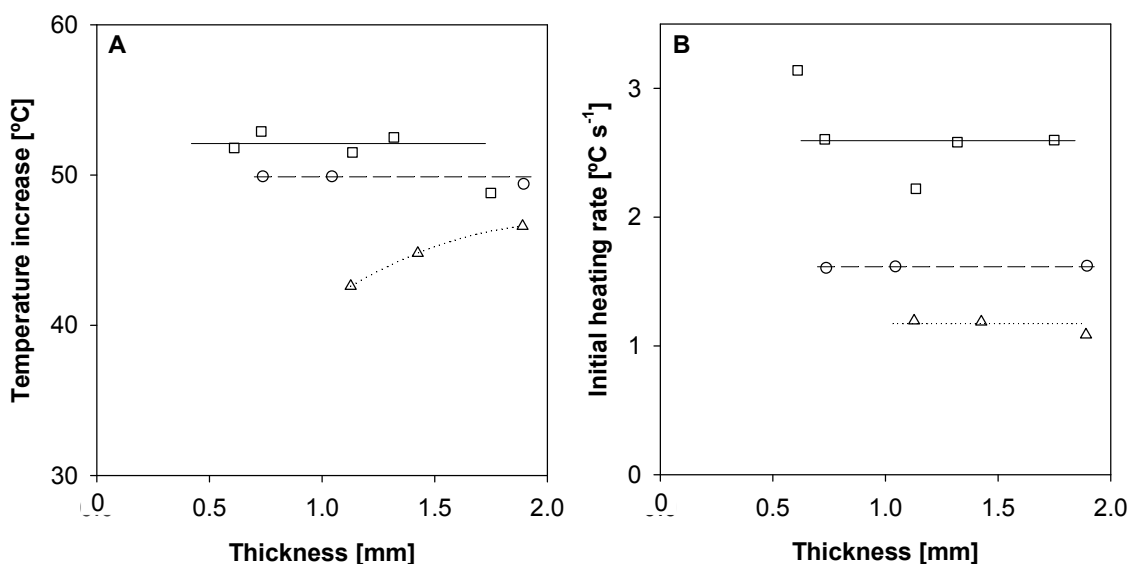

Figure 2.11: Influence of sample thickness on NIR-induced heating. **A** Steady state temperature increase for compression molded discs at a laser power of 400 mW and a spot size of 24 mm. △: 60 μg/mL, ○: 234 μg/mL, □: 615 μg/mL, respectively. **B** Initial heating rates of the same discs under the same circumstances.

2.4.3.3 *NIR-induced heating of a polymer in aqueous environment*

The results discussed so far involved heating of polymer samples in air. A more relevant environment for drug delivery applications is an aqueous environment. Compared to the thermal insulating properties of air, heat transfer in water is much faster. The higher heat dissipation should ultimately lead to lower surface temperatures than measured in air. However, infrared thermometry cannot be used in water due to the strong absorption of mid- and far-infrared radiation by water. To verify that NIR-induced heating is feasible in aqueous environment, the temperature is measured inside a polymer disc using a Pt100-electrode using the set-up in Figure 2.4.
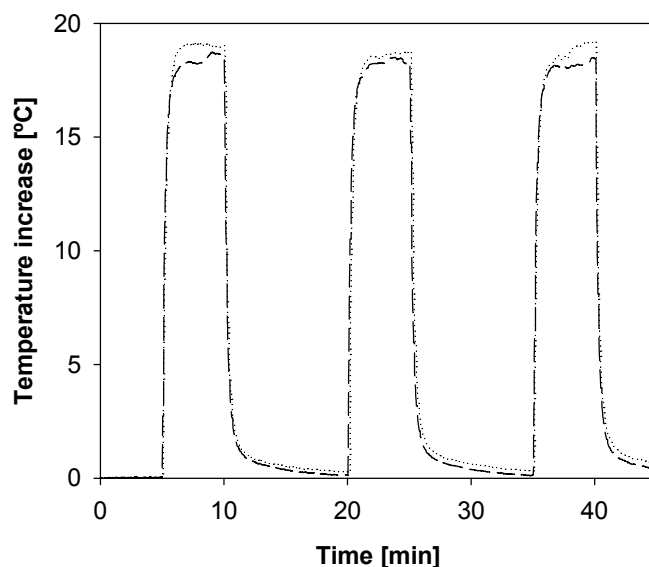
Figure 2.12: NIR-induced heating of a polymer disc (C_{IR788}: 118 μg/mL, L: 3.93 mm) measured with a Pt100 inserted approximately 1 mm beneath the irradiated surface in the center of the disc. Initial temperature is 20ºC (··········) or 37ºC (− − ·), laser power: 750 mW, spot size: ~14.4 mm.

Figure 2.12 demonstrates that NIR-induced heating in aqueous environment is indeed possible. Three heating cycles of 5 minutes are performed with 10 minute intervals in between each heating cycle. The measurements show that the environmental temperature of either 20ºC or 37ºC does not influence the absolute temperature increase and that heating is reproducible. It should be noted that the Pt100 heats up slightly (~4ºC) in the absence of the dye, too. However, since most of the irradiation is absorbed in the surface layer (~ 94%), the effect on the temperature in Figure 2.12 is negligible. Finally, it is

35

stressed that direct comparison with the other results in this chapter is hard due to the location of temperature measurement, but these results clearly demonstrate the feasibility of NIR-induced drug release.

2.5 Conclusions

NIR-induced heating of polymer matrices using a near-infrared dye has been demonstrated, achieving initial heating rates of over $3^{\circ}C\ s^{-1}$ and steady state temperature increases as high as $80^{\circ}C$. Incorporation of the quaterrylene-bisdicarboximide dye into PMMA leads to the formation of H-aggregates, which can be suppressed by incorporation or post-processing at elevated temperature. Any H-aggregates still present after incorporation do not necessarily influence the efficiency of heat generation since these aggregates do not exhibit photoluminescent properties. However, absorption at the desired wavelength is diminished by the presence of these aggregates. The final surface temperature reached displays an exponential relationship with dye concentration, thus rendering the influence of aggregation negligible. In contrast, the initial heating rate shows a dependence in between linear and exponential on concentration. The deviation from the theoretical linear dependence (in the absence of aggregation) is attributed to the measurement of the average temperature of a (small) finite slice of polymer as opposed to the actual surface temperature. Aggregation should decrease the initial heating rate, but this has not been quantified in this research due to the aforementioned temperature measurement. Finally, it has been shown that a significant temperature increase can also be attained in aqueous environment, thus offering a promising starting point for NIR-induced drug release.

References

[1] Weissleder, R. A clearer vision for *in vivo* imaging. *Nat. Biotechnol.* **19**, 316-317 (2001).

[2] Mobley, J. & Vo-Dinh, T. in *Biomedical Photonics* (ed. Vo-Dinh, T.) 2-1 – 2-75 (CRC, Boca Raton, 2003).

[3] Sershen, S. R., Westcott, S. L., Halas, N. J., West, J. L. Temperature-sensitive polymer-nanoshell composites for photothermally modulated drug delivery. *J. Biomed. Mater. Res.* **51**, 293-298 (2000).

[4] Sershen, S. R., Westcott, S. L., West, J. L., Halas, N. J. An opto-mechanical nanoshell-polymer composite. *Appl Phys. B.* **73**, 379-381 (2001).

[5]   Wu, G., Mikhailovsky, A., Khant, H. A., Fu, C., Chiu, W., Zasadzinski, J. A. Remotely triggered liposome release by near-infrared-light absorption via hollow gold nanoshells. *J. Am. Chem. Soc.* **130**, 8175-8177 (2008).

[6]   Geerts, Y. *et al.* Quaterrylenebis(dicarboximides)s: near infrared absorbing and emitting dyes. *J. Mater. Chem.* **8**, 2357-2369 (1998).

[7]   Kasha, M., Rawls, H. R., Ashraf El-Bayoumi, M. The exciton model in molecular spectroscopy. *Pure Appl. Chem.* **11**, 371-392 (1965).

[8]   Neuteboom, E. E., Meskers, S. C. J., Meijer, E. W., Janssen, R. A. Photoluminescence of self-organized perylene bisimide polymers. *Marcomol. Chem. Phys.* **205**, 217-222 (2004).

[9]   Rybtchinski, B., Sinks, L. E., Wasielewski, M. R. Combining light-harvesting and charge separation in a self-assembled artificial photosynthetic system based on a perylenediimide chromophores. *J. Am. Chem. Soc.* **126**, 12268-12269 (2004).

[10] Kazmeier, P. M., Hoffmann, R. A theoretical study of crystallochromy. Quantum interference effects in the spectra of perylene pigments. *J. Am. Chem. Soc.* **116**, 9684-9691 (1994).

[11] Giaimo, J. M., Gusev, A. V., Wasielewski, M. R. Excited-state breaking in cofacial and linear dimers of a green perylenediimide chlorophyll analogue leading to ultrafast charge separation. *J. Am. Chem. Soc.* **124**, 8530-8531 (2002).

[12] Fuller, M. J. *et al.* Ultrafast photoinduced charge separation resulting from self-assembly of a green perylene-based dye into π-stacked arrays. *J. Phys. Chem. A* **109**, 970-975 (2005).

[13] Würthner, F., Chen, Z., Dehm, V., Stepanenko, V. One-dimensional luminescent nanoaggregates of perylene bisimides. *Chem. Commun.*, 1188-1190 (2006).

[14] Reichardt, C. *Solvents and Solvent Effects in Organic Chemistry*, 3rd ed., 329-388 (Wiley, Weinheim, 2003).

[15] Barton, A. F. M. *Handbook of Solubility Parameters and Other Cohesion Parameters*, 94-110 (CRC, Boca Raton, 1983).

[16] Barton, A. F. M. *Handbook of Solubility Parameters and Other Cohesion Parameters*, 314 (CRC, Boca Raton, 1983).

[17] Paley, M. S., McGill, R. A., Howard, S. C., Wallace, S. E., Harris, J. M. Solvatochromism. A new method for polymer characterization. *Macromolecules* **23**, 4557-4564 (1990).

[18] Hubert, C. Fichou, D., Valat, P., Garnier, F., Villeret, B. A solvatochromic dye-doped polymer for detection of polar additives in hydrocarbon blends. *Polymer* **36**, 2663-2666 (1995).

CHAPTER 3

Heat and Mass Transfer in NIR-Induced Drug Release

Abstract

A model for NIR-induced heating based on the finite element method (FEM) is developed and validated based on the experimental results described in Chapter 3. Subsequently, the effect of NIR-dye distribution on heat generation inside the polymer matrix is modeled in aqueous environment. Since the main resistance to mass transfer is located at the polymer/water interface, heat generation should mainly be located at the surface of the implant. Coating the implant with a dye containing layer therefore yields the best combination of high surface temperatures without exposing the inside of the implant to excessive temperatures. Based on the Pennes bioheat equation, the FEM model is then used to estimate the temperatures that can be achieved *in vivo* using NIR, taking into account scattering and absorption by skin and subcutaneous tissue. Higher temperatures are induced *in vivo* due to a lower amount of heat dissipation compared to aqueous environment. By using an insulating layer, the tissue can be protected from high temperatures, thus preventing tissue damage from occurring and enabling NIR-induced drug release.

3.1 Introduction

The finite element method (FEM) is a numerical approach to approximate solutions of partial differential equations and integral equations. Its use ranges from mechanical and chemical engineering to optics and fluid dynamics and enables rapid prototype design. FEM is based on subdivision of a continuous domain into discrete subdomains (elements), termed the mesh. In each element, the governing equations are solved and used as input for neighboring elements. By increasing the density of the mesh, the accuracy of the solution is enhanced, but computation time is simultaneously increased. To save computation time, the mesh density can be selectively increased in areas of interest. For symmetric geometries, computation time can be further reduced by solving the equations in 2-dimensions, after which rotation around the symmetry axis results in a 3-dimensional solution (Figure 3.1). By defining dimensionless models, the size of a geometrical model can be varied without actually having to redraw the geometry, thus further simplifying the modeling.
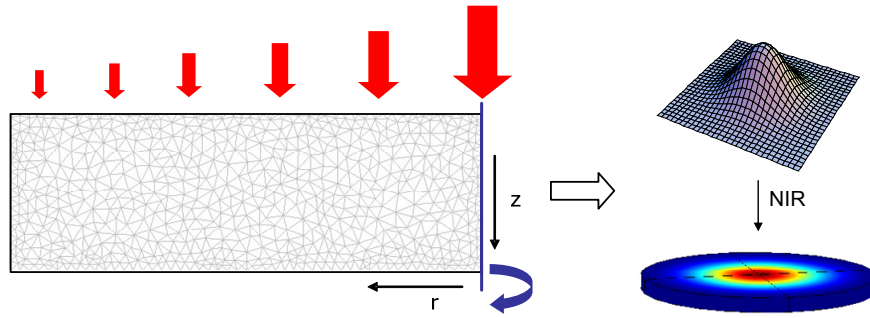
Figure 3.1: Example of FEM modeling of heating induced by an NIR source exhibiting a Gaussian intensity distribution.

In this chapter, the transient heat transfer balance is solved in order to compare drug delivery implants of different geometries and designs. First, a general description of the prerequisites for drug delivery based on the glass transition temperature switch are discussed. Then, the heat transfer model is tested by comparing modeling results to experimental results discussed in Chapter 3. Based on this model, various possible designs for a drug delivery implant are modeled and discussed, and its feasibility in subdermal applications is demonstrated. Finally, some considerations for mass transfer in an on-demand drug delivery system based on the glass transition switch are presented.

40

3.2   Mass transfer around the glass transition temperature

The glass transition temperature (T_g) of polymers has been extensively discussed in Chapter 2. An important aspect of the T_g is that it is influenced by several factors, such as thermal history, the environment of the polymer, and polymer additives [1,2]. Inclusion of drug molecules in a polymer matrix often leads to an increase in free volume and a consequent decrease of T_g. Since T_g plays a central role in achieving on-demand drug release in the current system, the effect of drug incoporation on T_g is of great importance.

The T_g inside a polymer matrix containing a plasticizing drug depends on the local drug concentration. Assuming a homogeneous distribution of drugs inside the polymer matrix, the T_g is equal throughout, resulting in a constant diffusion coefficient inside the polymer. If a sufficient amount of drug is dissolved in the polymer to decrease the T_g to below the environmental temperature, the entire implant is in a rubbery state (Figure 3.2, top left). However, when the implant is placed in aqueous environment, the main resistance to mass transfer is located inside the polymer, since the diffusion coefficient in water is several orders of magnitude higher than the diffusion coefficient in a rubbery polymer. As a result, the drug concentration outside the polymer can be assumed to be zero, and except for a small partitioning coefficient, the surface concentration of the drug inside the polymer is also close to zero. The resulting concentration gradient implies that the glass transition temperature at the surface of the implant is close to that of the pure polymer. If the T_g of the pure polymer is higher than the environmental temperature, this actually means that the rubbery bulk of the implant is surrounded by a glassy surface layer (Figure 3.2, top right). The rate limiting step for diffusion is thus located at the surface of the implant. To trigger drug release, the temperature should be increased so that the outer glassy layer becomes rubbery (Figure 3.2, bottom). The main temperature increase induced by NIR should therefore be located at the surface of the implant. After switching off NIR irradiation, the surface layer returns to the glassy state, resulting in negligible drug release. This process is fully reversible, as long as the driving force for release remains constant, which is further addressed in section 3.8. In Figure 3.2, the temperature is assumed to be equal throughout the disc, but in reality, a temperature profile exists depending on NIR dye concentration and distribution in the polymer matrix, which is discussed in section 3.6. First, the basic modeling equations are discussed.
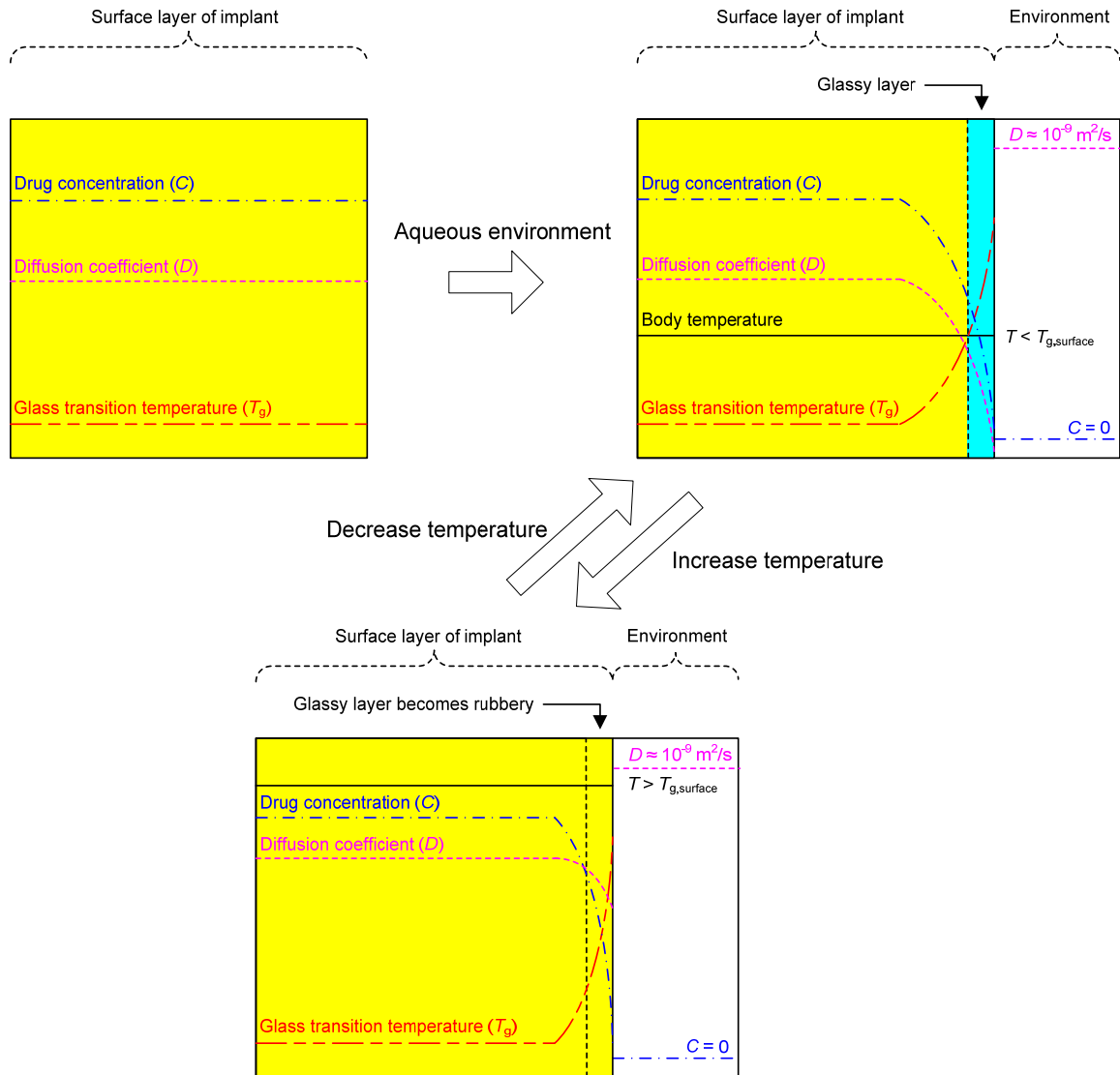
Figure 3.2: Schematic representation of drug delivery concept based on the glass transition temperature.

3.3   Modeling equations

The Comsol Multiphysics software package includes heat and mass transfer modules with predefined differential equations. The equations for heat and mass transfer inside the polymer implant are given by Eqns. 3-1 and 3-2, respectively.

$$\rho \cdot C_p \frac{\partial T}{\partial t} = \nabla \bullet (k\nabla T) + Q \qquad\qquad [3\text{-}1]$$

$$\frac{\partial C}{\partial t} = \nabla \bullet (D\nabla C) \qquad\qquad [3\text{-}2]$$

where ρ : density   [kg m^{-3}]

   C_p : heat capacity   [J kg^{-1} K^{-1}]

   T : temperature   [K]

   t : time   [s]

   k : thermal conductivity   [W m^{-1} K^{-1}]

   Q : heat production   [W m^{-3}]

   C : concentration of diffusing species   [kg m^{-3}]

   D : diffusion coefficient   [m^2 s^{-1}]

Due to the plasticizing effect discussed in section 3.2, the diffusion coefficient is described as a concentration dependent function. The heat production term in Eqn 3-1 is given by the local heat generation equation in Figure 2.1, differing only in an initial intensity depending on radial postion due to the Gaussian laser intensity distibution (Eqns. 3-3 and 3-4). Eqns. 3-3 and 3-4 are used for validation of the model in sections 3.4 and 3.5, in which modeling results are compared to experimental results from Chapter 2. However, when considering various implant designs in section 3.6, it is assumed that a source with a homogeneous intensity distribution is available (i.e. I$_0$ has a constant value for all values of r).

$$Q = \frac{ln(10) \cdot I_0(r)}{\varepsilon_\lambda \cdot C_{IR788}} \cdot 10^{-\varepsilon_\lambda \cdot C_{IR788} \cdot Z} \tag{3-3}$$

$$I_0(r) = \frac{P}{2 \cdot \pi \cdot \sigma^2} e^{-\left(\frac{r}{\sigma}\right)^2} \tag{3-4}$$

where $I_0(r)$: incident laser intensity distribution   [W m^{-2}]

   r, z : radial and axial coordinate, resp. (Figure 3.1)   [m]

   P : power   [W]

   σ : standard deviation from normal distribution   [m]

In the modeling approach followed in this work, the equations for heat and mass transfer in the surrounding medium are not solved explicitly, but rather, boundary conditions are defined by equations 3-5 and 3-6.

43

$$n \bullet (k\nabla T) = h\,(T_0 - T) + e \cdot \sigma_b\,(T_0^4 - T^4)$$ [3-5]

$$n \bullet (D\nabla C) = k_m\,(C_\infty - C)$$ [3-6]

where n : vector normal to the boundary   [-]

      h : heat transfer coefficient (= $Nu \cdot k_{env}/L_c$)   [W m^{-2} K^{-1}]

      Nu : Nusselt number   [-]

      k_{env} : Thermal conductivity of the environment   [W m^{-1} K^{-1}]

      L_c : Characteristic length   [m]

      T_0 : ambient temperature   [K]

      e : emissivity factor   [-]

      σ_b : Stefan-Boltzmann constant (= $5.67 \cdot 10^{-8}$)   [W m^{-2} K^{-4}]

      k_m : mass transfer coefficient   [kg m^{-2} K^{-1}]

      C_∞ : bulk concentration of surrounding medium   [kg m^{-3}]

The boundary conditions for heat transfer are a balance between heat conduction into the implant (left-hand side of Eqn 3-5) and heat transport into the surrounding medium due to convection and conduction, or due to radiation (first and second term on the right-hand side, respectively). The radiative term in Eqn. 3-5 is only relevant for heat transfer in air.

Experiments have been performed in a stagnant medium, implying convective transport is due to natural convection. For a vertical plate, as is the situation for the heating experiments in air described in Chapter 2, Churchill and Chu proposed an expression for the Nusselt number for the laminar range, i.e. $Ra_L < 10^9$ (Eqn. 3-7) [3]:

$$Nu_L = 0.68 + \frac{0.670 \cdot Ra_L^{1/4}}{[1 + (0.492/Pr)^{9/16}]^{4/9}}$$ [3-7]

where Nu_L : mean Nusselt number   [-]

      Ra_L : mean Rayleigh number (=$Gr_L \cdot Pr$)   [-]

      Gr_L : mean Grashof number (Eqn. 3-8)   [-]

      Pr : Prandtl number (=v/a)   [-]

      v : kinematic viscosity   [m^2 s^{-1}]

      a : thermal diffusivity   [m^2 s^{-1}]

$$Gr_L = \frac{\beta \cdot g \cdot L_c^{\ 3} \cdot \Delta T}{\nu^2}$$ [3-8]

where β : thermal expansion coefficient $[K^{-1}]$

g : gravitational acceleration $[m^2\ s^{-1}]$

ΔT : temperature difference between heated fluid

and bulk (evaluated at film temperature T_f)   [K]

These equations have actually been developed for uniform surface temperatures, and as has been demonstrated in Chapter 2, a clear surface temperature profile exists. Moreover, the normal definition of L_c, i.e. the length of the vertical plate, or in our case the diameter of the disc, is presumably not correct. L_c is based on the direction in which the boundary layer develops, and since the main temperature increase occurs in the center of the disc, L_c is more likely related to the spot size of the laser. In this work, even though it is a rather crude approximation, Eqns. 3-7 and 3-8 are assumed to be applicable to calculate a local Nu_x, based on the local surface temperature. L_c is then used to fit the model to the cooling period of the experimental results presented in Figure 2.9. In this approach, the other fitting parameter, i.e. the quantum yield of thermal relaxation, does not interfere as laser irradiation no longer plays a role.

For a horizontal configuration of a flat plate, as is the case for the experimental set-up for heating in aqueous environment, McAdams has suggested correlations depending on whether the heated surface is facing up (Eqn. 3-9) or down (Eqn. 3-10) [4]. In these equations, L_c is defined differently, i.e. the ratio between the surface area and perimeter of the polymer disc. The same limitations arise here as the temperature distribution is not uniform, which is addressed in section 3.5.

$Nu_L = 0.54 \cdot Ra_L^{\ 1/4}$ for $10^5 < Ra_L < 2 \cdot 10^7$ [3-9]

$Nu_L = 0.27 \cdot Ra_L^{\ 1/4}$ for $3 \cdot 10^5 < Ra_L < 10^{10}$ [3-10]

For mass transfer, the boundary conditions depend on the ratio of mass transfer within the implant (left-hand side of Eqn. 3-6) and in the surrounding medium (right-hand side). Similar to Nu for heat transfer, the Sherwood number (Sh) is introduced. Based on heat

and mass transfer analogy, correlations for *Sh* can be defined identically to those for heat transfer (i.e. Eqns. 3-9 and 3-10), when replacing Ra_L by $Sc \cdot Gr_L$, where *Sc* is the Schmidt number, defined as ν/D. However, since mass transfer outside the implant is assumed to be much faster than inside the polymer matrix (section 3.2), the surface concentration is simply set to zero, thus not requiring the correlations for *Sh*.

3.4 Heat transfer in air

In order to determine whether the model is in good agreement with experimental data, the heating graphs in Figure 2.9 are compared to modeling results. Ra_L is well below 10^9, allowing the use of Eqn. 3-7 for the boundary conditions. The input parameters used in the model are given in the appendix 3.10.1. Two parameters in the model remain unknown, i.e. the characteristic length, L_c, and the quantum yield of thermal relaxation, $\eta_{thermal}$. By setting L_c equal to 4 mm, a good correlation with the experimental cooling rate (i.e. t > 600 s) is obtained. Then, assuming that $\eta_{thermal}$ is constant throughout the implant, this parameter is chosen such that the equilibrium temperature of model and experiment at an intermediate power of 400 mW coincide. The value found for $\eta_{thermal}$ equals 57%, which is significantly lower than the expected value approaching 100% in the absence of any photophysical processes. Nevertheless, these parameters are used to model the heating curves for the other laser powers.

The results of the surface temperatures in the hot spot on the irradiated side of the polymer sample up to 500 mW are in good agreement with the experimental results (maximum deviation: 1.7°C). However, a significant deviation is observed for the highest power. This may be explained by the fact that the T_g of the polymer is approached. The correlation used for the heat capacity in this model is valid (i.e. verified experimentally) up to 80°C. However, a temperature of over 100°C (T_g: 99°C) is reached in this experiment, and as explained in other chapters, a jump in heat capacity occurs around T_g. An increasing heat capacity ultimately leads to a lower temperature than predicted by the model. It is therefore important to incorporate a correlation for the heat capacity near T_g in the polymer or temperatures may be overpredicted.

The prediction for transient heating is not as good as for the steady state temperatures. The modeled initial heating rate is about twice as high and the modeled temperature

remains higher throughout the whole transient period. Assuming that the boundary conditions for transient cooling satisfactorily describe transient heating, the deviation originates from the energy input term for laser irradiation. Indeed, since both the lateral temperature profile (dashed line in Figure 3.3B) and $\eta_{thermal}$ differ considerably from experimental and expected values, respectively, the laser intensity distribution might actually be broader than measured by the manufacturer at the fiber exit (Figure 2.3). When increasing the Gaussian parameter, σ, by a factor of 1.45 and simultaneously increasing $\eta_{thermal}$ to 94%, the resulting lateral temperature profile provides a much better fit to the experimental profile (Figure 3.4). In addition, the approximation of the transient state for all laser powers has improved significantly, with initial heating rates in the correct range. Also, the temperature difference between the modeled surface temperature at the front and back of the sample has decreased, showing more similarities with the experimental values.
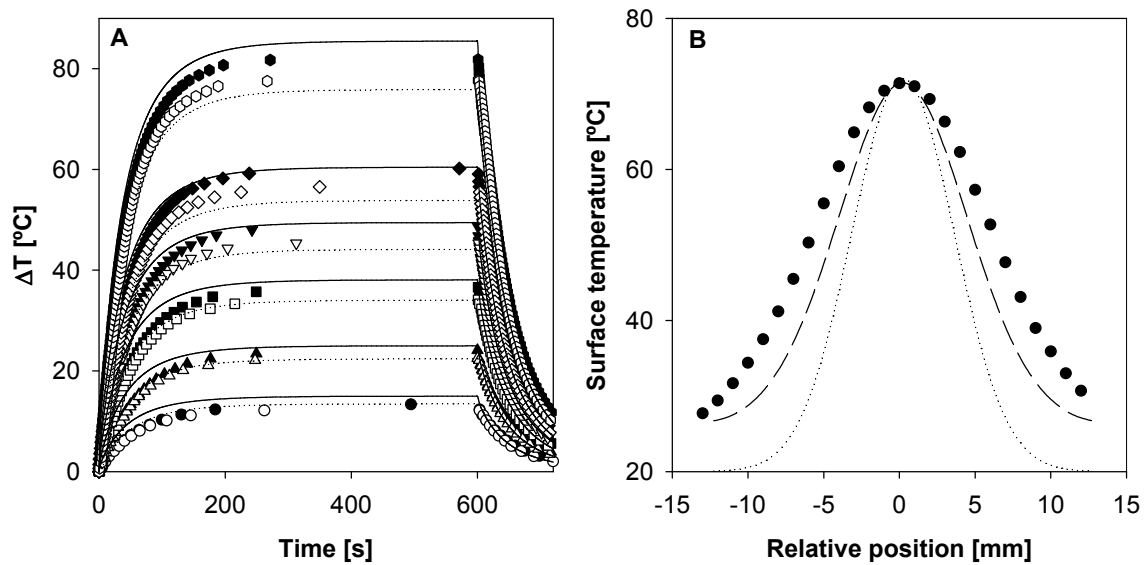
Figure 3.3: Comparison of FEM model to experimental data presented in Figure 2.9 for heating of a disc in air (T_0: 22°C). **A** Modeled surface temperatures at the irradiated side (——) and back of sample (⋯⋯⋯) for powers of 110 to 740 mW. Symbols represent experimental data at the front (filled) and back (open) of the polymer sample and are identical to those in Figure 2.9. **B** Experimental data points (●) of radial temperature profile, modeled temperature profile (- - - -), and the normalized radial laser intensity distribution used in the model (⋯⋯⋯) for a laser power of 400 mW, illustrating broadening of the temperature profile due to lateral conduction.

47
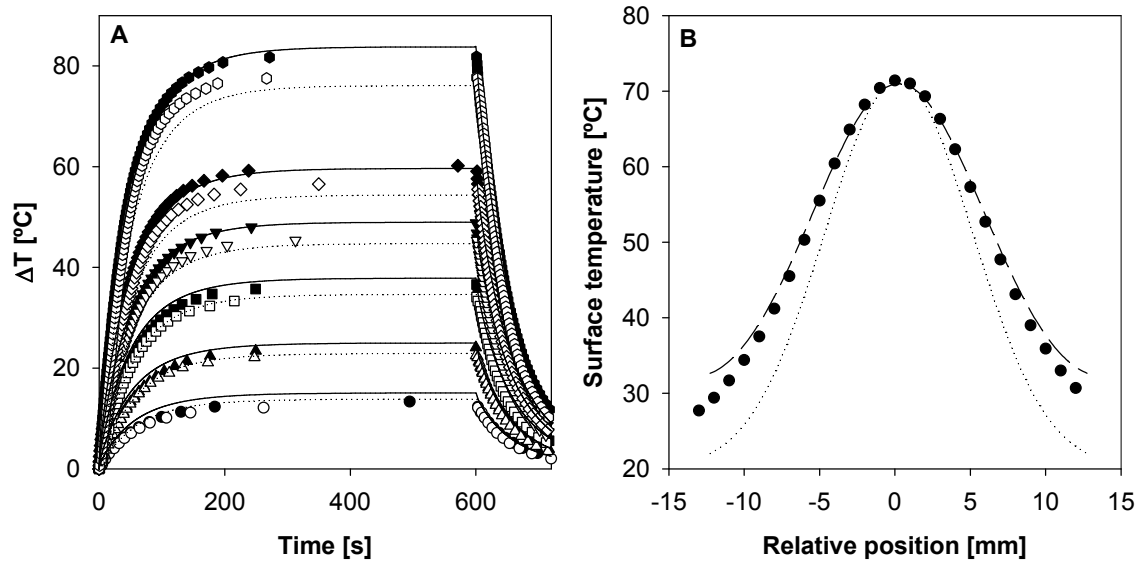
Figure 3.4: New modeling results using $\sigma = 1.45 \cdot \sigma_{laser}$ and $\eta_{thermal} = 94\%$. All symbols and lines are identical to those in Figure 3.3.

Although a satisfactory fit has now been obtained, the intensity profile of the diverging laser beam should not change this dramatically after exiting the fiber. This large increase in σ therefore seems unexpected. Another explanation is that scattering in the polymer disc occurs due to small inhomogeneities, since the disc was not completely transparent. This scattering effect would become increasingly large with increasing penetration depth. The fitted value for σ would then not just describe the laser intensity profile, but would also comprise an effective average scattering parameter. Scattering of light greatly depends on the exact morphology and the existence of microdomains in the polymer matrix, and has not been investigated in detail in this work. Based on the results presented in this section, it is assumed that $\eta_{thermal}$ is around 94% and is used to verify NIR-induced heating in aqueous environment in the following section.

3.5 Heat transfer in aqueous environment

Verification of the model in aqueous environment is performed by comparing modeling results to experimental heating results of the polymer disc presented in Figure 2.12. In order to use Eqns. 3-9 and 3-10, Ra_L should exceed 10^5 according to the original report [4]. However, various authors report the use of this equation with a lower limit of 10^4 [5,6], which is the range of Ra_L for the present system, and it is therefore assumed that

these equation can in fact be used. L_c is taken to be the ratio of the surface area to the perimeter of the spot size, as opposed to the diameter of the entire disc. As it turns out, the choice of the characteristic length has little influence on the modeling results. Other input parameters are given in appendix 3.10.1. The resulting modeled temperature at a depth of approximately 1 mm show a very good correlation with the experimental results (Figure 3.5A), especially considering the fact that no other fitting parameters are used. The reason for the experimental cooling rate being much slower may be due to the fact that the surrounding water heats up slightly during irradiation, thus not satisfying the sink conditions assumed in the model. This result does demonstrate that this FEM model is capable of predicting temperature increases in aqueous environment.
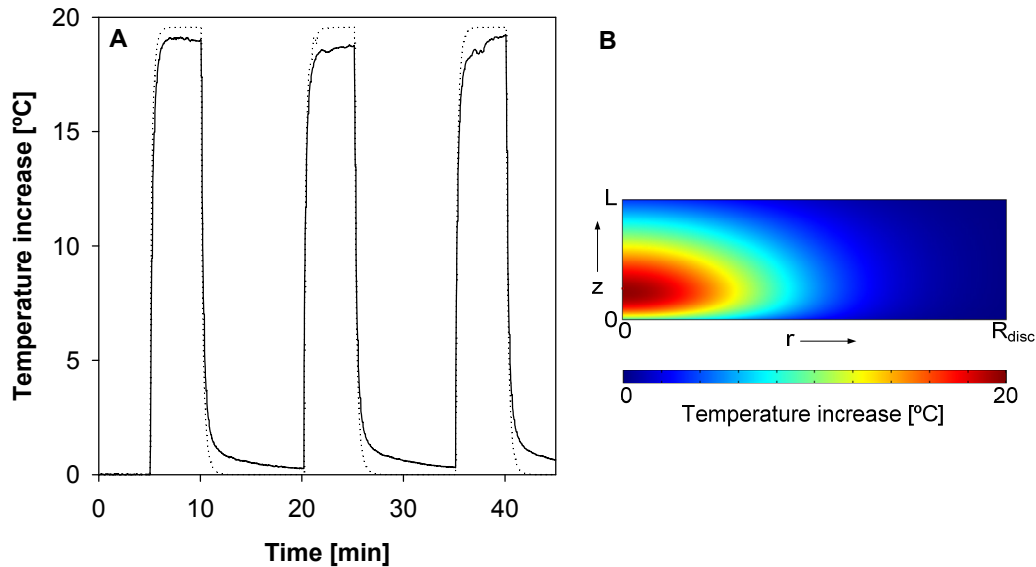
Figure 3.5: Comparison of FEM model to experimental data presented in Figure 3.12 (T_0: 37°C) for a polymer disc (L: 3.93 mm, R_{disc}: 12.5 mm, laser power: 750 mW, spot size: 14.4 mm). **A** Experimental data, measured at approximately 1 mm from the surface (——), and modeled surface temperatures at the same position (········). **B** Modeled temperature distribution of the disc (L: 3.9 mm, R_{disc}: 12.5 mm in a 2-dimensional slice as explained in Figure 3.1. NIR irradiation occurs from the bottom (z = 0).

The modeled temperature profile inside the polymer implant is depicted in Figure 3.5B. This figure clearly illustrates that for a laser spot size of 14.4 mm used in this experiment, only a small part of the disc is effectively heated. Moreover, the surface temperature is considerably lower (maximum of 8.5°C) than the inside temperature measured in Figure

3.5A, and a temperature increase is hardly induced at the back of the disc due to the relatively large thickness. This temperature distribution is further addressed in the following section.

3.6 Comparison of designs with different dye distributions

In the polymer matrices discussed so far, the dye was homogeneously distributed throughout the polymer matrix. There are two downsides to distributing the dye homogeneously throughout the matrix. First of all, the exponential nature of absorption results in an asymmetric axial temperature profile inside the polymer, as can be seen in Figure 3.5B. The surface temperature at the irradiated side is therefore higher than at the back of the sample, resulting in lower drug release at the non-irradiated side. Secondly, heat generation in a homogeneous design also occurs on the inside of the polymer implant, whereas the main temperature increase is required at the surface. These two aspects are addressed in two limiting laminar designs, i.e. a 'sandwich' design, in which a symmetric temperature profile is achieved (Figure 3.6A), and a coated design, in which heat generation indeed only occurs at the surface (Figure 3.6B). In contrast to the modeling results described in the previous sections, the results in this section are based on the availability of an NIR source exhibiting a homogeneous intensity distribution, e.g. a light emitting diode (LED) assembly (see Chapter 7). Due to the homogeneous intensity distribution, the surface temperature is essentially equal over the entire surface (except for the outer boundary effects), and L_c is assumed to have its usual value, i.e. ½·R$_{disc}$. Modeling has been performed using PMMA polymer properties, so there is no sudden increase in heat capacity up to approximately 100ºC. Any modeled temperatures higher than this temperature should therefore not be assumed realistic. The use of a dimensionless model allows easy adaptation of the size of the implant without having to actually redraw it. The radial and axial coordinates are then defined as R = r / R$_{disc}$ and Z = z / L, respectively, where R$_{disc}$ is the radius and L the thickness of the disc. Both R and Z thus range from 0 to 1. This also implies that parameters containing a directional component, e.g. thermal conductivity (Eqn. 3-11), need to be redefined. The modeling parameters used in the models discussed in this section are given in the appendix 3.10.1.
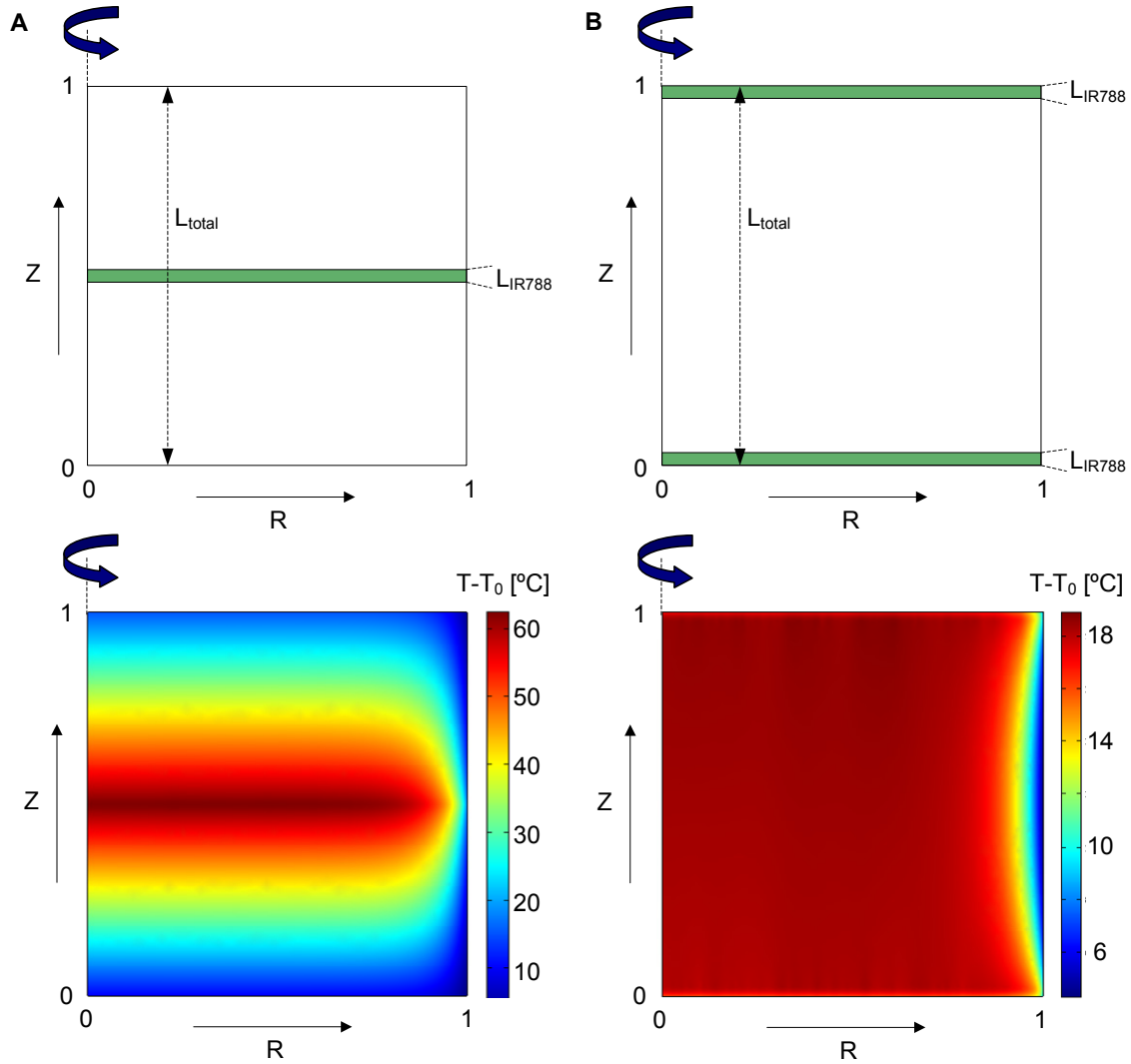
Figure 3.6: Two limiting designs regarding dye distribution. **A** Sandwich design, in which a high dye concentration is incorporated in a thin layer at the center of polymer disc (top), and resulting steady state temperature profile (bottom) where R_{disc}: 25 mm, L_{total}: 2 mm, L_{IR788}: 50 μm, C_{IR788}: 500 μg mL^{-1}, I: 5 W cm^{-2}. **B** Coated design, in which the dye is only present at in the outer surface layer of the polymer implant (top), and resulting temperature profile (bottom, identical parameters to those in panel A).

$$k_r = \frac{k}{R^2}; \quad k_z = \frac{k}{L^2} \qquad\qquad\qquad [3\text{-}11]$$

where k_r, k_z : radial and axial component of k [W m^{-1} K^{-1}]

The steady state temperature profile in Figure 3.6A, obtained after approximately 25 seconds, illustrates the problem when trying to obtain a symmetric temperature profile

using the sandwich design. The main temperature increase is located inside the polymer implant (as is expected for heat generation inside the implant), resulting in a large linear temperature gradient inside the polymer implant. In the steady state, the difference between the inner and surface temperature is given by the difference form of the Fourier equation (Eqn. 3-12):

$$\Delta T = \phi_h'' \frac{\Delta L}{k} \qquad\qquad [3\text{-}12]$$

where ΔT : difference between inner and surface temperature [ºC]
     ϕ_h'' : heat flux   [W m^{-2}]
     ΔL : distance between center and surface of disc   [m]

For constant thickness and thermal conductivity of the polymer disc, the steady state heat flux depends on the amount of generated heat (i.e. on dye concentration and thickness of the dye containing layer, and NIR intensity) and on the amount of heat dissipation at the surface. The latter mainly depends on the surface temperature (Eqn. 3-5) and governing boundary conditions. Since Nu_L, and thus the heat transfer coefficient, is a factor 2 higher for the side facing up than down (Eqns. 3-9 and 3-10), the temperature at the non-irradiated side is actually higher, thus making the temperature profile slightly asymmetric. However, this is of minor concern compared to the large temperature gradient. According to Eqn. 3-13, a further increase of the surface temperature to the desired 20ºC, which would necessarily be achieved by increasing heat generation and thus heat flux, implies that the temperature difference increases even further, which is also depicted in Figure 3.7A. Again, an almost linear dependence on increasing intensity is observed, whereas the exponential nature of absorption results in a clear downward curvature with increasing dye concentration. High temperatures inside the implant could lead to both drug and polymer degradation, and should therefore be avoided. Of course, the temperature difference can be reduced by decreasing the thickness (Figure 3.7B), but a certain thickness is required to contain sufficient drugs for long-term drug delivery. The sandwich design is therefore not a feasible implant design.

The temperature profile illustrated in Figure 3.6B for the coated design offers a more promising prospect. Here, more moderate temperatures are reached inside the polymer

NIR intensity [W cm^{-2}]
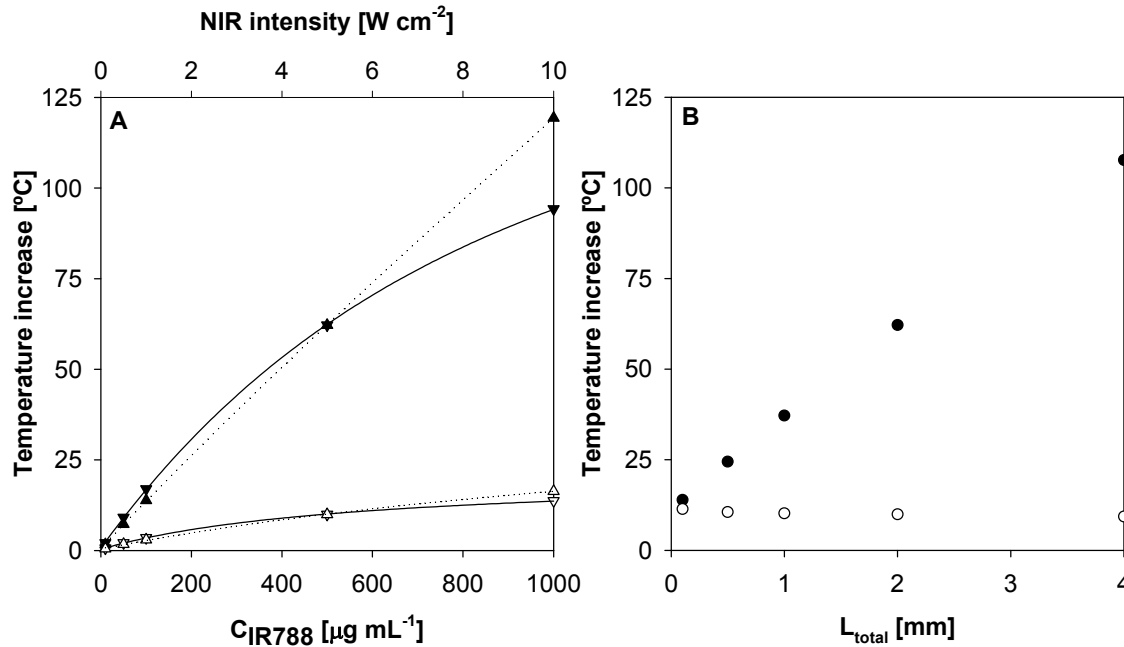
Figure 3.7: Modeling results for a sandwich design (parameters as given in Figure 3.6). **A** Effect of both concentration (▼) and power (▲) on the inner (filled symbols) and irradiated surface temperature (open symbols). **B** Effect of thickness on the inner (●) and irradiated surface temperature (O).

implant, where heating only occurs due to conduction. The development of the temperature profile inside the implant in time is illustrated in Figure 3.8. Since almost half of the intensity (44%) has already been absorbed by the coating on the irradiated side of the sample, the generated heat at the back of the sample is almost half (56%) of that generated in the first layer. Even so, due to a lower amount of heat loss by free convection at the non-irradiated side, an almost perfect temperature distribution inside the polymer disc is obtained. However, it should be mentioned that, when taking into account that heat transport inside the human body is more or less equal over the entire surface of the implant, the temperature at the irradiated side ($Z = 0$) will be higher than at the non-irradiated side ($Z = 1$). Moreover, this temperature difference continues to increase as the dye concentration is increased (Figure 3.8B), since an increasing amount of the incident NIR radiation is absorbed in the first dye containing layer. A more effective method of increasing the surface temperature without affecting the homogeneous temperature distribution is increasing the NIR intensity. The temperature profile is hardly affected, whereas the surface temperature increases almost linearly (data not shown), only

deviating from linearity due to an increasing heat transfer coefficient with increasing surface temperature. When the total thickness of the polymer implant is increased, the surface temperature is hardly affected, since the boundary conditions and heat generation remain unchanged. In contrast, the inner temperature profile is slower to develop when the concentration is increased. However, a slightly lower temperature inside the implant does not affect drug diffusion (Figure 3.2), thus making the thickness of the implant irrelevant where surface temperature is concerned.
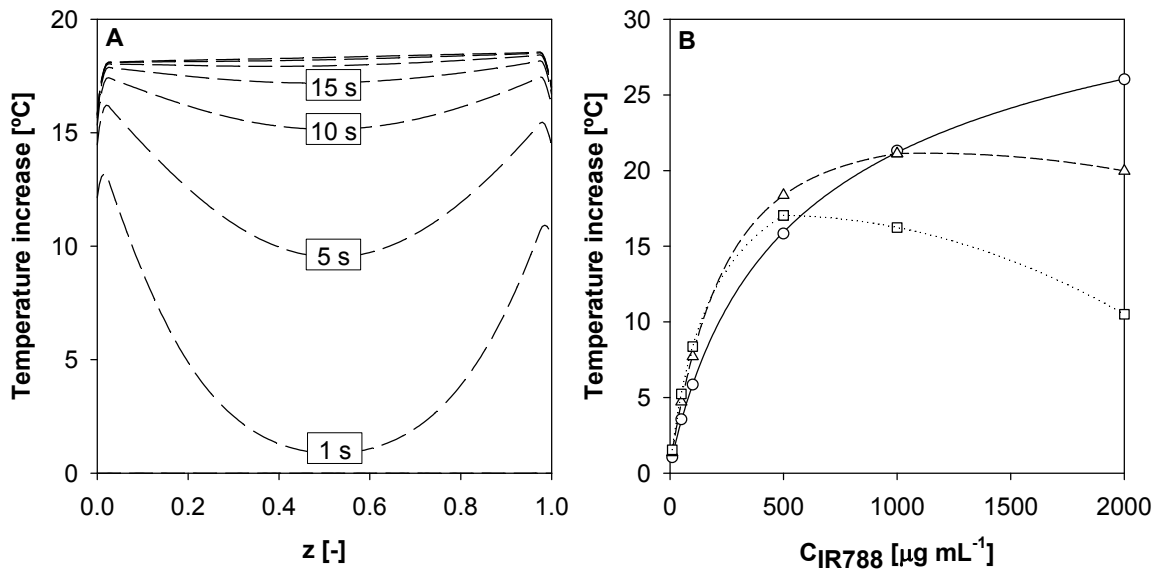
Figure 3.8: Modeling results for a coated design (parameters as given in Figure 3.6). **A** Development of the temperature profile inside the polymer implant in time (t = 1, 5, 10, 15, 20, 25 and 30 s). **B** Effect of concentration on inner temperature ($\triangle$), irradiated surface (O), and non-irradiated surface temperature ($\square$).

A parameter that has not been addressed in this section is the thickness of the dye containing layer. In principle, an infinitely thin dye containing layer is desired, in which case all heat is generated at the surface, where the temperature increase is required, and heat conduction ensures the rest of the implant is heated sufficiently. The main controlling parameter for the amount of heat generation should be the NIR intensity, where the threshold of the human skin determines the maximum allowable intensity. The dye concentration should be kept as low as possible so that the amount of heat generated at both sides of the implant is more or less equal. Figure 3.9 summarizes the difference in

axial temperature profile for the three different designs for the same dye concentration, resulting in the choice for a coated design.
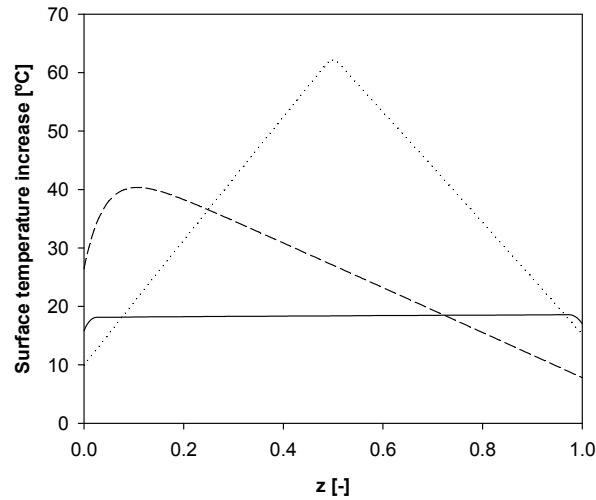
Figure 3.9: Summary of axial steady state temperature profiles for a homogeneous (- - - -), sandwich (··········), and coated design (——), where L_{total}: 2 mm, L_{IR788}: 50 µm, C_{IR788}: 500 µg mL^{-1}, and I: 5 W cm^{-2}. At these relatively low dye concentrations, the coated design offers moderate surface temperatures with a relatively symmetric temperature profile.

Although the modeling results in this section are based on a disc-shaped polymer implant, other geometries, such as a rod-shaped implant, are subject to the same design considerations. A rod is often a more likely geometry from a practical point of view, e.g. to enable implantation by injection as opposed to a more complicated invasive procedure. From a modeling point of view, a polymer rod that is irradiated perpendicularly to its vertical axis is more complicated, as a simplified axisymmetric model is not possible. Since the following chapter deals with both *in vitro* and *in vivo* release from a coated polymer rod, Figure 3.10 contains modeling results of a 3D model of a polymer rod, serving as an indication of the achieved surface temperature. The release experiments are performed using a laser, once again resulting in a Gaussian temperature profile. The laser peak intensity at the spot size employed equals 5.7 W cm^{-2}, which is in the same range as the intensity used for modeling earlier in this section. Indeed, the surface temperatures obtained are the same order of magnitude as obtained in Figure 3.9, except that now, since the concentration in the coating is so high, all energy is basically absorbed at the surface.
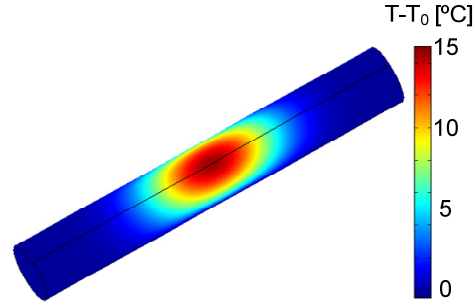
Figure 3.10: Minimum steady state surface temperature profile for a rod-shaped implant as used in the following chapter. L: 2 cm, D: 3 mm D_{IR788}: ~50 μm, C_{IR788}: ~7500 μg mL^{-1}, P: 750 mW, and D_{spot}: ~8.8 mm (i.e. I_{peak}: ~5.7 W cm^{-2}).

However, there are several points of attention when considering these results. The polymer thermal properties are assumed to be the same as for PMMA and the heat capacity increase due to the glass transition temperature is not considered. However, this is of minor importance compared to the choice of *Nu*. A correlation for *Nu* for a horizontal cylinder with a uniform surface temperature has been assumed (Eqn. 3-13) [7], thus resulting in a value for *Nu* that is certainly overestimated, since only a relatively small part of the cylinder is heated. Therefore, the obtained result in Figure 3.10 most likely underestimates the surface temperature. When a limiting value of 0.36 is chosen for pure conduction as proposed by Tsubouchi and Masuda [8] (on which Eqn. 3-14 is partially based), a maximum surface temperature increase is reached which is more than a factor 5 higher, thus illustrating the importance for a correct correlation for the boundary conditions. Therefore, it is concluded that a surface temperature increase of at least 15ºC is achieved, but higher temperatures seem more likely. Moreover, the temperatures reached in a tissue environment are expected to be significantly higher than in water, as is explained in the following section, thus providing a sufficient increase in temperature to achieve drug release *in vivo*.

$$Nu = \left[0.60 + 0.387 \left[\frac{Ra}{\left[1 + (0.559/\mathrm{Pr})^{9/16} \right]^{16/9}} \right]^{1/6} \right]^{2}$$

[Eqn. 3-13]

3.7   Heat transfer inside the human body

The previous section discussed modeling in aqueous environment. A more relevant modeling approach would be to consider a polymer matrix inside human tissue. However, modeling in tissue is far more complicated, mainly due to its inhomogeneity, causing strong scattering of incident NIR radiation, and the occurrence of blood perfusion [9-12]. The extent of scattering depends on tissue type, but does mainly occur in forward direction, resulting in a relatively high penetration depth. The amount and diameter of the blood vessels near the implant greatly influences the extent of convective heat transfer, and thus heat removal. When the tissue temperature is increased locally, vasodilatation leads to increased blood flow and consequently higher heat removal. Therefore, the exact location of the implant inside the human body determines the achieved temperature increase. In addition, skin color due to the presence of melanin affects the transmittance of NIR radiation, where dark skin absorbs more radiation than lighter skin.

Furthermore, the implant should not be brought into direct contact with the tissue, since exposing tissue to high temperatures for a long period of time can lead to permanent tissue damage [13]. The final implant should therefore be enveloped by an insulating layer, which is permeable to drug molecules, and prevents the occurrence of tissue damage. This layer could consist of for example a rubbery polymer exhibiting a very low T_g or a hydrogel structure. The former would lead to a higher resistance to mass transfer (diffusion coefficients in the order of 10^{-12} m^2 s^{-1}), whereas diffusion in a hydrogel with very high water content would approach the diffusion rate in water (in the order of 10^{-9} m^2 s^{-1}). A similar effect could be achieved by simply wrapping the implant inside a porous structure, e.g. a tissue bag, thus creating a stagnant water layer. An additional advantage of using an insulating layer is that it can serve to solve biocompatibility issues.

For modeling NIR-induced heating *in vivo*, a simplified approach is followed, in which the drug delivery device (disc-shaped to enable axial symmetric modeling) is subdermally implanted in the arm. Heat transfer is modeled using the Pennes bioheat equation [14], where average thermal tissue properties [12] and an average blood perfusion term [15,16] are assumed for each tissue layer (i.e. epidermis, dermis and subcutaneous fat). Heat transfer at the air/skin interface is supposed to be described by

free convection (Eqn. 3-9). Average scattering and absorption coefficients [17,18] are assumed to describe light penetration in tissue according to the radiation transport theory [19], where the NIR source is supposed to exhibit a homogeneous radial intensity distribution. A more detailed description of the model is given in appendix 3.10.2.
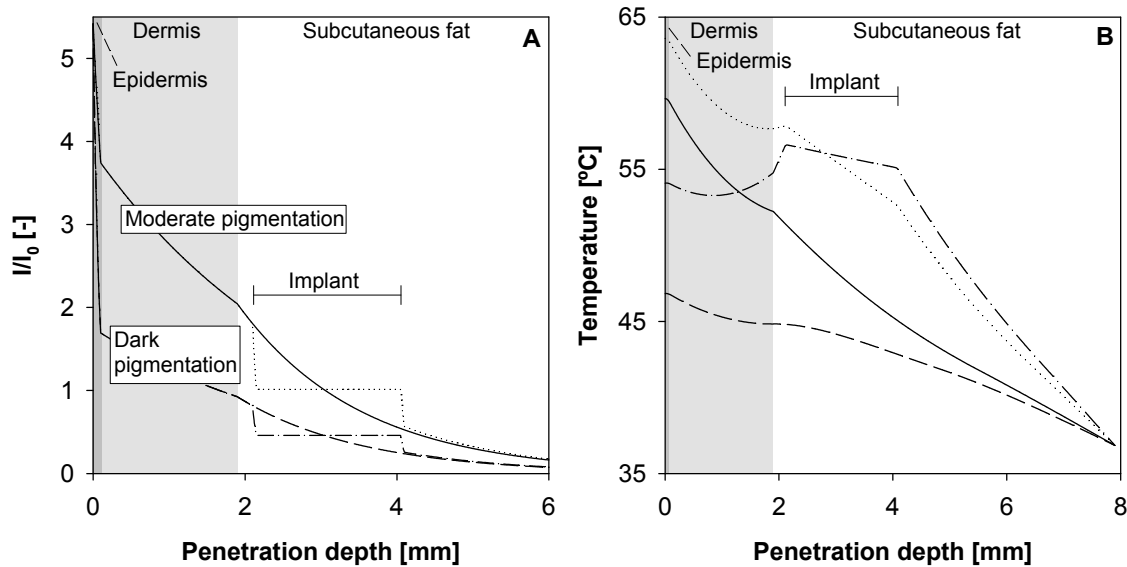
Figure 3.11: NIR intensity and induced temperature modeled i*n vivo*. **A** Intensity profile in the absence of an implant for moderate (10 %v/v melanin,——) and dark pigmentation (40 %v/v melanin,- - - -), and in the presence of an implant (········ and − · −, respectively) at a depth of 2.1 mm (0.3 mm below the skin). **B** Steady state temperature profiles after 10 minutes of radiation (temperature increase in time is given in appendix 3.10.2) for the implants in panel A, assuming an NIR source exhibiting a homogeneous radial intensity profile (0.2 W cm^{-2}). Lines are identical to those in panel A.

Figure 3.11 illustrates the pronounced effect of skin color on the temperature reached at the surface of the implant. An increased pigmentation results in a much higher absorption of NIR by the epidermis. As a consequence, the amount of energy reaching the implant decreases significantly, resulting in only 10% absorption of incident radiation for dark pigmentation compared to 23% absorption in the case of moderate pigmentation, leading to a significantly lower temperature increase of the implant. In contrast, the skin surface temperature increases considerably with a higher degree of pigmentation, even in the absence of an implant. It should be noted that scattering effects in tissue actually increase the heat flux inside the tissue, resulting in a higher intensity than the incident intensity, thus explaining the values higher than 1 on the y-axis. The aforementioned percentages of

absorption of incident radiation refer to absorption of the heat flux resulting due to scattering. When expressing the amount of absorption in terms of the intensity of the heat source, these percentages should actually be multiplied by approximately a factor of 5, implying that in the case of moderately pigmented skin, 115% of the incident intensity is converted into heat. This is only possible due to the assumption that the radius of the NIR source is much larger than the radius of the implant.
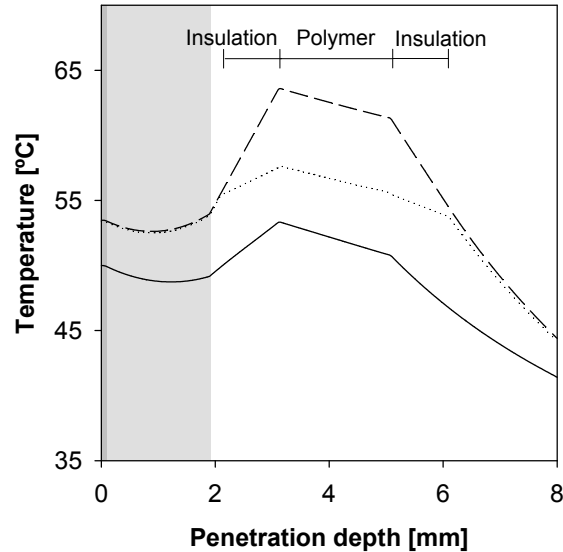
Figure 3.12: Effect of addition of an insulating layer of 1 mm thickness on the temperature profile inside the tissue. ——: no insulating layer, ··········: stagnant water layer , - - - -: rubbery polymer. Implant and NIR intensity are as described in Figure 3.11.

In order to decrease the temperature to which the tissue is exposed, the effect of an insulating layer on the temperature profile inside the tissue is investigated (Figure 3.12). For these calculations, the implant has been moved to a depth of 3.1 mm, compared to 2.1 mm in Figure 3.11, thus allowing for an insulating layer of 1 mm thickness. This naturally lowers the temperature increase induced in the polymer due to decreased NIR intensity at this depth. Two types of insulating layer have been assumed, i.e. consisting of a stagnant water layer or of a rubbery polymer, where the thermal properties of poly(vinyl acetate) have been assumed for the latter. From the results in Figure 3.12, it is obvious, that at the same NIR intensity, it is not so much the temperature at the implant/tissue interface that is decreased, but the temperature inside the polymer that is increased. The increase in the temperature of the skin is partly explained by the fact that

absorption inside the insulating layer is assumed to be negligible, whereas without an insulation layer, a certain amount of heat is still generated inside the subcutaneous tissue. The remainder of the increase in skin temperature can be attributed to the increase in temperature of the implant. Figure 3.12 also demonstrates that water is quite a poor insulator, and insulation based on for example a hydrogel would require a rather thick insulating layer. Poly(vinyl acetate) is quite an efficient insulator, inducing a large temperature difference of about 10ºC for an insulator thickness of only 1 mm. Nevertheless, the tissue is exposed to a temperature of almost 55ºC, which is still quite high. Tissue should not be exposed to this temperature for longer than 1 minute, or irreversible damage will occur [20]. Therefore, the required drug dose should be delivered within this time frame.

3.8   Mass transfer considerations

This chapter has mainly dealt with heat transfer effects without considering mass transfer. Before discussing mass transfer, it should be noted that the dissolved drug affects thermal properties to a certain extent due to differences in thermal conductivity, density and heat capacity. These values are in the same range as the polymer properties (e.g. [21] for density and heat capacity of ibuprofen), and are therefore not expected to have a major impact on heating of the polymer. The thermal diffusivity can be affected to some extent, thus possibly slowing down or speeding up the heating process slightly. The steady state surface temperatures should however hardly be affected.

An idealized picture of the principle of NIR-induced drug release based on the T_g is depicted in Figure 3.2. There, it is assumed that after switching off the temperature trigger, the surface concentration profile returns to its original state. However, even in the glassy state, a certain amount of drug always diffuses out of the implant, which implies that the concentration of drug dissolved in the implant continuously decreases, resulting in a reduced driving force for diffusion. For a constant diffusion coefficient, this driving force depends on the thickness of the surface layer (i.e. the depth at which the local concentration starts to differ from the bulk concentration), which can be described using the penetration theory (Eqn. 3-15). Since the local glass transition temperature inside this surface layer changes dramatically, the assumption of a constant diffusion coefficient is

not justified. However, the penetration depth does in fact solely depend on the diffusion coefficient at the 'diffusing front', i.e. where the concentration equals the bulk concentration, even though the shape of the concentration profile is affected. This is illustrated in Figure 3.13A, where a correlation derived from experimental data of ibuprofen diffusion in poly(butyl methacrylate-co-methyl methacrylate) (appendix 3.10.3) is used in combination with FEM to determine the concentration profile in the surface layer of a polymer matrix. Here, the surface concentration is assumed to be equal to zero, and the bulk ibuprofen concentration equals 20 wt%, resulting in a bulk diffusion coefficient of $4.72 \cdot 10^{-15}$ m^2 s^{-1} at 37ºC. The penetration depths for both cases are practically identical, corresponding quite well to values predicted by Eqn. 3-15. According to Eqn. 3-15, the penetration depth equals half the thickness of the implant after 195 days at 37ºC, after which the concentration in the center starts to decrease.

$$\delta_m = 2\sqrt{\pi \cdot D \cdot t}$$ [3-15]

where δ_m : penetration depth [m]

Even though the penetration depth is identical for both a concentration dependent and a constant diffusion coefficient, the effect of a glassy surface layer is clearly illustrated in Figure 3.13. The rate determining step for diffusion is located at the surface of the implant resulting in a steeper concentration profile near the surface (Figure 3.13A), and a slower release from the implant (Figure 3.13B). For a constant diffusion coefficient, Eqn. 3-16 describes desorption (i.e. release) from a plane flat sheet [22].

$$\frac{M_t}{M_{\text{inf}}} = 1 - \sum_{n=0}^{\infty} \frac{8}{(2n+1)^2 \pi^2} \exp(-D \cdot (2n+1)^2 \pi^2 t / L^2)$$ [3-16]

where M_t : amount released at time t [kg]

M_{inf} : amount released after infinite time (i.e. initial
        drug content) [kg]

A good approximation based on this equation, which is valid up to $M_t / M_{inf} = 0.6$ is given by Eqn. 3-17 [22].

$$\frac{M_t}{M_{\text{inf}}} = 4 \cdot \sqrt{\left(\frac{Dt}{\pi \cdot L^2}\right)}$$ [3-17]

A

B
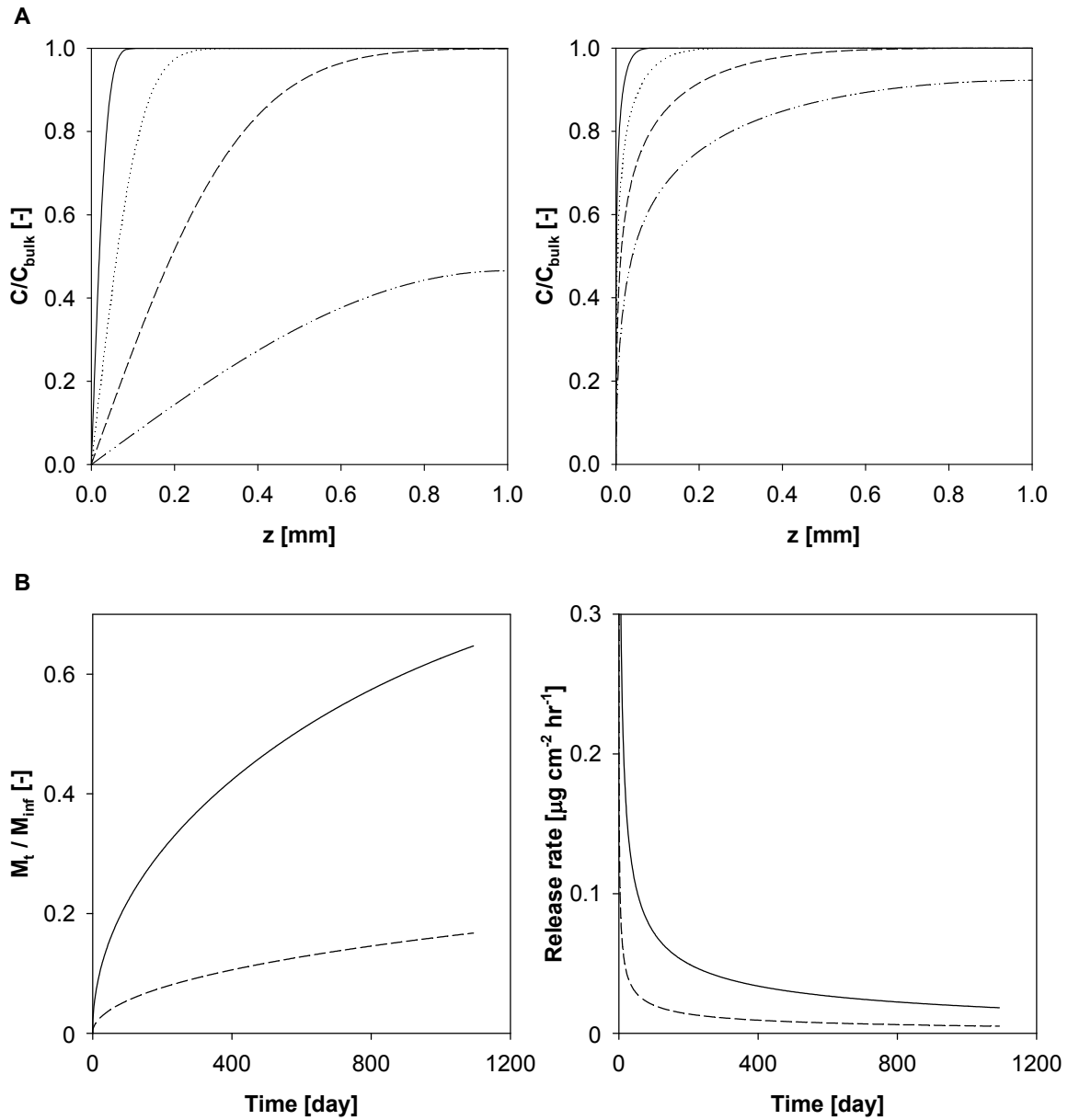
Figure 3.13: Concentration depletion inside a polymer implant (L = 2 mm). **A** Numerical solution of the change in concentration profile in time, assuming a constant diffusion coefficient (left) or a correlation for the diffusion coefficient as given in appendix 3.10.3 (right), T = 37ºC, t = 1 day (——), 10 days (········), 100 days (‑ ‑ ‑ ‑) and 1000 days (– · –). **B** Effect of concentration profiles in panel A on the cumulative release (left) and release rate (right) for a constant (——) or concentration dependent (‑ ‑ ‑ ‑) diffusion coefficient.

The diffusion coefficient determined from Eqn. 3-17 for the case of a constant diffusion coefficient is indeed in good agreement with the expected bulk diffusion coefficient ($4.63 \cdot 10^{-15}$ m^2 s^{-1} compared to $4.72 \cdot 10^{-15}$ m^2 s^{-1}). In contrast, a higher diffusion coefficient

by an order of magnitude is found for the concentration dependent diffusion coefficient ($2.78 \cdot 10^{-16}$ m^2 s^{-1} versus $1.27 \cdot 10^{-17}$ m^2 s^{-1}). This can be explained by the fact that a higher concentration gradient exists at the surface than in the situation where the diffusion coefficient has a constant (lower) value throughout the implant. Since drug release is a product of the local concentration gradient and diffusion coefficient (Fick's first law), this results in a higher apparent diffusion coefficient based on Eqn. 3-17. Similarly, this higher apparent diffusion coefficient occurs at higher temperatures (i.e. in the on-state), albeit to a lesser extent, since the difference between the bulk and surface diffusion coefficient at higher temperatures is lower due to the exponential relationship with temperature.

In both cases, the drug release rate slowly diminishes in time due to the decreased driving force (Figure 3.13B). Drug depletion thus has a pronounced effect on drug release from the implant, implying that longer periods at higher temperatures (on-state) are required for the same amount of drug to be released. This is also illustrated in Figure 3.14, where NIR-induced heating results in an increasingly lower amount of drug release per heating cycle. In addition, drug release diminishes significantly during the 15-minute heating period due to the decreasing concentration gradient (inset in Figure 3.14).

There are two designs that can overcome these problems and achieve a (more) constant driving force over a long period of time (Figure 3.15). Firstly, a drug reservoir, comprising of a rubbery polymer or hydrogel (over)saturated with drugs, can be coated with a dye-doped polymer exhibiting a T_g in the correct range (T_g-layer) (Figure 3.15A). This guarantees a constant driving force as long as the concentration at the interface of the reservoir and the T_g-layer remains constant. The concentration at the interface depends on the partitioning coefficient (K) between the two phases. In this system, the partitioning coefficient should favor solubility in the coating, so that the concentration at the interface is as high as possible, resulting in a large driving force. The NIR dye should only be incorporated into the T_g-layer, for the reasons discussed in section 3.6.
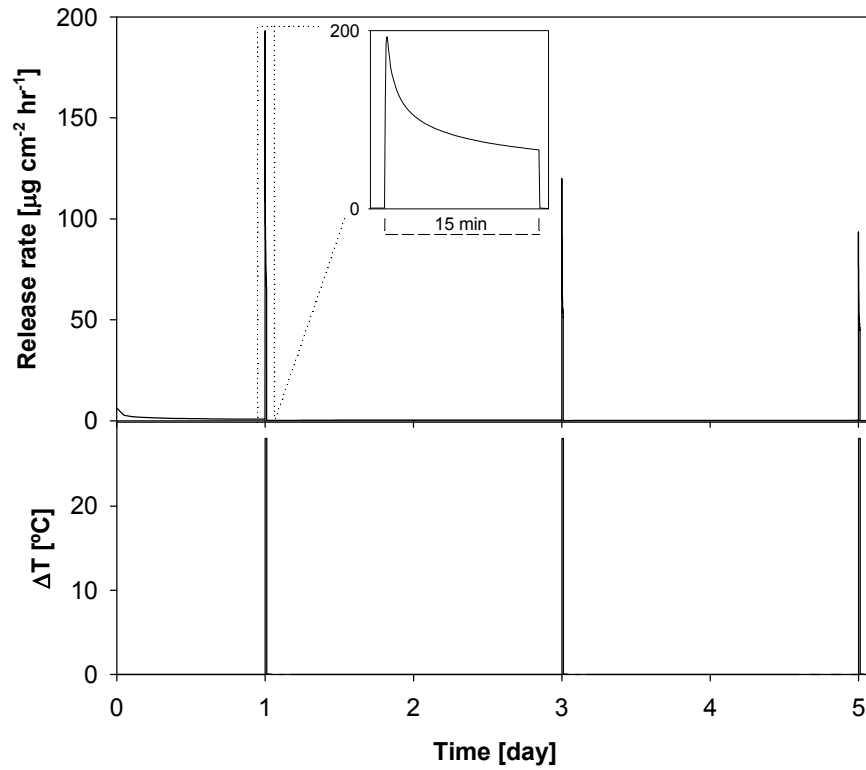
Figure 3.14: Effect of increasing temperature induced by NIR irradiation on drug release at the irradiated side of a disc (L_{total}: 2 mm) with a homogeneous dye distribution (C_{IR788}: 500 µg mL^{-1}) for an NIR intensity of 5 W cm^{-2} (homogeneous intensity distribution).
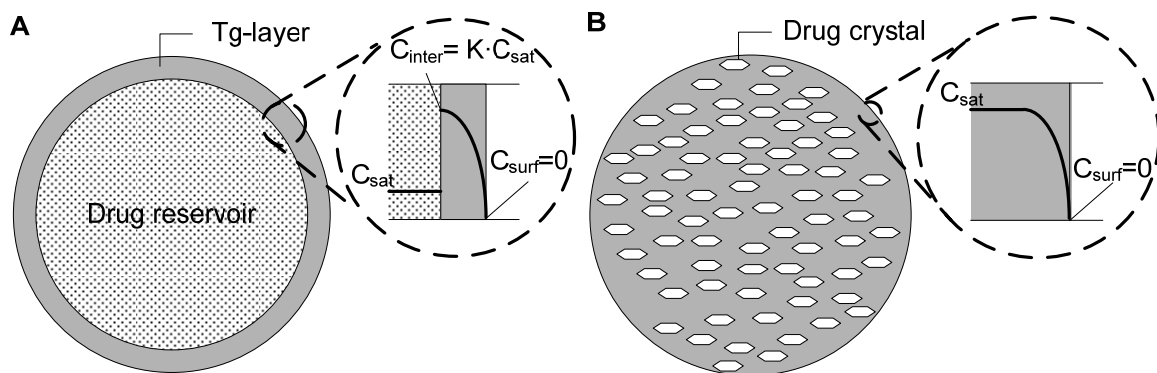
Figure 3.15: Cross sections of drug delivery designs for achieving a constant driving force. **A** Drug reservoir with a T_g-layer, which should also contain the NIR dye. **B** Implant consisting entirely of the 'T_g-polymer' oversaturated with the drug. The implant should be coated with the same polymer containing the NIR dye, although homogeneous dye distribution is not necessarily precluded.

In a more simple approach, the polymer implant can consists of the T_g-polymer directly oversatured with drugs (Figure 3.15B). In an oversaturated system, the bulk concentration inside the polymer implant remains constant as long as drug crystals are present inside the polymer matrix. The major advantage of this system over the reservoir design is that preparation of the implant is much easier. In addition, the patient is protected from dose dumping of the drug in the case of implant rupture, since a surface concentration profile sets in, resulting in the formation of a glassy layer when in contact with human tissue. The implant is thus 'self-sealing', in contrast to the reservoir system, where rupture leads to fast release of the drug from the reservoir when exposed to the outer environment. A disadvantage of the oversaturated design is that a trade-off needs to be made between release rate and the time period over which a constant release can be achieved. High drug solubility implies a high rate of release on the one hand, whereas on the other hand, crystal depletion is reached relatively quickly, which means that from that point on, a decrease in release rate occurs. In contrast, low drug solubility results in a relatively low release rate, while resulting in a constant drug release rate over a long period of time. It should be realized, though, that the driving force depends on the distance from the crystals to the surface. Crystals closer to the surface (i.e. where the concentration of dissolved drugs starts to decrease first) will dissolve first, thus resulting in a slight decrease in release rate. However, if temperatures are reached so that crystals melt, subsequent recrystallization may lead to the formation of new crystals near the surface, thus maintaining a constant driving force. In addition, melting drug crystals increase the dissolved concentration of drugs inside the polymer matrix and may thus even enhance drug release.

To a certain extent, the relatively low release rate can be counteracted by increasing the available surface area for mass transfer. Of course, the size of the implant is limited due to both the size of the external triggering device and for placement in the human body. An alternative method for increasing surface area is the use of polymer spheres. These spheres can be incorporated into a hydrogel or wrapped into a porous structure described earlier. Assuming a rod-like design filled with spheres, Figure 3.16 illustrates the surface area increase, and thus the increase in drug release rate, that can be obtained, assuming all spheres have the same size. In this case, an increase in surface area of at least a factor of

10 is obtained for spheres smaller than 225 μm. Of course, the actual increase depends on the both the diameter of the implant and the volume fraction of spheres.

$$R = \frac{N_{spheres} \cdot A_{sphere}}{A_{cylinder}} = \frac{3 \cdot d_{cylinder}}{2 \cdot d_{sphere}} \phi_{spheres}$$
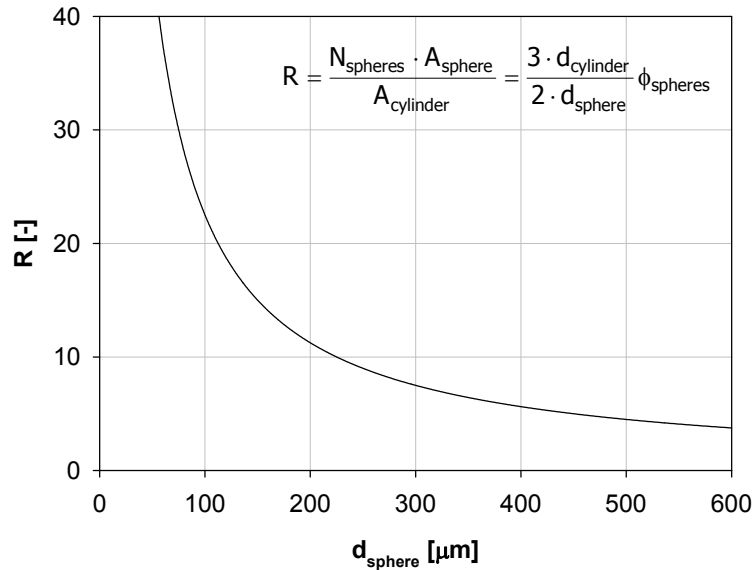
Figure 3.16: Illustration of surface area increase (R) with decreasing sphere size, assuming the volume fraction of the spheres ($\phi_{spheres}$) is 0.5, and a rod diameter ($d_{cylinder}$) of 3 mm.

If a large size distribution in the polymer spheres exists, the driving force for release will decrease as smaller spheres become depleted, whereas the larger spheres still contain a significant amount of drugs. A narrow size distribution is therefore important to achieve a constant release rate in time. In addition, the spheres should be packed in such a way that no isolated voids exist in between the spheres, so that drug molecules released from the polymer spheres can pass freely through the insulating layer. Possible preparation procedures for polymer spheres containing drugs and an NIR dye are discussed in Chapter 7.

3.9 Conclusions

The feasibility of NIR as an external trigger for on-demand drug release has been demonstrated. Since the main resistance to mass transfer occurs inside the polymer implant, the rate limiting step for diffusion is located at the surface of the implant due to the formation of a glassy surface layer. The most effective design in terms of heat generation therefore involves a coated design, so that heat is mainly generated at the

surface. Subsequent thermal conduction ensures the temperature inside the implant increases sufficiently. Compared to surface temperatures achieved in water, modeling results show that higher temperatures should be achieved *in vivo*. Addition of a thermal insulating layer can protect tissue from excessive temperatures to some extent, and in addition, results in higher temperatures at the glassy surface, thus requiring a lower NIR intensity to achieve the same increase in temperature. The availability of an NIR source capable of supplying a homogeneous intensity profile offers promising possibilities for NIR-induced on-demand drug delivery, providing optical tissue parameters of a patient are taken into account.

3.10 Appendix

3.10.1 In vitro *modeling parameters*

Table 3.1: Input parameters for polymer and environmental properties

Parameter	Symbol	Value	Unit
Volumetric heat capacity PMMA [23]	ρC_p	$1614.1 \cdot [-0.0564 + 1.05638 \cdot (T/298.15)] \cdot 10^3$	$[\text{J m}^{-3} \text{ K}^{-1}]$
Thermal conductivity PMMA [23]	k	$0.18987 \cdot [-0.02222 + 1.67196 \cdot (T/298.15) - 0.64984 \cdot (T/298.15)^2] \cdot 10^3$	$[\text{W m}^{-1} \text{ K}^{-1}]$
Emissivity PMMA[†]	ε	0.9	[-]
Reflection at polymer-air interface[‡]	*Refl*	0.04	[-]
Thermal conductivity air[*] [24]	k_{air}	$[1.5207 \cdot 10^{-7} \cdot T_f^3 - 4.8574 \cdot 10^{-4} \cdot T_f^2 + 1.0184 \cdot T_f - 3.9333] \cdot 10^{-4}$	$[\text{W m}^{-1} \text{ K}^{-1}]$
Kinematic viscosity air[*] [24]	v_{air}	$[0.001 \cdot T_f^2 + 0.032 \cdot T_f - 2.9776] \cdot 10^{-6}$	$[\text{m}^2 \text{ s}^{-1}]$
Thermal expansion coefficient air[*] [24]	β_{air}	$[3 \cdot 10^{-5} \cdot T_f^2 - 0.0298 \cdot T_f + 9.5197] \cdot 10^{-3}$	$[\text{K}^{-1}]$
Prandtl number for air [24]	Pr	$4 \cdot 10^{-7} \cdot T_f^2 - 0.0003 \cdot T_f + 0.7741$	[-]
Thermal conductivity water[*] [24]	k_{water}	$-9.3741 \cdot 10^{-6} \cdot T_f^2 - 0.0072455 \cdot T_f + 0.719416$	$[\text{W m}^{-1} \text{ K}^{-1}]$
Kinematic viscosity water[*] [24]	v_{water}	$[3.3583 \cdot 10^{-5} \cdot T_f^4 + 4.6037 \cdot 10^{-5} \cdot T_f^3 + 0.0237 \cdot T_f^2 - 5.4364 \cdot T_f + 469.73] \cdot 10^{-6}$	$[\text{m}^2 \text{ s}^{-1}]$
Thermal expansion coefficient water[*] [24]	β_{water}	$[-0.0036081 \cdot T_f^2 - 3.0176 \cdot T_f + 553.325] \cdot 10^{-5}$	$[\text{K}^{-1}]$
Prandtl number for water [24]	Pr	$[2.9766 \cdot 10^{-7} \cdot T_f^4 - 0.004075 \cdot T_f^3 + 0.20942 \cdot T_f^2 - 47.924 \cdot T_f + 4127]$	[-]

[†] Emissivity of polymers ranges from 0.85-0.95 [25].

[‡] A certain amount of incident radiation is reflected due to the difference in refractive index, according to the Fresnel equation: $Refl = (n_1 - n_2)^2/(n_1 + n_2)^2$, where R is reflection and n_i is the refractive index of i.

[*] Fluid properties are evaluated at the film temperature T_f, i.e. the arithmetic mean between bulk and surface temperature. Equation is derived from data in reference [24].

Table 3.2: Modeling parameters for heating of a PMMA disc in air (section 3.4) and in aqueous environment (section 3.5).

Parameter	Symbol	In air	In water	Unit
Radius	R	0.0125	0.0125	[-]
Thickness	L	0.0015	0.0039	[m]
Absorbance (determined experimentally at λ: 785 nm)	Abs	1.67	2.93	[a.u.]
Ambient temperature	T_0	22	37	[ºC]
Laser power	P	0 - 0.750	0.750	[W]
Spot size	D_{spot}	0.0198	0.0144	[m]
Gaussian laser parameter, fit to Figure 2.3	σ	$(1.45\cdot)0.17127\cdot D_{spot}$	$1.45\cdot0.17127\cdot D_{spot}$	[-]
Characteristic length	L_c	Fitting parameter	0.004	[m]
Quantum yield of thermal relaxation	η_{eff}	Fitting parameter	0.94	[-]

Table 3.3: Modeling parameters for heating of a polymer discs of different designs, i.e. a sandwich design and a coated design (section 3.6).

Parameter	Symbol	In water	Unit
Radius	R_{disc}	0.0125	[-]
Thickness	L_{total}	0.002	[m]
Absorption coefficient (Chapter 2, Table 2.1)	ε_{IR788}	10.1	[mL μg^{-1} m^{-1}]
Dye concentration	C_{IR788}	500	[μg mL^{-1}]
Thickness of dye containing layer	L_{IR788}	$50\cdot10^{-6}$	[m]
Ambient temperature	T_0	37	[ºC]
NIR incident intensity	I	5	[W cm^{-2}]
Quantum yield of thermal relaxation	η_{eff}	0.94	[-]
Characteristic length	L_c	0.00625 ($R_{disc}/2$)	[m]

3.10.2 **In vivo *modeling parameters***
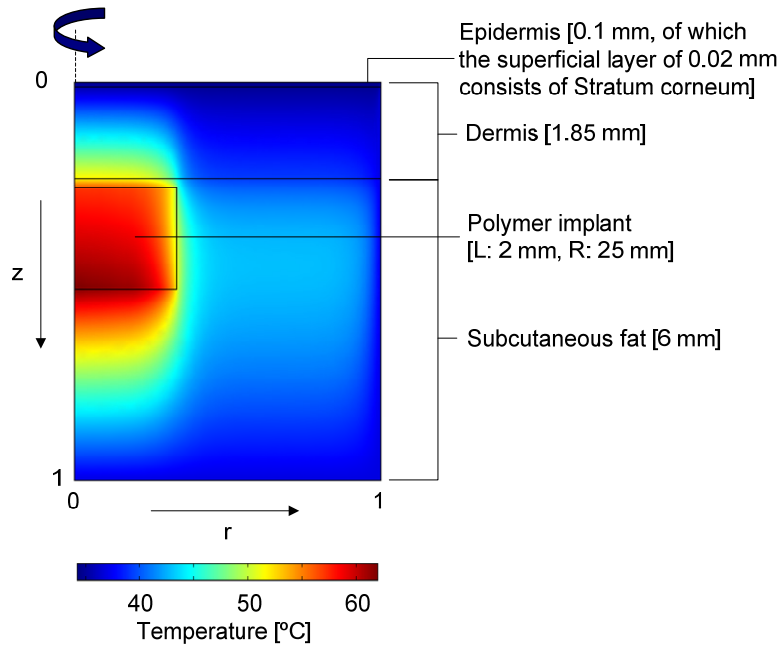
Figure 3.17: Example of modeling result using a dimensionless axisymmetric model for *in vivo* heating. The resulting temperature profile corresponds to the axial temperature profile presented in Figure 3.11B (solid line).

A dimensionless axisymmetric model was used to estimate temperatures reached *in vivo* when irradiated by NIR (Figure 3.17), by solving the Pennes bioheat equation (Eqn. 3-18) [14] with the addition of an NIR energy source term (exhibiting a homogeneous intensity). The model assumed tissue could be represented by a layered model of epidermis, dermis and subcutaneous fat, in which each layer exhibited homogeneous thermal and optical properties. Blood perfusion was assumed to increase linearly with temperature from its base value at 37ºC (Table 3.4) up to 4 times its base value at 42ºC, after which it remains constant [26]. The temperature at the lower and right boundary was set to 37ºC (heat sink), whereas the skin temperature was modeled by assuming free convection from a flat plate (Eqn. 3-9). Since the temperature increase is mainly induced above the implant, the boundary conditions are based on the radius of the polymer disc. The blood perfusion term in Eqn. 3-18 is critical for determining the amount of heat generation in tissue, and is strongly influenced by the amount of blood vessels inside the tissue. An average value was assumed for skin perfusion in the fore arm [27], whereas

perfusion in subcutaneous fat was assumed to be lower [15,16] (Table 3.4). Although the choice of the perfusion parameters definitely influences the induced temperatures, the effect of perfusion can be counteracted by changing the incident NIR radiation.

$$\rho_t \cdot C_{p,t} \frac{\partial T}{\partial t} = \nabla \bullet (k_t \nabla T) - \rho_{bl} \cdot C_{p,bl} \cdot w_{bl} \cdot (T - T_{bl}) + Q_{NIR} \qquad \text{[Eqn. 3-18]}$$

where ρ_t, ρ_{bl}: density of tissue (t) and blood (b), respectively   [kg m^{-3}]

$C_{p,i}$: heat capacity of component i   [J kg^{-1} K^{-1}]

k_t : thermal conducivity of tissue   [W m^{-1} K^{-1}]

w_{bl} : blood perfusion rate   [s^{-1}]

T_{bl} : temperature of blood (= 37ºC)   [K]

Q_{NIR} : heat production due to NIR radiation (Eqn. 3-3)   [W]

The radiation transport theory in the scattering-dominant limit (i.e. diffusion approximation) was used to calculate light propagation inside the tissue [13,19,28,29]. The dermis and subcutaneous fat are both strongly scattering, whereas melanin in the epidermis causes significant absorption of NIR irradiation. Since the epidermis is very thin in comparison to the dermis, it was assumed that the dermis accounted for the radiation distribution inside the entire cutaneous layer, given by Eqn. 3-19 (detailed derivation in reference 29). The assumed optical and thermal properties of the different tissue types are summarized in Table 3.4.

Table 3.4: Tissue optical and thermal properties assumed in the model [12,15-18,27,28].

Tissue	μ_a [m^{-1}]	μ'_s [m^{-1}]	w_{bl} [m^3 m^{-3} s^{-1}]	ρ [kg m^{-3}]	k [W m^{-1} K^{-1}]	C_p [J kg^{-1} K^{-1}]
Epidermis	1535†	1436	0	1085	0.47	3680
Dermis	25.8	1436	5·10^{-3}	1085	0.47	3680
Subcutaneous fat	103	1130	1·10^{-3}	850	0.16	2300

† For a dark pigmented skin, a value of 6064 m^{-1} was used corresponding to 40% pigmentation, calculated based on ref [17].

The effect of scattering in the subcutaneous layer was neglected to simplify calculations. Since a significant decrease in intensity has already occurred at the skin/fatty interface (Figure 3.11), it is assumed the error introduced here was not too large. Local heat

production inside the different tissue layers is then given by multiplying the local heat flux by the absorption coefficient of the corresponding tissue, thus assuming all absorbed radiation is transformed into heat. For the polymer implant, Eqns. 3-3 and 3-4 remain valid for heat generated in the polymer disc.

$$I(z) = I_0 \cdot \frac{4}{1-r_{21}} [1 - \frac{2\mu_a / \mu_{eff}}{(1-r_{21})/(1+r_{21}) + 2\mu_a / \mu_{eff}}] \cdot e^{-\mu_{eff} \cdot z} \qquad \text{[Eqn. 3-19]}$$

$$\frac{1}{\mu_{eff}} = \sqrt{\frac{1}{3 \cdot \mu_a \cdot (\mu_a + \mu'_s)}} \qquad \text{[Eqn. 3-20]}$$

where $I(z)$: local heat flux [W m^{-2}]

$\quad\quad\quad I_0$: indicident intensity (different for each layer!) [W m^{-2}]

$\quad\quad\quad r_{21}$: diffuse reflection factor ($\approx 1 - n_2^{-2}$) [-]

$\quad\quad\quad n_2$: tissue refractive index [-]

$\quad\quad\quad \mu_a$: absorption coefficient [m^{-1}]

$\quad\quad\quad 1/\mu_{eff}$: diffusion length (Eqn. 3-20) [m]

$\quad\quad\quad \mu'_s$: reduced scattering coefficient ($= g \cdot \mu_s$) [m^{-1}]

$\quad\quad\quad g$: anisotropy factor (indicates scattering direction) [-]

$\quad\quad\quad \mu_s$: scattering coefficient [m^{-1}]

To investigate the influence of the depth of the implant on the temperature increase, the implant in Figure 3.17 was shifted to the appropriate depth, while simultaneously moving the lower boundary, thus maintaining the same distance between implant and heat sink. It was further assumed that the insulating layer (either a stagnant water layer or a rubbery polymer) was completely transparent, which is a reasonable assumption for both water and polymers.

The main modeling results are presented and discussed in section 3.7. In addition to these results, Figure 3.18 illustrates the temperature increase in time, corresponding to the steady state temperature profiles presented in Figure 3.11. Finally, it should be stressed, that this model has not been verified experimentally, which is essential when considering radiation transport inside complicated biological structures. It is a highly simplified model of reality, but does serve as an indication of the possibilities of NIR in drug delivery.
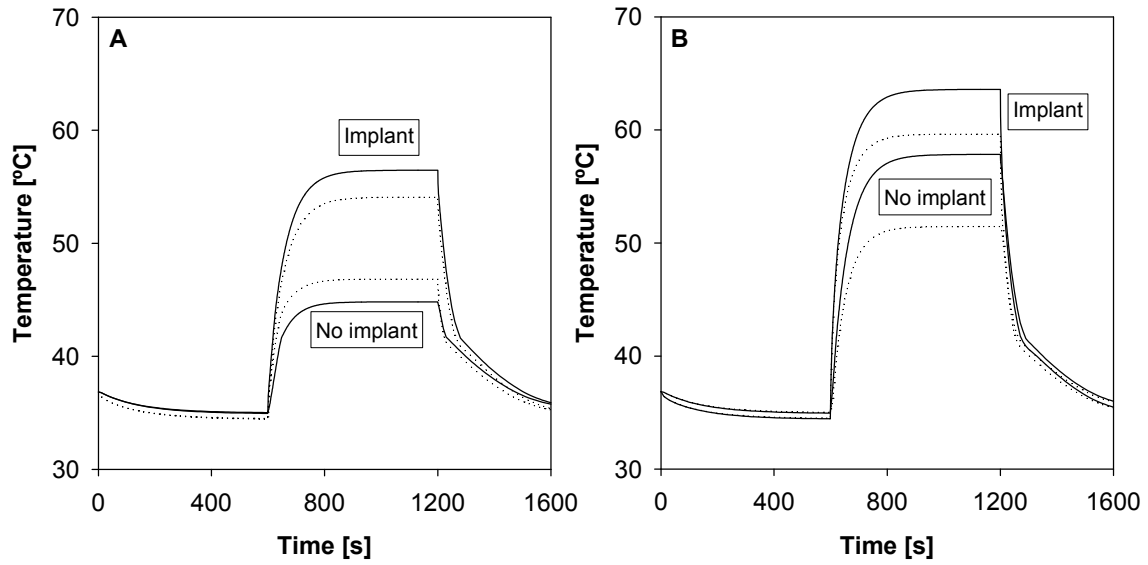
Figure 3.18: Temperature increase in time, corresponding to results presented in Figure 3.11, where solid lines correspond to temperatures at the irradiated surface of the implant, and dotted lines represent the skin surface temperatures. Results are presented for moderately pigmented (**A**) and dark pigmented (**B**) skin, both in the presence and absence of the implant.

3.10.3 Concentration dependent diffusion coefficient

Diffusion coefficients were determined by following the release of ibuprofen from polymer films (solvent cast in dichloromethane according to procedure described in section 2.3.2.1, L: ~ 200 μm) into phosphate buffered saline (PBS) in time at different temperatures and initial drug concentrations inside the polymer. Using Eqn. 3-17, the diffusion coefficient at a certain concentration and temperature was determined from the initial slope of the square root of time versus the fractional release (M_t/M_{inf}). Based on these data, a reasonable fit was found for the diffusion coefficient as a function of temperature and ibuprofen concentration (Eqn. 3-21, lines in graph).

$$D = 3 \cdot 10^{-50} \, e^{0.152 \cdot C} \, e^{-(0.00042 \cdot C - 0.2424) \cdot T} \qquad \text{[Eqn. 3-21]}$$

where D : diffusion coefficient $[\text{m}^2 \, \text{s}^{-1}]$
C : concentration [(%w/w polymer)]
T : temperature [K]

Figure 3.19: Diffusion of ibuprofen (Genfarma) in poly(butyl methacrylate-*co*-methyl methacrylate) (Sigma-Aldrich, T_g ~ 48ºC) for different drug concentrations at various temperatures. Ibuprofen concentrations (%w/w polymer): 0.5 (○), 5.0 (△), 10.8 (□) 19.8 (◇), and 29.4 (▽), where inserted lines are calculated using Eqn. 3-21.

References

[1] Peyser, P. in *Polymer Handbook* (eds. Brandrup, J. & Immergut, E. H.) VI/209 – VI/277 (Wiley, New York, 1989).

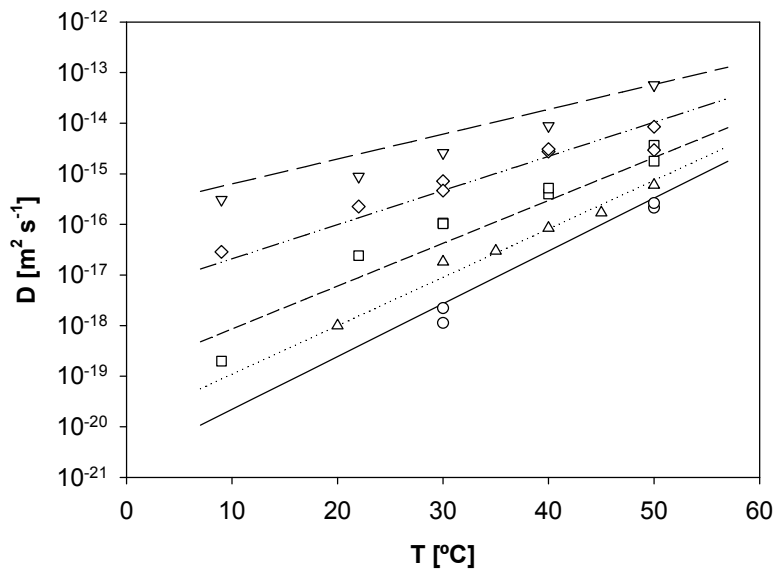[2] Plazek, D. J., Ngai, K. L. in *Polymer Data Handbook* (ed. Mark, J. E.) 139-159 (Oxford University Press, Oxford, 1999).

[3] Churchill, S. W. & Chu, H. H. S. Correlating equations for laminar and turbulent free convection from a vertical plate. *Int. J. Heat Mass Transf.* **18**, 1323-1329 (1975).

[4] McAdams, W. H. *Heat Transmission*, 3rd ed., 165-183 (McGraw-Hill, New York, 1957).

[5] Chiasson, A. D., Spitler, S. J., Smith, M. D. A model for simulating the performance of a shallow pond as a supplemental heat rejecter with closed-loop ground-source heat pump systems. *ASHRAE Trans.* **106**, 107-121 (2000).

[6] Incorpera, F. P., DeWitt, D. P. *Introduction to heat transfer*, 3rd ed. (Wiley, New York, 1996).

[7] Churchill, S. W. & Chu, H. H. S. Correlating equations for laminar and turbulent free convection from a horizontal cylinder. *Int. J. Heat Mass Transf.* **18**, 1049-1053 (1975).

[8] Tsubouchi, T. & Masuda, H. Heat transfer by natural convection from horizontal cylinders at low Rayleigh numbers. *Rept. Inst. High Sp. Mech., Japan* **19**, 205-219 (1967/1968).

[9] Crezee, J., Mooibroek, J., Lagendijk, J. J. W., Van Leeuwen, G. M. J., The theoretical and experimental evaluation of the heat balance in perfused tissue. *Phys. Med. Biol.* **39**, 813-832 (1994).

[10] Jiang, S. C. & Zhang, X. X. Effects of dynamic changes of tissue properties during laser-induced interstitial thermotherapy (LITT). *LaserMed. Sci* **19**, 197-202 (2005).

[11] Lv, Y.-G. & Liu, J. Measurement of local tissue perfusion through a minimally invasive heating bead. *Heat Mass Transf.* **44**, 201-211 (2007).

[12] Fiala, D., Lomas, K. J., Stohrer, M. A computer model of human thermoregulation for a wide range of environmental conditions: the passive system. *J. Appl. Physiol.* **87**, 1957-1972 (1999).

[13] Tuchin, V. V. in *Biomedical Photonics* (ed. Vo-Dinh, T.) 3-1 – 3-26 (CRC, Boca Raton, 2003).

[14] Pennes, H. H. Analysis of tissue and arterial blood temperatures in the resting human forearm. *J. Appl. Physiol.* **1**, 93-121 (1948).

[15] Virtanen, K. A. *et al.* Glucose uptake and perfusion in subcutaneous and visceral adipose tissue during insulin stimulation in nonobese and obese humans. *J. Clin. Endocrinol. Metabolism.* **87**, 3902-3910 (2002).

[16] Valvano, J. W. in *Optical-Thermal Response of Laser-Irradiated Tissue* (eds. Welch, A. J., Van Gemert, M. J. C.) 445-488 (Plenum Press, New York, 1995).

[17] Jacques, S. L. Skin optics, *Oregon Medical Laser Center News* (Jan 1998).

[18] Baskatov, A. N., Genina, E. A., Kochubey, V. I., Tuchin, V. V. Optical properties of human skin, subcutaneous and mucous tissues in the wavelength range from 400 to 2000 nm. *J. Phys. D: Appl. Phys* **38**, 2543-2555.

[19] Mobley, J. & Vo-Dinh, T. in *Biomedical Photonics* (ed. Vo-Dinh, T.) 2-1 – 2-75 (CRC, Boca Raton, 2003).

[20] Van Gemert, M. J. C., Welch, A. J., Pickering, J. W., Tan, O. T. in *Optical-Thermal Response of Laser-Irradiated Tissue* (eds. Welch, A. J., Van Gemert, M. J. C.) 789-829 (Plenum Press, New York, 1995).

[21] Xu, F., Sun, L.-X., Tan, Z.-C., Liang, J.-G., Li, R.-L. Thermodynamic study of ibuprofen by adiabatic calorimetry and thermal analysis. *Thermochimica Acta* **412**, 33-37 (2004).

[22] Crank, J. *The Mathematics of Diffusion*, 2nd ed., 44-68 (Oxford University Press, London, 1975).

[23] Assael, M. J., Botsios, S., Gialou, K., Metaxa, I. N. Thermal conductivity of polymethyl methacrylate and borosilicate crown glass BK7. *Int. J. Thermophys.* **26**, 1595-1605 (2005).

[24] *CRC Handbook of Chemistry and Physics*, 88th ed., Section 6 (CRC press, Bocan Raton, 2008).

[25] McAdams, W. H. *Heat Transmission*, 3rd ed., 55-125 (McGraw-Hill, New York, 1957).

[26] London, R. A. *et al.* Laser-tissue interaction modeling with LATIS, *Appl. Optics* **36**, 9068-9074 (1997).

[27] Li, H. J., Zhang, X. X., Yi, Y. F., Measurement of blood perfusion using the temperature response to constant surface flux heating. *Int. J. Thermophys.* **23**, 1631-1644 (2002).

[28] Jacques, S. L. & Pogue, B. W. Tutorial on diffuse light transport. *J. Biomed. Optics* **13**, 041302-1 – 041302-19.

[29] Star, W. M. in *Optical-Thermal Response of Laser-Irradiated Tissue* (eds. Welch, A. J., Van Gemert, M. J. C.) 131-206 (Plenum Press, New York, 1995).

CHAPTER 4

Externally Triggered Glass Transition Switch for Localized On-Demand Drug Delivery

Abstract

Controlling the precise level and location of a drug in the human body can greatly improve drug safety and efficacy. Here, we demonstrate repeated and reproducible on-off drug release by non-invasive selective heating of the implant using near-infrared radiation, both during *in vitro* and *in vivo* experiments, attaining on/off-ratios in excess of 1,000. Release of ibuprofen below the glass transition temperature (T_g) was extremely low, attributed to the spontaneous formation of a glassy surface layer, whereas in the rubbery state ($T > T_g$) ibuprofen readily diffused out of the implant. We anticipate that the results described here can lead to the development of new clinical treatment systems and enable patient-controlled self-administration.

4.1 Introduction

Controlled release of drugs from polymeric implants has been studied extensively, mainly focusing on achieving zero-order release in time [1-3]. However, many therapeutic applications do not require constant drug release or, in the case of habituation or resistance to medication, even benefit from pulsatile administration, such as post-surgical pain control and the treatment of infections [4-6]. By non-invasive external triggering of drug release from an implant, pulsewise administration can be realized according to the patient's needs and at specific locations in the human body. This localized on-demand delivery allows for lower doses of potent drugs, thereby reducing the toxic side effects commonly associated with systemic administration [7].

External regulation of on-demand drug release has been reported using a number of different stimuli [6]. Release based on polymer degradation or dissolution has been induced by ultrasound [8,9] and electrical triggering [10,11], but these mechanisms prohibit long-term applications. Electrochemical [12] or electrothermal activation [13] has been applied for drug delivery from multireservoir microchips that require complex multistep lithographic fabrication. Alternatively, thermal triggers can be used for non-destructive on-off switching of drug release based on the lower critical solution temperature (LCST) [14,15]. For non-invasive thermal triggering, oscillating magnetic fields [16], near-infrared radiation [17], and a radiofrequency field [18] have been used. However, the attained on-off ratios using the LCST transition are limited to values in the order of 70 [17,19-21], and the relatively high leakage in the off-state reduces the effective lifetime of the implant.

Here we show that the large variation in diffusivity occurring near the glass transition temperature (T_g) of a polymer [22] can be used to activate drug release by thermal triggering. When the polymer is in the glassy state ($T < T_g$), the entrapped drug is virtually immobile, while in the rubbery state ($T > T_g$) it diffuses out of the implant.

4.2 Materials and methods

Strands of poly(D,L-lactic acid) (PLDL, M_w: 460 kDa relative to PS standard, Purac) oversaturated with 40 wt% ibuprofen (Genfarma) were prepared in a custom-built twin

screw mini compounder (capacity: 5 g, T_{set}: 165 ºC). Compounded strands (diameter: 3 mm, length: 20 mm) were coated with a quaterrylenebis(dicarboximide) derivative (QBDC, BASF) by dip-coating twice in a 4.5 % w/w solution of PLDL in tetrahydrofuran (Biosolve) containing QBDC.

In vitro temperature induced release studies were performed by transferring a screw-cap jar containing a PLDL strand in 50 mL phosphate buffered saline (PBS, pH: 7.4, Sigma) from a 37ºC to a 55ºC water bath (Grant OLS 200). *In vitro* NIR induced release studies of a PLDL strand were performed in a custom-made 54 mL jacketed glass vessel (T: 37ºC) completely filled with PBS and sealed with a glass cover. The fiber-coupled CW-laser diode module (HPM [Power Technology, Inc.], λ: 785 nm, N.A.: 0.22) was fixed 16 mm above the PLDL strand. All *in vitro* samples (500 μL) were analyzed by HPLC (C18 Discovery® HS 150 x 4.6 mm - 3μm, 50/50 % v/v acetonitrile/water (with 0.1 % v/v TFA), flow: 1.2 mL min^{-1}, UV detection at 223 nm). Fresh PBS solution was added to maintain a constant system volume.

For the *in vivo* study, a PLDL strand was wrapped in a tissue specimen bag (Shandon) and implanted subdermally in male Sprague-Dawley rats (280-300 g). The laser was kept at the same distance (14 mm) from the skin of the lightly anaesthetized rat (isofluorane inhalation; 2% at 250 mL min^{-1}) throughout NIR irradiation. Blood plasma samples (200 μL) were taken at predefined intervals from a hind leg of the rats. Samples were centrifuged (3,000 rpm, 20 min) and analyzed by LC-MS/MS (Xterra C18, 50 x 2.1 mm - 3.5 μm, turbo ion spray (ESI) negative ion mode mass detection). The protocol was approved by the Ethics Committee on Animal Experiments of the University of Maastricht (DEC protocol #2006-066).

4.3   Results and discussion

To demonstrate the effect of temperature on the release of ibuprofen near the T_g of PLDL (T_g midpoint = 56ºC; T_g trajectory = 50-60ºC), we placed compounded strands of polymer oversaturated with ibuprofen in a water bath kept at 37ºC. Transferring the strands into a bath of 55ºC resulted in a stepwise release of ibuprofen with an on/off-ratio of about 400 (Figure 4.1). During the 15-minute release pulses, the amount of ibuprofen liberated was very reproducible (60.9 ± 12.6 μg), which can be attributed to
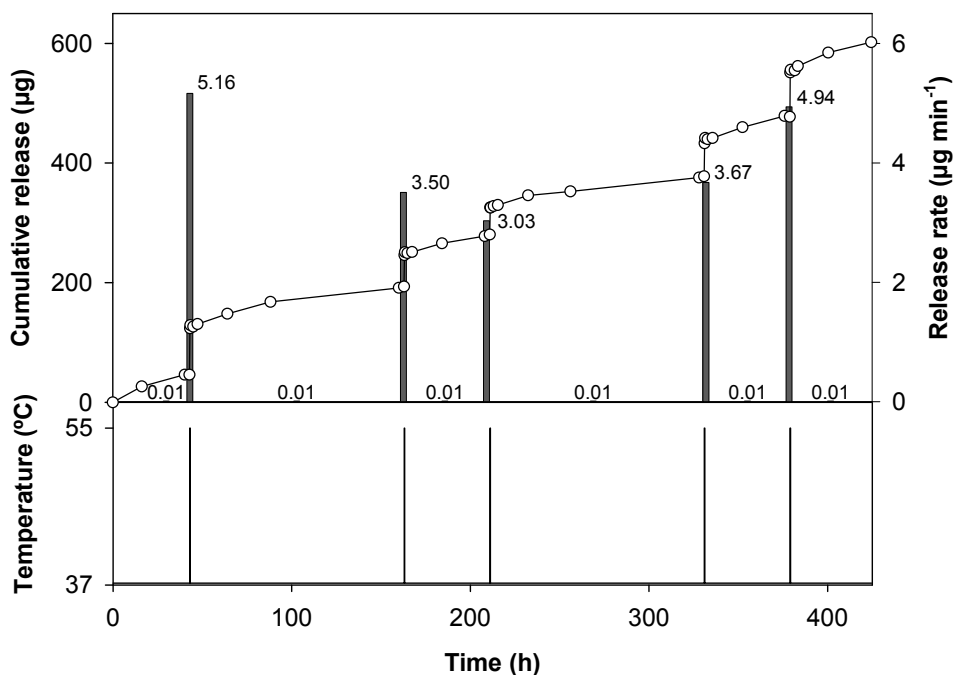
Figure 4.1: Repeated on-off switching of a PLDL strand containing ibuprofen crystals in PBS by transferring the strand from a 37 ºC to a 55 ºC water bath. Circles represent cumulative release, bars indicate the average release rate in a certain time interval. Each on-switch lasts 15 min.

oversaturation of ibuprofen. This oversaturation ensures replenishment of released ibuprofen by partial dissolution of the drug crystals providing a constant concentration of ibuprofen dissolved in the polymer and, consequently, a constant driving force for release (Figure 4.2). Although the large plasticizing effect of ibuprofen decreases the T_g of the polymer to about 0ºC, no significant release is found at 37ºC, which can be attributed to the self-sealing property of the system. As the diffusion coefficient of ibuprofen outside the strand is much higher than inside the polymer, the ibuprofen surface concentration is close to zero, resulting in a concentration gradient in the surface layer of the polymer strand. This gradient causes a T_g-profile, with the highest T_g located at the polymer/water interface. Therefore, although the bulk polymer is in the rubbery state, the outer surface of the polymer is in a glassy state at body temperature providing a switching layer (Figure 4.2). This self-sealing mechanism accounts for the extremely low release in the off-state and, in addition, provides an intrinsic safety precaution, as rupture of the implant will not result in dose dumping. Drug release is thus controlled by changing the temperature of this switching layer around T_g.
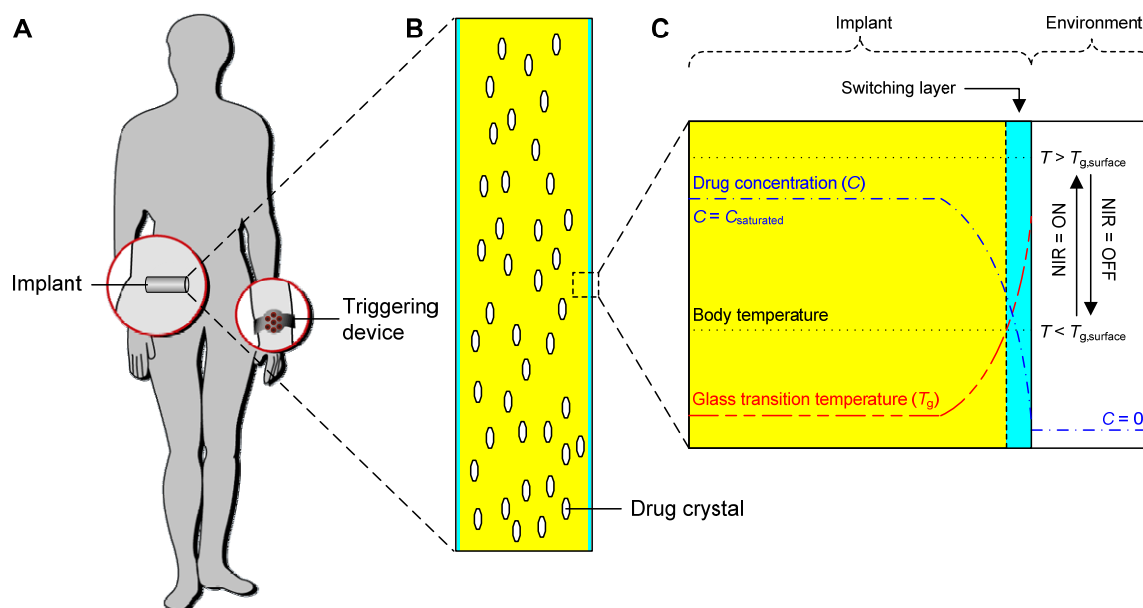
Figure 4.2: Schematic overview of the glass transition switch. **A** Drug release from a subdermal implant can be remotely switched on using a 'watch-type' triggering device. **B** The crystals in the implant ensure a constant saturated concentration of dissolved drug. **C** The surface of the implant is glassy due to the concentration profile in the switching layer, making the implant 'self-sealing'.

To remotely induce the required temperature change, near-infrared radiation (NIR) was applied as external trigger. The minimum in absorption of blood and tissue material around 780 nm allows a significant penetration depth of NIR in tissue [23,24]. This wavelength can effectively be transformed into heat by a quaterrylenebis(dicarboximide) derivative acting as a dye with a high quantum yield of thermal relaxation [25]. To ensure sufficient heating by NIR, the implant was dip-coated with a layer of PLDL containing the dye. Figure 4.3 displays heating of coated PLDL rods, clearly demonstrating a rapid increase in surface temperature with initial heating rates up to 2°C s^{-1}. In this system, steady state surface temperatures are attained within 1-2 minutes. The heating rate and the increase in temperature can be controlled by the NIR intensity applied. The use of NIR for repeated *in vitro* ibuprofen release from PLDL implants is demonstrated in Figure 4.4. The off-situation is characterized by a very low release rate (<0.01 μg min^{-1}), whereas high release rates of approximately 8-10 μg min^{-1} are obtained in the on-state, leading to on/off-ratios in excess of 1,000.
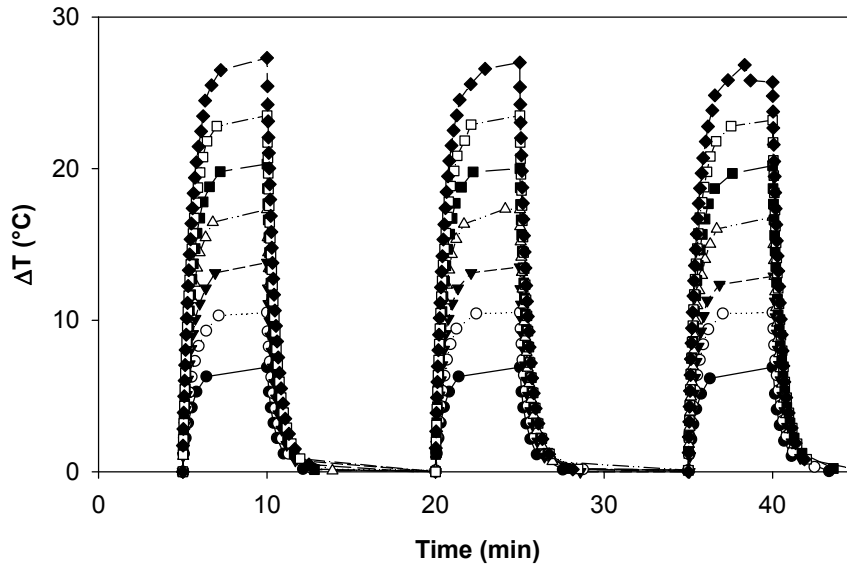
Figure 4.3: External heating of a PLDL strand using a fiber-coupled NIR laser as external trigger. Surface temperature increase (ΔT) of a PLDL strand dip-coated with dye-doped PLDL ([QBDC]: 6,000 ppm) at different laser powers (● 200 mW, ○ 270 mW, ▼ 350 mW, △ 450 mW, ■ 550 mW, □ 650 mW, and ◆ 750 mW).
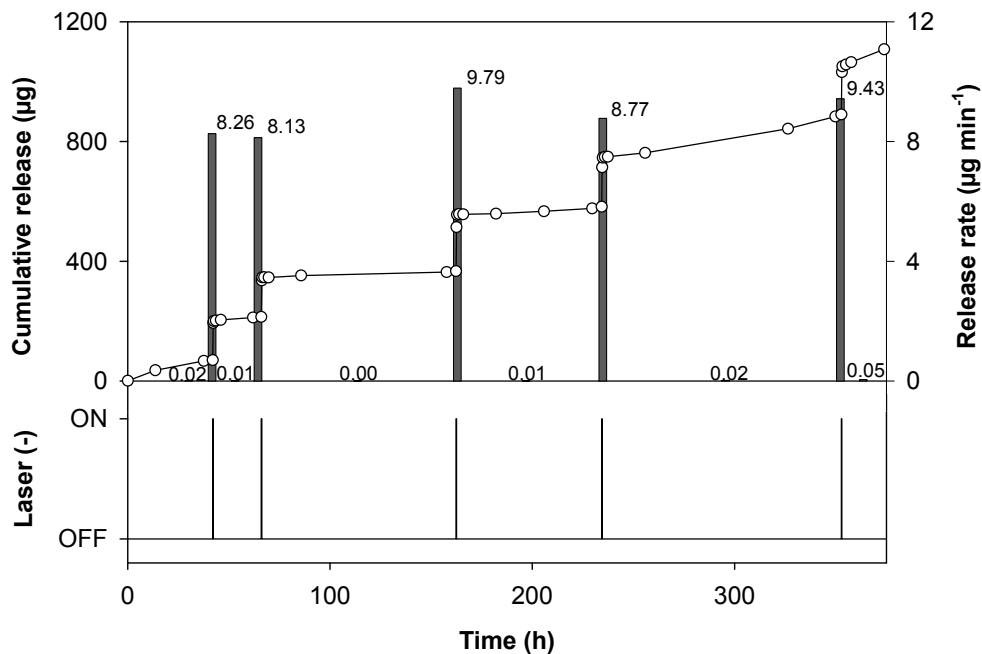
Figure 4.4: Repeated on-off switching of a PLDL strand oversaturated with ibuprofen and dip-coated with dye-doped PLDL ([QBDC]: 15,000 ppm) in PBS (T = 37ºC) at a power of 750 mW. Circles represent cumulative release, bars indicate the average release rate in a certain time interval. Each NIR irradiation lasts 15 min.
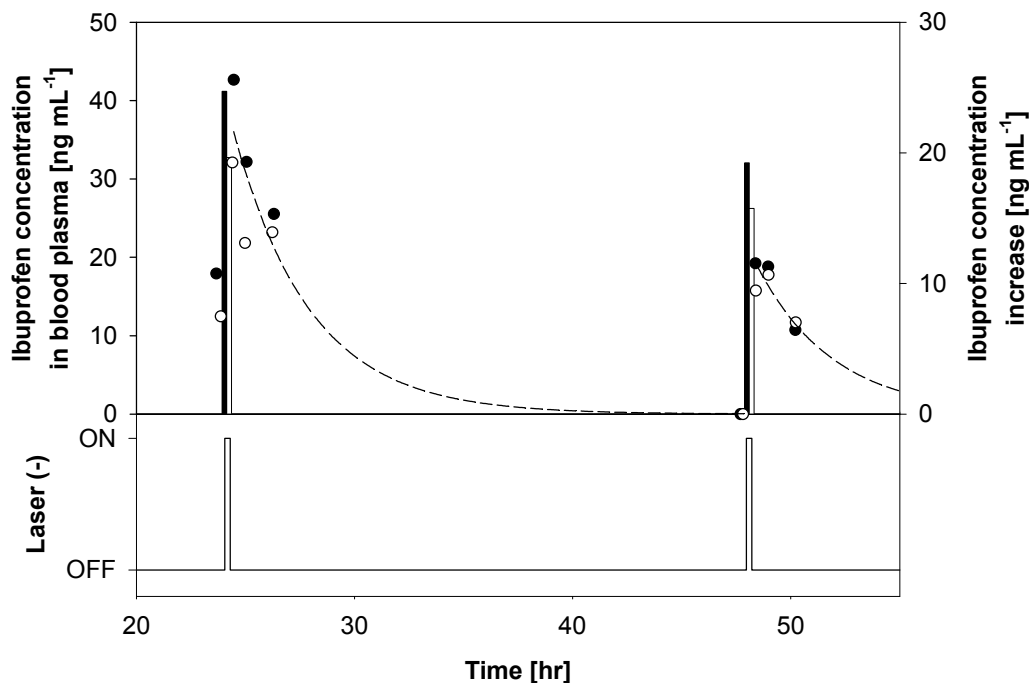
Figure 4.5: NIR-induced *in vivo* release from PLDL strands oversaturated with ibuprofen and dip-coated with dye-doped PLDL ([QBDC]: 6,000 ppm) implanted subdermally in the back of male Sprague-Dawley rats (Rat A: ○, Rat B: ●) at a laser power of 750 mW. Circles represent ibuprofen concentration in the blood plasma, bars indicate increase in ibuprofen concentration during NIR irradiation. Each irradiation lasts 15 min. Inserted lines serve as a guide to the eye.

The potential of this drug delivery concept was further explored by performing *in vivo* experiments with male Sprague-Dawley rats (Figure 4.5). To avoid surrounding tissue from being exposed to excessive temperatures (> 43 ℃), the polymer strand was wrapped in a biopsy bag that is permeable for diffusing species. The stagnant film of bodily fluid in the biopsy bag provides effective insulation, since no tissue damage was detected after the *in vivo* release experiments. The significant increase in systemic ibuprofen concentration upon NIR irradiation clearly illustrates successful *in vivo* release based on the glass transition switch. When the trigger is turned off, the level of ibuprofen in the blood plasma decreases rapidly due to drug metabolism. The increase in systemic ibuprofen concentration (19.8 ± 3.2 ng mL^{-1}) was similar during both cycles of on-demand release in the two rats. The presence of ibuprofen in the blood plasma before the first cycle is presumably caused by residual ibuprofen on the surface of the implant.

NIR is especially effective for triggering of drug release from implants located at depths up to several centimeters [24]. For higher penetration depths, scattering by tissue in this wavelength region limits the use of NIR. Therefore, we have performed explorative experiments, similar to those described above, in which the applicability of alternative external temperature triggers was demonstrated. On-demand drug delivery was induced using therapeutic ultrasound (1-3 MHz) [26], which is suitable for soft tissue applications due to the difference in attenuation between water/tissue and the polymer. Drug release was also triggered using an alternating magnetic field to heat polymer strands containing superparamagnetic iron oxide nanoparticles [27]. Magnetism is especially promising, since it allows triggering inside the entire human body. The use of various triggers underlines the versatility of this T_g-based switching mechanism for pulsatile drug release.

4.4 Conclusions

The concept presented here permits long-term and patient-friendly administration of a wide variety of medicines, ranging from systemic dosing of drugs with low oral bioavailability to drugs required locally. Potential applications are envisioned for patients suffering from a chronic pain disorder or recurring inflammations, such as rheumatoid arthritis, who would benefit from dosing at will. Cell damage caused by relatively potent drugs during chemotherapy could be suppressed by localized on-demand administration [28]. Patients known to be at risk of acute and lethal conditions could instantly provide the required antidote, like antihistamines in the case of anaphylactic shock. The current availability of hand-held ultrasound- and NIR-probes further emphasizes that treatment will be possible in both a clinical and home environment.

References

[1] Langer, R. Invited review polymeric delivery systems for controlled drug release. *Chem. Eng. Commun.* **6**, 1-48 (1980).

[2] Ghosh, S. Recent research and development in synthetic polymer-based drug delivery systems. *J. Chem. Res.* **4**, 241-246 (2004).

[3] Freiburg, S. & Zhu, X. X. Polymer microspheres for controlled drug release. *Int. J. Pharm.* **282**, 1-18 (2004).

[4] Sershen, S. R. & West, J. L. Implantable, polymeric systems for modulated drug delivery. *Adv. Drug Deliver. Rev.* **54**, 1225-1235 (2002).

[5] Richards Grayson, A. C. *et al.* Multi-pulse drug delivery from a resorbable polymeric microchip device. *Nat. Mater.* **2**, 767-772 (2003).

[6] Kost, J. & Langer, R. Responsive polymeric delivery systems. *Adv. Drug Deliver. Rev.* **46**, 125-148 (2001).

[7] Langer, R. Drug delivery and targeting. *Nature* **392** (Suppl.), 5-10 (1998).

[8] Kost, J., Leong, K., Langer, R. Ultrasound-enhanced polymer degradation and release of incorporated substances. *P. Natl. Acad. Sci. USA* **86**, 7663-7666 (1989).

[9] Aschkenasy, C. & Kost, J. On-demand release by ultrasound from osmotically swollen hydrophobic matrices. *J. Control. Release* **110**, 58-66 (2005).

[10] Kwon, I. C., Bae, Y. H., Kim, S. W. Electrically erodible polymer gel for controlled release of drugs. *Nature* **354**, 291-293 (1991).

[11] Wood, K. C. *et al.* Electroactive controlled release thin films. *P. Natl. Acad. Sci. USA* **105**, 2280-2285 (2008).

[12] Santini, J. T., Cima, M. J., Langer, R. A controlled-release microchip *Nature* **397**, 335-338 (1999).

[13] Prescott, J. H. *et al.* Chronic, programmed polypeptide delivery from an implanted, multireservoir microchip device, *Nat. Biotechnol.* **24**, 437-438 (2006).

[14] Hoffman, A. S., Afrassiabi, A., Dong, L. C. Thermally reversible hydrogels: II. Delivery and selective removal of substances from aqueous solutions. *J. Control. Release* **4**, 213-222 (1986).

[15] Bae, Y. H., Okano, T., Hsu, R., Kim, S. W. Thermo-sensitive polymers as on-off switches for drug release. *Makromol. Chem.-Rapid* **8**, 481-485 (1987).

[16] Hergt, R. *et al.* Maghemite nanoparticles with very high AC-losses for applications in RF-magnetic hyperthermia. *J. Magn. Magn. Mater.* **270**, 345-357 (2004).

[17] Sershen, S. R., Westcott, S. L., Halas, N. J., West, J. L. Temperature-sensitive polymer-nanoshell composites for photothermally modulated drug delivery. J. Biomed. Mater. Res. 51, 293-298 (2000).

[18] Gannon, C. J. *et al.* Carbon nanotube-enhanced thermal destruction of cancer cells in a noninvasive radiofrequency field. *Cancer* **110**, 2654-2665 (2007).

[19] Satarkar, N. S., Hilt, J. Z. Magnetic hydrogel nanocomposites for remote controlled pulsatile drug release. *J. Control. Release* (2008), doi: 10.1016/j.jconrel.2008.06.008.

[20] Peng, T. & Cheng, Y.-L. Temperature-responsive permeability of porous PNIPAAm-*g*-PE membranes, *J. Appl. Polym. Sci.* **70**, 2133-2142 (1998).

[21] Li, S. K., D'Emanuele, A. On-off transport though a thermoresponsive hydrogel comoposite membrane. *J. Control. Release* **75**, 55-67 (2001).

[22] Zhang, J. & Wang, C. H. Application of the laser-induced holographic grating relaxation technique to the study of physical aging of an amorphous polymer. Macromolecules 20, 683-685 (1987).

[23] Mobley, J. & Vo-Dinh, T. in *Biomedical Photonics* (ed. Vo-Dinh, T.) 2-1 – 2-75 (CRC, Boca Raton, 2003).

[24] Weissleder, R. A clearer vision for *in vivo* imaging. *Nat. Biotechnol.* **19**, 316-317 (2001).

[25] Geerts, Y. *et al.* Quaterrylenebis(dicarboximides)s: near infrared absorbing and emitting dyes. *J. Mater. Chem.* **8**, 2357-2369 (1998).

[26] Bruinewoud, H. *Ultrasound-induced drug release from polymer matrices: the glass transition temperature as a thermo-responsive switch*. PhD dissertation, Eindhoven: TU Eindhoven (2005).

[27] Rovers, S.A., Dietz, C.H.J.T., Hoogenboom, R., Kemmere, M.F., Keurentjes, J.T.F. Reversible on-demand drug release from iron oxide incorporated polymeric matrices using an alternating magnetic field as external trigger, *in preparation*.

[28] Ismael, G. F. V., Rosa, D. D., Mano, M. S., Awada, A. Novel cytotoxic drugs: Old challenges, new solutions. *Cancer Treat. Rev.* **34**, 81-91 (2008).

CHAPTER 5

Diffusion in Polymers near the Glass Transition Temperature

Abstract

The free volume theory (FVT) has primarily been successful in describing diffusion of relatively small solutes in rubbery polymer-solute systems, whereas only a limited amount of research has dealt with its application to large solutes, such as drug molecules, and to diffusion in glassy polymers. This chapter reviews the status of the FVT and its extension into the glassy state, mainly focusing on the effect of size, shape and flexibility of the solute. Sorption measurements of a homologous series of ethylene glycol dimethyl ethers from aqueous solution are performed to verify modeling results based on the FVT. Unfortunately, water sorption prevents quantitative evaluation of these diffusion coefficients. In an alternative approach, comparison of experimental diffusion data of ibuprofen to modeling results based on the FVT indicates that the diffusion coefficient is underestimated by several orders of magnitude, suggesting that either shape or flexibility effects are not taken into account satisfactorily, or that polymer dynamics perhaps change as the solute approaches the size of the jumping unit of the polymer.

5.1 Introduction

Diffusion of solutes in polymers is important in a variety of applications. In drug delivery applications, diffusion of the active pharmaceutical ingredient determines the rate of release. The diffusion rate of different species determines selectivity and speed of the separation process in dense membrane applications. During polymer processing operations, such as extrusion, dry blending and coating, diffusion of incorporated solutes and solvents is critical for the final properties. Residual monomer removal and drying processes are also dominated by diffusion of the monomer or solvent through the polymer matrix.

Cohen and Turnbull's free volume theory (FVT) [1], later modified by Fujita [2] and extended by Vrentas and Duda [3,4-6], is often used to describe diffusion in such systems. Originally, the theory was developed for concentrated polymer solutions above the glass transition temperature (T_g), but attempts have also been made, predominantly by Vrentas and Duda [], to apply the theory to polymers below T_g. The theory has mostly been developed for small solutes such as gases and solvents, often assuming rigid, spherical particles. Only a limited amount of research on larger solutes (several hundreds of grams per mole), and on shape and flexibility of the solute [7-11] has been performed.

The challenge in describing diffusion processes below T_g is that relaxation processes are comparable to or much slower than the experimental time-scale. T_g is usually defined as the temperature at which the relaxation time is 100 s (i.e. viscosity $\approx 10^{12}$ Pa·s). Therefore, the diffusion coefficient of solutes in a glassy system can change in time, and also depends on the history of the sample (e.g. the rate of cooling from a rubbery to a glassy state). This relaxation time increases exponentially with decreasing temperature leading to extremely long relaxation times, thus complicating the gathering and interpretation of experimental data.

In the current work, drug diffusion in a polymer matrix around T_g is investigated. Drug molecules generally have higher molecular weights than the solvents for which the theory has primarily been developed and tested. This research therefore deals with the influence of size and shape of solutes on the diffusion around the T_g of the polymer, specifically

aiming at determining the validity of the FVT for these systems. First, an overview of the status of the FVT around T_g is given in section 5.2.

5.2 Free volume theory

The FVT is based on the idea that diffusion of a molecule in a polymer matrix proceeds by jumping of the solute from one location to the next. The rate at which the molecule jumps is determined by the available free volume relative to the size of the diffusing species, and the energy required to overcome interaction with neighboring molecules. The theory provides expressions for the *self*-diffusion coefficients for both polymer and solute, although the focus generally tends to lie on that of the solute [12]. The *mutual* diffusion coefficient, which is the diffusion coefficient usually observed experimentally, can then be estimated using correlations containing the self-diffusion coefficient(s) [4,13]. It should be kept in mind that the FVT is only valid over a temperature interval, in which volume driven diffusion dominates. As the temperature increases, the relative contribution of free volume term decreases. In addition, the contribution of the energy term becomes significant at lower temperatures as the size of the diffusing solute decreases [14]. The upper temperature for the FVT is often assumed to be about 100ºC above T_g, although Arnould and Laurence report a smaller temperature range [15]. At high temperatures, when the energy term governs the diffusion process, an exponential (Arrhenius) temperature dependence of the diffusion coefficient exists. At the lower temperature end, the T_g limits the validity of the FVT, although several researchers have tried to extend it to below T_g [6,17].

Here, a summary of the FVT is presented as it has been proposed by Vrentas and Duda []. First, section 5.2.1 describes the theory for a rubbery polymer-solute system, after which the extension into the glassy region by various researchers is discussed [6,17]. Then, the effect of solute size is discussed in section 5.2.2.

5.2.1 Basic theory

An expression for the self-diffusion coefficient, on which the FVT is based, is given in Eqn. 5-1. As is common practice, subscripts 1 and 2 represent the solute and polymer, respectively. An important assumption is that no volume change on mixing occurs, i.e.

the partial specific volumes and corresponding hole free volumes are additive. This simplistic assumption maintains the purely predictive character of the theory based on free volume data determined from viscosity and density data of the pure components, and allows the use of Eqn. 5-2 to describe the average hole free volume. All polymer parameters described in these equations refer to the polymer in equilibrium, i.e. in a fully relaxed state.

$$D_1 = D_0 \, exp[-\frac{E^*}{RT}] \, exp[-\frac{\omega_1 \hat{V}_1^* + \omega_2 \xi \hat{V}_2^*}{\hat{V}_{FH} / \gamma}] \qquad\qquad [5\text{-}1]$$

$$\frac{\hat{V}_{FH}}{\gamma} = \omega_1 \frac{K_{11}}{\gamma_1} [K_{21} + T - T_{g1}] + \frac{\omega_2 \hat{V}_{FH2}}{\gamma_2} \qquad\qquad [5\text{-}2]$$

where D_0 : weakly temperature dependent pre-exponential
    factor that is assumed constant $[m^2 \, s^{-1}]$

  E^* : energy a molecule requires to overcome
    attractive forces to neighboring molecules[i] $[J \, mol^{-1}]$

  R : universal gas constant $[J \, mol^{-1} \, K^{-1}]$

  T : temperature $[K]$

  ω_i : mass fraction of component i $[-]$

  V_i^* : specific hole free volume of i required for a jump $[m^3 \, kg^{-1}]$

  ξ : ratio of the molar volume of the solute jumping
    unit to that of the polymer jumping unit $[-]$

  V_{FH} : average hole free volume per gram of mixture $[m^3 \, kg^{-1}]$

  γ : average overlap factor for the mixture[ii] $[-]$

  K_{1i} : free volume parameter of component i $[m^3 \, kg^{-1} \, K^{-1}]$

  K_{2i} : free volume parameter of component i $[K]$

  γ_i : overlap factor for pure component i $[-]$

  T_{gi} : glass transition temperature of component i $[K]$

  V_{FH2} : hole free volume of equilibrium liquid polymer $[m^3 \, kg^{-1}]$

---

[i] In the pure solvent limit, $E^* \rightarrow 0$. In the pure polymer limit up to $\omega_1 = 0.9$, E^* is assumed constant.

[ii] Introduced because the same free volume is available to more than one jumping unit ($\frac{1}{2} < \gamma < 1$).

V_{FH2} is represented by the free volume parameters K_{12} and K_{22}, which can also be expressed in terms of the Williams-Landel-Ferry (WLF) parameters (Eqns. 5-3 and 5-4) that are used to describe viscosity in glass forming materials [16].

$$K_{12} = \hat{V}_2^0 (T_{g2}) [\alpha_2 - (1 - f_{H2}^G) \alpha_{c2}] , \qquad \frac{K_{12}}{\gamma_2} = \frac{\hat{V}_2^*}{2.303 \cdot C_{12}^g \cdot C_{22}^g} \qquad [5\text{-}3]$$

$$K_{22} = \frac{f_{H2}^G}{\alpha_2 - (1 - f_{H2}^G) \alpha_{c2}} , \qquad\qquad K_{22} = C_{22}^g \qquad [5\text{-}4]$$

where $V_2^0(T_{g2})$: specific volume of polymer at T_{g2} [m³ kg⁻¹]

$f_{H2}{}^G$: fractional hole free volume at T_{g2} [-]

α_2 : polymer specific thermal expansion coefficient   [K⁻¹]

α_{c2} : thermal expansion coefficient for sum of specific
core volume and specific interstitial free volume   [K⁻¹]

$C_{12}{}^g$: WLF parameter (reference temperature: T_{g2})   [-]

$C_{22}{}^g$: WLF parameter (reference temperature: T_{g2})   [K]

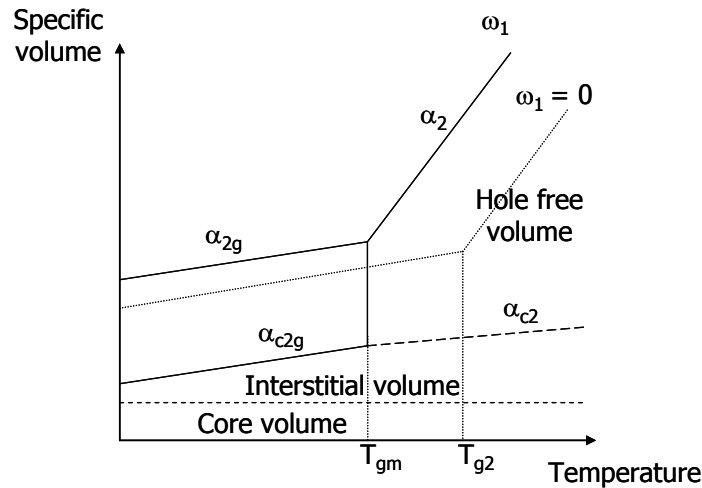**Figure 5.1**: Free volume theory around the glass transition temperature [17].

Figure 5.1 illustrates the basic idea behind the FVT around T_g. The core volume is the volume occupied by compact polymer chains (and thus remains the same at all temperatures), whereas the interstitial free volume arises due to increasing segmental vibration. The interstitial volume is supposed to be inaccessible for diffusion, as the

energy for redistribution of this volume is very high [5]. The difference between the specific volume of the equilibrium liquid polymer and the sum of core and interstitial volume yields the free volume available for diffusion. It is assumed that displacement within this free volume requires no energy. V_{FH2} is then defined according to Eqns. 5-5 and 5-6:

$$\hat{V}_{FH2} = \hat{V}_2^0(T_{g2})[f_{H2}^G + \int_{T_{g2}}^{T}(\alpha_2 - \alpha_{c2})dT], \; T \geq T_{g2} \qquad [5\text{-}5]$$

$$\hat{V}_{FH2} = \hat{V}_2^0(T_{g2})[f_{H2}^G - \int_{T}^{T_{g2}}(\alpha_2 - \alpha_{c2})dT], \; T_{gm} < T < T_{g2} \qquad [5\text{-}6]$$

It should be kept in mind that these equations are valid for a *rubbery* polymer-solute system. On addition of a solute in a polymer matrix, the glass transition temperature of the mixture (T_{gm}) is usually lowered (plasticization). The extent of the T_g depression can be estimated based on the Fox [18] or Gordon-Taylor equation [19]. Since the latter is based on volume additivity as opposed to weight additivity, the Gordon-Taylor equation (Eqn. 5-7) seems the most appropriate equation in light of the free volume theory.

$$T_{gm} = \frac{\omega_1 T_{g1} + K\omega_2 T_{g2}}{\omega_1 + K\omega_2}, \; K = \frac{\rho_1 \Delta\alpha_2}{\rho_2 \Delta\alpha_1} \approx \frac{\rho_1 T_{g2}}{\rho_2 T_{g2}} \qquad [5\text{-}7]$$

where $\Delta\alpha_i$: difference in specific thermal expansion
                 coefficient in the rubbery and glassy state of
                 component i (i.e. α_i-α_{ig})   [K^{-1}]
       α_{ig} : specific thermal expansion coefficient of
                 component i in the glassy state   [K^{-1}]
       ρ_i : density of component i at T_{gi} [kg m^{-3}]

The approximation for K in Eqn. 5-7 assumes the Simha-Boyer relationship is valid, i.e. $(\alpha_i-\alpha_{gi}) \cdot T_{gi}$ is constant [20]. This is in fact true for a wide range of polymers and low molecular weight compounds, and can be used in good approximation. However, when polymer chains contain groups which cause considerable side chain motion, e.g. in the case of poly(*n*-alkyl methacrylate)s, the thermal expansion coefficient below T_g (α_{2g}) is

still relatively high. At lower temperatures, a second transition occurs below which the side chains lose all mobility, resulting in a thermal expansion coefficient in the normal range of α_{2g}. The glass transition temperatures for these polymers are therefore not as sharp as for many other polymers [21].

The thermal expansion coefficients of the polymer are crucial parameters in modeling and predicting the increase in diffusion around T_g, as this determines the amount of free volume available. α_2 can be assumed to have a constant value above T_{g2}, and α_{c2} is supposed to be zero over the same temperature interval, thus simplifying Eqn. 5-5, and allowing an expression using the free volume parameters (Eqn. 5-8). These assumptions imply that α_2 can be determined directly from volume-temperature measurements above T_{g2}. Below T_{g2}, a constant value for both α_{c2} and α_2 is often assumed, although any experimentally determined temperature dependency of α_2 should be taken into account where possible. α_{c2} cannot be measured directly, but is calculated based on the assumption that it remains constant down to 0 K [5].

$$\hat{V}_{FH2} = \hat{V}_2^0(T_{g2})[f_{H2}^G + \alpha_2(T - T_{g2})] = K_{12}(K_{22} + T - T_{g2}), \; T \geq T_{g2} \quad \text{[5-8]}$$

Although the FVT has been successfully applied in rubbery systems for quite a few polymer-solute systems, extension into the glassy region, i.e. below T_{gm}, has proven more difficult. In principle, the free volume below T_{gm} can be defined by adding an extra term to Eqn. 5-6 [6] (Eqn. 5-9):

$$\hat{V}_{FH2} = \hat{V}_2^0(T_{g2})[f_{H2}^G - \int_{T_{gm}}^{T_{g2}}(\alpha_2 - \alpha_{c2})dT - \int_{T}^{T_{gm}}(\alpha_{2g} - \alpha_{c2g})dT], \; T < T_{gm} \quad \text{[5-9]}$$

where α_{2g} : specific thermal expansion coefficient of the
   polymer in the glassy state   [K^{-1}]

   α_{c2g} : specific thermal expansion coefficient of the
   core volume in the glassy state   [K^{-1}]

The expansion coefficient for the glassy state (α_{2g}) can be measured directly, although it should be kept in mind that measurements on an experimental time-scale involve the *non-*

equilibrium polymer liquid. Free volume below the glass transition temperature is time-dependent due to relaxation processes being much slower than experimentally observable. The thermal expansion coefficient of the core volume (α_{c2g}) requires an assumption, since it cannot be measured directly. Vrentas and Vrentas proposed that the ratios of the thermal expansion coefficients for total specific volume and for the core volume are expected to be equal (Eqn. 5-10) [6]:

$$\frac{\alpha_{c2g}}{\alpha_{2g}} = \frac{\alpha_{c2}}{\alpha_2}$$ [5-10]

In contrast, Wang *et al.* [17] adopt the view that the polymer in the glassy state is basically a frozen state, leading to the assumption that $\alpha_{2g} = \alpha_{c2g}$ and, consequently that the hole free volume, V_{FH2}, does not change with temperature below T_{gm}. They state that Eqn. 5-10 leads to an underestimation of the diffusion coefficient, and that their assumption corresponds better to experimental results. In the present work, the latter assumption is therefore followed. However, it is probable that below T_g, the free volume will actually decrease slightly, although this is a time-dependent process, depending on the rate of relaxation.

5.2.2 Effect of solute size

5.2.2.1 Apparent activation energy for diffusion

The effect of solute size on diffusion through a polymer matrix has mostly been investigated in rubbery polymer systems by measuring mutual diffusion coefficients in the limit of zero solute concentration (i.e. the self-diffusion coefficient). In this limit, substitution of Eqn. 5-8 into Eqn. 5-1 yields Eqn. 5-11:

$$ln\, D_1 = ln\, D_0 - \frac{E^*}{RT} - \frac{\gamma_2 \hat{V}_2^* \xi}{K_{12}(K_{22} + T - T_{g2})}$$ [5-11]

For sufficiently low temperatures near T_g, the energy term can be neglected, since diffusion is volume driven at these temperatures, although any knowledge of the energy

term could be taken into account. Eqn. 5-11 contains both a pure solute property (D_0), pure polymer properties ($\gamma_2 V_2^*/K_{12}$, K_{22} and T_{g2}) and a parameter specific to the mixture (ξ). The pure solute property, D_0, bears no direct correlation with the size of the solute, as it also depends on its chemical nature. Based on Eqn. 5-11, an apparent activation energy for diffusion is defined (Eqns. 5-12 and 5-13) as [22]:

$$E_D = RT^2 \left(\frac{\partial \ln D_1}{\partial T} \right)_P = E^* + \frac{RT^2}{(K_{22} + T - T_{g2})^2} \left(\frac{\gamma_2 \hat{V}_2^* \xi}{K_{12}} \right) \qquad [5\text{-}12]$$

$$\xi = \frac{\widetilde{V}_1^*}{\widetilde{V}_2^*} \qquad [5\text{-}13]$$

where $\tilde{V}_i^*$: critical molar volume of the jumping unit of i $\qquad$ [m^3 mol^{-1}]

Again, at low temperatures, the activation energy can be neglected. Now, the most important parameter to determine the effect of solute size, ξ, is the only solute related property in Eqn. 5-12, illustrating that the increase in diffusion coefficient with temperature is affected by the size of the penetrant [23]. A larger solute, or more specifically a larger solute jumping unit, results in a larger change in diffusion since ξ increases. In addition, for an increasingly smaller solute, the energy term E^* becomes more and more important. Eqn. 5-12 also demonstrates that the increase in diffusion coefficient becomes stronger as T_g is approached. The equation implies that the apparent activation energy for diffusion depends on T_g of the polymer itself. In the limit of $T = T_{g2}$, Eqn. 5-12 is identical to the apparent activation energy (E_g) based on the dynamic fragility concept [24] reported by Qin and McKenna [25] for pure polymers (i.e. neglecting E^* and ξ). The dynamic fragility (or steepness index [26]) characterizes the rapidity with which a liquid's dynamic properties (e.g. viscosity and relaxation time) change as T_g is approached, and can be expressed in terms of WLF-parameters, and consequently in terms of the polymer free volume parameters. Indeed, Qin and McKenna have found that E_g increases with T_g for a large range of glass forming polymers, although there is a considerable scatter in the data points.

5.2.2.2 Size, shape and flexibility of solute

If a solute-polymer system obeys the FVT, a plot of $[K_{22}+T-T_{g2}]^{-1}$ versus $ln\ D$ yields a straight line with slope $\gamma_2 V_2^* \xi / K_{12}$ and intercept $ln\ D_{01}$ (Eqn. 5-11). The polymer properties γ_2, V_2^* and K_{12} are known for many common polymers, so that a value for ξ for a polymer/solute combination can thus be found. For solutes jumping as a whole, it has been shown that the molar volume of the jumping unit ($\tilde{V}_1^*$ in Eqn. 5-13) corresponds to the molar volume at 0 K, and can be estimated by methods discussed by Haward [27]. In that case, if diffusion experiments of several of such solutes in the same polymer are performed, plotting $\tilde{V}_1^*$ versus ξ yields a linear relationship for solutes jumping as a whole, with a slope corresponding to the inverse of the critical molar volume of the polymer jumping unit. Any deviation from linearity indicates that it is not just the size of the solute that influences diffusion, but also the shape of the solute, or that segmentwise diffusion may take place. If the polymer parameters are not known, the term $\gamma_2 V_2^* \xi / K_{12}$ can simply be plotted instead of ξ, similarly obtaining a straight line through the origin.

Several studies have focused on the effect of solute size in various polymers, e.g. poly(styrene) (PS) [22,28,29,30], poly(methyl acrylate) (PMA) [14,28], poly(isobutylene) (PiB) [14], poly(vinyl acetate) (PVAc) [15,28], poly(methyl methacrylate) (PMMA) [], and poly(ethyl methacrylate) (PEMA) [28]. An example of such a plot is displayed in Figure 5.2 for PS [29,30]. A clear linear relationship exists for a large number of solutes (open symbols) that are expected to jump as single units. For a series of linear alkanes (▲), a clear leveling off around $\xi = 0.4$ is observed, indicating that the jumping unit for higher alkanes is similar. In addition to the alkanes, two other (large) compounds (◆) clearly deviate from the linear trend. These compounds contain two or three aromatic rings, connected by azo-bonds. Although it is reasonable to assume that higher alkanes move in a flexible segmentwise manner, this seems unlikely for the large rigid structures of the other two compounds. Here, it is more likely that the shape of the solutes influences the rate of diffusion. When comparing a spherical compound to a long cylindrical compound of the same molar volume, it is probable that the latter is able to diffuse more easily through a polymer matrix along its elongated axis than a rigid sphere

[7,11]. Both flexibility of a solute and its shape are therefore important parameters, and influence the parameter ξ. In an effort to predict ξ, Vrentas *et al.* have proposed an expression which takes into account the geometry of a solute (Eqn. 5-14) [11].
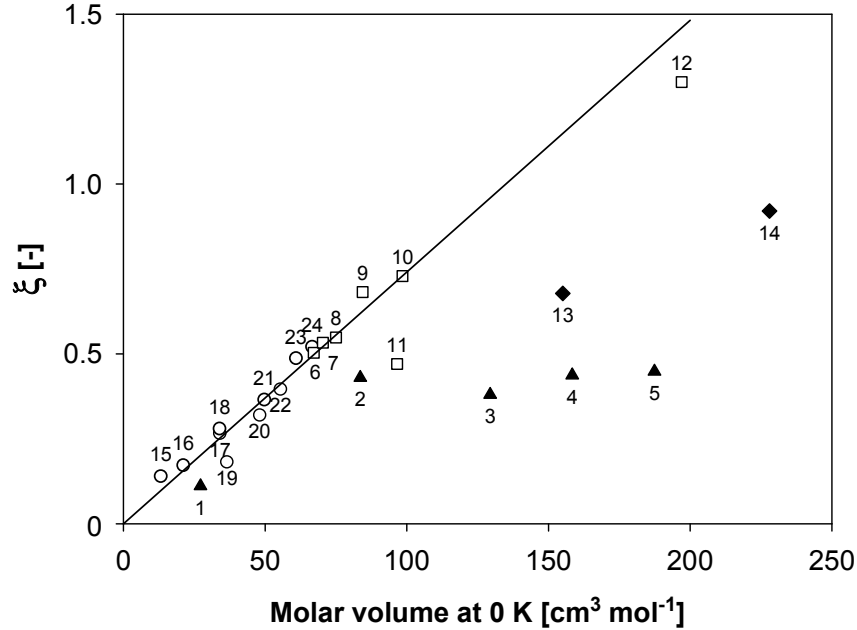
Figure 5.2: Example of ξ-parameter dependence on critical molar volume of diffusing solutes in polystyrene based on data presented by references [29,30]. (▲) Alkanes: (1) Methane, (2) *n*-Pentane, (3) *n*-Octane, (4) *n*-Decane, (5) *n*-Dodecane. (□) Aromatics: (6) Pyridine, (7) Benzene, (8) Fluorobenzene, (9) Toluene, (10) Ethyl benzene, (11) *p*-nitroaniline, (12) 1,3,5-Triisopropylbenzene. (◆) Azo-compounds: (13) *p*-Amino azobenzene, (14) 2-methyl-4-[[4-(phenylazo)penhyl]azo] phenol. (○) Other: (15) Hydrogen, (16) Nitrogen, (17) Methanol, (18) Carbon dioxide, (19) Ethylene, (20) Ethanol, (21) Methylene chloride, (22) Ethyl bromide, (23) Chloroform, (24) *n*-Propyl chloride.

$$\xi = \frac{\xi_L}{1 + \xi_L(1 - \frac{A}{B})}, \quad \xi_L = \frac{\widetilde{V}_1^*}{\widetilde{V}_2^*} \qquad [5\text{-}14]$$

where ξ_L : ratio of the critical molar volumes of the solute and polymer (value of ξ for a rigid spherical solute)   [-]

B/A : aspect ratio of the square cuboid by which it is supposed to be represented (Figure 5.3, left)   [-]
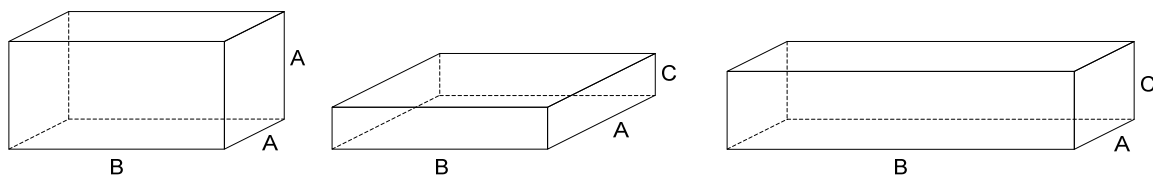
Figure 5.3: Representation of a molecule to determine the aspect ratio as given in Eqn. 5-14 (left), and a more general representation of a disc-like (middle) and rod-like (right) molecule.

Eqn. 5-14 is based on the assumption that asymmetrically shaped solutes enhance the accumulation of average free volume, whereas symmetric solutes do not affect the free volume distribution. A detailed derivation of Eqn. 5-14 is given in reference [11]. The authors assumed that the solutes move as rigid molecules, stating they found no evidence of segmentwise motion for aspect ratios as high as 3. In our opinion, completely neglecting segmentwise diffusion is unrealistic for several solutes, such as higher alkanes. Furthermore, the assumption that asymmetric solutes accumulate more hole free volume is not substantiated. Also, this theory only takes into account prolate (rod-shaped) solutes, whereas oblate (disc-shaped) molecules could affect diffusion in a different way, as noted by Mauritz *et al.* [7,8] for diffusion of extremely large molecules (i.e. $\tilde{V}_1^* >> \tilde{V}_2^*$). In a slightly different free volume approach, they take into account the effect of solute shape by considering the maximum cross-sectional areas (A_i) perpendicular to the three principal orthogonal axes of motion with length L_i, and the statistical occurrence of movement in these directions. They also allow movement along a fraction of length L_i, thus incorporating the allowance for segmentwise diffusion (although flexibility is thus not necessarily incorporated). Similarly to Mauritz *et al.*, Von Meerwal *et al.* [9] studied diffusion of large plasticizer molecules in PVC and found a rough correlation between the frontal diameter of the plasticizers (i.e. corresponding to A_i) which was improved when ignoring flexible side groups. Berens and Hopfenberg [31] investigated the sorption of organic vapors in glassy polymers and found that even for relatively small molecules, like carbon dioxide, shape effects result in a higher diffusion rate than expected based on the frontal diameter assuming a spherical molecule. They find that the effective frontal diameter is somewhere between the two smallest dimensions (i.e. in between A and C in Figure 5.3). It would therefore seem that if an expression for ξ could be obtained based on these assumptions, this would be a considerable improvement to Eqn. 5-14, while

98

remaining in the spirit of the Vrentas and Duda free volume theory. However, as is obvious from the previous, many researchers have focused their efforts on finding a predictive equation for ξ without finding a definite correlation.

Opposing theories exist on whether there is a ceiling value for the diffusion coefficient (i.e. where the volume of the solute and polymer jumping unit coincide) [32], or whether the solute 'creates its own space', thus further increasing the rate of diffusion [29]. The main evidence posed by the proponents of the fact that a ceiling value of 1 does not exist, is the value of 1.3 found for ξ of 1,3,5-triisopropylbezene (TIPB) in polystyrene (Figure 5.3). However, Zielinski *et al.* [10] have reevaluated this value and presented new experimental findings claiming a value of around 1, but they cannot say within experimental certainty whether the value is higher or lower than unity. Another argument used for the non-existence of the ceiling value is that leveling off occurs at lower values than 1, e.g. around 0.42 for the alkane series in polystyrene (Figure 5.3). However, it is our opinion that a ceiling value does not preclude the existence of leveling off at lower values due to solute geometry or flexibility. Supporters of a ceiling value [e.g. 33] state that it is probably more appropriate to speak of a decoupling parameter equal to (1-ξ), thus implicitly supposing a ceiling value of 1. It is conceivable, that as the size of the solute jumping unit approaches that of the polymer, the movement of the solute is in fact strongly coupled to polymer dynamics, thus causing the deviation from the linear relationship of a spherical molecule jumping as a singe unit to occur earlier, even if it does jump as a single unit. In addition, it is imaginable that the effective polymer jumping unit might increase due to interaction of the solute with the polymer as ξ approaches 1, thus increasing diffusion of the solute.

Finally, it is stressed that leveling off of ξ at any value does not imply that the diffusion coefficient becomes constant. Diffusion is then simply governed by the pre-exponential term (D_0). For instance, Bueche [34] has shown that D_1 should be inversely proportional to molecular weight assuming there are no entanglements. This does indeed seem to be the case for long-chain alkanes (ranging up to C_{36}) [35]. However, for short alkanes (C_8-C_{12}) this is not the case, indicating that segmentwise movement of shorter alkane chains involves a more complex mechanism than of longer alkane chains [30].

5.2.3 *Modeling of diffusion by molecular dynamics simulations*

The free volume theory is based on macroscopically observable properties. An alternative to understand the influence of size on diffusion is the use of simulations to study the effect of solute size on the diffusion coefficient. The ever increasing computational power of computers enables more and more processes to be studied *in silico*. Where diffusion of small molecules in polymeric matrices has already been studied using molecular dynamics (MD) simulations [e.g. 36- 40], the study of larger molecules is hardly found, specifically where glassy polymers are concerned. Zhao *et al.* [41,42] are one of the few authors who have studied drug diffusion in a dense polymer matrix (i.e. a copolymer of ethylene glycol [EG] and lactic acid [LA]) using MD simulations. However, no experimental verification of these results is presented, and their reported diffusion coefficients in the order of 10^{-11}-10^{-12} m^2 s^{-1} for diffusion of a solute as large as nifedipine in polylactide (PLA), which is in a glassy state at the modeled temperature of 37ºC, seem rather high. Indeed, modeling of diffusion coefficients as low as 10^{-18} m^2 s^{-1}, which are typical values for self-diffusion coefficients of drugs in glassy polymers, is hardly possible with the current state of computers. Nevertheless, they introduce an interesting concept in this modeling effort, when comparing diffusion of benzene, aspirin and nifedipine (78, 180 and 346 g/mol, respectively) in PLA-PEG copolymers. They state that diffusion of these solutes proceeds by two competitive mechanisms, i.e. diffusion governed by available free volume (i.e. 'hopping diffusion' mechanism found for small penetrants) and diffusion governed by thermal motion of the polymer chains, termed 'wriggling'. As the size of the penetrant increases, the latter becomes more and more important, finally dominating the diffusion process. Diffusion then no longer occurs by jumping from one cavity to the next, but occurs due to the movement of the cavity itself (i.e. wriggling). This process, simulated on a molecular scale, is actually identical to the coupling of solute diffusion to polymer dynamics referred to in the previous section. This basically implies that for large solutes, the diffusion coefficient will display more of an Arrhenius-type trend with increasing temperature, as opposed to a relationship predicted by the free volume theory.

Due to the earlier mentioned fact that the timescale of diffusion in glassy polymers can still not be realistically modeled using MD simulations with the current computational

resources, this is not further pursued in this research. However, we do believe this is certainly a viable route in the near future.

5.3 Materials and methods

5.3.1 Materials

Diethylene glycol dimethyl ether (DEGDME, ≥99.5%), triethylene glycol dimethyl ether (TEGDME, ≥99%), and tetraethylene glycol dimethyl ether (TetraEGDME, 99%) were obtained from Sigma-Aldrich, Fluka, and Aldrich, respectively. Poly(ethyl methacrylate) (PEMA) and poly(iso butyl methacrylate) (PiBMA) were purchased from Scientific Polymer Products. Dichloromethane (DCM, ≥99.5%) was received from Merck. Ibuprofen was obtained from Genfarma. All chemicals were used as received. Demineralized water was used for all experiments.

5.3.2 Methods

5.3.2.1 EGDME sorption experiments

Polymer discs were prepared by compression molding of approximately 500 mg of PEMA or PiBMA at 150ºC in a custom built press. The resulting polymer discs (25 mm in diameter and approximately 1 mm in thickness) were placed in an oven overnight at a temperature of 75ºC without pressure applied in order to minimize the effects of thermal history. A slight deformation of the samples occurred ('saddle-like'), indicating relaxation of internal stress as a consequence of cooling after compression. It was assumed that this did not influence the surface area available for diffusion. The polymer discs were rapidly transferred from the oven into a beaker with screw top containing EGDME/water mixtures (5 mL EGDME, 45 mL demineralized water) at a temperature of 70ºC in a water bath. At fixed time intervals, the polymer disc was removed from the solution, dried with a tissue (thus removing liquid adsorbed to the surface), and weighed on a balance (Sartorius BP 211D, accurate to 0.01 mg). The sample was placed back in the solution within one minute of removal. The exact time of removal and return were recorded and taken into account in the time present in solution (which is especially important for sampling near t = 0).

5.3.2.2 Ibuprofen release experiments

Ibuprofen was incorporated into the PEMA and PiBMA matrix by a solvent casting process. 1 g of polymer and 0.111 g of ibuprofen (i.e. 10 wt%) were dissolved in 4 mL of DCM, after which the solution was poured into a Petri dish (∅: 76 mm) and covered with perforated Parafilm® for 4 hours to allow slow evaporation of the solvent. The films were then removed from the Petri dish and placed in a vacuum oven for 5 days. 5 pieces of 24 mm were then punched from the resulting polymer films, and placed on top of each other in a custom built press. After 2 hours in the oven at a temperature of 150ºC, pressure was applied for 2 minutes, after which the press was cooled to room temperature, resulting in polymer discs with a diameter of 25 mm, and a thickness of approximately 0.9-1 mm.

20 hours after compression molding, these discs were placed in 50 mL of phosphate buffered saline (PBS, pH: 7.4) at various fixed temperatures (37, 55, 70 and 80ºC). Release of ibuprofen from the polymer matrices was monitored in time by taking 500 μL samples, which were analyzed by HPLC (C18 Discovery® HS 150 x 4.6 mm - 3μm, 50/50 % v/v acetonitrile/water (with 0.1 % v/v TFA), flow: 1.2 mL min^{-1}, UV detection at 223 nm). After each sample, 500 mL of fresh PBS was added to maintain a constant system volume (concentrations were corrected accordingly).

5.4 Results and discussion

5.4.1 FVT modeling results for EGDME's

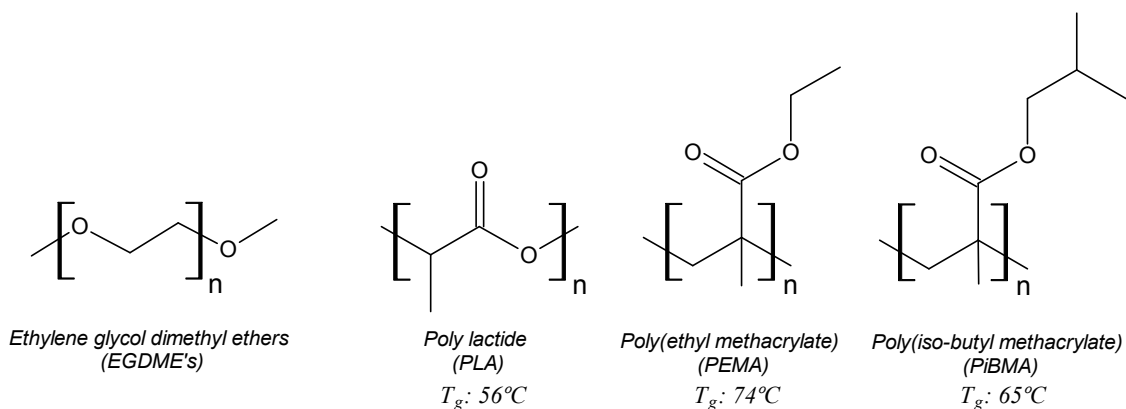|			
Ethylene glycol dimethyl ethers (EGDME's)	Poly lactide (PLA) T_g: 56ºC	Poly(ethyl methacrylate) (PEMA) T_g: 74ºC	Poly(iso-butyl methacrylate) (PiBMA) T_g: 65ºC

Figure 5.4: Chemical structure of solutes and polymers. For EGDME's, n equals 2, 3 and 4 for di-, tri-, and tetraethylene glycol dimethyl ether, respectively.

The effect of size was investigated by modeling diffusion of a homologous series of ethylene glycol dimethyl ethers (Figure 5.4) in three different polymer matrices, i.e. PEMA, PiBMA, and PLA. These polymers all exhibit a T_g around 60-70°C, but based on their chemical structure (Figure 5.4), a different behavior with respect to diffusion is expected. PLA has the most compact structure with an ester group within the main polymer backbone, containing only a small methyl side group. In contrast, both the acrylates contain a bulky side group, thus supposedly causing a less compact packing of the polymer chains resulting in slightly more free volume. Based on these structures, diffusion of solutes inside PiBMA is expected to be highest, followed by PEMA and PLA. Figure 5.5 displays modeling results obtained based on Eqn. 5-1, illustrating the difference in self-diffusion coefficient of the EGDME's in the three different polymers. In principle, mutual diffusion coefficients can be calculated based on these self-diffusion coefficients, but since the main interest in this research is on the diffusion coefficient in the limit of zero concentration of the solute (see Chapters 3 and 4), the results presented in this section concern self-diffusion coefficients.
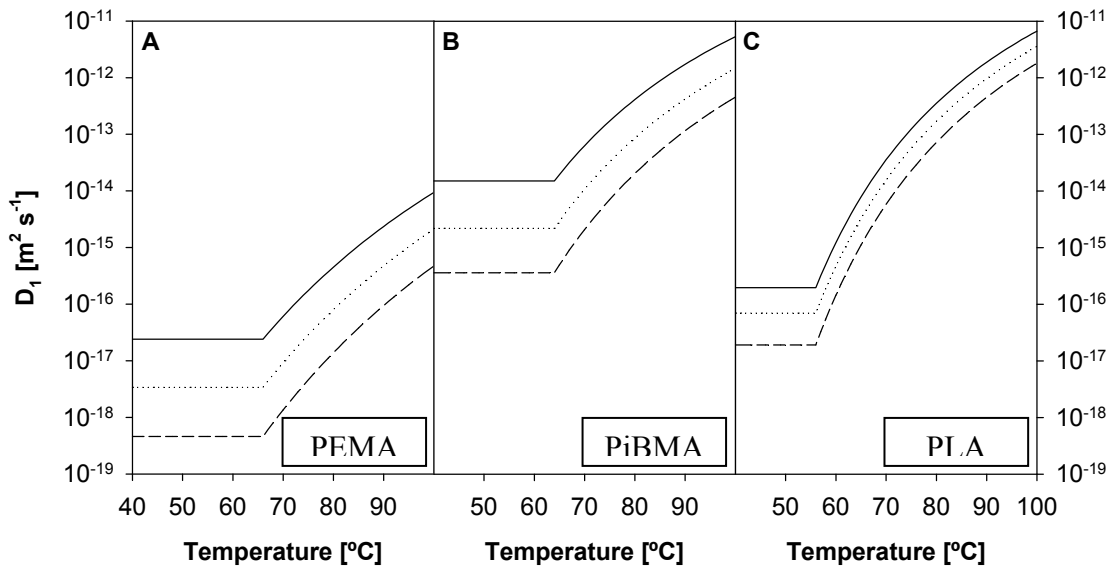
Figure 5.5: Modeled self-diffusion coefficients of EGDME's in **A** PEMA, **B** PiBMA, and **C** PLA. ———: DEGDME, ⋯⋯⋯: TEGDME, - - - -: TetraEGDME, in the limit of $\omega_1 = 0$, using Eqn. 5-14 to take into account the shape effect of the solute: $\xi_{DEG-PEMA}$: 0.610, $\xi_{TEG-PEMA}$: 0.657, $\xi_{TetraEG-PEMA}$: 0.709, $\xi_{DEG-PiBMA}$: 0.512, $\xi_{TEG-PiBMA}$: 0.568, $\xi_{TetraEG-PiBMA}$: 0.623, $\xi_{DEG-PLA}$: 0.849, $\xi_{TEG-PLA}$: 0.856, $\xi_{TetraEG-PLA}$: 0.892.

The input parameters used to obtain Figure 5.5 are given in appendix 5.6.1. Since the assumption of Wang *et al.* is used that α_{2g} equals α_{c2g}, the diffusion coefficient is constant in the limit of $\omega_1 = 0$ below the glass transition temperature of the polymer. The predicted increase in diffusion coefficient is modeled as a sharp point, where in reality this is much smoother. In fact, the transition for the acrylates is rather broad in comparison to many other polymers due to the bulky side group, as has been explained earlier. Nevertheless, these results give an indication of the magnitude of increase in diffusion coefficient around T_g.

First of all, the large differences in diffusion coefficients in the glassy state should be addressed. In the limit of zero solvent concentration, Eqn. 5-1 reduces to Eqn. 5-15:

$$D_1 = D_0 \, exp(-2.303 \cdot \xi \cdot C_{12}^g) \tag{5-15}$$

D_0 is a pure solute property, and is therefore the same in all polymers. Naturally, ξ is important, since this is the parameter used to determine the size effect. In addition, the choice of the WLF parameter C_{12}^g is of crucial importance for the absolute value of the diffusion coefficient at T_{g2}. As both parameters appear in the exponent, small differences in both these parameters can have quite a large effect on the calculated diffusion coefficient at T_{g2}. The effect of varying C_{12}^g is illustrated in Figure 5.6A for DEGDME diffusion in the three different polymers, using the same ξ-values as in Figure 5.5, where the markers on the lines indicate the range of literature values given in 5.6.1 (Table 5.2). The absolute slope of the graphs equals the ξ-value, thus resulting in the largest uncertainty for PLA by almost two orders of magnitude. Conversely, the slope in Figure 5.6B (ξ vs. D_1) is determined by C_{12}^g, and since C_{12}^g is about a factor 10 higher than ξ, the influence of the latter on the diffusion coefficient is higher, where the uncertainty lies in both the solute jumping unit (M_{1j}), as described in section 5.2.2.2, and the polymer jumping unit (M_{2j}). If no shape-effect of the diffusing solute is taken into account (i.e. a spherical solute is assumed), the diffusion coefficient decreases by many orders of magnitude. Clearly, this is a worst-case scenario in terms of rate of diffusion, and is not a realistic value. On the lower end, M_{1j} is limited by assuming a single ethylene glycol segment as jumping unit, which, again, would not seem realistic. This range simply

serves to illustrate the importance of taking shape and flexibility effects into account, which easily affects D_1 by several orders of magnitude.
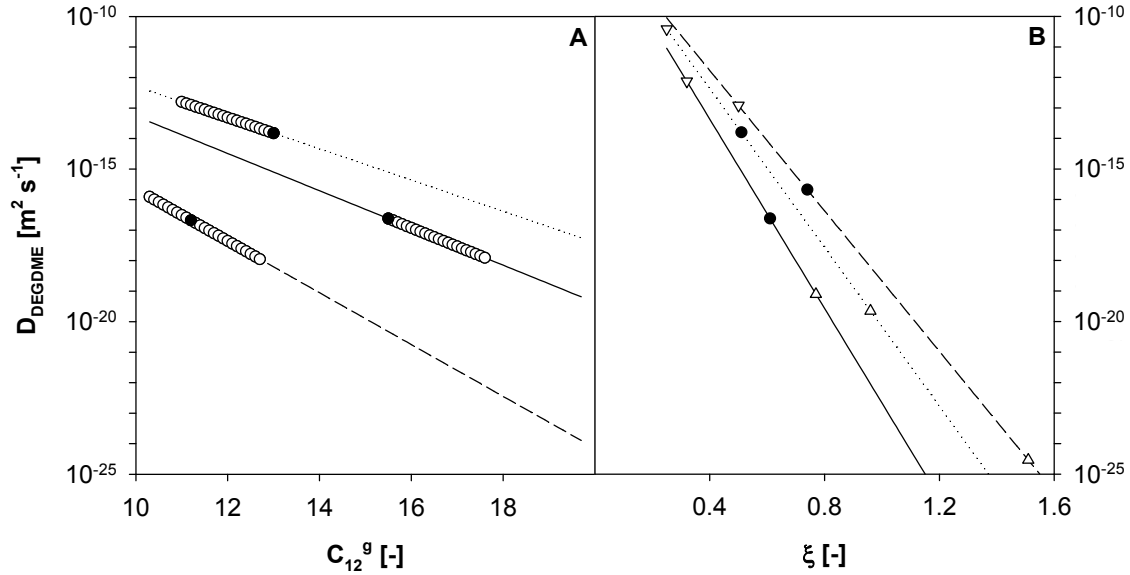

Figure 5.6: Sensitivity analysis of parameters C_{12}^g and ξ for the calculated value of the self-diffusion coefficient of DEGDME at T_{g2}. **A** Effect of C_{12}^g on D_1 ($\omega_1=0$, T_{g2}) for PEMA (———), PiBMA (·········), and PLA (- - - -), where ○ indicates the range based on literature values. **B** Effect of ξ on D_1 ($\omega_1=0$, T_{g2}) for PEMA (———), PiBMA (·········), and PLA (- - - -), where ▽: spherical solute, ●: modeled value, △: single spherical ethylene glycol jumping unit.

For the polymer jumping unit of PEMA, a value for M_{2j} has been determined previously from a plot such as illustrated for PS in Figure 5.2, equaling 140 g mol^{-1} (i.e. $1.23 \cdot M_{monomer}$). However, for the other two polymers, no values have been reported in literature. Since PiBMA only differs from PEMA by two additional methylene groups in the side chain, a similar value of 1.23 times the size of its monomer unit has been assumed in Figure 5.5. However, the different chemical structure of PLA (i.e. a linear polyester, without a bulky side group), does not necessarily allow such a direct comparison with PEMA. A more appropriate value may therefore be based on the T_g of the polymer, as proposed by Zielinski and Duda [43], and further investigated by Hong [44]. For PLA, this would result in a jumping unit of 118 g mol^{-1}, or $1.63 \cdot M_{monomer}$. This jumping unit is quite a bit smaller than for the two acrylates, leading to a larger value of ξ_L. Even the jumping unit of the smallest of the three solutes is larger than that of PLA

(i.e. $\xi_L > 1$), which might lead to the conclusion that an increase in solute size results in a fast decrease of the diffusion coefficient. However, quite the opposite is observed in Figure 5.5, where the decrease in diffusion coefficient with increasing solute size is larger for the acrylates. This is due to the assumed validity of Eqn. 5-14, as demonstrated in Figure 5.7. At higher ratios of the jumping units, ξ starts to level off, resulting in a relatively small increase of ξ (and thus small decrease of D_1) with increasing solute size. It would be interesting to see whether this trend can also be observed experimentally, or whether Eqn. 5-14 can no longer be assumed to be valid for these large solutes.
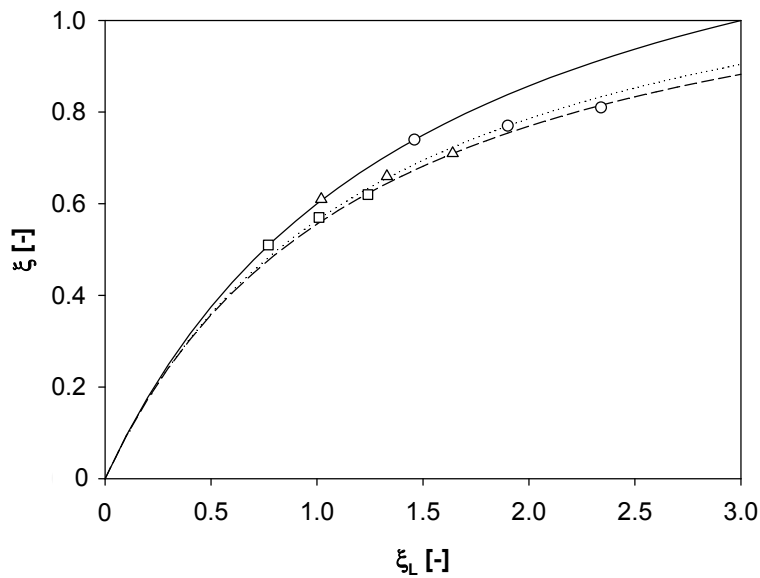
Figure 5.7: Influence of ratio of jumping units ξ_L (= $\tilde{V}_1/\tilde{V}_2$) on ξ.. Lines indicate plots according to Eqn. 5-14 (——: DEGDME, ·········: TEGDME, - - - -: TetraEGDME) for computed aspect ratios of 2.96, 4.35 and 5.00, respectively. $\triangle$: PEMA, $\square$: PiBMA, $\bigcirc$: PLA

Before showing the modeling results, it was mentioned that the rate of diffusion was expected to decrease in the order PiBMA > PEMA > PLA, but the modeling results in Figure 5.5 indicate otherwise. As has been mentioned before, the diffusion coefficient at T_g is very sensitive to the choice of C_{12}^g, and since the parameters of PLA are the most uncertain and C_{12}^g is quite low, it is imaginable that the diffusion coefficient is overestimated here. Figure 5.5 does illustrate that for PLA, the increase in diffusion coefficient above T_g is expected to be larger than in the two acrylate polymers, which

would indeed fit with the compacter structure of PLA. Experiments are required for any definite conclusions to be drawn.

Finally, it should be noted that, keeping in mind controlled release, a quadratic relationship exists between the diffusion coefficient and release from a polymeric implant. This means that an uncertainty of two orders of magnitude in the diffusion coefficient results in an error in the release rate of one order of magnitude. The error in the diffusion coefficient is a summation of the errors described above, and amounts to at least several orders of magnitude without any prior experiments. Clearly, experimental verification of this model is required, in order to say anything about the diffusion of these large molecules inside polymer matrices. The next section deals with sorption measurements of EGDME's in these polymers to determine these diffusion coefficients.

5.4.2 EGDME diffusion coefficient by sorption measurements

Often, diffusion coefficients are determined by vapor sorption measurements, in which the weight increase of a polymer sample, hanging from a quartz spring and exposed to solvent at a fixed vapor pressure, is measured in time [45]. Since the EGDMEs have relatively high boiling points and low flash points, thus imposing quite some safety restrictions on this kind of measurement, a different approach has been chosen. Polymer discs, prepared by compression molding, are placed in mixtures of EGDMEs and water, which are completely miscible at all concentrations. The EGDMEs also have a high affinity with the polymer matrix, evidenced by complete dissolution of the polymer in the pure compounds. It is therefore assumed no partitioning occurs at the polymer-water interface. Furthermore, it was assumed that since methacrylates are hydrophobic polymers, water sorption would not play a significant role during the sorption process. However, the sorption results in Figure 5.8 prove otherwise. If normal Fickian diffusion occurs (typical for diffusion in rubbery polymers), the initial sorption period is characterized by a linear plot of the fractional uptake versus the square root of time (Eqn. 5-16):

$$\frac{M_t}{M_{inf}} = 4 \cdot \sqrt{\left(\frac{Dt}{\pi \cdot L^2}\right)} \qquad\qquad [5\text{-}16]$$

where M_t : amount released at time t   [kg]

         M_{inf} : amount released after infinite time (i.e. initial

                drug content)   [kg]

         D : mutual diffusion coefficient   [m^2 s^{-1}]

         L : sample thickness   [m]
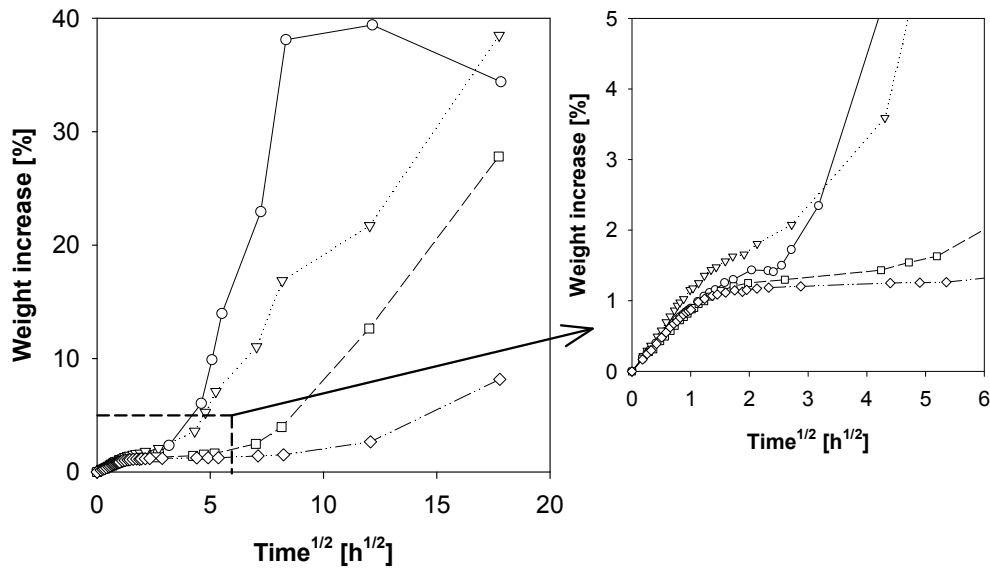
Figure 5.8: Experimental sorption graph for a 10 wt% solution of DEGDME (○), TEGDME (▽), and TetraEGDME (□) in water, as well as pure water (◇) in a PEMA matrix at T=70ºC.

For a given thickness of the polymer film, the slope of this plot yields the diffusion coefficient. However, the initial sorption period is dominated by water diffusion, thus impeding a direct determination of the diffusion coefficient of the EGDME's. In fact, the diffusion coefficient of $9.2 \cdot 10^{-11}$ m^2 s^{-1} determined in this way (assuming M_{inf} = 1.26 %, i.e. the value obtained after 24 hours, where the fractional uptake seems to have reached its plateau value), is in good agreement with water diffusion reported previously (1.1 and $35 \cdot 10^{-11}$ m^2 s^{-1} at 25 and 90ºC, respectively [46]), further strengthening the fact that diffusion in the initial period is indeed solely attributed to water. In time, all polymer matrices become opaque, indicating association (clustering) of water molecules inside the

polymer [47], thus possibly influencing both the available free volume and hydrophobicity of the matrix. Following the initial period of approximately 4-5 hours dominated by water, significant sorption of the EGDME's starts to take place. As there is a considerable time lag before EGDME diffusion occurs, it seems safe to say that EGDME sorption is not described by Fickian diffusion, but that anomalous diffusion occurs. Indeed, anomalous diffusion has been reported in the vicinity of T_g [32], which can be attributed to the comparable time-scale of diffusion and polymer dynamics. However, the interference of water sorption impedes quantification of the EGDME diffusion coefficient.

It should be noted that the renewed weight increase in pure water after approximately 100 h seems somewhat unexpected. For PEMA, the equilibrium sorption has been reported to be in the order of a few percent based on vapor sorption experiments, even at temperatures well above T_g [46,48]. However, sorption behavior in solution or in the vapor phase is not necessarily identical, sometimes leading to different results [49]. In this case, since the polymer is close to or in the rubbery state, the relatively high absorption may be explained by experimental findings for 'soft methacrylates' (i.e. in the rubbery state) [50,51]. It is supposed that clustering of water droplets inside the polymer matrix occurs, while dissolving water-soluble impurities, such as ionic impurities, inhibitors, or benzoic acid (by-product of polymerization with benzoyl peroxide) in these droplets. This results in an osmotic pressure of these bound water droplets compared to the bulk solution, leading to increased swelling of the polymer matrix. This phenomenon would not occur in vapor sorption, but definitely affects sorption of polymer in a bulk fluid. Since the polymer is very close to its T_g, the matrix is only 'moderately rubbery' thus presumably causing the swelling effect to be relatively slow, and only occurring significantly after approximately 5 days.

In conclusion, the method described here does not lead to conclusive quantitative results regarding the diffusion coefficients. The EGDME compounds were chosen because of their compatibility with both polymer and water, but this seems to lead to more complications than elucidations. Qualitatively, the results in Figure 5.8 indeed indicate that the diffusion rate decreases with increasing penetrant size, but swelling of the polymer due to water sorption, as well as simultaneous diffusion of water during

EGDME sorption prohibit any quantification. For a proper consideration of self-diffusion of these compounds in polymer matrices, techniques such as pulsed-field gradient NMR [52] might be suitable. Alternatively, a set-up could be built in which sorption measurement could be measured in the vapor phase, thus eliminating the effect of liquid water. This is beyond the scope of this research, but could provide valuable insights into diffusion around T_g. However, it should be kept in mind that the aim of this research is to describe release of drug molecules from a polymer matrix, which always entails the presence of water inside the polymer, thus influencing the polymer matrix to a certain extent.

5.4.3 FVT modeling and experimental results for ibuprofen

Since the application of the FVT to EGDME sorption in liquid form has proven difficult, an attempt is made to describe the release of a model drug (ibuprofen) from a polymer matrix. Normally, the FVT is applied to diffusion of solvents and gases inside a polymer matrix. In principle, there is no restriction to application of the theory for diffusion of drug molecules. However, free volume parameters for these substances have generally not been determined, and determination in the same way as has been done for the EGDME's (appendix 5.6.1) is not possible since this requires the temperature dependence of viscosity and density (i.e. in the melt) that are not available in literature. However, dielectric relaxation measurements of ibuprofen near its T_g (~ -50ºC) have been reported [53], yielding the WLF-parameters for this ultraviscous melt. Using Eqns. 5-3 and 5-4, the free volume parameters K_{12}/γ_2 and K_{22} can be calculated for ibuprofen, although they should be used with caution, since the temperature range in which these parameters have been measured is well below the temperatures of interest for controlled release. Assuming these parameters are in fact valid, this leaves the pre-exponential as only unknown. In terms of size, ibuprofen falls in between that of TEGDME and TetraEGDME, and a similar D_0 may therefore be expected. However, ibuprofen is a much more spherical molecule compared to the EGDME's ($B/A_{ibuprofen}$ = 2.11), thus potentially affecting D_0. In addition, the difference in interaction parameter δ between ibuprofen and methacrylates is quite large (20.9 for ibuprofen compared to 18-18.5 for acrylates), thus causing E^* to exhibit an appreciable value (19.4 kJ/mol, according to a universal curve

relating $\delta_1 - \delta_2$ to E^* [54]). Although these values can be used for ibuprofen, an alternative is to follow a procedure as described in section 5.2.2.2, in which experimental values of the diffusion coefficient are plotted against $[K_{22} + T - T_g]^{-1}$, thus yielding a (lumped) pre-exponential factor and a value for ξ.
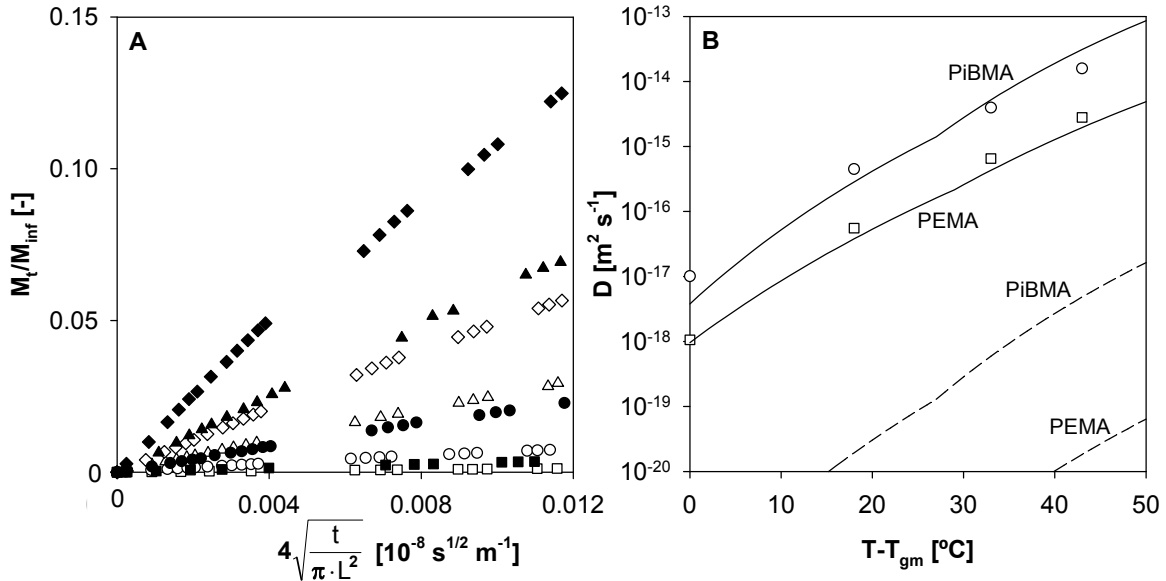

Figure 5.9: Release of ibuprofen from PEMA and PiBMA discs (diameter: 25 mm, thickness: ~ 1 mm, [ibuprofen]: 10% w/w). **A** Release at temperatures of 37 (squares), 55 (circles), 70 (triangles) and 80ºC (diamonds) for PEMA (open symbols) and PiBMA (closed symbols). **B** Mutual diffusion coefficients of ibuprofen in PEMA ($\square$) and PiBMA ($\bigcirc$), as well as mutual diffusion coefficients obtained from FVT, for purely predictive (----) and fitted values of the pre-exponential term and ξ to PEMA diffusion (——) at T = 55ºC.

Figure 5.9 demonstrates release of ibuprofen from the polymer matrix. The initial slopes of the graphs presented in Figure 5.9A equal $\sqrt{D}$, of which the squared values are presented in Figure 5.9B relative to T_g of the plasticized polymer (T_{gm}). As expected, an increasing deviation from linearity is observed as T_{gm} is approached. However, based on a purely predictive model (i.e. assuming a value of $D_0 = 10^{-8}$ m^2 s^{-1}, and $E^* = 19.4$ kJ/mol), the diffusion coefficient is estimated to be about 5 magnitudes lower than the experimental value (dashed lines)! Clearly, these supposed values are incorrect. Therefore, the fitting procedure is followed, in which the pre-exponential factor (i.e. a lumped factor containing both D_0 and E^*) and ξ are determined for PEMA (Figure 5.10),

111

and used as input for PiBMA. The plot in Figure 5.10A is indeed a straight line, indicating that the FVT (or at least a similar temperature dependence) is valid, yielding a pre-exponential factor of $3.4 \cdot 10^{-8}$ m^2 s^{-1} and a value of 0.68 for ξ. The latter is lower than the value obtained when calculated using Eqn. 5-14, which yields $\xi = 0.86$. It should be noted that in this calculation, the T_g of the mixture has been chosen as a reference point, when in fact the equation is meant to be applied to calculations involving the self-diffusion coefficient as the solute concentration approaches zero. Therefore, this result cannot be used as a definitive conclusion as to the validity of Eqn. 5-14, but it would seem that this equation overestimates ξ, thus leading to an underprediction of the diffusion coefficient by two orders of magnitude.
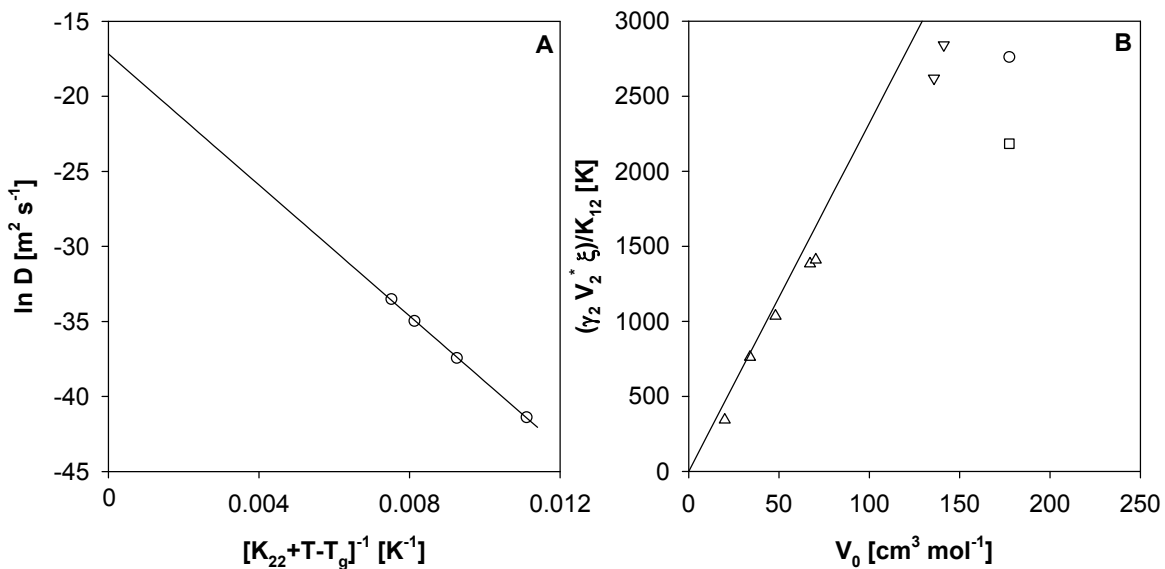
Figure 5.10: **A** Fit to experimental data of ibuprofen diffusion in PEMA. Slope and intercept equal γ_2 $V_2^* \xi / K_{12}$ and $\ln D_0$, respectively. **B** Comparison to diffusion of smaller compounds in PEMA [$\triangle$: ref 23, $\triangledown$: ref 28, $\square$: ibuprofen, determined from experimental curve in panel A, $\bigcirc$: ibuprofen, determined from Eqn. 5-14].

Nevertheless, the resulting fit in Figure 5.9B for PEMA is very good. These same values also provide quite a good fit for PiBMA. However, since the jumping unit of PiBMA is presumably higher than for PEMA, a lower ξ-value for PiBMA would be expected, which could easily lead to a higher diffusion coefficient by an order of magnitude. As has been stressed earlier, an error by an order of magnitude cannot be excluded based on the

various uncertainties in the input parameters. For a proper comparison of the two polymers, a plot comparable to Figure 5.2 should be constructed for PiBMA, in order to establish the jumping unit of PiBMA. Then, diffusion at various other drug concentrations should be measured experimentally, to see whether the theory holds, or improves, as the drug concentration approaches zero concentration. In light of the uncertainties in the modeling results for PEMA and PiBMA, modeling of drug diffusion in PLA is not attempted here, since this would cause even more uncertainties.

5.4.4 Relaxation below T_g

The free volume theory assumes that the polymer is always in an equilibrium state. However, it is well known that free volume decreases in time due to relaxation processes. Phenomenologically, this may be described by introducing a time dependent volume contraction parameter, similar to the static parameter λ introduced by Vrentas and Duda (Eqn. 5-17) [55]. From Eqn. 5-17, it is evident, that this parameter can range between 0 (i.e. no change in volume contraction below T_g) and α_{2g}/α_2, which is incorporated in the FVT by substituting K_{22} in Eqn. 5-8 by K_{22}/λ. By making this parameter time dependent, the FVT could in principle account for these relaxation effects. However, this parameter cannot be determined in a predictive sense, and the FVT was never developed to be able to take into account these time dependent effects. No attempt is therefore made to incorporate a time dependency here either, but a consideration of the relaxation effects and its importance in the drug delivery system at hand is given in the final chapter of this thesis.

$$\lambda = \frac{\alpha_{2g} - (1 - f_{H2}^G) \cdot \alpha_{c2}}{\alpha_2 - (1 - f_{H2}^G) \cdot \alpha_{c2}} \qquad [5\text{-}17]$$

5.5 Conclusions and outlook

The applicability of the free volume theory (FVT) as a predictive model for drug diffusion near the glass transition temperature has been investigated, mainly focusing on the effect of size, shape and flexibility. The most elusive parameter in the free volume theory is the parameter ξ, which is a measure for the ratio of the size of the jumping units of solute and polymer. As the size of the solute increases, the importance of taking into

account size and shape effects becomes increasingly important. The use of ethylene glycol dimethyl ethers as a homologous series to investigate these effects on diffusion in PEMA has proven impossible using a sorption method due to the relatively fast absorption of water into the polymer matrix during the initial sorption period. Pulsed-field gradient NMR measurements provide an interesting alternative to measure self-diffusion coefficients of large molecules directly in a polymer matrix, and is suggested for future research.

In a different approach to investigate the validity of the FVT for diffusion of large molecules in polymer matrices, the diffusion coefficient of ibuprofen in PEMA and PiBMA matrices has been determined from release measurements. Comparison with modeling results has revealed that the FVT overestimates ξ, and thus underestimates the diffusion coefficient of ibuprofen in these polymers by two orders of magnitude. This may indicate that shape and/or flexibility of ibuprofen are not taken into account satisfactorily. Alternatively, polymer dynamics may change as the solute approaches the size of the jumping unit of the polymer, basically causing cooperative motion between drug and polymer. Nevertheless, the difference in diffusion of ibuprofen in PEMA and PiBMA seems at least approximately described by the FVT.

For a purely predictive model, some large steps still need to be taken, most notably regarding the parameter ξ. For validation of a proposed model, the number of parameters in the FVT model impose the need for further diffusional data of (homologous series of) different large (drug) molecules differing in either size or shape, as well as diffusion of these same molecules in various polymer homologues, e.g. polyacrylates and polyalkanes. Before an extension into the glassy region can be considered, optionally with a time-dependency based on relaxation, a proposed model should be validated in the rubbery state.

5.6 Appendix

5.6.1 Modeling parameters for diffusion of EGDME's in different polymer matrices

Tables 5.1 and 5.2 contain the solute and polymer modeling parameters, respectively. The free volume parameters K_{11}/γ_1, $K_{21}-T_{g1}$, and D_0 of the EGDME's have not been reported in literature. Therefore, these parameters have been determined by fitting experimental viscosity and density data [56] to Eqn. 5-18, assuming energy effects are negligible, i.e. $E^*=0$ [57] (Figure 5.11). The parameters for PLA in Table 5-2 are affected by the relative amount of L- and D-lactide, as well as its crystallinity. Intermediate values are chosen for modeling, since the polylactide in Chapter 4 is a copolymer of D- and L-lactide, exhibting partial crystallinity, with a T_g around 56ºC. The parameters should, however, be used with caution since some values are rough estimates.

Table 5.1: Ethylene glycol dimethyl ether parameters

	DEGDME	TEGDME	TetraEGDME	Comment
V_1^0 [m³ kg⁻¹]	8.56·10⁻⁴	8.39·10⁻⁴	8.27·10⁻⁴	Estimate using Goldhamer's rule [27]
M_1 [kg mol⁻¹]	0.13418	0.17823	0.2228	
B/A [-]	2.96	4.35	5	Estimate based on its stereo structure
E^* [-]	0	0	0	
D_0 [m⁻² s⁻¹]	6.80·10⁻⁸	5.27·10⁻⁸	4.56·10⁻⁸	Eqn. 5-18
K_{11}/γ_1 [m³ kg⁻¹ K⁻¹]	9.55·10⁻⁷	9.33·10⁻⁷	8.71·10⁻⁷	Eqn. 5-18
$K_{21}-T_{g1}$ [-]	-75	-98	-106	Eqn. 5-18
V_c [m³ mol⁻¹]	4.31·10⁻⁴	5.61·10⁻⁴	6.91·10⁻⁴	[56]

$$ln\,\eta_1 = ln\left(\frac{0.124\cdot10^{-16}\,\tilde{V}_c^{2/3}R\cdot T}{M_1\cdot\hat{V}_1^0}\right) - ln\,D_0 + \frac{\hat{V}_1^*}{(K_{11}/\gamma_1)\cdot(K_{21}+T-T_{g1})}\ \text{[Eqn. 5-18]}$$

where η_1 : dynamic viscosity   [Pa s]

   $\tilde{V}_c$: critical molar volume   [m³ mol⁻¹]

Table 5.2: Polymer parameters

	PLA	PEMA	PiBMA	Comment
V_2^* [m^3 mol^{-1}]	0.481·10^{-4} [a]	0.916·10^{-4} [a] 0.934·10^{-4} [b]	1.206·10^{-4} [a]	
V_2^0 (T_{g2}) [m^3 kg^{-1}]	8.13·10^{-4} [c]	8.93·10^{-4} [d,e]	9.51·10^{-4} [e]	
T_{g2} [K]	323, 344 [f] 329 [g]	335 [b] 343 [d,g]	335 [g] 337 [h]	
α_2 [K^{-1}]	7.4·10^{-4} [c]	6.0·10^{-4} [i,j]	6.032 - 6.344 ·10^{-4} [k]	
α_{2g} [K^{-1}]	[l]	3.0·10^{-4} [i] 2.7·10^{-4} [j]	2.288 - 2.6·10^{-4} [k]	In the limit of $\omega_1 = 0$, the value of α_{2g} is irrelevant.
C_{12}^g [-]	10.3 [f] 12.7 [f]	15.5 [m] 17.6 [n]	11 [o] 13 [h]	
C_{22}^g [K] / K_{22} [K]	48.6 [f] 29.1 [f]	90 [m] 65.5 [n]	49 [o] 58 [h]	
M_{2j} [kg mol^{-1}]	[l]	0.1400 [p]	[l]	$M_{2j} = 3/2 \cdot M_{monomer}$ for many polymers. Also, a correlation with T_g is available [43,44]
K_{12}/γ_2 [m^3 kg^{-1} K^{-1}]	5.79·10^{-7} / 6.48·10^{-7} [q]	3.02·10^{-7}	4.88·10^{-7}	Eqn. 5-3
γ_2 [-]	1.04 / 0.93 [q]	1.77	1.20	$V_2^0(T_{g2})\cdot\alpha_2/(K_{12}/\gamma_2)$ [5]
f_{H2}^G [-]	0.036 / 0.029 [q]	0.039	0.036	$\alpha_2\cdot K_{22}$ (as $\alpha_{c2} = 0$ above T_{g2}) [5]

[a] Sugden's group contribution method [27]

[b] Ref [58]

[c] Amorphous PLA [59]

[d] Ref [60]

[e] Ref [61]

[f] Fully amorphous and highly rigid/crystalline, respectively [62]

[g] Determined experimentally (DSC)

[h] Ref [63]

[i] Ref [64]

[j] Ref [65]

[k] Ref [66]

[l] Unknown

[m] Ref [33]

[n] Ref [67]

[o] Ref [68]

[p] Ref [43]

[q] Fully amorphous / Intermediate amorphous and highly crystalline. The latter are used for modeling.
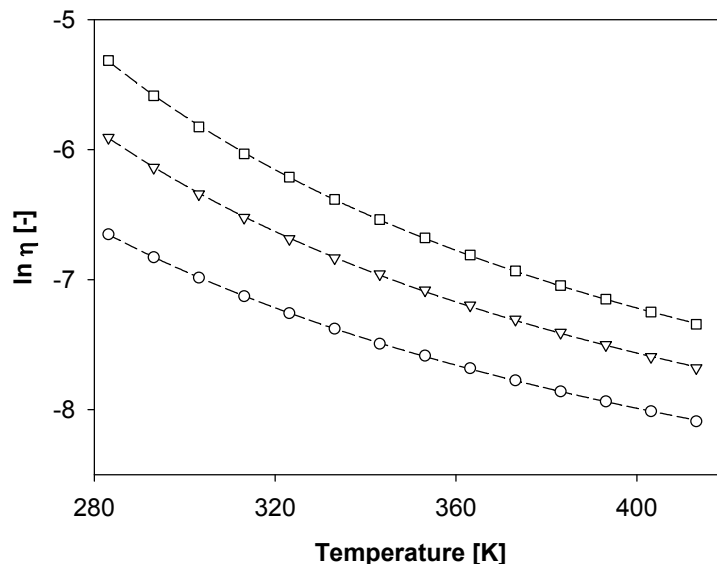
Figure 5.11: Determination of free volume parameters by fitting viscosity and density data to Eqn. 5-18. ○: DEGDME, ▽: TEGDME, □: TetraEGDME, lines indicate resulting fit.

References

[1] Cohen, M. H. & Turnbull, D. Molecular transport in liquids and glasses. *J. Chem. Phys.* **31**, 1164-1169 (1959).

[2] Fujita, H. Diffusion in polymer-diluent systems. *Fortschr. Hochpolym.-Forsch.* **3**, 1-47 (1961).

[3] Vrentas, J. S. and Duda, J. L. Diffusion in polymer-solvent systems. I. Reexamination of the free-volume theory. *J. Polym. Sci., Polym. Phys Ed.* **15**, 403-416 (1977).

[4] Vrentas, J. S. & Duda, J. L. Diffusion in polymer-solvent systems. II. A predictive theory for the dependence of diffusion coefficients on temperature, concentration, and coefficients on temperature, concentration and molecular weight. *J. Polym. Sci., Polym. Phys. Ed.* **15**, 417-439 (1977).

[5] Vrentas, J. S. & Vrentas, C. M. Solvent self-diffusion in rubbery polymer-solvent systems. *Macromolecules* **27**, 4684-4690 (1994).

[6] Vrentas, J. S. & Vrentas, C. M. Solvent self-diffusion in glassy polymer-solvent systems. *Macromolecules* **27**, 5570-5576 (1994).

[7] Mauritz, K. A., Storey, R. F. A general free volume based theory for the diffusion of large molecules in amorphous polymers above T_g. 2. Molecular shape dependence. *Macromolecules* **23**, 2033-2038 (1990).

[8] Mauritz, K. A., Storey, R. F., George, S. E. A general free volume based theory for the diffusion of large molecules in amorphous polymers above T_g. 1. Application to di-*n*-alkyl phthalates in PVC. *Macromolecules* **23**, 441-450 (1990).

[9] Von Meerwall, E., Skowronski, D., Hariharan, A. Diffusion of plasticizers in rubbery poly(vinyl chloride): effects of molecular shape. *Macromolecules* **24**, 2441-2449 (1991).

[10] Zielinski, J. M., Sillescu, H., Romdhane, I. H. 1,3,5-triisopropylbenzene diffusion in polystyrene solutions. *J. Polym. Sci. Part B: Polym. Phys.* **34**, 121-130 (1996).

[11] Vrentas, J. S., Vrentas, C. M., Faridi, N. Effect of solvent size on solvent self-diffusion in polymer-solvent systems. *Macromolecules* **29**, 3272-3276 (1996).

[12] Zielinski, J. M. An alternate interpretation of polymer/solvent jump size units for free-volume diffusion models. *Macromolecules* **29**, 6044-6047 (1996).

[13] Vrentas, J. S., Vrentas, C. M. A new equation relating self-diffusion and mutual diffusion coefficients in polymer-solvent systems. *Macromolecules* **26**, 6129-6131 (1993).

[14] Vrentas, J. S., Duda, J. L. Diffusion of large penetrant molecules in amorphous polymers. *J. Polym. Sci., Polym. Phys. Ed.* **17**, 1085-1096 (1979).

[15] Arnould, D., Laurence, R. L. Size effects on solvent diffusion in polymers. *Ind. Eng. Chem. Res.* **31**, 218-228 (1992).

[16] Williams, M. L., Landel, R. F., Ferry, J. D. The temperature dependence of relaxation mechanisms in amorphous polymers and other glass forming liquids. *JACS* **77**, 3701-3707 (1955).

[17] Wang, B.-G., Yamaguchi, T., Nakao, S.-I. Solvent diffusion in amorphous glassy polymers. *J. Polym. Sci., Part B : Polym. Phys.* **38**, 846-856 (2000).

[18] Fox, T. G. Influence of diluent and of copolymer composition on the glass temperature of a polymer system. *Bull. Am. Phys. Soc.* **1**, 123-135 (1956).

[19] Gordon, M., Taylor, J. S. Ideal copolymers and the second-order transitions of synthetic rubbers. I. Noncrystalline copolymers. *J. Appl. Chem.* **2**, 493-500 (1952).

[20] Simha, R., Boyer, R. F. On a general relation involving the glass temperature and coefficients of expansion of polymers. *J. Chem. Phys* **37**, 1003-1007 (1962).

[21] Beiner, M., Schröter, K., Hempel, E., Reissig, S., Donth, E. Multiple glass transition and nanophase separation in poly(*n*-alkyl methacrylate) homopolymers. *Macromolecules* **32**, 6278-6282 (1999).

[22] Vrentas, J. S., Duda, J. L. Solvent and temperature effects on diffusion in polymer-solvent systems. *J. Appl. Polym. Sci.* **21**, 1715-1728 (1977).

[23] Xia, J.-L., Wang , C. H. Probing the glass transition process of poly(ethyl methacrylate) by the mass diffusion of thymorquinone. *J. Phys. Chem.* **93**, 3839-3841 (1989).

[24] Angell, C. A. in *Relaxations in complex systems* (eds. K.L. Ngai, G.B. Wright), National Technical Information Service, US Department of Commerce, Springfield, VA, pp. 3-11).

[25] Qin, Q. , McKenna, G. B. Correlation between dynamic fragility and glass transition temperature for different classes of glass forming liquids. *J. Non-Crystalline Solids* **352**, 2977-2985 (2006).

[26] Plazek, D. J. & Ngai, K. L. Correlation of polymer segmental chain dynamics with temperature-dependent time-scale shifts. *Macromolecules* **24**, 1222-1224 (1991).

[27] Haward, R. N. Occupied volume of liquids and polymers. *J. Macromol Sci., Rev. Macromol. Chem* **C4**, 191-242 (1970).

[28] Ju, S. T., Duda, J. L., Vrentas, J. S. Influence of temperature on the diffusion of solvents in polymers above the glass transition temperature. *Ind. Eng. Chem. Res. Dev.* **20**, 330-335 (1981).

[29] Vrentas, J. S., Liu, H. T., Duda, J. L. Effect of solvent size on diffusion in polymer-solvent systems. *J. Appl. Polym. Sci.* **25**, 1793-1797 (1980).

[30] Vrentas, J. S., Duda, J. L., Hou, A. C. Segmentwise diffusion in molten polystyrene. *J. Appl. Polym. Sci.* **31**, 739-745 (1986).

[31] Berens, A. R, Hopfenberg, H.B. Diffusion of organic vapors at low concentrations in glassy PVC, polystyrene and PMMA. *J. Membr. Sci.* **10**, 283-303 (1982).

[32] Fujita, H. in *Diffusion in Polymers* (Eds. Crank, J. & Park, G. S., Academic Press, London, 1968), 75-105.

[33] Ehlich, D., Sillescu, H. Tracer diffusion at the glass transition, *Macromolecules* **23**, 1600-1610 (1990).

[34] Bueche, F. *Physical Properties of Polymers*, Wiley-Interscience, New York, 1962.

[35] Von Meerwall, E., Ferguson, R. D. Diffusion of hydrocarbons in rubber, measured by the pulsed gradient NMR method. *J. Appl. Polym. Sci.* **23**, 3657-3669 (1979).

[36] Tamai, Y., Tanaka, H., Nakanishi, K. Molecular simulation of small penetrants through membranes. 1. Diffusion coefficients. *Macromolecules* **27**, 4498-4508 (1994).

[37] Wang, X.-Y. *et al.* Molecular simulation and experimental study of substituted polyacetylenes: fractional free volume, cavity size distributions and diffusion coefficients. *J. Phys Chem. B.* **110**, 12666-12672 (2006).

[38] Hofmann, D., Fritz, L., Ulbrich, J., Schepers, C., Böhning, M. Detailed-atomistic modeling of small molecule diffusion and solution processes in polymeric membrane materials. *Marcomol. Theory Simul.* **9**, 293-327 (2000).

[39] Pavel, D., Shanks, R. Molecular dynamics simulation of diffusion of O_2 and CO_2 in blends of amorphous poly(ethylene terephthalate) and related polyesters. *Polymer* **46**, 6135-6147 (2005).

[40] Van der Vegt, N. F. A. Temperature dependence of gas transport in polymer melts: molecular dynamics simulations of CO_2 in polyethylene. *Macromolecules* **33**, 3153-3160 (2000).

[41] Z.-J. Zhao, Q. Wang, L. Zhang, Y.-C. Liu, A different mechanism for drug molecules in amorphous polymers. *J. Phys. Chem. B* **111**, 4411-4416 (2007).

[42] Z.-J. Zhao, Q. Wang, L. Zhang, Size effects on competition of two diffusion mechanisms for drug molecules in amorphous polymers. *J. Phys. Chem. B* **111**, 13167-13172 (2007).

[43] Zielinksi, J. M. & Duda, J. L. Predicting polymer/solvent diffusion coefficients using free-volume theory. *AIChE J.* **38**, 405-415 (1992).

[44] Hong, S.-U. Predicting ability of free-volume theory for solvent self-diffusion coefficients in rubbers. *J. Appl. Polym. Sci.* **61**, 833-841 (1996).

[45] Crank, J. & Park, G. S. in *Diffusion in Polymers* (Eds. Crank, J. & Park, G. S., Academic Press, London, 1968), 1-39.

[46] Stannett, V., and Williams, J. L. Permeability of poly(ethylmethacrylate) to gases and water vapour. *J. Polym. Sci. C* **10**, 45-59 (1965).

[47] Barrie, J. A. in *Diffusion in Polymers* (Eds. Crank, J. & Park, G. S., Academic Press, London, 1968), 259-313.

[48] Barrie, J. A. & Machin, D. Diffusion and association of water in some polyalkylmethacrylates. *Trans. Faraday Soc.* **67**, 244-256 (1971).

[49] Vallieres, C. *et al.* On Schroeder's paradox. *J. Membr. Sci.* **278**, 357-364 (2006).

[50] Parker, S. & Braden, M. Water absorption of methacrylate soft lining materials. *Biomaterials* **10**, 91-95 (1989).

[51] Kalachandra, S. & Kusy, R. P. Comparison of water sorption by methacrylate and dimethacrylate monomers and their corresponding polymers. *Polymer* **32**, 2428-2434 (1991).

[52] Von Meerwall, E. D. Pulsed and steady field gradient NMR diffusion measurements in polymers. *Rubber Chem. Technol.* **58**, 527-560 (1985).

[53] Johari, G. P., Kim, S., Shanker, R. M. Dielectric relaxation and crystallization of ultraviscous melt and glassy states of aspirin, ibuprofen, progesterone, and quinidine. *J. Pharm. Sci.* **96**, 1159-1175 (2007).

[54] Vrentas, J. S. & Vrentas, C. M. Predictive methods for self-diffusion and mutual diffusion coefficients in polymer-solvent systems. *Eur. Polym. J.* **34**, 797-803 (1998).

[55] Vrentas, J. S. & Duda, J. L. A free volume interpretation of the influence of the glass transition on diffusion in amorphous polymers. *J. Appl Polym. Sci.* **22**, 2325-2339 (1978).

[56] Conesa, A., Shen, S., Coronas, A. Liquid denisities, kinematic viscosities, and heat capacities of some ethylene glycol dimethyl ethers at temperatures from 283.15 K to 423.15 K. *Int. J. Thermophys.* **19**, 1343-1358 (1998).

[57] Hong, S.-U. Prediction of polymer/solvent diffusion behavior using free-volume theory. *Ind. Eng. Chem. Res.* **34**, 2536-2544 (1995).

[58] Yamaguchi, T., Wang, B.-G., Matsuda, E., Suzuki, S., Nakao, S.-I. Prediction and estimation of solvent diffusivities in polyacrylate and polymethacrylates. *J. Polym. Sci., Part B: Polym. Phys.* **41**, 1393-1400.

[59] Auras, R., Harte, B., Selke, S. An overview of polylactides as packaging materials. *Macromol. Biosci.* **4**, 835-864 (2004).

[60] Kilburn, D., Dlubek, G., Pionteck, J., Alam, M. A. Free volume in poly(*n*-alkyl methacrylate)s from positron lifetime and PVT experiments and its relation to the structural relaxation. *Polymer* **47**, 7774-7785 (2006).

[61] Davy, K. W. M., Braden, M. Thermal expansion of glassy polymers. *Biomaterials* **13**, 1043-1046 (1992).

[62] Zuza, E. Glass transition behavior and dynamic fragility in polylactides containing mobile and rigid amorphous fractions. *Polymer* **49**, 4427-4432 (2008).

[63] Deppe, D. D., Miller, R. D., Torkelson, J. M. Small molecule diffusion in a rubbery polymer near T_g: effects of probe size, shape and flexibility. *J. Polym. Sci.,Part B: Polym. Phys.* **34**, 2987-2997 (1998).

[64] Berry, G. C., Fox, T. G. The Viscosity of polymers and their concentrated solutions. *Adv. Polym. Sci.* **5**, 261-357 (1967).

[65] Orwoll, R. A. in *Physical properties of polymers handbook* (Ed. Mark, J. E., AIP Press, New York, 1996), 81-89.

[66] Van Krevelen, D.W., *Properties of Polymers*, 3rd ed. (Elsevier, Amsterdam, 1997), 71-127.

[67] Ferry, J. D. *Viscoelastic Properties of Polymers*, 2nd ed. (Wiley, New York, 1970).

[68] Hooker, J. C. & Torkelson, J. M. Coupling of probe reorientation dynamis and rotor motions to polymer relaxation as sensed by second harmonic generation and fluorescence. *Macromolecules* **28**, 7683-7692 (1995).

120

CHAPTER 6

Pore-Covered Thermoresponsive Membranes for Repeated On-Demand Release of Large Drug Molecules

Abstract

Reversible on/off-switching of bovine serum albumin (BSA) permeation through a thermoresponsive composite membrane with negligible permeation in the off-state is demonstrated. UV-photografting of poly(*N*-isopropylacrylamide) onto a poly(ethylene terephthalate) microfiltration membrane results in the formation of a hydrogel graft layer on the irradiated side of the membrane only. The amount of hydrogel grafted onto the membrane can be controlled by the amount of crosslinker. Above the lower critical solution temperature (LCST) of the hydrogel (on-state), the shrunken state of the graft layer appears to only partially cover the membrane, allowing BSA permeation through the uncovered pores. Provided the grafting degree is high enough, the swollen hydrogel covers the membrane completely below the LCST (off-state), thus preventing BSA permeation. The on-demand release mechanism proposed here is based on switching the membrane surface coverage rather than previously reported switches based on effective pore size or hydrogel mesh size. The main advantage of our mechanism is that higher fluxes can be achieved in the on-state, since permeation is not limited by pore-narrowing.

6.1 Introduction

A large number of drug administration applications, such as insulin delivery and many hormone treatments, require pulsatile release, which is often achieved using difficult or painful dosing methods (e.g. injections) [1]. Therefore, delivery systems have been designed to release a drug according to a preprogrammed pattern [2]. In addition, on-demand release systems have been developed releasing drugs in response to external stimuli, such as an electric or magnetic field, ultrasound, electromagnetic radiation, pH, and temperature [3-5].

In the current work, on-demand release from a hydrogel based system is achieved using temperature as the external stimulus, making use of the hydrogel's thermoreversible swelling capability. A well-known thermoresponsive hydrogel is poly(N-isopropylacrylamide) (pNIPAAm), exhibiting a strong volume phase transition around 32ºC, i.e. the lower critical solution temperature (LCST) of the polymer, which can be tuned to the desired temperature by incorporation of other monomers [6-12]. Below the LCST, the hydrogel is strongly swollen, whereas entropy driven collapse due to hydrophobic interactions occurs above the LCST. This thermoresponsive behavior has been applied in various monolithic on-demand drug delivery designs, where release is determined either by a squeezing mechanism [13,14], or by entrapment in the collapsed state, followed by enhanced permeation in the swollen state [15,16]. To overcome the limitations of such monolithic systems, including negative thermoresponsivity and high permeation in the off-state, various hydrogel/membrane composites have been proposed to reversibly affect the diffusion rate by grafting a thermoresponsive hydrogel inside the voids [7,17-25] or on top of the porous solid membrane [11,24,26-28]. The grafting degree determines whether the composite exhibits positive or negative thermo-responsivity, which is schematically depicted in Figure 6.1. These mechanisms do not differ for the pore-filled or pore-covered approach, although the thin hydrogel layer of the pore-covered membranes provides a faster response than the thicker confined layer in the pore-filled membranes [26]. Therefore, the work described here focuses on pore-covered membranes.

Pore-covered membranes can be prepared by several grafting procedures, like controlled atom transfer radical polymerization from gold coated track-etched membranes [29], corona induced grafting [30] and UV-photografting [11,26,28]. UV-photografting is an attractive technique because of its ease and the use of inexpensive equipment. Moreover, any polymer membrane containing abstractable hydrogen atoms is suitable for UV-photografting, making it a versatile technique. Since poly(ethylene terephthalate) (PET) is among the polymer substrates with the highest photografting reactivity [31], it is used in this work. The strong absorption of far UV-radiation by PET ensures that grafting predominantly takes place at the surface of the membrane and not inside the pores [26].
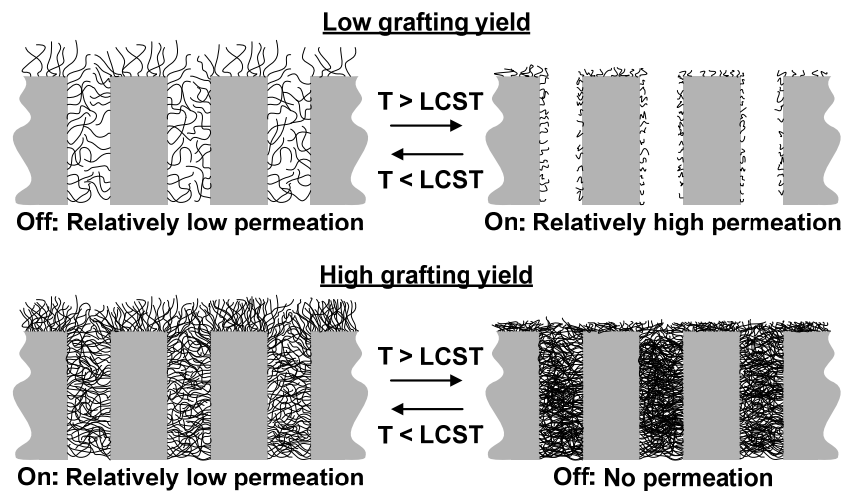

Figure 6.1: Thermoresponsive mechanisms for permeation through hydrogel/membrane composites. At low grafting degrees, the polymer grafts inside or on top of the pores inhibit permeation below the LCST, whereas above the LCST, the effective pore size determines permeation (positive thermoresponsivity). At high grafting degrees, there is a limited amount of permeation below the LCST, whereas the dense polymer network inhibits permeation completely above the LCST (negative thermoresponsivity). In drug delivery applications, positive thermoresponsivity is usually desired, but this mechanism suffers from relatively high permeation in the off-state.

The present work demonstrates a thermoresponsive switching mechanism that cannot be achieved with pore-filled membranes. The effect of crosslinker on the grafting process is discussed, after which reversible on/off-switching of the permeation of a model protein is demonstrated, even attaining negligible release in the off-situation.

6.2 Experimental

6.2.1 Materials

N-isopropylacrylamide (NIPAAm, 99%, stabilized) was obtained from Acros Organics and was purified by recrystallization from n-hexane prior to use. n-Hexane (≥98%) was obtained from Riedel - de Haën. Benzophenone (BP, 99%), *N,N'*-methylenebisacryl-amide (mBAAm, 99%) and acetone (≥99%) were purchased from Sigma-Aldrich. Bovine serum albumin (BSA, ≥98%) and trifluoroacetic acid (TFA) were acquired from Merck. Acetonitrile (≥99.97%) was obtained from Biosolve. Except for NIPAAm, all chemicals were used as received.

Hydrophilic poly(ethylene terephthalate) (PET) Cyclopore™ track etched membranes (pore diameter: 0.2 μm, diameter: 25 mm, weight: ~10 mg, thickness: ~20 μm) were purchased from Whatman and were washed 3 times with demineralized water prior to use.

6.2.2 Methods

6.2.2.1 Photografting

The PET membranes were soaked in a 5 mL acetone solution containing the monomer ([NIPAAm]: 0.1-2.0 M), photoinitiator ([BP]: 0.01-0.20 M) and crosslinking agent ([mBAAm]: 0.015-0.073 M) for 10 minutes. The membrane was then rapidly transferred onto a Teflon covered glass plate, 100 μL of the soaking solution was added, followed by covering with a second quartz glass plate. Pressure was applied to the quartz plate using a custom-made screwing system resulting in a thickness of the reaction solution of ~11 μm. The membrane was irradiated for 30 minutes with a Spectroline EF-180 UV-C lamp (λ: 254 nm) at a distance of 8 cm, resulting in an average intensity of approximately 4 mW cm^{-2}. After irradiation, the membrane was washed with demineralized water to remove residual monomer and homopolymer. After drying the grafted membrane in air, the membrane was weighed and a grafting degree was calculated according to:

$$D_g = \frac{W_g - W_0}{W_0} \cdot 100\%,$$

where D_g is the grafting degree (%), W_g is the air-dried weight of the membrane after the grafting procedure, and W_0 is the air-dried weight of the membrane prior to photografting. After weighing, the membrane was stored in water at ambient conditions until permeation experiments were performed.

6.2.2.2 Protein permeation

A vial (5 or 12 mL) containing a solution of 20 mg mL^{-1} of BSA in water was covered with a membrane and was closed with a screw cap with a hole. The effective membrane diameter for the two types of vials was 0.50 and 2.54 cm^2, respectively. The vial was suspended in a glass beaker containing 100 mL of demineralized water (bulk solution). The grafted surface of the membrane, i.e. the surface facing the UV source during irradiation, was in contact with the bulk solution. The bulk solution was preheated to the required temperature before suspending the vial. Both solutions were mixed with a magnetic stirrer.

Samples were taken from the bulk solution at several time intervals and analyzed by high performance liquid chromatography (HPLC) according to the procedure described in section 6.2.2.3. The samples were kept in a fridge (T: 4ºC) until HPLC analysis was performed, which was always within one week after sampling. After taking a sample (500 μL), an equal amount of water was added to the bulk solution to maintain a constant volume (the subsequent measured concentrations were corrected for this sampling effect).

6.2.2.3 High performance liquid chromatography (HPLC)

HPLC analysis (Shimadzu VP series) of BSA was performed on a Nucleosil C18 column (Supelco, 150 x 3.2 mm – 5 μm) using UV detection at 280 nm (Shimadzu, SPD-10Avp) at a temperature of 40ºC. The injection temperature of the auto sampler was 15ºC. A composition gradient in time of acetonitrile (A) and water (B) as mobile phase was used, both containing 0.05% (v/v) TFA. A linear gradient was applied in the first 10 minutes, going from 20% to 80% A. Another linear gradient was applied in the next minute, returning to the original composition. The run proceeded for another 4 minutes at this composition, resulting in a total analysis time of 15 minutes.

6.2.2.4 Surface analysis

Attenuated total reflectance – Fourier transform infrared spectroscopy (ATR-FTIR) was performed on an FTIR-8400 S Shimadzu spectrometer with ATR attachment. Scanning electron microscope (SEM) images were made with a JEOL JSM-5600, after the surface of the membrane was covered with a gold layer by vacuum deposition. The applied accelerating voltage, spot size and working distance were 15 kV, 12, and 8 mm, respectively.

6.3 Results and discussion

6.3.1 Preparation of thermoresponsive membranes

The UV-photografting process is schematically depicted in Figure 6.2. In general, increasing monomer concentration or reaction time results in a higher grafting degree [17,26,32]. An optimum concentration exists for the photoinitiator, due to the opposing effects of an increasing amount of radical species on the one hand, and increasing absorbance of the reaction solution on the other hand (i.e. the strong absorption of UV light at high concentrations leads to the formation of radicals in the surface layer of the reaction solution, rather than at the surface of the membrane where the grafting reaction takes place). For a detailed discussion on the grafting procedure, see references [17,26,32].
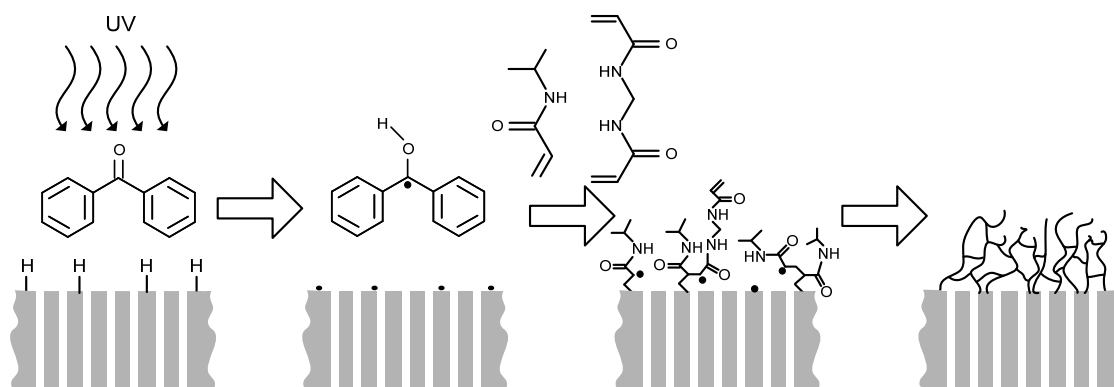

Figure 6.2: Schematic representation of photografting process: upon UV-irradiation, benzophenone abstracts a hydrogen atom from the track-etched PET membrane, resulting in a semipinacol radical and a surface free radical, which initiates graft polymerization. The crosslinking agent yields a hydrogel network on the surface of the membrane.

To the best of our knowledge, no clear effect of crosslinker on the grafting degree has been reported up to this moment. Nonetheless, a linear increase in grafting degree is observed in this work with increasing crosslinker concentration (Figure 6.3). This can be attributed to two effects of the crosslinker on the grafting process. In the first place, addition of crosslinker leads to an increased probability of adding homopolymer from the reaction solution to the graft network. Addition of a crosslinker unit to a growing polymer graft chain introduces a vinyl monomer capable of binding homopolymer from solution, while the radical coupling reaction from the main polymer chain remains unaffected (Figure 6.2). In the second place, the homopolymer in solution is also crosslinked, meaning a larger amount of hydrogel is added to the surface when such a solution polymer reacts with a growing polymer graft or surface free radical.
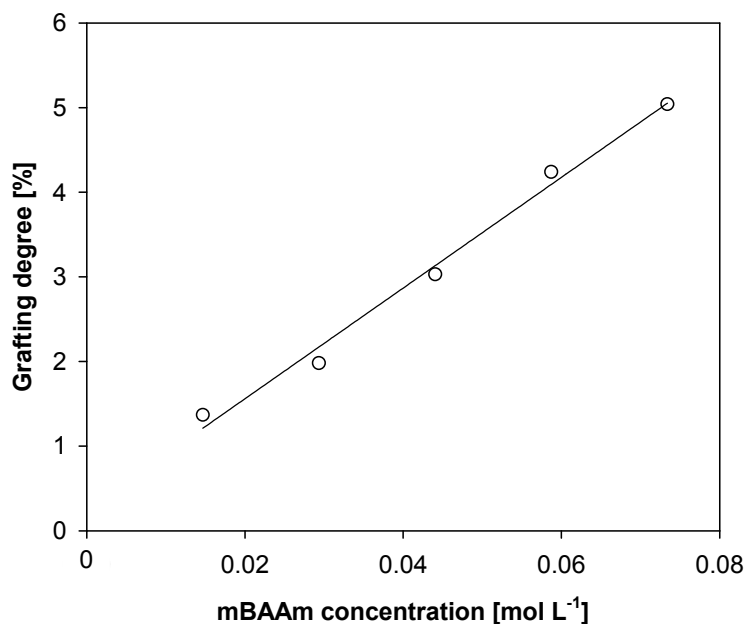

Figure 6.3: Effect of crosslinker concentration on grafting degree (D_g). *Grafting conditions*: [NIPAAm]: 2.0 M; [BP]: 0.10 M; irradiation time: 30 min.

Characterization of the UV-grafted membranes by ATR-FTIR spectroscopy reveals that grafting only occurs at the irradiated side of the membrane. The amide peaks at 3290, 1635, and 1541 cm^{-1}, as well as the disappearance of the PET carbonyl peak at 1715 cm^{-1}, in the ATR-FTIR spectra indicate the formation of the pNIPAAm graft layer (Figure 6.4). In contrast, these peaks are not observed for the opposite side of the membrane. It should

also be noted that these peaks are not observed over the whole surface of the membrane, seemingly indicating inhomogeneous grafting, resulting in incomplete surface coverage in the dry state.
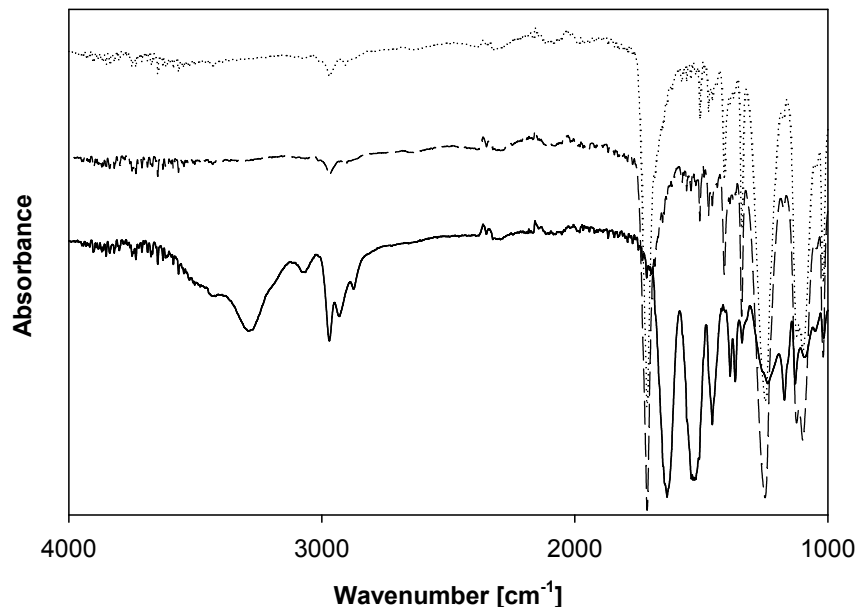

Figure 6.4: ATR-FTIR spectra of irradiated surface (front,────) and back of a grafted membrane (----), and an untreated membrane (·········), shifted along the y-axis for clarity. *Grafting conditions*: [NIPAAm]: 2.0 M; [BP]: 0.01 M; [mBAAm]: 0.07 M; irradiation time: 30 min.

SEM images confirm that grafting only occurs at the irradiated side of the membrane (Figure 6.5). A clear graft layer is observed on top of the membrane, and similarly to ATR-FTIR results, there appears to be incomplete surface coverage (Figure 6.5C). However, it should be noted, that both these techniques are performed with dry membranes, i.e. the graft layer is in a shrunken state. These samples have not been freeze-dried, so the morphological characteristics observed in the SEM images do not necessarily reflect the wet state of the grafted membranes. However, these images do reveal that a dense polymer network layer is formed on top of the membrane. Moreover, a clear gap between the hydrogel layer and the membrane surface is present, giving the impression of a hydrogel layer lying on top of the membrane as opposed to being covalently attached to the surface. Possibly, the hydrogel only has a limited number of anchoring points connected to the membrane surface. Finally, no graft layer is observed

inside the pores, which is an important given for the thermoresponsive switching mechanism explained in the following section.
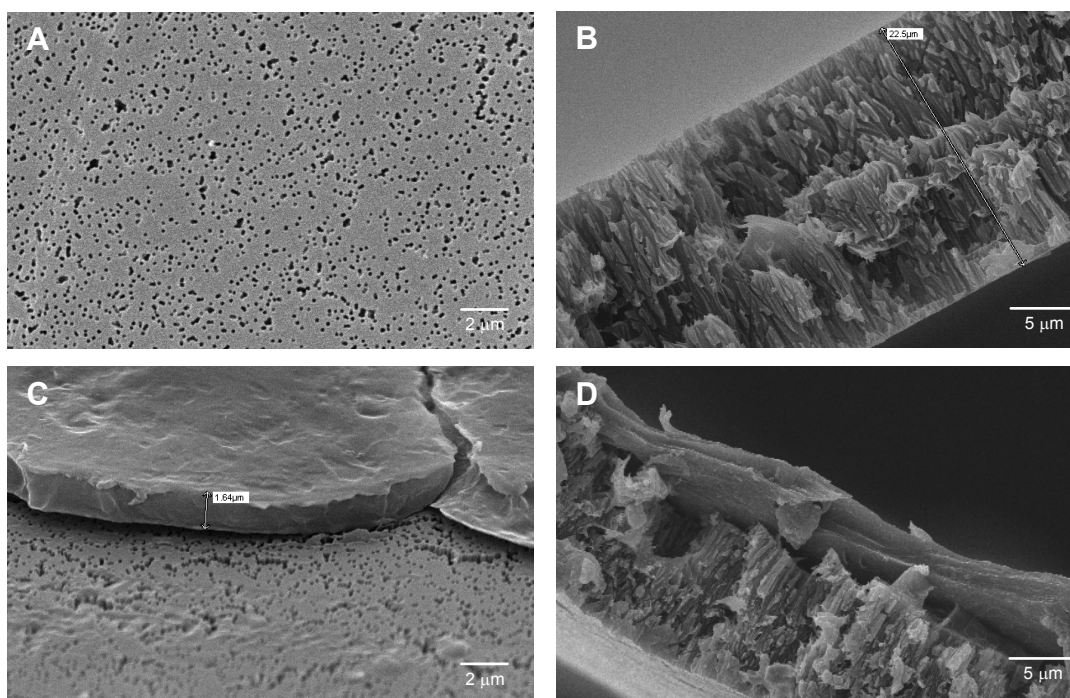

Figure 6.5: Representative SEM-images of surface (A) and cross-section (B) of untreated PET track-etched membrane compared to surface (C) and cross-section (D) of grafted membranes.

6.3.2 On/off-switching of bovine serum albumin permeation

In order to investigate whether on-demand release can be achieved using these grafted membranes, the permeation of bovine serum albumin (BSA) is measured above and below the LCST for hydrogels with different crosslinker concentrations, and thus grafting degree. In Figure 6.6, a clear trend is demonstrated in the off-situation at 20ºC, where increasing crosslinker concentration leads to increased BSA retention. Above the LCST, the trend is less obvious due to the significant error bars, but the permeation seems to be more or less constant. These results differ from other reports in literature on the effect of grafting degree on membrane permeation. Peng and Cheng [17], for instance, have investigated the influence of the grafting degree and have found a continuously decreasing permeability of vitamine B_{12} through a pore-filled grafted membrane with increasing grafting degree for any temperature. Similarly, Park et al. [7] have observed decreasing tryptophan permeation with increasing grafting degree. Furthermore, both

authors [7,17] observe a change in switching effect at high grafting degrees, as the collapsed network becomes too dense for permeation to occur above the LCST (Figure 6.1). In a pore-covering approach, Yang and Yang [26] have measured a decreasing water flux with increasing grafting degree at all temperatures, and for constant grafting degree with increasing crosslinker concentration, the same trend was observed.
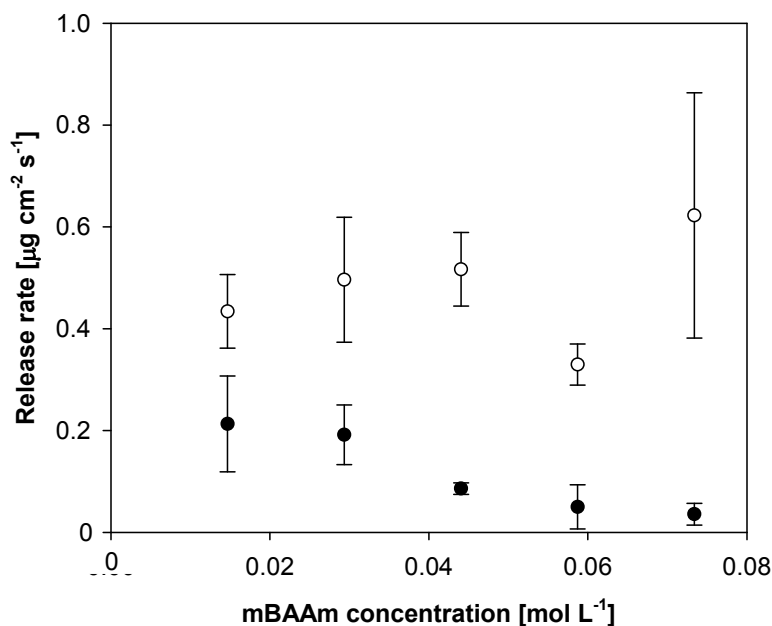

Figure 6.6: Effect of crosslinker concentration in graft layer on permeation of BSA at 20ºC (●) and 50ºC (O). *Grafting conditions*: [NIPAAm]: 2.0 M; [BP]: 0.10 M; irradiation time: 30 min.

However, in the current work, the observed decrease in permeation below the LCST, as well as the constant permeation above the LCST, can be explained bearing in mind the SEM observation, that the graft layer only partially covers the membrane surface in the dry state (resembling the collapsed state of the hydrogel) above the LCST. Furthermore, this layer is formed on top instead of inside the pores of the membrane, presumably with a limited number of anchoring points. Above the lower critical solution temperature (LCST) of the hydrogel, the graft layer is in the shrunken state, and the membrane surface is not completely covered, resulting in permeation through the open membrane pores. Provided the grafting degree is high enough, the swollen hydrogel covers the membrane completely below the LCST, thus preventing permeation of BSA. As the grafting degree decreases, an increasing number of pores remain uncovered in the fully swollen state,

130

allowing diffusion of BSA through the open membrane pores. In contrast, the permeation above the LCST is independent of the grafting degree, and presumably depends on the number of anchoring points. This can be assumed to be practically independent of crosslinker concentration, since it mainly depends on the amount of surface free radicals present during the grafting process, which in turn depends on the photoinitiator concentration and to a lesser extent on the concentration of vinyl species available for polymerization. The amount of crosslinker never exceeds 5% of the concentration of monomer, thus hardly influencing the number of grafts attached to the surface. Therefore, when the network contracts at higher temperatures, the gel collapses towards the anchoring points, thus opening approximately the same number of pores, independent of grafting degree. A representation of the proposed mechanism is schematically illustrated in Figure 6.7.
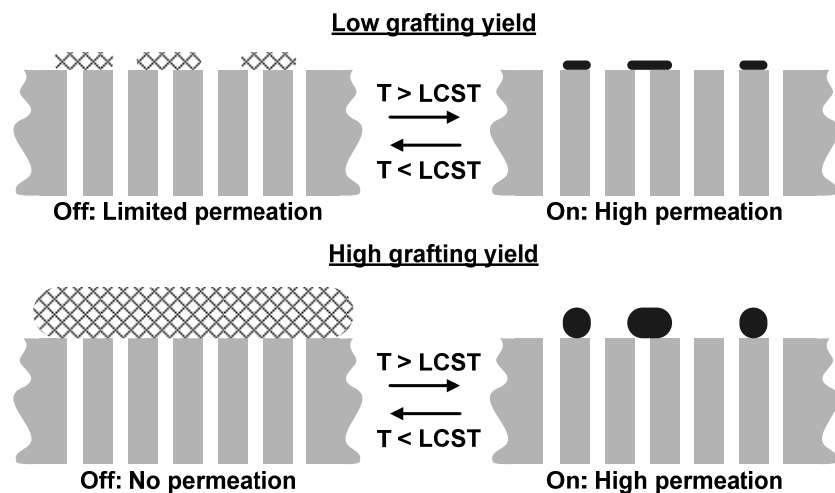
Figure 6.7: Proposed mechanism of thermoresponsive switching. An important difference with the mechanisms in Figure 6.1, is that permeation is now controlled by swelling and contracting of small gel networks anchored to the surface and covering the pores, instead of swelling and contracting of individual polymer grafts distributed homogeneously over the membrane surface. In this mechanism, positive thermoresponsivity (i.e. on-state above the LCST) is always achieved, and as long as the grafting degree is sufficiently high, negligible permeation in the off-state can be obtained.

In this mechanism, the limiting factor for permeation is not an effective pore diameter due to the graft layer narrowing the pore, nor is it the mesh size of the crosslinked hydrogel. In fact, the pore size of the neat membrane determines which species are able to

permeate. As the number of grafts is not assumed to be affected, the available area for permeation is approximately the same for all membranes above the LCST. Naturally, permeation through these grafted membranes is lower in comparison to blank membranes, as some pores remain covered by the collapsed graft layer. An important advantage of this switching mechanism is that it offers the possibility of obtaining higher fluxes in the on-state. The permeating species is not limited by pore-narrowing due to grafts filling or partially covering the pores in the shrunken state.
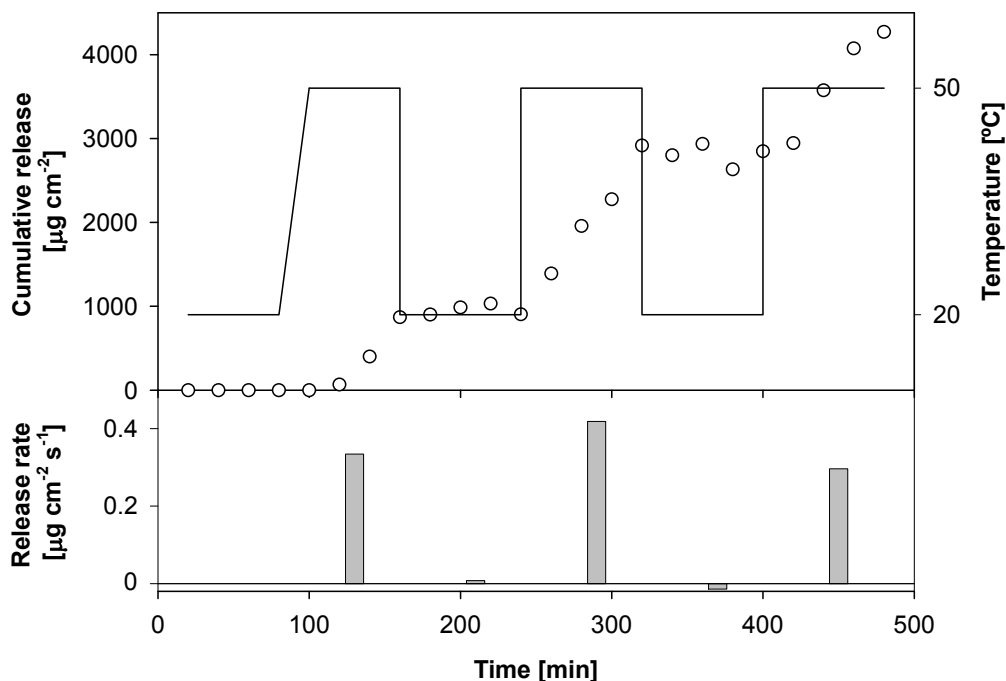
Figure 6.8: Repeated on/off-switching of crosslinked grafted membrane. The temperature (——) in the off- and on-situation is 20 and 50ºC, respectively. Top: cumulative release (O); bottom: release rate. *Grafting conditions*: [NIPAAm]: 2.0 M; [BP]: 0.10 M; [mBAAm]: 0.073 M; irradiation time: 30 min.

To demonstrate reversible on/off-switching of BSA permeation, the membrane with the highest grafting degree is repeatedly heated above and cooled below the LCST of the grafted membrane (Figure 6.8). At 20ºC, no BSA permeation is detected over a period of 80 minutes, whereas at 50ºC a reproducible amount of BSA passes through the membrane. The response to a change in temperature is very fast. There is only a lag in permeation in the first heating step, due to the fact that the temperature was gradually increased from 20 to 50ºC, whereas the other cycles involved an instantaneous change in

132

temperature. Above the LCST, the permeation rate of BSA is a factor 2.2 lower than permeation through an ungrafted membrane, which indicates that approximately half of the membrane surface is covered by the hydrogel in the on-state (shrunken state). In order for the surface of the membrane to become completely covered by the hydrogel layer in the swollen state (i.e. surface area increase by a factor of 2.2), and assuming equal swelling of the hydrogel in all directions, the thickness of the hydrogel should increase by a factor of $\sqrt{2.2}$. This results in a total minimum required swelling ratio of 3.3, which is entirely reasonable for a pNIPAAm hydrogel [33,34].

6.4 Design of an LCST based drug delivery device

Based on the thermoresponsive mechanism described in this chapter, a drug delivery device can be designed to release relatively large drug molecules, such as peptide hormones. Although any temperature trigger can be used in combination with the LCST, the focus in this section is on the NIR technology presented in this thesis. The device should comprise of: (1) a drug reservoir surrounded by (2) a highly porous polymeric membrane containing an NIR dye which is (3) grafted with a crosslinked p(NIPAAm) copolymer exhibiting an LCST around 43ºC. This temperature is just above the fever temperature, so that no undesired release occurs when a patient falls ill.

In order to prepare a porous membrane, several methods exist besides the track-etched membranes used in this work, e.g. sintering of polymer particles, stretching of (semi-) crystalline polymer films, and a variety of phase inversion approaches [35]. The most common commercially applied method, immersion precipitation, is a phase inversion approach. It is based on solvent exchange occurring when a viscous polymer solution is immersed in a non-solvent for the polymer. Demixing occurs when the polymer phase becomes thermodynamically unstable. The resulting membrane morphology depends on a large number of parameters, e.g. viscosity of the polymer solution, solvent/nonsolvent pair, temperature, and other additives, which is not discussed here. For the sake of argument, it is assumed that the correct parameters can be obtained.

There are two basic membrane designs, i.e. a flat sheet and a tubular membrane. Examples of possible procedures for the preparation of a drug delivery device based on these designs are illustrated in Figure 6.9. In the case of a flat sheet membrane, a
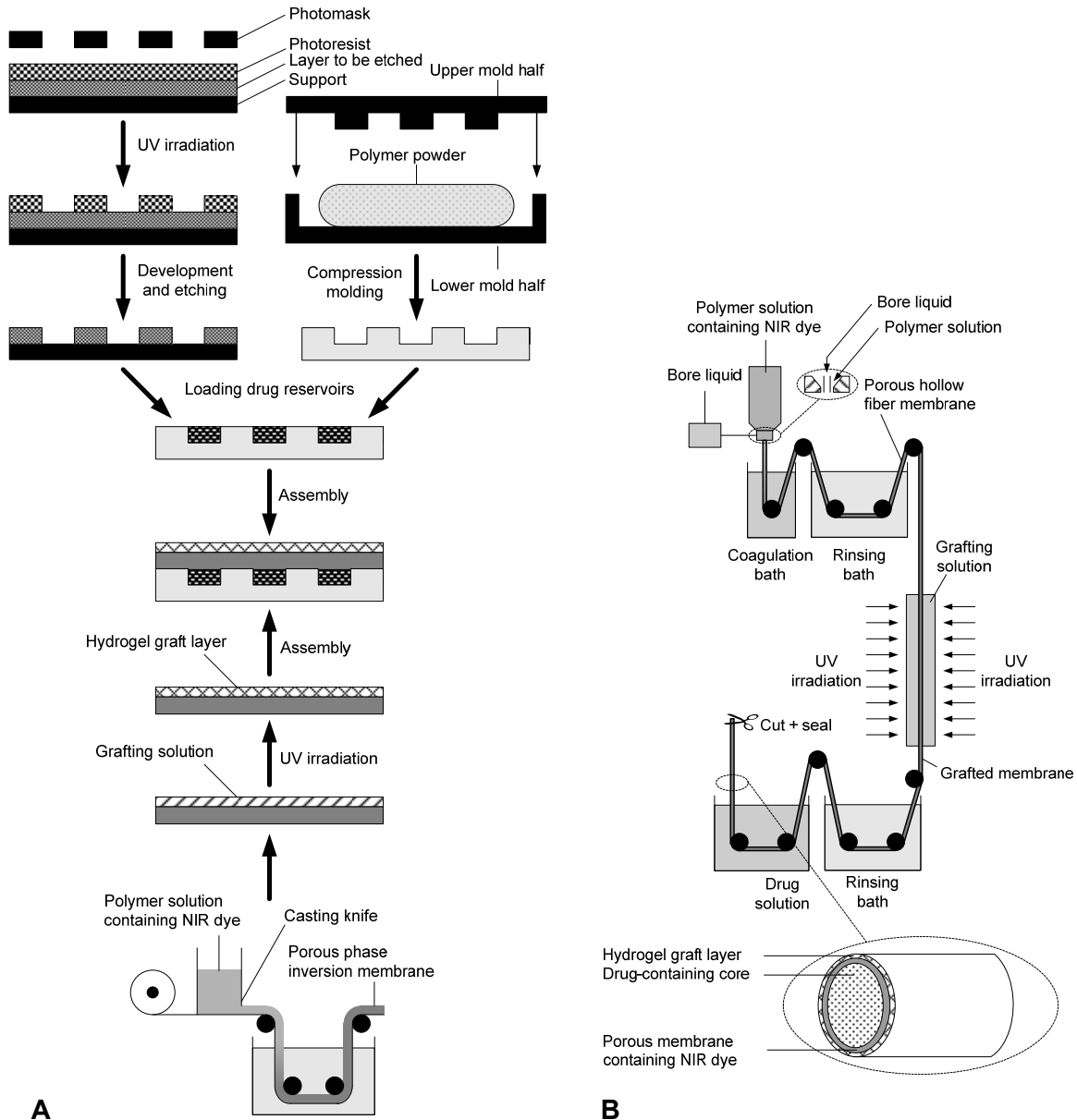
Figure 6.9: Process for preparation of LCST based drug delivery devices for NIR-induced on-demand release. The device can be based on a flat sheet membrane (**A**) or a hollow fiber membrane (**B**). Immersion precipitation and spinning process are an adaptation from Figures III-5 and III-6 in [35].

sequential procedure is followed, in which the different components are prepared independently, followed by lamination. The flat sheet design in Figure 6.9A consists of a solid support with a compartment for the active ingredients. The support can be a lithographically fabricated microchip (optionally with multiple compartments), or a dense (compression molded) polymeric support. The compartments can then be loaded with

drugs in either a liquid or suspension form, or a (semi-)solid form, like a hydrogel. The compartments are subsequently sealed with an NIR-responsive grafted membrane. The membrane is prepared by immersion precipitation in the presence of the NIR dye, after which grafting is performed as is described in this chapter. The membrane should exhibit as high a porosity as is acceptable without compromising its mechanical stability. The exact pore size is not crucial, as long as the pores allow permeation of the drug.

A tubular design may allow (semi-)continuous processing, although the process is by no means straightforward (Figure 6.9B). First, a hollow fiber membrane is prepared using a wet-spinning process in the presence of an NIR dye [35]. The resulting fiber can then be directly fed into a tubular reactor together with the NIPAAm reaction solution while being continuously irradiated by UV [36]. Subsequently, the resulting grafted hollow fiber membrane passes through a rinsing bath to get rid of residual monomer and initiator, followed by a passage through a drug-containing bath, after which the hollow fiber membrane is cut and sealed at both ends. Alternatively, if addition of the drug in solid form is required or preferred, the passage through the drug-containing bath should be omitted, and filled at a later stage, making the process semi-continuous. The advantage of this design over a flat geometry is an increased surface area available for release, as well as a more practical shape for implantation in the human body. As long as the diameter of the implant is not too large, injection of the implant would be possible as opposed to surgical implantation.

The effect of permeant size has not been investigated in this work, but it is obvious that this mechanism is more easily applied as the drug molecules become larger. Successful application of this technology to smaller molecules depends on the smallest achievable mesh size, without losing all swelling capability. If the minimum mesh size is still too large, small molecules will diffuse through the swollen hydrogel, thus exhibiting release in the off-state. Measuring the permeation of a series of oligo(ethylene glycol)s, or another homologous series, above and below LCST would reveal the order of magnitude for the size of the molecules for which this technology is still applicable.

6.5 Conclusions

Repeated on/off-switching of the model protein bovine serum albumin through hydrogel-grafted membranes has been demonstrated, in which permeation can be triggered by temperature. If the grafting degree of the hydrogel on the membrane is sufficiently high to cover the membrane completely in the swollen state, the off-permeation is negligible below the LCST. Above the LCST, the pore size of the ungrafted membrane determines whether solutes can pass through the membrane. This mechanism differs from thermoresponsive membranes described previously, in which permeation is governed by either the effective pore size of the membrane due to swelling and contraction of the hydrogel, or the mesh size of the hydrogel network itself, and can lead to higher fluxes in the on-state. This technology offers promising possibilities for designing on-demand drug delivery implants that can be triggered internally by local hyperthermia, or externally by any kind of source capable of supplying heat to the implant, such as ultrasound, magnetism or the NIR technology discussed in this thesis.

References

[1]   West, J. L. Pulsed polymers. *Nature Mater.* **2**, 709-710 (2003).

[2]   Richardson Grayson, A. C. *et al.* Multi-pulse drug delivery from a resorbable polymeric microchip device. *Nature Mater.* **2**, 767-772 (2003).

[3]   Peppas, N. A. Hydrogels and drug delivery. *Curr. Opin. Colloid Interface Sci.* **2**, 531-537 (1997).

[4]   Langer, R. & Peppas, N. A. Advances in biomaterials, drug delivery, and bionanotechnology. *AIChE J.* **49**, 2990-3006 (2003).

[5]   Gupta, P., Vermani, K., Garg, S. Hydrogels: from controlled release to pH-responsive drug delivery. *Drug Discov. Today* **7**, 569-579 (2002).

[6]   Jeong, B., Kim, S. W., Bae, Y. H., Thermosensitive sol-gel reversible hydrogels. *Adv. Drug Delivery Rev.* **54** 37-51 (2002).

[7]   Park, Y. S., Ito, Y., Imanishi, Y. Permeation control through porous membranes immobilized with thermosensitive polymer. *Langmuir* **14**, 910-914 (1998).

[8]   Chen, G. & Hoffman, A. S. Graft copolymers that exhibit temperature-induced phase transitions over a wide range of pH. *Nature* **373**, 49-52 (1995).

[9]   Yoshida, R., Sakai, Y., Okano, T., Sakurai, Y. Modulating the phase transition temperature and thermosensitivity in *N*-isopropylacrylamide copolymer gels. *J. Biomater. Sci., Polym. Ed.* **6**, 585-598 (1995).

[10]   Shild, H. G., Poly(*N*-isopropylacrylamide): experiment, theory and application. *Prog. Polym. Sci.* **17**, 163-249, (1992).

[11] Iwata, H., Oodate, M., Uyama, Y., Amemiya, H., Ikada, Y. Preparation of temperature-sensitive membranes by graft polymerization onto a porous membrane. *J. Membr. Sci.* **55**, 119-130 (1991).

[12] Feil, H., Bae, Y. H., Feijen, J., Kim, S. W. Effect of comonomer hydrophilicity and ionization on the lower critical solution temperature of *N*-isopropylacrylamide copolymers. *Macromolecules* **26**, 2496-2500 (1993).

[13] Yoshida, R. *et al.* Positive thermosensitive pulsatile drug release using negative thermosensitive hydrogels. *J. Controlled Release* **32**, 97-102 (1994).

[14] Gutowska, A. *et al.* Squeezing hydrogels for controlled oral drug delivery. *J. Controlled Release* **48**, 141-148 (1997).

[15] Brazel, C.S. & Peppas, N.A. Pulsatile local delivery of thrombolytic and antithrombotic agents using poly(*N*-isopropylacrylamide-co-methacrylic acid) hydrogels, *J. Controlled Release* **39**, 57-64 (1996).

[16] Okano, T., Bae, Y. H., Jacobs, H., Kim, S. W. Thermally on-off switching polymers for drug permeation and release. *J. Controlled Release* **11** 255-265 (1990).

[17] Peng, T. & Cheng, Y.-L. Temperature-responsive permeability of porous PNIPAAm-g-PE membranes. *J. Appl. Polym. Sci.* **70**, 2133-2142 (1998).

[18] Xie, R., Li, Y., Chu, L.-Y. Preparation of thermo-responsive gating membranes with controllable response temperature. *J. Membr. Sci.* **289**, 76-85 (2007).

[19] Ichikawa, H. & Fukomori, Y. A novel positively thermosensitive controlled-release microcapsule with membrane of nano-sized poly(*N*-isopropylacrylamide) gel dispersed in ethylcellulose matrix, *J. Controlled Release* **63**, 107-119 (2000).

[20] Xie, R. *et al.* Characterization of microstructure of poly(*N*-isopropylacrylamide)-grafted polycarbonate track-etched membranes prepared by plasma-graft pore-filling polymerization. *J. Membr. Sci.* **258**, 157-166 (2005).

[21] Chu, L.-Y., Niitsuma, T., Yamaguchi, T., Nakao, S. Thermoresponsive transport through porous membranes with grafted PNIPAM gates. *AIChE J.* **49**, 896-909 (2003).

[22] Li, Y., Chu, L.-Y., Zhu, J.-H., Wang, H.-D., Xia, S.-L., Chen, W.-M. Thermoresponsive gating characteristics of poly(*N*-isopropylacrylamide)-grafted porous poly(vinylidene fluoride) membranes. *Ind. Eng. Chem. Res.* **43**, 2643-2649 (2004).

[23] Reber, N., Küchel, A., Spohr, R., Wolf, A., Yoshida, M. Transport properties of thermo-responsive ion track membranes. *J. Membr. Sci.* **193**, 49-58 (2001).

[24] Alem, H. *et al.* Microstructure and thermo-responsive behavior of poly(*N*-isopropylacrylamide) brushes grafted in nanopores of track-etched membranes. *J. Membr. Sci.* **308**, 75-86 (2008).

[25] Lue,, S.J. Hsu, J.-J., Chen, C.-H., Chen, B.-C. Thermally on-off switching membranes of poly(*N*-isopropylacrylamide) immobilized in track-etched polycarbonate films, *J. Membr. Sci.* **301**, 142-150 (2007).

[26] Yang, B. & Yang, W. Thermo-sensitive switching membranes regulated by pore-covering polymer brushes. *J. Membr. Sci.* **218**, 247-255 (2003).

[27] Wu, G., Li, Y., Han, M., Liu, X. Novel thermo-sensitive membranes prepared by rapid bulk photo-grafting polymerization of *N,N*-diethylacrylamide onto the microfiltration membranes Nylon, *J. Membr. Sci.* **283**, 13-20 (2006).

[28] Liang, L., Feng, X., Peurrung, L., Viswanathan, V. Temperature-sensitive membranes prepared by UV photopolymerization of *N*-isopropylacrylamide on a surface of porous hydrophilic polypropylene membranes. *J. Membr. Sci.* **162**, 235-246 (1999).

[29] Lokuge, I., Wang, X., Bohn, P.W. Temperature-controlled flow switching in nanocapillary array membranes mediated by poly(*N*-isopropylacrylamide) polymer brushes grafted by atom transfer radical polymerization. *Langmuir* **23**, 305-311 (2007).

[30] Hesampour, M., Huuhilo, T., Mäkinen, K., Mänttäri, M., Nyström, M. Grafting of temperature sensitive PNIPAAm on hydrophylised polysulfone UF membranes. *J. Membr. Sci.* **310**, 85-92 (2008).

[31] Yang, W. & Rånby, B. Bulk surface photografting process and its applications. II Principle factors affecting surface photgrafting. *J. Appl. Polym. Sci.* **62**, 545-555 (1996).

[32] Ma, H., Davis, R.H., Bowman C.N. A novel sequential photoinduced living graft polymerization. *Macromolecules* **33**, 331-335 (2000).

[33] Friebe, A. & Ulbricht, M. Controlled pore functionalization of poly(ethylene terephthalate) track-etched membranes via surface-initiated atom transfer radical polymerization. *Langmuir* **23**, 10316-10322 (2007).

[34] Zhao, Z., Li, Z., Xia, Q., Xi, H., Lin, Y. Fast synthesis of temperature-sensitive PNIPAAm hydrogels by microwave irradiation., *Eur. Polym. J.* **44**, 1217-1224 (2008).

[35] Mulder, M., *Basic Principles of Membrane Technology*, 2nd ed., 71-138 (Kluwer Academic Publishers, Dordrecht, 1996).

[36] Goma-Bilongo, T., Akbari, A., Clifton, M. J., Remigy, J.-C. Numerical simulation of a UV photografting process for hollow-fiber membranes. *J. Membr. Sci.* **278**, 308-317 (2006).

138

CHAPTER 7

Challenges and Prospects of the Glass Transition Temperature as a Switch for On-Demand Drug Delivery

Abstract

Several aspects concerning the success of the glass transition switch in drug delivery applications is addressed. First, the influence of ibuprofen on enthalpy recovery as a measure for polymer relaxation processes following an on-switch is discussed, suggesting that faster relaxation in the presence of ibuprofen is solely attributed to its plasticizing effect. Then, preparation of polymer spheres as a means to enhance the release rate due to an increased surface area available for release is dealt with, leading to the conclusion that in contrast to suspension polymerization, a solvent evaporation approach is a viable method to prepare drug and dye containing polymer spheres. Subsequently, the potential of a light emitting diode (LED) as an alternative NIR source is discussed, which is especially important for patient-controlled self-administration in a home environment. Finally, the prospects of the glass transition switch are addressed, specifically focusing on clinical applications.

7.1 Introduction

In this thesis, on-demand drug delivery based on the glass transition switch using a near-infrared laser source as an external trigger has been demonstrated. Although this work provides a proof of principle, even achieving non-invasive triggering *in vivo*, several hurdles need to be overcome before a fully operational drug delivery technology suitable for clinical and self-administration applications is to reach the market. This chapter deals with some of these hurdles, first focusing on the time-dependent properties of polymers in the vicinity of T_g, and the consequent implications for on-demand drug delivery (section 7.2). In order to enable appreciable dosing within an acceptable time frame for triggering, section 7.3 deals with increasing the surface area available for mass transfer using drug loaded polymer microspheres, as briefly introduced in Chapter 3. In section 7.4, the use of a light emitting diode (LED) as a less costly alternative triggering device compared to the NIR laser used in this research is addressed. Finally, the prospects and future development of this delivery technology are discussed, specifically where clinical application is concerned.

7.2 Relaxation phenomena in glassy polymers

7.2.1 Introduction

Even after decades of research, the glass transition still remains an elusive phenomenon, warranting further study to understand the fundamentals behind this transition [1-3]. The physical state of polymers below T_g is characterized by strong non-ergodic behavior, i.e. depending on the thermal history, among which the time and temperature of annealing and the rate of cooling to below T_g (Figure 7.1A). Coming from temperatures higher than T_g, where the polymer essentially exists as an equilibrium liquid, the viscosity (and many other dynamic properties) increasingly deviate from an Arrhenius-relationship as T_g is approached. This is often described by the empirical Vogel-Tammann-Fulcher (VTF) equation [4-6], or more frequently in the polymer field by the Williams-Landel-Ferry (WLF) equation [7], used in the free volume theory described in Chapter 5. Around T_g, relaxation processes of polymer chains become comparable to experimental time-scales, resulting in time-dependent properties in this region. Far below T_g, the relaxation

processes become so slow, that the polymers can again be assumed to have time-independent properties, although the properties do depend on the (thermal) path followed to get there.
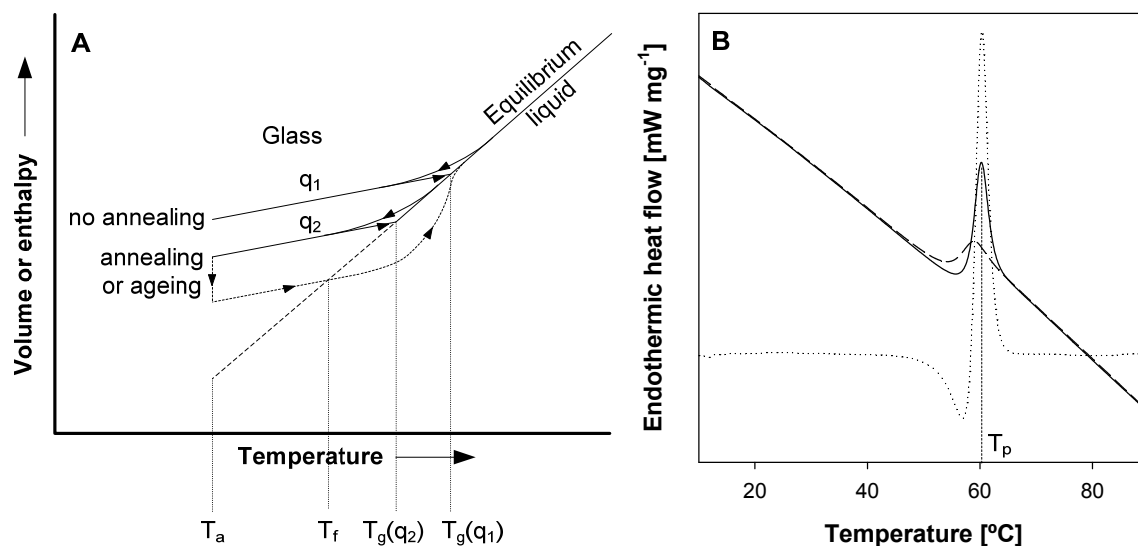

Figure 7.1: Effect of thermal history in polymers around T_g. **A** Schematic illustration of temperature dependence of extensive thermodynamic properties, such as volume and enthalpy, around T_g, adapted from ref. 8. Arrows indicate the direction of volume/enthalpy change. T_a is the annealing temperature, q_1 and q_2 are cooling rates, where $q_1 < q_2$, and T_f is the fictive temperature, which reduces as ageing proceeds and represents the equilibrium volume if it were instantaneously removed to that temperature [9]. **B** Representative experimentally determined DSC-scans (from 0 to 100°C, heating rate: 10°C min^{-1}) of a polylactide sample (17.68 mg) aged for 12 h at 37°C, after equilibration at 100°C for 2 minutes followed by rapid cooling to the annealing temperature of 37°C (details in section 7.2.2). ———: scan after 12 h at 37°C (1st run), - - - -: scan immediately after 1st run, serving as baseline (2nd run), ·········: Subtraction of 2nd from 1st run, T_p: peak temperature (section 7.2.3).

Although Figure 7.1A insinuates that the glass transition is represented by a sharp transition temperature, Figure 7.1B illustrates that the glass transition is actually a temperature trajectory, which is additionally complicated by the fact that it depends on the cooling rate, leading to various definitions of T_g. A commonly applied heating and cooling rate is 10°C min^{-1}, which leads to an 'onset' definition of T_g (i.e. where the enthalpy first starts to increase above the glassy state background) around a relaxation time of 100 s [e.g. 10]. The 'midpoint' of T_g is defined at the temperature where the heat

capacity (which is the temperature derivative of enthalpy) has risen to half of its final increase from the glassy to rubbery state. The latter is the most commonly employed definition, which is also used throughout this thesis.

As is illustrated in Figure 7.1A, the experimentally determined position of T_g depends on the cooling rate. Moreover, maintaining the polymer sample at a fixed annealing temperature for a certain period of time below T_g results in a decrease in volume and enthalpy, termed volume and enthalpy relaxation. A lot of research has focused on studying volumetric relaxation by dilatometric measurements, or enthalpy relaxation by differential scanning calorimetry (DSC) due to the more widespread availability of DSC-equipment, to gain understanding of sub-T_g processes. In this thesis, the central issue of attention is drug diffusion, which is influenced by the amount of available free volume (Chapter 5), and is thus presumably affected by volume relaxation processes. In addition, the presence of additives inside a polymer matrix may affect these relaxation processes. This section therefore focuses on whether additives (i.e. drug molecules) influence relaxation processes in polymers, using the more facile DSC-technique to investigate enthalpy relaxation.

There are two points of attention when using DSC to quantify polymer relaxation. First of all, enthalpy relaxation is not necessarily representative for volume relaxation, and their timescales can therefore differ [11]. Secondly, where the use of dilatometry directly measures a decrease in volume over time (i.e. volume relaxation), enthalpy relaxation involves the measurement of the *regain* in enthalpy on reheating of a polymer sample to above T_g (Figure 7.1B). A better term would therefore be enthalpy recovery, which is determined by retardation times rather than relaxation times [10]. The non-exponentiality of relaxation and retardation times implies that these times can be distinctly different from each other, so that a comparison of the retardation of one property (e.g. enthalpy) cannot be compared directly with the relaxation of another (e.g. volume). Nevertheless, enthalpy recovery is used here to present at least a qualitative comparison between relaxation properties of polymers with and without additives.

Most studies involving relaxation phenomena in polymers focus on determination of the different parameters in the Tool-Narayanaswamy-Moynihan (TNM) or Kovacs-Aklonis-

Hutchinson-Ramos (KAHR) model [10], which take into account the nonlinear and non-exponential behavior below T_g. Since the principal goal in this research is to qualitatively study the effect of additives on relaxation, these parameters are not determined as such, but a comparison of enthalpy recovery between different materials is performed.

7.2.2 *Materials and methods*

7.2.2.1 *Materials*

Poly(*D,L*-lactic acid) (PLDL, M_w: 460 kDa relative to PS standard, $T_g \sim 56^\circ C$) was obtained from Purac, and stored in a freezer (-18ºC) until used. Poly(*n*-butyl methacrylate-*co*-methyl methacrylate) (PBMA-MMA, M_w: 150,000 g mol^{-1}, $T_g \sim 48^\circ C$) was purchased from Aldrich. Dichloromethane (≥99.5%) (DCM) was received from Merck KGaA. Ibuprofen was obtained from Genfarma. All chemicals were used as received.

7.2.2.2 *Methods*

7.2.2.2.1 <u>Solvent casting</u>

Solvent casting was performed using a 16% (w/w) polymer solution. Typically, the solution contained 1.0 g of polymer, 4 mL DCM, and optionally 1% (w/w polymer) of ibuprofen. After stirring with a magnetic stirrer for two hours to ensure complete dissolution, the solution was cast in a glass Petri dish (∅: 76 mm) and covered with perforated Parafilm® to allow slow evaporation of the solvent in the fume hood. After several days, the resulting polymer film (typically around 200 μm in thickness) was removed from the Petri dish. Finally, it was placed in a vacuum oven overnight.

7.2.2.2.2 <u>Differential scanning calorimetry (DSC)</u>

Enthalpy recovery measurements were performed on a Perkin-Elmer differential scanning calorimeter (Pyris Diamond). 10-20 mg of the polymer samples prepared by solvent casting was placed in aluminum pans (50 μL). Dry nitrogen was applied as purging gas, cooling during the temperature cycles proceeded using an Intracooler 1P (Perkin Elmer). All DSC runs were performed without baseline correction (thus explaining the downward slope in Figure 7.1B), as calculations with raw data was preferred. The calculations were

carried out with the difference curve, i.e. the subtraction between 2 runs, thus not influencing the results.

For annealing times of 12 hours and less, ageing was performed inside the DSC-apparatus using the following temperature program:

1. Maintain at 0ºC for 2 minutes
2. Heat from 0 to 100ºC at 10ºC min^{-1}
3. Maintain at 100ºC for 2 minutes
4. Cool from 100ºC to annealing temperature at 50ºC min^{-1} (quench)
5. Maintain at annealing temperature for a certain time
6. Cool from annealing temperature to 0ºC min^{-1} at maximum rate
7. Maintain at 0ºC for 2 minutes
8. Heat from 0 to 100ºC at 10ºC min^{-1} (1st run)
9. Maintain at 100ºC for 2 minutes
10. Cool from 100 to 0ºC at 10ºC min^{-1}
11. Maintain at 0ºC for 2 minutes
12. Heat from 0 to 100ºC at 10ºC min^{-1} (2nd run)
13. Maintain at 100ºC for 2 minutes

For annealing times longer than 12 hours, the samples were placed in an oven at 100ºC for 1 h, after which the samples (contained within a plastic sample holder to protect the DSC pan from water) were rapidly transferred to a water bath at the desired annealing temperature. After a certain annealing time, the samples were rapidly transferred to the DSC-apparatus, where the same temperature program was performed, starting from step 7. In this approach, it was assumed that step 4 is satisfactorily mimicked by transferring the samples from the oven to the water bath. A similar value for the enthalpy recovery was indeed found for the same annealing time.

7.2.3 Results and discussion

In the determination of relaxation/retardation phenomena from calorimetric measurements, there are two methods that can be applied. As explained in section 7.2.1, the increase of enthalpy recovery (δ_H) in time gives an indication of relaxation processes. Alternatively, the shift of the peak temperature T_p (Figure 7.1B) can be followed in time. This temperature solely depends on the heating and cooling rate, the annealing temperature, and the amount of annealing, which is directly related with annealing time

and measured by the amount of enthalpy recovery. In theory, plotting δ_H versus T_p should result in a straight line, if thermal lag is taken into account [12]. Thermal lag can be quantified by measuring enthalpy retardation in time at several heating rates [13]. As this study merely aims at qualitative determination, quantification of the influence of thermal lag has been omitted here.
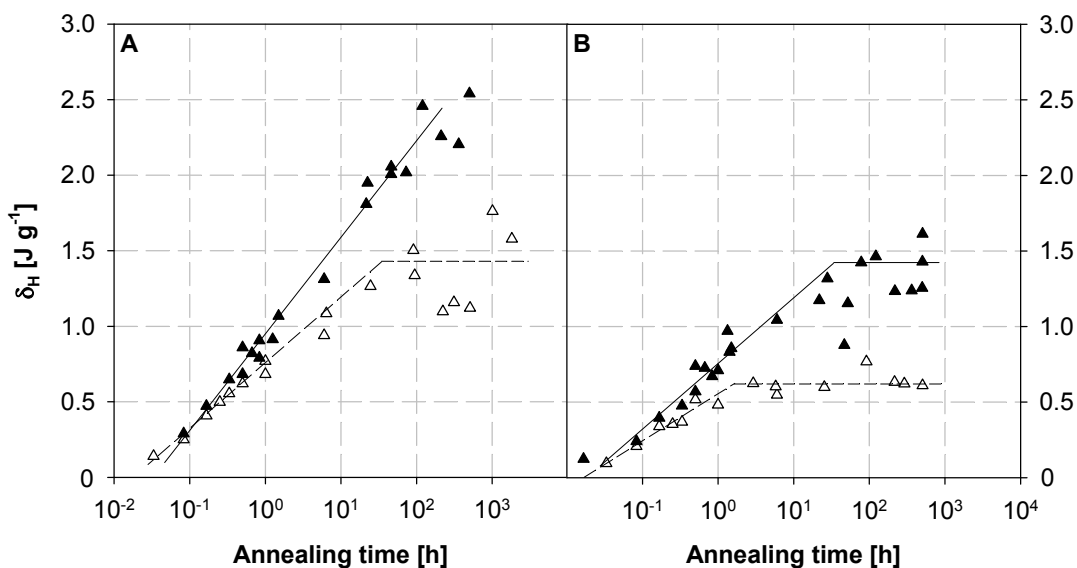

Figure 7.2: Enthalpy recovery in (**A**) PBMA-MMA and (**B**) PBMA-MMA containing 1% ibuprofen. Closed symbols represent an annealing temperature of 37ºC, open symbols represent an annealing temperature of 40ºC. Inserted lines serve as guides to the eye.

Figure 7.2 illustrates the effect of addition of ibuprofen on the relaxation behavior in a polymethacrylate copolymer in terms of δ_H. Annealing has been performed at two different temperatures of 37 and 40ºC, which is approximately 11 and 8ºC below the glass transition temperature of the pure polymer, respectively. The enthalpy recovery at infinite times increases with decreasing annealing temperature (Figure 7.1A), as is also obvious from Figure 7.2. At an annealing temperature of 40ºC, the equilibrium value for the samples containing 1% ibuprofen has clearly been reached after approximately 2 hours. Due to considerable scatter of the data, especially at higher annealing times, it is hard to definitely state whether complete relaxation for the other samples has been reached. However, it is clear from this figure that the relaxation rate and extent of relaxation of PBMA-MMA at 40ºC, and PBMA-MMA with ibuprofen at 37ºC are very

similar. The difference in annealing temperatures of 3ºC coincides with the plasticizing effect of ibuprofen in the polymer matrix, suggesting that the additive does not influence relaxation other than affecting the position of T_g.
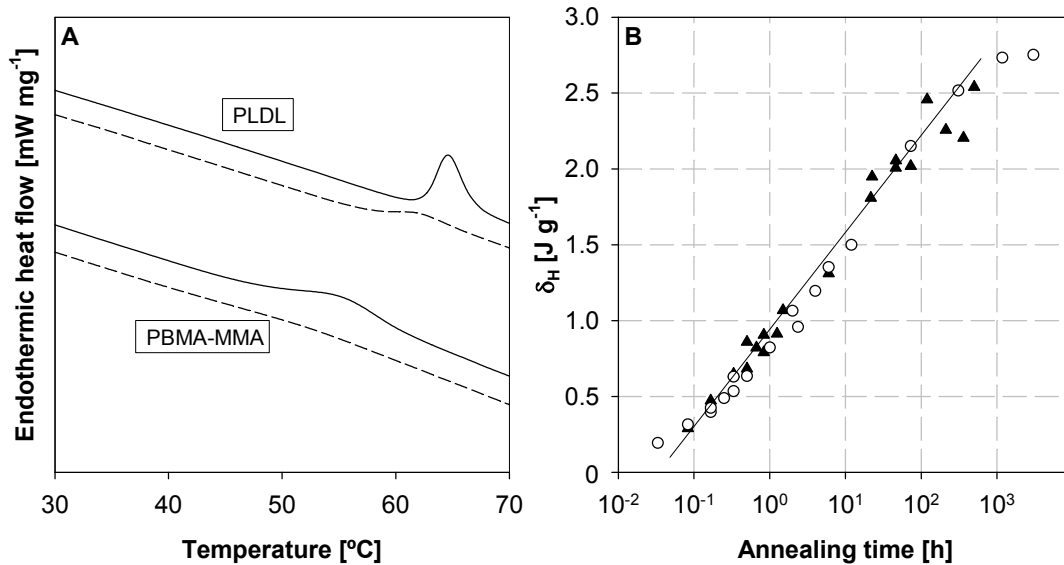

Figure 7.3: Comparison of relaxation in PBMA-MMA and PLDL. **A** DSC scans of samples annealed for 72 h at 37ºC (——) and scans immediately after first run, i.e. reference run (- - - -) as was explained in Figure 7.1B. **B** Enthalpy relaxation in PBMA-MMA (▲) and PLDL (O) at 37ºC.

Since the *in vitro* and *in vivo* studies have been performed with a polylactide, it is interesting to compare this polymer with PBMA-MMA. Figure 7.3A illustrates the difference generally observed between a methacrylate polymer and the polylactide used in this research. PLDL has a much stronger and narrower glass transition, as evidenced in both the annealed (——) and unannealed (- - - -) state. Even though there is a marked difference between the glass transitions of these two polymers, no difference is observed in their relaxational behavior (Figure 7.3B). This is rather surprising, since there is a difference in glass transition temperatures between the two polymers of approximately 8ºC, implying that PLDL should be in a more rigid state than PBMA-MMA at 37ºC, thus commonly leading to slower relaxation. Possibly, this unexpected behavior can be explained by the more linear structure of PLDL, which may allow easier reorientation of the polymer chains, resulting in relatively fast relaxation. If this is indeed the case, it

would in fact be beneficial for 'closing' of the polymer following an on-switch, as this results in a more rapid decrease in free volume.
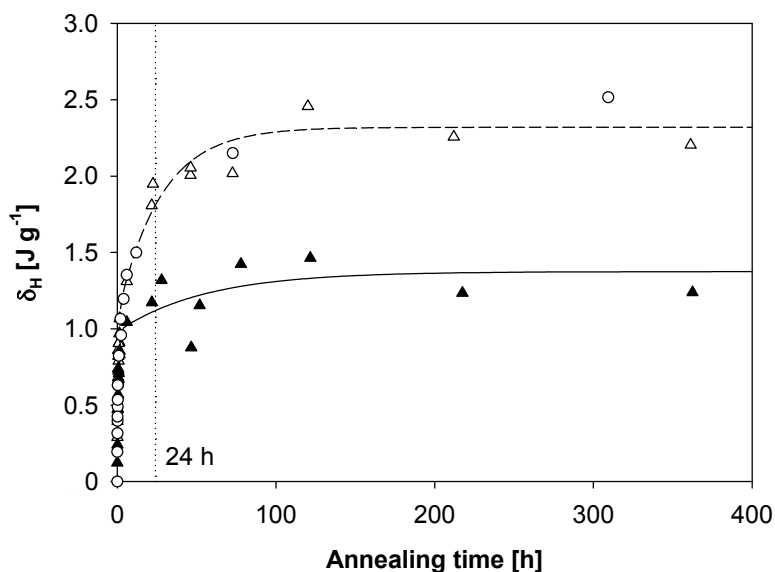

Figure 7.4: Enthalpy relaxation for PBMA-MMA (△), PLDL (○), and PBMA-MMA containing 1% ibuprofen (▲) at 37°C presented on a regular time scale.

In conclusion, the enthalpy recovery results suggest the effect of the addition of drugs on polymer relaxation processes is solely related to the plasticizing effect of the drug. It would seem that at body temperature, it takes several days or even weeks for the polymer to fully relax. However, it should be kept in mind that the graphs in this section have been presented on a logarithmic time-scale. When plotted on a regular time scale, it becomes obvious that most of the relaxation takes place within the first day (Figure 7.4). A more detailed investigation of volume relaxation at small time scales in the order of minutes, most preferably in combination with drug release studies, would have to indicate whether these relaxation processes noticeably affect drug release in the off-state.

7.3 Preparation of polymer spheres

7.3.1 Introduction

As discussed in Chapter 3, the use of polymer spheres enhances the surface area available for mass transfer. Spheres with a size of 100-200 μm incorporated in a rod-shaped permeable matrix can result in an increase in release rate in the order of 10-20 times compared to a solid polymeric implant of the same dimensions (Figure 3.16). Preferably, the spheres should contain both the drugs to be released and the NIR dye. Since the dye coatings discussed in Chapter 3 are in the order of several tens of microns (typically 30 to 50 μm), it hardly seems worthwhile to prepare the spheres in a two-step process, in which the polymer spheres are first loaded with drugs, followed by a coating step. Instead, a preparation procedure should be developed, in which the dye and drug are incorporated into the polymer matrix in a single step. In this chapter, two such procedures are discussed, i.e. a suspension polymerization and a solvent evaporation approach, both in the presence of the dye and drug. In a second step, these spheres are incorporated in a matrix, which either consists of a rubbery polymer matrix or a hydrogel. As has been discussed in Chapter 3, the former is preferred due to its superior insulating properties, although it is at the expense of the rate of mass transfer. Incorporation of the spheres in a matrix could proceed by a compression molding step, in which the spheres are thoroughly mixed with the rubbery polymer in granulated form, followed by a compression step into the desired (rod-)shape. Compression can be performed at relatively low temperatures, due to the low T_g of the rubbery encapsulating matrix, thus hardly inducing drug release from the spheres into the surrounding matrix during the production process. However, it is important to realize that if the implant is prepared a long time before implantation, the drug will slowly diffuse into the surrounding matrix (the rate determining step being diffusion from the glassy surface layer of the spheres). As the drug cannot diffuse out of the implant, the concentration level in the rubbery matrix will continuously increase, thus further accelerating diffusion of drugs out of the spheres, since the drug concentration, and thus diffusion coefficient, at the sphere/matrix interface increases. Implantation of such a device would result in a significant burst release. This may be resolved by a pretreatment step prior to implantation, in which the implant is placed in aqueous solution

at elevated temperature to induce this burst release in solution. However, a lot of (costly) drugs is lost in this way, thus limiting the shelf-life of such an implant. This section does not focus on these limitations, but on the first step of implant preparation, i.e. the preparation of the polymer spheres.

7.3.2 *Suspension polymerization*

A typical suspension polymerization is depicted in Figure 7.5. The polymerization takes place in the monomer droplets, suspended in aqueous solution by mechanical stirring. These droplets are stabilized to a certain extent by a surfactant and poly(vinyl alcohol) (PVA), but stirring is required to prevent coagulation of the droplets. The stirring speed can be used to control the size of the droplets, which can range from ~100 – 1000 μm. The initiator should be completely insoluble in water, so that emulsion polymerization in the water phase (causing the formation of small polymer spheres and instability of the suspension) is prevented.

In addition to the constituents of the organic droplets in Figure 7.5, a lipophilic drug (ibuprofen) and the NIR dye (L-IR788) can be added to this phase. Suspension polymerization of ethyl methacrylate has been performed with both peroxides (lauroyl peroxide, perkadox-16, and benzoyl peroxide) and azo-compounds (V-65 and V-70) as radical initiators, which are all reported to be insoluble in water, and should therefore not induce polymerization in the aqueous phase. However, for both the azo-compounds and lauroyl peroxide the reaction solution turned white (both in the presence and absence of drug and dye), indicative of a significant amount of emulsion polymerization, causing instability during the suspension polymerization and leading to partial coagulation of the organic droplets. In contrast, the solution remained transparent when using either benzoyl peroxide or Perkadox-16, which implies that a negligible amount of polymerization occurred in the aqueous phase, rendering these initiators suitable for suspension polymerization. It is not quite clear why these initiators perform better than lauroyl peroxide and the azo-initiators. Perhaps it is related to the water solubility of the initiator and/or formed radicals, since dissolution of even a very small amount in the aqueous phase can result in a significant amount of emulsion polymerization.
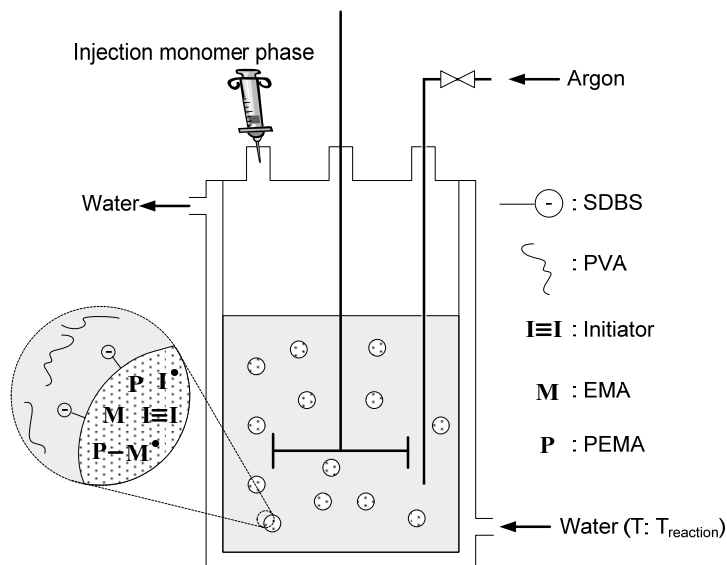
Figure 7.5: Schematic representation of a suspension polymerization set-up. Ethyl methacrylate (EMA) was used as monomer, sodium dodecyl benzene sulphonate (SDBS) and poly(vinyl alcohol) were used to stabilize the suspension. Five different initiators have been used, i.e. lauroyl peroxide, benzoyl peroxide, di(4-tert-butylcyclohexyl) peroxydicarbonate (Perkadox-16), 2-2'-azobis(2,4-dimethylvaleronitrile) (V-65), 2-2'-azobis(4-methoxy-2,4-dimethylvaleronitrile) (V-70). The reaction solution was maintained at the desired reaction temperature in a jacketed vessel and kept under argon atmosphere during the reaction to exclude oxygen. The stirrer had six blades at equal angles with a total diameter of 4.5 cm.

The addition of L-IR788 does not interfere with the polymerization process, resulting in polymer spheres of approximately the same size range (i.e. ~50 - 400 μm at a stirring speed of 300 rpm). However, in contrast to the other investigated initiators, benzoyl peroxide and Perkadox-16 resulted in a change of color of the spheres from the usual light green color of L-IR788 to a brownish color, suggesting either a chemical or physical change (i.e. aggregation). Redissolving the spheres in dichloromethane indeed results in a shift of the absorption spectrum to lower wavelengths (λ_{max}: 715 nm, negligible absorbance at 785 nm). The induced change during the polymerization is therefore irreversible, thus implying that these radicals are powerful enough to attack the dye molecule, presumably at one of the pendant groups. Apparently, these initiators are too powerful to use in conjunction with the dye. This observation, in combination with the fact that a significant amount of residual toxic monomer (several percent) is still present in the polymer spheres, has led to the conclusion that the suspension polymerization route is not a viable route towards near-infrared absorbing polymer spheres for drug delivery.

7.3.3 Solvent evaporation

The solvent evaporation approach [14] entails preparation of spheres using a pre-synthesized polymer, thus avoiding the need of polymerization during sphere formation. The polymer, drug, and NIR dye are dissolved in an organic solvent, which is usually dichloromethane. This solution is dispersed in an aqueous solution containing a stabilizer (most often poly(vinyl alcohol), PVA) by vigorous stirring. After evaporation of dichloromethane, drug and dye containing polymer spheres remain, thus providing a relatively simple method of preparation. This section merely aims to demonstrate the potential of this procedure, rather than providing an extensive study of the influence of the parameters affecting the sphere size of the resulting polymer particles, such as temperature, viscosity, amount of stabilizer, and stirring speed.

In this work, all preparation procedures were conducted at room temperature (without active cooling) and at a fixed PVA concentration of 0.4 % (w/w H_2O), typical for this evaporation procedure. After complete dissolution of PVA, 3 mL of the organic phase containing PEMA dissolved in DCM (and optionally ibuprofen or L-IR788) was rapidly injected into 50 mL PVA-solution in a 100 mL glass beaker, while stirring with a magnetic stirrer at 800 rpm. The solutions were left to stir overnight to allow DCM evaporation. The polymer spheres were then washed in water several times to remove PVA, and dried in the vacuum oven overnight prior to analysis.

Figure 7.6 displays the effect of PEMA and ibuprofen concentration in the organic phase on the size and bulk glass transition temperature of the polymer spheres. First of all, the viscosity of the organic phase determined by the PEMA concentration has a tremendous influence on the sphere size. An increasing viscosity leads to both larger spheres, as expected, and a larger sphere size distribution. The latter can presumably be explained by the fact that the simple stirrer bar used in these experiments does not create homogeneous shear forces throughout the beaker. In contrast to polymer concentration, the addition of ibuprofen has no noticeable effect on the sphere size, even up to ibuprofen concentrations of 20% (Figure 7.6A). Naturally, the T_g is lowered as the ibuprofen concentration decreases. However, the absolute value of the slopes in Figure 7.6B is slightly lower than expected based on films of ibuprofen and PEMA cast from DCM (●). This might indicate

that as the ibuprofen concentration increases, the encapsulation efficiency decreases slightly, since the driving force for ibuprofen to diffuse into the aqueous phase increases. More surprising is the absolute downward shift of these graphs as the viscosity of the organic phase increases. Most likely, DCM has been entrapped inside these larger polymer spheres, which is an important aspect to clarify before these spheres can be used in drug delivery applications.
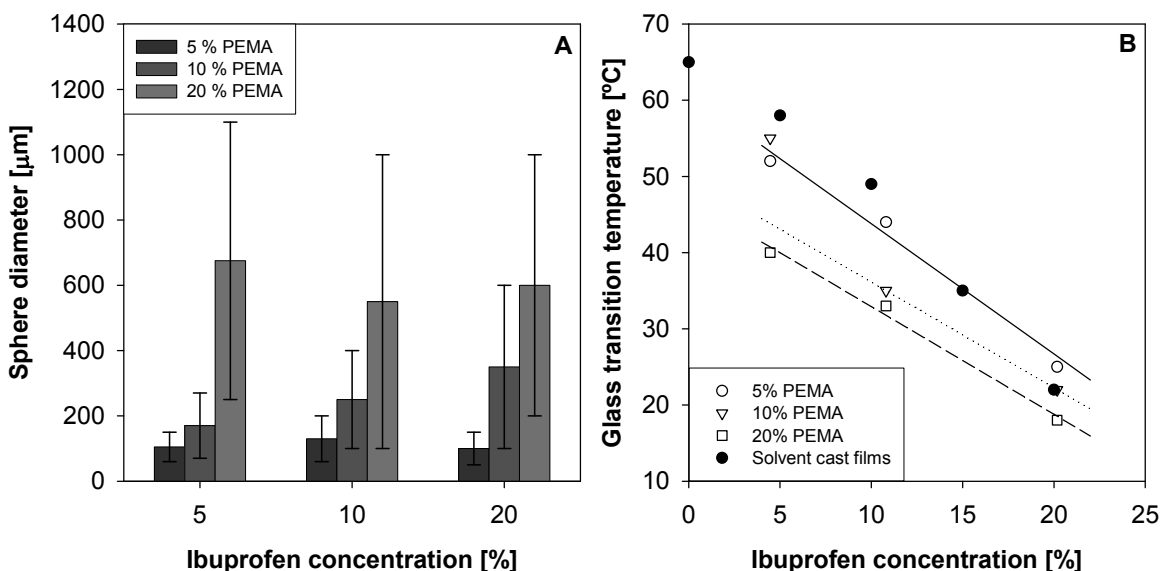

Figure 7.6: Influence of polymer content and ibuprofen concentration in the organic phase on the size (**A**) and glass transition temperature (**B**) of the resulting polymer spheres. The values of the bars in panel A do not represent average values, but rather the center point between the error bars, which in turn represent approximate minimum and maximum sphere size values determined by visual inspection from SEM images. This graph merely serves as an indication of the sphere size, and is not an attempt at statistical evaluation of the sphere size distributions. The linear fits in panel B are meant as a guide to the eye. The 5% ibuprofen and 10% PEMA data point was assumed to be an outlier and is not incorporated in the fit.

In order to determine the influence of stirring speed on the sphere size, spheres have also been prepared using an Ultra-Turrax® disperser at a stirring speed of 11,000 rpm. Indeed, the resulting sphere size decreases dramatically using the same organic to aqueous phase ratio and viscosity of the organic phase (Figure 7.7). Clearly these spheres are too small for the current drug delivery application. However, increasing the polymer content in the organic phase should lead to larger spheres. Alternatively, increasing the ratio of the organic to water phase ratio should also result in larger spheres (due to higher solution

viscosity), although this may also result in more porous spheres [14], which is undesired for the drug delivery concept presented here.
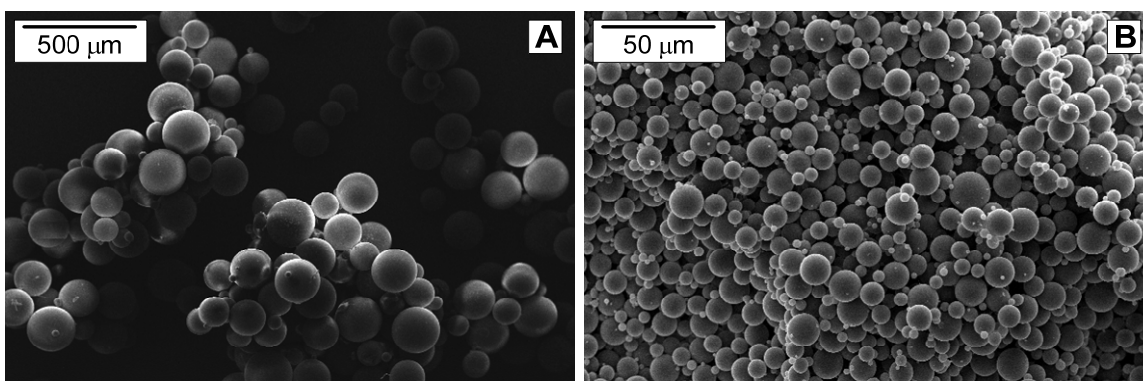

Figure 7.7: Spheres prepared at a stirring speed of 600 rpm (**A**) and 11,000 rpm (**B**). The former were prepared by dispersing 3 mL of organic phase ([PEMA] = 6% (w/w DCM)) in 50 mL 0.4% PVA solution, whereas the latter were formed by dispersing 4.8 mL of the same organic phase in 80 mL 0.4% PVA solution, in order to ensure complete immersion of the stirring shaft of the Ultra Turrax® T25 Basic with S25N-18G dispersing element. Note that the magnification in panel B is 10 times higher than panel A.

In conclusion, the solvent evaporation method seems a promising approach for the preparation of drug and dye containing polymer spheres. Initial investigations have revealed that L-IR788 has no effect on the process of sphere formation, other than giving the spheres its characteristic green color, thus enabling easy incorporation into the polymer spheres. Release studies should reveal whether the increase in release rate predicted by Figure 3.16 is indeed reached. Although the size distribution of the spheres is still rather large, a simple filtration step could narrow this distribution, thus guaranteeing long-term and reproducible on-off switching. Further study is required to investigate the optimal preparation conditions, as well as the minimum size suitable for the current drug delivery application. Also, factors such as sphere porosity, encapsulation efficiency of the drug during sphere formation, and residual DCM content should be thoroughly investigated. It should finally be realized, that although the spheres are expected to increase the release *rate* for each triggering step, the total amount of drug incorporated in an implant of the same size, in which the drug is homogeneously distributed throughout the implant, is inevitably lower, thus reducing the effective lifetime of the implant. In addition, the release rate in the off-state increases by the same

factor as the release rate in the on-state. A trade-off therefore has to be made between release rate (and thus triggering time) and lifetime of the implant.

7.4   Light Emitting Diode (LED) as an NIR source

The NIR-induced release studies, as well as the heating experiments in this thesis have been performed using an NIR laser diode. A relatively cheap alternative for such a laser is a light emitting diode (LED). The main differences between a laser and an LED are listed in Table 7.1.

Table 7.1: Comparison between a laser (Light Amplification by Stimulated Emission of Radiation) and an LED (Light Emitting Diode)

Laser	LED
Coherent light	Incoherent light
Monochromatic ($\Delta\lambda < 2$ nm)	'Less monochromatic' ($\Delta\lambda > 10$ nm)
Collimated beam	Divergent beam
High powers available (up to 40 W)	Relatively low power around 780 nm currently available (maximum of ~1 W)
Relatively expensive	Relatively cheap

The coherence of laser light is of no consequence for the current application, as it is the particle-character of light (i.e. photons exhibiting energy) determining the amount of induced heat and heating rate. Coherence refers to the wave-character of light, which can cause interference effects. In fact, coherence may have an adverse effect on tissue heating since constructive interference following scattering events can lead to local regions of higher intensity (speckle pattern). Incoherent light should results in a more homogeneous intensity distribution, thus minimizing locally higher temperatures. It should be noted that a considerable debate exists concerning the difference in penetration depth of light/radiation originating from an LED or a laser, which mainly focuses on depth at which photobiological effects still occur [15]. It is presumed that the higher length of coherence of a laser results in photobiological effects at greater depths (related to the speckle pattern), but there seems to be no evidence that coherence should affect the penetration depth of the total amount of photons.

The fact that an LED has a larger wavelength distribution (i.e. is less monochromatic) could be disadvantageous, since the amount of heat produced depends directly on the absorbance at a given wavelength. However, as long as the width of the wavelength variation is not too high and is known, this can be corrected for, either by increasing the dye concentration or triggering time.
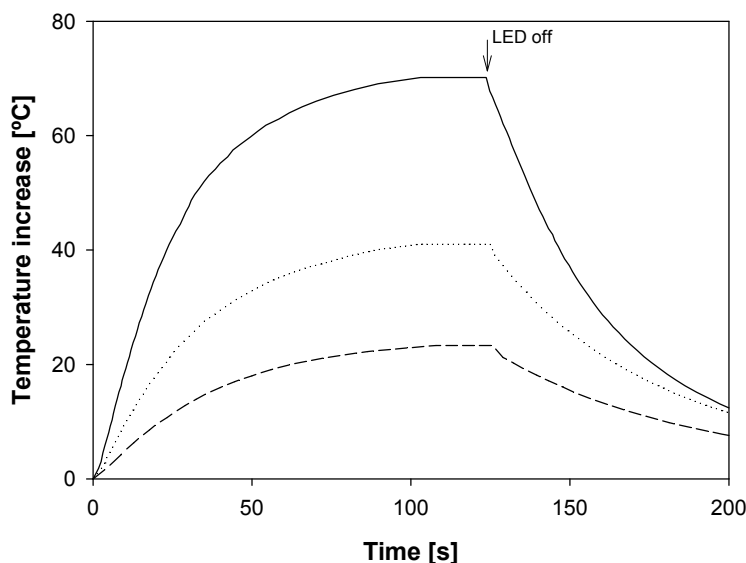

Figure 7.8: Surface temperature increase of an L-IR788 containing PMMA disc induced by an LED (LED780-66-60, 1.1 W @ 600 mA, Roithner Lasertechnik, Vienna, Austria, λ_{max}: 780 nm) at an LED to sample distance of 2 (——), 5 (·········) and 9 mm (- - - -), respectively. The temperature is measured at the back of the sample with an infrared temperature sensor.

The divergence of an LED source is more of a problem, as is illustrated in Figure 7.8. Although a significant increase in temperature of 70ºC is induced at close range (2 mm), the temperature increase rapidly decreases to approximately 23ºC at a distance of only 9 mm due to the wide diverging beam, thus decreasing intensity. When applying LEDs as an energy source, the use of a focusing unit is therefore required. Moreover, the commercial availability of high power LEDs is limited, where the LED used in Figure 7.8 is the most powerful found to date. An LED triggering device should therefore exist of multiple LED sources, creating one focused beam by an optical system consisting of lenses and reflectors, comparable to the commercially available optic in Figure 7.9. Alternatively, a more sophisticated design could consist of multiple convergent beams

which coincide at a focal point (or actually 'focal area'), i.e. the location of the implant. Over the past few years, the power output of LEDs has increased considerably, and is expected to continue over the next few years [16], thus possibly leading to the design of a more simple 'single source' battery-operated hand-held LED triggering device. Important in the design of any LED (or laser) triggering device is that the intensity distribution at the surface of the implant is as homogeneous as possible, thus inducing a temperature increase over the whole surface area of the implant.
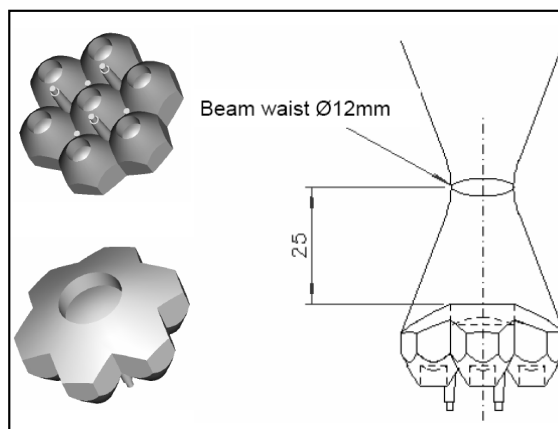

Figure 7.9: 7 Cell Cluster Concentrator Optic produced by Polymer Optics, Ltd., Wokingham, England.

7.5 Outlook

The success of the T_g as an effective and long-term on/off-switch for drug release lies in achieving a close to zero release rate at body temperature, yet being able to induce significant and reproducible drug release with a modest temperature increase to prevent tissue damage from occurring. The required temperature increase depends on the breadth of the glass transition, as well as the strength of it. The methacrylate model polymers with a T_g in the correct temperature range, as used in this research, exhibit a relatively weak glass transition temperature, thus making them unsuitable for this application. The choice of polymers commercially available is therefore limited, and finding the optimal polymer may require synthesis of suitable candidates. The polylactide used in the *in vitro* and *in vivo* studies displays a sharp glass transition temperature, resulting in good on/off-ratios. However, a polymer with a slightly lower T_g (and preferably an even narrower glass transition trajectory) could result in the same on/off-ratio at lower induced temperatures

156

inside the implant. This would relieve the requirement, or perhaps even eliminate the need, of an insulation layer to protect tissue from thermal damage. Moreover, although not tested for sufficiently long times in this research, the potential biodegradability of PLDL in the long-term could pose complications, and limit the lifetime of the implant, thus favoring the use of a non-biodegradable polymer.

The simple design of an implant based on the glass transition switch also imposes strict requirements to the polymer. Besides exhibiting a sharp glass transition trajectory in the correct temperature range, it should provide a suitable matrix for the drugs to be delivered, balancing between high drug solubility (to obtain a high driving force) and low drug solubility (to guarantee a constant driving force in the long term). In this respect, the reservoir system in Figure 3.15A would alleviate the restrictions to the T_g-polymer and would be the preferred system, were it not for the more complex production process and safety issues concerning leakage of the system. The complications concerning the glass transition switch therefore certainly warrant further investigation into the triggering mechanism based on the LCST discussed in Chapter 6, and its applicability to smaller molecules. The volume phase transition occurring around the LCST is generally a much sharper transition and, in combination with a porous support, provides a promising method for on-demand drug delivery.

The clinical application of either of these systems, in combination with NIR as external trigger, should primarily focus on local delivery of drugs, in particular of potent drugs, thus enabling long-term use of the implant. Examples include the treatment of chronic pain by local anesthetics, patients suffering from recurring inflammations, e.g. rheumatoid arthritis, or delivery of drugs for chemotherapy. It should be realized that for each different drug-polymer system, new experiments are required to determine drug solubility and diffusivity in the polymer matrix. Knowledge of the influence of molecule size, shape and flexibility, as well as the influence of specific interactions on diffusion in a polymer matrix, as has been attempted in Chapter 5, would greatly aid the process of design of the drug delivery device for other drug substances.

A potentially interesting application is delivery of drugs directly to the brain by intracerebral implantation, thus circumventing the blood-brain barrier, which is very

efficient in preventing substances from entering the neural tissue through the blood stream [17]. NIR radiation is able to pass through the skull, thus allowing remote triggering of drug release from the implant. However, since intracerebral implantation is not an easy operation, this should only be undertaken if pulsatile release is indeed beneficial for the specific disease.

Finally, it should be stressed that delivery of a sufficient amount of NIR radiation exhibiting a homogeneous intensity distribution into various types of human tissue is not an easy task, and a lot depends on proper design of the NIR device. However, it is expected that using LED technology, hand-held devices can be designed which are suitable for near-infrared induced drug delivery either by the glass transition or LCST switch.

References

[1]   McKenna, G. B. Glass dynamics: Diverging views on glass transition. *Nat. Phys.* **6**, 673-674 (2008).

[2]   Hecksher, T., Nielsen, A. I., Olsen, N. B., Dyre, J. C. Little evidence for dynamic divergences in ultraviscous molecular liquids. *Nat. Phys.***6**, 737-741(2008).

[3]   Angell, C. A. Ngai, K. L., McKenna, G. B., McMillan, P. F., Martin, S. W. Relaxation in glassforming liquids and amorphous solids. *J. Appl. Phys.* **88**, 3113-3157.

[4]   Vogel, H. The law of relation between the viscosity of liquids and the temperature. *Phys. Z.* **22**, 645-646 (1921).

[5]   Tammann, G. & Hesse, W. Die Abhängigkeit der Viscosität von der Temperatur bei unterkühlten Flüssigkeiten. *Z. Anorg. Allg. Chem.* **156**, 245-257 (1926).

[6]   Fulcher, G. S., Analysis of recent measurements of the viscosity of glasses. *J. Am. Ceram. Soc.* **8**, 339-355 (1925).

[7]   Williams, M. L., Landel, R. F., Ferry, J. D. The temperature dependence of relaxation mechanisms in amorphous polymers and other glass forming liquids. *J. Am. Chem. Soc.* **77**, 3701-3707 (1955).

[8]   Hutchinson, J. M. in *The Physics of Glassy Polymers*, 2nd ed. (eds. Haward, R. N. & Young, R. J.) 85-153 (Chapman & Hall, London, 1997).

[9]   Tool, A. Q. Relation between inelastic deformability and thermal expansion of glass in its annealing range. *J. Am. Ceram. Soc.* **29**, 240-253 (1946).

[10]   Hodge, I. M. Enthalpy relaxation and recovery in amorphous materials. *J. Non-Cryst. Solids* **169**, 211-266 (1994).

[11]   Badrinarayanan, P. & Simon, S. L. Origin of the divergence of the timescales for volume and enthalpy recovery. *Polymer* **48**, 1464-1470 (2007).

[12]   Hutchinson, J. M. & Ruddy, M. Thermal cycling of glasses. II. Experimental evaluation of the structure (or nonlinearity) parameter x. *J. Polym. Sci., Part B: Polym. Phys.* **26**, 2341-2366 (1988).

[13]   Hutchinson, J. M., Ruddy, M., Wilson, M. R. Differential scanning calorimetry of polymer glasses: corrections for thermal lag. *Polymer* **29**,152-159 (1988).

[14] Freiburg, S. & Zhu, X. X. Polymer microspheres for controlled drug release. *Int. J. Pharm.* **282**, 1-18 (2004).

[15] Karu, T. I. in *Biomedical Photonics* (ed. Vo-Dinh, T.) 48-1 – 48-25 (CRC, Boca Raton, 2003).

[16] Personal communication: Veltman, M.-J., LEDexpert B.V., Eindhoven, The Netherlands.

[17] Pardridge, W. M. Blood-brain barrier delivery. *Drug Discovery Today* **12**, 54-61 (2006).

Dankwoord

Bijna 5 jaar na aanvang van mijn promotieonderzoek verschijnen hier de allerlaatste woorden van het proefschrift op papier. Bij de totstandkoming van dit proefschrift zijn er een aantal mensen, direct of indirect, betrokken geweest die ik graag wil bedanken.

Allereerst wil ik Jos bedanken voor de mogelijkheid die hij geboden heeft om mijn promotie binnen zijn vakgroep uit te voeren. Jos, ik heb onze samenwerking van begin af aan als zeer prettig ervaren, en ben erg dankbaar voor de vrijheid die je me hebt gegeven tijdens dit onderzoek. Jouw enthousiasme en positieve instelling hebben zeker geholpen om mij te doen inzien dat ik wel degelijk goed werk verrichtte (en daar is wel wat overtuigingskracht voor nodig!). Met even zoveel enthousiasme heeft Maartje mij gedurende de eerste paar jaar van mijn promotie begeleid. Maartje, samen met Jos heb jij de basis gelegd voor dit onderzoek dat mij zo aansprak toen ik voor het eerst in Eindhoven langskwam. Ik wil je heel erg bedanken voor alle discussies die we hebben gehad, je adviezen en motiverende woorden, en de moeite die je hebt gedaan om de begeleiding voort te zetten nadat je bij Friesland Foods (nu FrieslandCampina) aan de slag bent gegaan. Het was een groot plezier om een van jouw raspaardjes te zijn! Ik ben daarnaast ook erg blij dat Richard bereid is geweest om de dagelijkse begeleiding over te nemen van Maartje. Richard, jouw frisse blik binnen dit onderzoek is zeer waardevol geweest, en heeft tot belangrijke toevoegingen aan dit proefschrift geleid. Je bent tijdens een groot deel van de schrijverij betrokken geweest en ik ben je heel erg dankbaar voor het razendsnel, en tegelijkertijd heel goed en kritisch, doorlezen van alles wat ik aanleverde!

Dit werk was niet mogelijk geweest zonder de steun van iedereen bij Dolphys Medical B.V. Ik wil hierbij met name Dirk, Fabiènne, Naomi, Léon, Caroline, Guido en Raf bedanken voor al hun hulp, of dit nou ging om inhoudelijke discussies of praktische zaken op het lab. Binnen het project team heeft het Academisch Ziekenhuis Maastricht ook een belangrijke rol gespeeld, met name met betrekking tot de *in vivo* proeven,

waarvoor ik hen ook dankbaar ben. Ik ben SenterNovem erkentelijk voor de financiële steun die dit project en de samenwerking met de andere leden van het team mogelijk heeft gemaakt. Ik wil ook alle studenten bedanken die een bijdrage hebben geleverd aan het project: Marion Eggink, Dah-Kee Chan, Henk-Jan Cornelissen en Peter van den Crommenacker. Van ieder van jullie is in meer of mindere mate een gedeelte van jullie werk terug te vinden in diverse hoofdstukken van dit proefschrift. Jullie hebben allemaal ervaren, dat onderzoek zelden gaat zoals verwacht, en wil jullie allemaal dan ook heel erg bedanken voor jullie inzet en doorzettingsvermogen. Op experimenteel vlak ben ik ook heel veel dank verschuldigd aan Carin. Carin, jouw hulp en creatieve oplossingen op het lab waren onmisbaar. Ik ben blij dat de geur van NIPAAm jou (en Henk-Jan) niet heeft kunnen afschrikken! Ik heb ook genoten van de vele niet-werkgerelateerde gesprekken die we hadden, waarbij tennis een vaak terugkomend onderwerp was. De drukpuntsmassage heeft ook wonderen gedaan voor mijn arm!

Daarnaast wil ik alle (ex-)collega's van SPD bedanken voor de fijne (werk)sfeer die er heerste, de gezelligheid tijdens de lunch en koffiepauzes (ongeacht waar de koffiekamer zich bevond), de vele vlaaien die hier geserveerd zijn en allerlei andere activiteiten die zich in de loop der jaren bij SPD hebben afgespeeld. Eén van de hoogtepunten is daarbij de studiereis naar Zuid-Afrika, die ik met veel plezier heb georganiseerd samen met Maikel. Maikel, dank je wel voor deze leuke ervaring en fijne samenwerking, waarbij ik kreten als "Thanks in advance, kind regards, …", "James!" en "Handig overzicht" niet snel zal vergeten. Daarnaast wil ik jou en Marcus bedanken voor een onvergetelijke vakantie voorafgaand aan de studiereis, ik heb er echt van genoten. Maikel, ik wil je verder nog bedanken voor alle "si's", wat vooral 's ochtends een onmisbaar ritueel was, en ik ben blij dat je mijn paranimf wilt zijn. Ik wil ook mijn andere paranimf, Stefan, bedanken voor het ongetwijfeld glansrijk vervullen van zijn taak. Stefan (ir. Rovers), je bent een geweldige kantoorgenoot geweest en dankzij jouw werkplek zag mijn bureau er ook nog eens relatief netjes uit. We hebben altijd de nodige gezelligheid en vermaak op ons kantoor gehad, in de vorm van hard meezingen met Nikki, Kies de Kluis, of gewoon gezellig kletsen. Die gezelligheid hebben we ook meegenomen naar de congressen en cursussen, die we samen hebben bezocht, met de aansluitende vakanties. Bedankt voor de leuke tijd die we samen hebben gehad, zowel op kantoor als op reis, als ook voor de

wetenschappelijke discussies die we hebben gehad, zeker gezien de raakvlakken die onze onderzoeken vertoonden. Vishal, I also enjoyed being your room mate for the first part of my PhD-period. You made my move to Eindhoven a very easy transition. Tom en Zwannet, ik wil jullie bedanken voor de nodige sportieve ontspanning in de vorm van tennis in de lunchpauze of na afloop van het werk. Het was een zeer welkome afwisseling op het promoveren. En alle andere SPD'ers, die ik nu niet allemaal bij naam noem: nogmaals bedankt voor de leuke tijd de afgelopen jaren!

Natuurlijk zijn er buiten de TU/e ook de vaste krachten in mijn leven. I want to thank my parents for simply being there and for their continual support, not only during the course of obtaining my PhD, but throughout my life. Westervoort is a place where I can relax and will always feel at home, which is also thanks to you, David and Lindsay. Ik wil daarnaast ook mijn schoonouders bedanken voor hun steun en de leuke weekendjes in Harlingen de afgelopen jaren, waar ik me altijd heel welkom heb gevoeld. Tot slot wil ik Ester bedanken. Ester, jij bent de belangrijkste persoon in mijn leven en jouw liefde betekent heel veel voor me. Ik weet dat wonen in Eindhoven niet jouw eerste keus was, maar je bent wel van studielocatie gewisseld zodat we konden samenwonen. Dank je wel voor je steun, geduld en je bemoedigende woorden die ik nu ook weer zie staan, en die ook voor jou gelden:

Komt goed, schatje!!

Micky

Oktober 2009

Curriculum Vitae

Micky Vertommen was born on September 6th 1980 in Ottignies (Belgium). After completing secondary school at the Thomas à Kempis college in Arnhem (The Netherlands), he studied Chemical Engineering at the University of Twente, in Enschede (The Netherlands). In 2003, he carried out an internship at the Ecole Nationale Supérieure des Arts et Industries Textiles in Roubaix (France). His final graduation project in the Textile Technology Group of professor Marijn Warmoeskerken involved enzymatic surface modification of poly(ethylene terephthalate) to improve hydrophilicity and processability of synthetic fibers. After receiving his master's degree in August 2004, he started his PhD-project in November of the same year in the field of controlled drug delivery, resulting in the thesis before you. In January 2009, he started working as pulp characterization specialist in the Pulp and Shaping group of the research institute of his current employer, Teijin Aramid B.V.

List of publications

J.T.F. Keurentjes, M.F. Kemmere, H. Bruinewoud, M.A.M.E. Vertommen, S.A. Rovers, R. Hoogenboom, L.F.S. Stemkens, F.L.A.M.A. Péters, N.J.C. Tielen, D.T.A. van Asseldonk, A.F. Gabriel, E.A. Joosten & M.A.E. Marcus, Externally Triggered Glass Transition Switch for Localized On-Demand Drug Delivery, *Angewandte Chemie International Edition*, submitted for publication.

M.A.M.E. Vertommen, H.J.L. Cornelissen, C.H.J.T. Dietz, R. Hoogenboom, M.F. Kemmere, J.T.F. Keurentjes, Pore-covered thermoresponsive membranes for repeated on-demand drug release, *Journal of Membrane Science* **322**, 243-248 (2008).

R. Hoogenboom, M.A.M.E. Vertommen, S.A. Rovers, D.T.A. van Asseldonk, J.T.F. Keurentjes, On-demand drug delivery from polymeric implants by external triggering, *Polymer Preprints* **49**(2), 1070 (2008).

M.A.M.E. Vertommen, D.T.A. van Asseldonk, M.F. Kemmere, J.T.F. Keurentjes, *Drug delivery device comprising a pharmaceutically biological active component and an infrared absorbing compound*, WO2008/016297 (A1), 2008.

M.A.M.E. Vertommen, V.A. Nierstrasz, M. van der Veer, M.M.C.G. Warmoeskerken, Enzymatic surface modification of poly(ethylene terephthalate), *Journal of Biotechnology* **120**, 376-386 (2005).